THE ROLE OF ADVANCED POLARIMETRIC CALIBRATION IN HIGH-PRECISION PULSAR TIMING

A THESIS SUBMITTED TO AUCKLAND UNIVERSITY OF TECHNOLOGY
IN FULFILMENT OF THE REQUIREMENTS FOR THE DEGREE OF
DOCTOR OF PHILOSOPHY

Supervisor
Prof. S. Gulyaev
A. Prof. W. van Straten

March 2025

By
Axl Floyd Rogers
Centre for Radio Astronomy and Space Research
School of Engineering, Computer and Mathematical Sciences

Abstract

This thesis explores the impact of instrumental errors in pulsar timing array (PTA) data. PTAs aim to detect low-frequency gravitational waves from a stochastic background of supermassive black hole mergers by monitoring the pulse arrival times of an array of millisecond pulsars with extreme precision. Although PTAs are making significant progress toward this goal, their measurements remain sensitive to unmodeled calibration errors.

Conventional methods employed by current timing pipelines are limited in their ability to handle complex instrumental effects and polarization distortions. The primary aim of this research is to enhance the sensitivity of PTA experiments by implementing more accurate methods for instrumental calibration and pulse arrival time estimation.

We employ Measurement Equation Template Matching (METM) for polarimetric calibration and Matrix Template Matching (MTM) for arrival time estimation. These techniques lead to a reduction in timing residuals and a decrease in white noise by up to sixfold in the Parkes Pulsar Timing Array data, compared to traditional Scalar Template Matching and conventional calibration based on the Ideal Feed Assumption.

While both METM and MTM enhance the time-of-arrival fit, our analysis shows that METM yields only a slight reduction in the median error scale factor—defined here as the multiplicative factor (EFAC) applied to ToA uncertainties to match observed scatter in timing residuals—whereas MTM produces significant improvements. Both methods decrease the overall error added in quadrature (EQUAD). However, METM slightly increases the median uncertainty-weighted standard deviation of the whitened (red-noise-removed) post-fit timing residuals, whereas MTM markedly reduces both the median and maximum values. These results underscore MTM's effectiveness in modeling and mitigating residual calibration errors, thereby significantly enhancing arrival time precision.

These findings have important implications for future PTA data releases, including

improved accuracy in arrival times, better sensitivity to errors in solar system ephemerides and terrestrial time models, more precise measurements of pulsar properties, and increased sensitivity to the stochastic gravitational wave background.

Contents

Abstract **2**

Attestation of Authorship **10**

Co-authorship Contribution **11**

Publications **12**

Acknowledgements **13**

1 Literature Review **14**
1.1 Stellar Evolution . . . 17
1.1.1 Star Formation . . . 17
1.1.2 White Dwarfs . . . 18
1.1.3 Neutron Stars . . . 20
1.1.4 Black holes . . . 21
1.2 Pulsars . . . 25
1.2.1 The Discovery . . . 25
1.2.2 Pulsar Properties . . . 27
1.3 Pulsar Timing . . . 33
1.3.1 Timing Basics . . . 33
1.3.2 Timing Model . . . 36
1.4 Pulsar Timing Arrays . . . 42
1.4.1 Introduction . . . 42
1.4.2 Collaborations . . . 46
1.4.3 Indirect Evidence . . . 46
1.4.4 Recent Progress . . . 50

2 Technical Introduction **52**
2.1 Polarization . . . 55
2.1.1 Position Angle . . . 57
2.1.2 Faraday Rotation . . . 59
2.1.3 Instrumental Effects . . . 60
2.2 Arrival Time Estimation . . . 65
2.2.1 Scalar Template Matching . . . 66

2.2.2 Matrix Template Matching . . . 67
2.3 Instrumental Calibration . . . 70
2.3.1 Ideal Feed Assumption . . . 70
2.3.2 Measurement Equation Modeling . . . 71
2.3.3 Measurement Equation Template Matching . . . 72
2.4 Noise Contributions . . . 74
2.4.1 Radio Frequency Interference . . . 74
2.4.2 White Noise . . . 76
2.4.3 Red Noise . . . 78
2.4.4 Dispersion Noise . . . 79
2.5 Software Tools . . . 82
2.5.1 PSRCHIVE . . . 82
2.5.2 CoastGuard . . . 83
2.5.3 Tempo2 . . . 85
2.5.4 TempoNest . . . 87
2.6 Research Questions . . . 89
2.6.1 Research Question 1 . . . 89
2.6.2 Research Question 2 . . . 89
2.6.3 Research Question 3 . . . 90
2.6.4 Research Question 4 . . . 90
2.6.5 Research Question 5 . . . 91

3 Manuscript 1 **92**
3.1 Introduction . . . 93
3.2 Observations . . . 97
3.3 Methods . . . 99
3.3.1 Polarimetric Calibration . . . 99
3.3.2 Arrival Time Estimation and Analysis . . . 106
3.4 Results . . . 111
3.5 Discussion . . . 117
3.5.1 Time-of-Arrival Goodness-of-Fit . . . 122
3.5.2 Error Scale Factor . . . 123
3.5.3 Error Added in Quadrature . . . 124
3.5.4 Red Noise . . . 125
3.5.5 Impact of METM . . . 127
3.5.6 Impact of MTM . . . 128
3.5.7 Comparison with PPTA DR2 . . . 129
3.6 Conclusion . . . 130
3.7 Appendix . . . 133
3.7.1 Arrival time uncertainty corrections . . . 133
3.7.2 Rejected Red-Noise Models . . . 136
3.7.3 Calibration Steps . . . 139

4 Manuscript 2 **145**
4.1 Introduction . . . 146
4.2 Observations . . . 148
4.3 Methods . . . 150
4.3.1 Template Creation . . . 150
4.3.2 ToA Estimation . . . 150
4.3.3 Noise Modeling . . . 153
4.4 Results . . . 157
4.4.1 Whitened RMS . . . 158
4.4.2 Noise Model Analysis . . . 161
4.5 Discussion . . . 170
4.6 Conclusion . . . 173
4.7 Appendix . . . 174
4.7.1 Noise Model Results . . . 174
4.7.2 Outliers . . . 181

5 Results and Discussion **183**
5.1 Introduction . . . 183
5.2 Polarization Calibration . . . 184
5.3 Timing Precision . . . 185
5.4 Noise Mitigation . . . 187
5.5 Future Directions . . . 188
5.6 Conclusion . . . 193

6 Glossary **227**

List of Tables

3.1 Observational Characteristics of PPTA Pulsars 98
3.2 Relative Arrival Time Uncertainties 107
3.3 Noise Model Priors 109
3.4 Outliers 111
3.5 Noise Statistics and Parameters 113
3.6 Minimum, Median, Maximum White Noise 116
3.7 Best-fit Estimates of EQUAD 117
3.8 Standard Deviations of Whitened Post-fit Timing Residuals 118

4.1 ToA Discrepancies: PSRSPLIT 151
4.2 ToA Discrepancies: MTM Flagged Channels 152
4.3 Noise Model Priors 156
4.4 Model Selection 156
4.5 Pre-fit RMS Residual Statistics 171
4.6 Whitened RMS Residual Statistics 171
4.7 Differences in White Noise 172
4.8 Noise Statistics and Parameters 175
4.9 Outlier Results 182

5.1 Relative Arrival Time Uncertainties at 50 cm 189
5.2 Relative Arrival Time Uncertainties at 10 cm 190

List of Figures

1.1 Hertzsprung-Russell Diagram . . . 19
1.2 M87 Black Hole Image . . . 23
1.3 Pulsar Discovery . . . 26
1.4 Pulsar Lighthouse Model . . . 28
1.5 $P - \dot{P}$ Diagram . . . 30
1.6 Pulsar Populations . . . 32
1.7 Timing Residual Errors . . . 35
1.8 Dispersion Delay . . . 39
1.9 Hellings-Downs Curve . . . 43
1.10 Gravitational Wave Characteristic Strain . . . 44
1.11 Galactic Distribution of IPTA Pulsars . . . 47
1.12 Orbital Decay of PSR B1913+16 . . . 49

2.1 Polarization State . . . 55
2.2 Galactic Magnetic Field . . . 61
2.3 Parallactic Angle Variation . . . 64

3.1 Average Polarization . . . 102
3.2 Faraday Rotation . . . 103
3.3 2D Smoothing Splines . . . 105
3.4 Median Goodness-of-Fit Heat Map . . . 112
3.5 Noise Model Parameters Distributions . . . 119
3.6 Reduced χ^2 Heatmap . . . 120
3.7 Model Comparison . . . 120
3.8 PSR J1600−3053 Noise Models . . . 137
3.9 PSR J1744−1134 Noise Models . . . 138

4.1 Comparison of Whitened Residuals . . . 158
4.2 Comparison of Whitened Residuals . . . 159
4.3 Density Distribution of Whitened RMS Residuals . . . 160
4.4 EFAC: MTM and MPTA_T . . . 162
4.5 EFAC: MTM and STM . . . 163
4.6 EQUAD: MTM and MPTA_T . . . 164
4.7 EQUAD: MTM and STM . . . 165
4.8 Correlation Matrix: MTM . . . 166

4.9 Correlation Matrix: STM 167
4.10 Correlation Matrix: MPTA_{T} 168

Attestation of Authorship

I hereby declare that this submission is my own work and that, to the best of my knowledge and belief, it contains no material previously published or written by another person nor material which to a substantial extent has been accepted for the qualification of any other degree or diploma of a university or other institution of higher learning.

Signature of candidate

Co-authorship Contribution

STUDENT AND SUPERVISOR APPROVALS

By signing you are confirming that the co-author contributions stated in the table(s) below are accurate.

Student Name	Axl Rogers	**Signature**		**Date**	18/02/25
Supervisor Name	Prof. Sergei Gulyaev	**Signature**		**Date**	19/02/25

Chapter Number:	3
Manuscript Title:	Reducing Instrumental Errors in Parkes Pulsar Timing Array Data
Publication Status:	Accepted for Publication
Reference if published:	DOI: 10.3847/1538-4357/ad656e

AUTHOR SURNAME: (order as per manuscript)	CONTRIBUTION (May copy from the guidelines above)
Rogers, Axl F.	Conception and design of the project; acquisition of research data; analysis and interpretation of research data; planning and drafting the research paper
van Straten, Willem	Conception and contribution to design of the project; judgement and planning; contribution of knowledge; contribution to analysis and interpretation of research data; editing significant parts of the research paper
Gulyaev, Sergei	Contribution of knowledge; contribution to analysis and interpretation of research data; editing the manuscript
Parthasarathy, Aditiya	Contribution to acquisition, analysis and interpretation of research data
Hobbs, George	Contribution to acquisition, analysis and interpretation of research data
Chen, Zu-Cheng	Contribution to acquisition, analysis and interpretation of research data
Feng, Yi	Contribution to acquisition, analysis and interpretation of research data
Goncharov, Boris	Contribution to acquisition, analysis and interpretation of research data
Kapur, Agastya	Contribution to acquisition, analysis and interpretation of research data
Liu, Xiaojin	Contribution to acquisition, analysis and interpretation of research data
Reardon, Daniel	Contribution to acquisition, analysis and interpretation of research data
Russell, Christopher, J.	Contribution to acquisition, analysis and interpretation of research data
Zic, Andrew	Contribution to acquisition, analysis and interpretation of research data

STUDENT AND SUPERVISOR APPROVALS

By signing you are confirming that the co-author contributions stated in the table(s) below are accurate.

Student Name	Axl Rogers	**Signature**		**Date**	18/02/25
Supervisor Name	Prof. Sergei Gulyaev	**Signature**		**Date**	19/02/25

Chapter Number:	4
Manuscript Title:	Reducing Instrumental Errors in MeerKAT Pulsar Timing Array Data (TBC)
Publication Status:	Unpublished/Ready for submission for Publication
Reference if published:	N/A

AUTHOR SURNAME: (order as per manuscript)	CONTRIBUTION (May copy from the guidelines above)
Rogers, Axl F.	Conception and design of the project; acquisition of research data; analysis and interpretation of research data; planning and drafting the research paper
van Straten, Willem	Conception and contribution to design of the project; significant intellectual judgement and planning; contribution of knowledge; contribution to analysis and interpretation of research data; editing significant parts of the research paper
Gulyaev, Sergei	Contribution of knowledge; contribution to analysis and interpretation of research data; editing the manuscript

Publications

Agazie, G. et al., “Comparing Recent Pulsar Timing Array Results on the Nanohertz Stochastic Gravitational-wave Background”, *The Astrophysical Journal*, vol. 966, no. 1, Art. no. 105, IOP, 2024. doi:10.3847/1538-4357/ad36be.

Granet, C. et al., "Testing the Warkworth 30m Antenna for Possible Deep Space Network Applications", *6th Australian Microwave Symposium*, Gold Coast, Australia, 10-11 February 2025.

McCallum, L. et al., “The Australian mixed-mode observing program”, *Journal of Geodesy*, vol. 96, no. 10, Art. no. 67, Springer, 2022. doi:10.1007/s00190-022-01657-2.

Reardon, D. J. et al., “Search for an Isotropic Gravitational-wave Background with the Parkes Pulsar Timing Array”, *The Astrophysical Journal*, vol. 951, no. 1, Art. no. L6, IOP, 2023. doi:10.3847/2041-8213/acdd02.

Reardon, D. J. et al., “The Gravitational-wave Background Null Hypothesis: Characterizing Noise in Millisecond Pulsar Arrival Times with the Parkes Pulsar Timing Array”, *The Astrophysical Journal*, vol. 951, no. 1, Art. no. L7, IOP, 2023. doi:10.3847/2041-8213/acdd03

Rogers, A. F. et al., “Reducing Instrumental Errors in Parkes Pulsar Timing Array Data”, *arXiv e-prints*, Art. no. arXiv:2407.20015, 2024. doi:10.48550/arXiv.2407.20015.

S. Weston, et al., "New Zealand VLBI Station Warkworth", *IVS 2021+2022 Biennial Report*, 2023. [Online]. Available: https://ivscc.gsfc.nasa.gov/publications/br2021+2022/nswark.pdf

Zic, A. et al., “The Parkes Pulsar Timing Array Third Data Release”, *Publications of the Astronomical Society of Australia*, vol. 40, Art. no. e049, 2023. doi:10.1017/pasa.2023.36.

Acknowledgements

First and foremost, I would like to express my deepest gratitude to my supervisor, Willem van Straten, whose guidance, encouragement, and immense knowledge have been invaluable throughout my PhD journey. Your unwavering support and constructive feedback have helped shape, not only this thesis, but also my approach to research.

I am also grateful to my co-supervisor, Sergei Gulyaev, whose insightful comments and suggestions greatly improved the quality of this work and challenged me to elevate my research.

A heartfelt thanks to my colleagues and friends in the Parkes Pulsar Timing Array and MeerKAT Pulsar Timing Array for the discussions, collaborations, and support during both the highs and lows of this journey.

I would also like to acknowledge the financial support from the AUT Doctoral Scholarship, without which this research would not have been possible.

On a personal note, I am forever indebted to my family. To my mum and nana, thank you for your endless love, patience, and belief in me. To my sister, for always lifting my spirits with your humor, encouragement, and steady presence. To my wife, Selena, for your unwavering support and understanding through every high and low—you have been my pillar of strength. To my daughter, Danika, whose childlike wonder has constantly reminded me of the curiosity and passion that inspired me to begin this journey. To my newborn daughter, Marcelene, whose arrival has brought a thrilling sense of new beginnings, filling our lives with joy, excitement, and hope for the future. And to my recently discovered son, Chase, whose presence is a beautiful reminder that life is full of extraordinary surprises, unexpected gifts, and reasons to marvel at the world. Each of you has been a profound source of motivation, inspiration, and grounding throughout this process, and this work would not have been possible without your love and support.

Finally, I would like to extend my deepest gratitude to all of those who contributed to this work in ways I may not have mentioned explicitly. This thesis is as much a result of your support as it is of my effort.

Chapter 1

Literature Review

A new era began in 2015 with the detection of gravitational waves (GWs) from a coalescing stellar-mass black hole (BH) binary system (GW150914; [Abbott et al., 2016a]). The Advanced Laser Interferometer Gravitational-Wave Observatory (LIGO; [Aasi et al., 2015]) and Virgo [Acernese et al., 2015] detectors reported three binary BH events during their initial observing run [Abbott et al., 2016b]. The second run detected seven more of these events [Abbott et al., 2019] and the first GWs from a coalescing binary neutron star (NS) system (GW170817; [Abbott et al., 2017a]), which was also observed in the electromagnetic spectrum [Abbott et al., 2017b]. By the end of the third observing run, a total of 50 GW events had been cataloged [Abbott et al., 2021].

While ground-based interferometers, like LIGO and Virgo, detect high-frequency (10^1–10^3 Hz) GWs from stellar-mass BHs and NS mergers [Abbott et al., 2023], Pulsar Timing Arrays (PTAs; [Foster and Backer, 1990]) aim to complement them by leveraging the exceptional long-term rotational stability of millisecond pulsars (MSPs) to detect low-frequency (10^{-9}–10^{-7} Hz) GWs in the form of a stochastic gravitational wave background (GWB)—an incoherent superposition of GWs from a cosmic population of supermassive black hole binary (SMBHB) mergers [Rajagopal and Romani, 1995, Jaffe and Backer, 2003, Wyithe and Loeb, 2003, Sesana et al., 2008, Sesana, 2013, Ravi

et al., 2015, Burke-Spolaor et al., 2019]. Other potential GW sources in the PTA band include primordial quantum fluctuations [Grishchuk, 2005, Boyle and Steinhardt, 2008, Lasky et al., 2016], cosmic strings [Vilenkin, 1981, Damour and Vilenkin, 2000, 2005, Siemens et al., 2007, Ölmez et al., 2010], and cosmological phase transitions [Caprini et al., 2010, Xue et al., 2021].

PTAs have recently uncovered compelling evidence for the stochastic GWB [Agazie et al., 2024, 2023b, Antoniadis et al., 2023c,a, Reardon et al., 2023, Zic et al., 2023, Xu et al., 2023]. Their next major goals are to characterize the detected signal more precisely, determine its sources, and detect continuous GWs from individual SMBHBs [Jenet et al., 2004, Caprini et al., 2010, Corbin and Cornish, 2010, Ellis, 2013, Taylor and Gair, 2013, Arzoumanian et al., 2014, 2015a, Huerta et al., 2015, Zhu et al., 2015b, Babak et al., 2016, Mingarelli et al., 2017]. Achieving these milestones requires highly precise pulse time-of-arrival (ToA) measurements from pulsar observations [Hotan et al., 2005]. Achieving these objectives also involves addressing challenges such as radio-frequency interference [Kocz et al., 2010, Nita and Gary, 2010] and mitigating the effects of the interstellar medium (ISM; [You et al., 2007, Keith et al., 2013, Cordes et al., 2016]).

High-precision pulsar timing also requires statistical analysis of the stochastic nature of a pulsar signal [Manchester et al., 1975, Rathnasree and Rankin, 1995, Osłowski et al., 2011] and a comprehensive understanding of timing noise [Cordes and Downs, 1985, Shannon and Cordes, 2010]. Errors in polarization calibration can also introduce systematic errors in ToAs that could obscure or mimic the expected signal of the GWB [van Straten, 2006]. Therefore, robust polarization calibration methods are required to reduce systematic noise in pulsar timing data for improved timing precision [van Straten, 2004, 2013].

This research explores the impact of implementing advanced instrumental calibration and ToA estimation techniques on improving the timing precision of PTA data.

The thesis is structured as follows: chapter 1 provides an introduction to pulsars and pulsar timing, and chapter 2 covers the technical methodologies employed in pulsar timing, and throughout this research. Manuscript 1, chapter 3, presents the application of these advanced techniques to historical data for all 26 high-priority Parkes PTA pulsars (from Rogers et al. [2024]), highlighting improvements in noise reduction and timing precision. Manuscript 2, chapter 4, presents the application of these methods to new wideband data for all MeerKAT PTA pulsars (from Rogers et al. [2025]). Finally, chapter 5 summarizes the key findings, highlighting the impact of this work on pulsar timing precision and its advantages over conventional methods, while also outlining future research directions for further refinement and to address remaining challenges.

1.1 Stellar Evolution

1.1.1 Star Formation

Star formation begins within giant molecular clouds (GMCs), which are cold, dense regions of gas and dust predominantly composed of molecular hydrogen (H), along with helium (He) and trace amounts of heavier elements [Larson, 1981, Shu et al., 1987, McKee and Ostriker, 2007]. These clouds, which often span tens to hundreds of parsecs, act as the primary reservoirs of star-forming material in galaxies. The internal dynamics of GMCs are governed by a complex interplay between turbulence [Elmegreen and Scalo, 2004, Krumholz and McKee, 2005, Ballesteros-Paredes et al., 2007], magnetic fields [Crutcher, 2012, Federrath and Klessen, 2012, Hennebelle and Inutsuka, 2019], and self-gravity. Together, these factors govern the fragmentation of GMCs into smaller gravitationally bound cores where individual stars begin to form.

The gravitational collapse of a molecular cloud (or a subregion within it) begins when self-gravity exceeds internal pressure support from thermal, turbulent, and magnetic forces. This occurs when the cloud's mass exceeds the Jeans mass (M_J; [Jeans, 1902]), given by

$$M_J = \left(\frac{5k_bT}{Gm}\right)^{3/2}\left(\frac{3}{4\pi\rho}\right)^{1/2}, \tag{1.1}$$

where k_b is the Boltzmann constant, T is the cloud's temperature, G is the gravitational constant, m is the mean molecular mass of gas particles, and ρ is the cloud's density.

A protostar, a newly forming star, gains mass by accreting material from its surroundings [Mac Low and Klessen, 2004], while simultaneously regulating its growth through the release of energy in bipolar outflows [Shu et al., 1994, Bachiller, 1996]. As this process continues, the protostar's core temperature and pressure rise until nuclear fusion occurs (i.e., conversion of H to He), marking the transition to a main-sequence star [Woosley et al., 2002].

Stars spend most of their lifetimes on the main sequence, maintaining hydrostatic equilibrium—a balance between the inward pull of gravity and the outward pressure from energy produced via H fusion in the stellar core [Heger and Woosley, 2002]. This balance prevents gravitational collapse and ensures the structural stability of the star. As H undergoes thermonuclear fusion into He, the core composition evolves, leading to an increase in mean molecular weight. This alters the core's temperature and density, which gradually increases the fusion rate to maintain pressure balance. As a result, the star's luminosity slowly rises over time. After a period spanning millions to billions of years (depending on the star's initial mass), the depletion of core H marks the end of the main-sequence phase [Iben, 1967].

1.1.2 White Dwarfs

Main-sequence stars with low-to-intermediate masses ($< 8\ M_{\odot}$) expand into red giants [Cummings et al., 2018] and eventually lose their outer layers via stellar winds or, in some cases, through mass exchange in a binary system [Iben and Tutukov, 1984]. The remaining core, now a white dwarf (WD), gradually cools over billions of years as it radiates away residual thermal energy [Althaus et al., 2010]. This evolutionary outcome occurs for the majority of main-sequence stars, including our Sun (see fig. 1.1).

WDs remain stable against further collapse due to electron degeneracy pressure (P_e), which counteracts gravitational contraction, and is given by

$$P_e = K_e \left(\frac{\rho}{\mu_e} \right)^{5/3}, \tag{1.2}$$

where ρ is the star's density, μ_e is the average molecular weight per electron (which depends upon the chemical composition of the star), and K_e is a constant that depends on the electron mass.

In contrast, higher-mass stars leave the main sequence and begin He fusion, followed

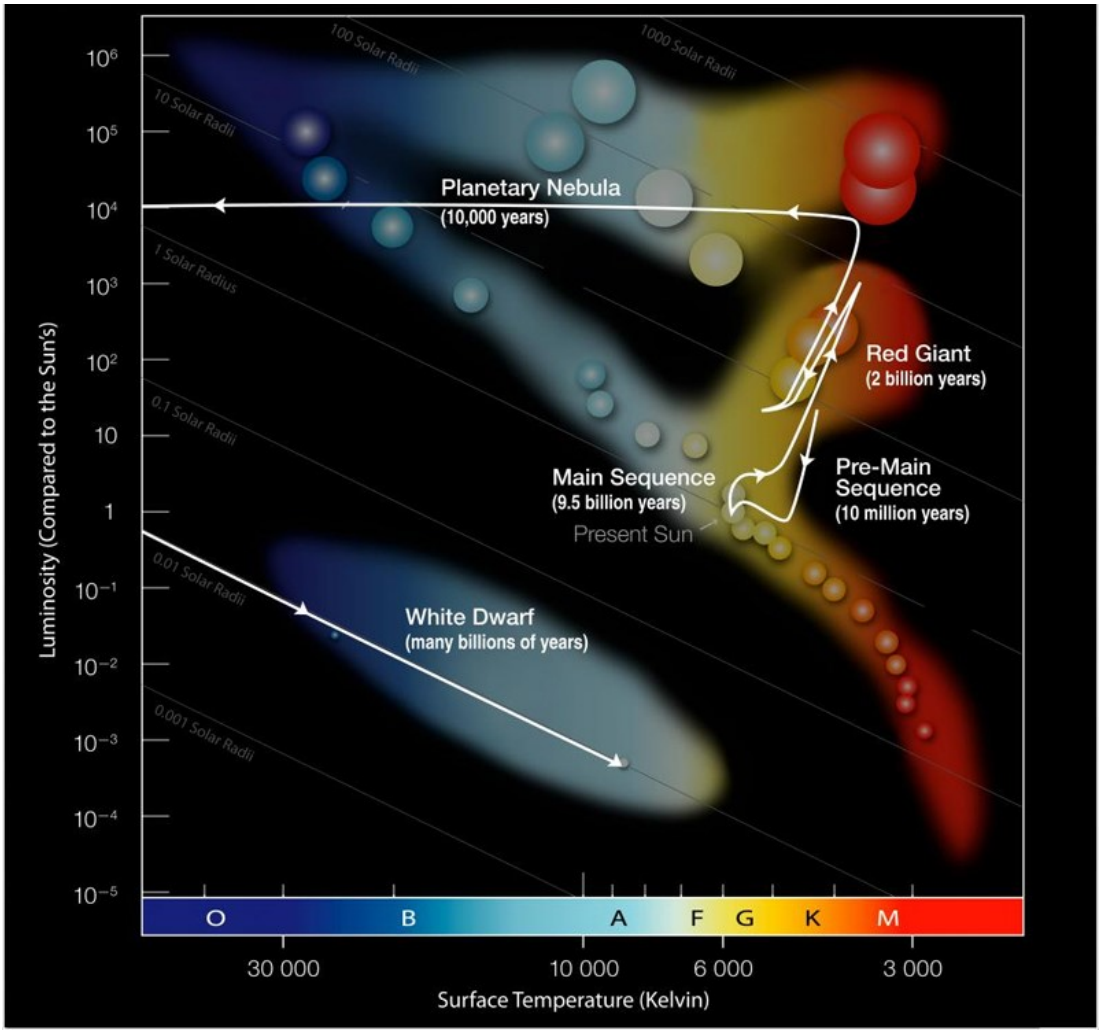

Figure 1.1: The Hertzsprung-Russell diagram depicting stellar evolution. The Sun's evolutionary track is illustrated in white, with annotations marking key phases and their durations. Figure credit: [Harvard-Smithsonian Center for Astrophysics, 2015].

by the successive burning of heavier elements (e.g., carbon, neon, oxygen, and silicon) until they form an inert iron core [Woosley et al., 2002]. Once iron accumulates in the core, nuclear fusion can no longer support the star against gravity. The core collapses, triggering a core-collapse supernova [Bethe, 1990, Janka, 2012]. Depending on the mass of the remnant:

1. If the core mass remains below the Tolman-Oppenheimer-Volkoff (TOV) limit—approximately 2–3 $M_\odot$—a NS forms [Tolman, 1939, Oppenheimer and Volkoff, 1939].

2. If it exceeds the TOV limit, collapse continues into a BH [Fryer, 1999].

Separately, if a WD exceeds the Chandrasekhar limit ($1.4\ M_\odot$; [Chandrasekhar, 1931])—often due to mass accretion in a binary system—further compression triggers electron capture reactions ($e + \rho \rightarrow n + \nu$). In the case of a carbon-oxygen WD, this leads to runaway thermonuclear fusion and results in a Type Ia supernova, which completely disrupts the star [Hillebrandt and Niemeyer, 2000, Nomoto et al., 1984].

1.1.3 Neutron Stars

NSs are the compact remnants of massive stars with initial masses between 8–20 $M_\odot$ that undergo core-collapse supernovae [Heger et al., 2003]. With typical radii of ~10–12 km and masses around 1.4 $M_\odot$, they are among the densest known objects in the Universe. Their interiors are composed predominantly of neutrons and are stabilized against further collapse by neutron degeneracy pressure (P_n), given by

$$P_n = K_n \left(\frac{\rho}{\mu_n} \right)^{5/3}, \tag{1.3}$$

where μ_n is the average molecular weight per neutron, and K_n is a constant that depends on the neutron mass.

NSs exhibit extremely strong gravitational and magnetic fields. Their surface gravity is about 10^{11} times that of Earth, and typical magnetic field strengths range from $B \sim 10^8$ to 10^{12} G. Due to the conservation of angular momentum during collapse, NSs rotate rapidly, with initial spin periods ranging from milliseconds to several seconds [Lattimer and Prakash, 2004].

1.1.4 Black holes

In classical General Relativity (GR), the gravitational collapse of a massive stellar core can lead to a spacetime singularity—a region where energy density and curvature theoretically diverge to infinity [Penrose, 1965]. A BH is characterized by an event horizon, a null hypersurface beyond which the escape velocity exceeds the speed of light [Shapiro and Teukolsky, 1983]. For non-rotating BHs, this boundary is described by the Schwarzschild metric, with radius

$$r_s = \frac{2GM}{c^2}, \tag{1.4}$$

where G is the gravitational constant, M is the BH's mass, and c is the speed of light [Schwarzschild, 1916].

For rotating BHs, described by the Kerr metric [Kerr, 1963], the event horizon depends on the BH's angular momentum. The event horizon's radius is given by

$$r_s = \frac{GM}{c^2}\left(1 + \sqrt{1 - \left(\frac{a}{M}\right)^2}\right), \tag{1.5}$$

where $a = \frac{J}{Mc}$ is the spin parameter, and J is the angular momentum. For a maximally spinning BH ($a = \frac{GM}{c}$), the event horizon radius is minimized to $r = \frac{GM}{c^2}$, illustrating how rotation reduces the BH's size relative to a Schwarzschild BH.

BHs are classified into three main categories based on mass:

- Stellar-mass BHs (a few to tens of $M_\odot$) form from the core-collapse of stars with initial masses $\gtrsim 20\ M_\odot$.
- Intermediate-mass BHs ($\sim 10^2$–$10^4\ M_\odot$) are hypothesized to form via the hierarchical merger of stellar-mass BHs or direct collapse in dense stellar environments [Miller and Colbert, 2004, Miller and Miller, 2015].
- Supermassive BHs (SMBHs) (10^6–$10^{10}\ M_\odot$) are found at the centers of most massive galaxies [Kormendy and Richstone, 1995, Magorrian et al., 1998]. Their growth is thought to occur primarily through a combination of accretion of gas and hierarchical galaxy mergers during galaxy evolution in the framework of the Lambda cold dark matter (ΛCDM) cosmological model [Kormendy and Ho, 2013].

Because no information, including electromagnetic radiation, escapes from within the event horizon, BHs are detectable only through their interactions with surrounding matter. For instance, matter accreting onto a BH forms a disk that radiates primarily in the X-ray band [Remillard and McClintock, 2006], and stellar dynamics near galactic centers can reveal the gravitational influence of SMBHs [Schödel et al., 2002]. A landmark observational breakthrough came in 2019, when the Event Horizon Telescope captured the first image of a BH shadow in the galaxy M87 [Akiyama et al., 2019]. This was later enhanced with polarization data, revealing the magnetic field structure in the BH's immediate environment (see fig. 1.2; [Event Horizon Telescope Collaboration et al., 2021]).

GWs provide another powerful means of probing BHs. The inspiral and mergers of stellar-mass BHs and NSs have been detected by ground-based interferometers such as LIGO and Virgo [Abbott et al., 2016a,b, 2017a,b, 2019, 2021]. These detectors are sensitive to compact binaries with component masses in the range $\sim$ 1–100 $M_\odot$. More recently, evidence for a stochastic GWB—likely arising from the cosmic population of

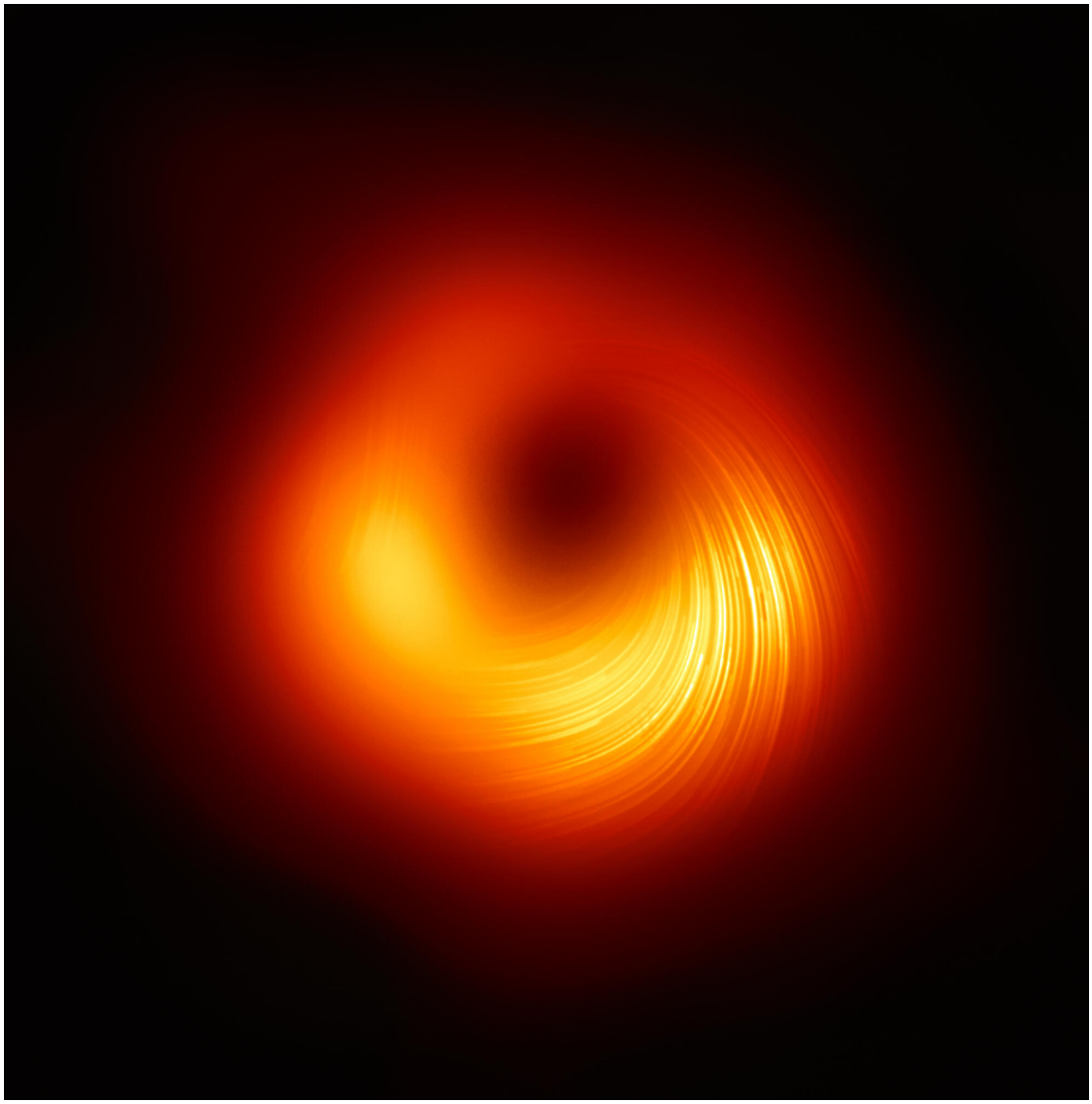

Figure 1.2: The first-ever image of a BH at the center of galaxy M87, with added polarization data that reveals the structure of its magnetic field. Figure credit: [Event Horizon Telescope Collaboration et al., 2021].

SMBHBs with masses ~ 10^7–10^9 $M_\odot$—has emerged from independent and parallel PTA experiments [Agazie et al., 2024, 2023b, Antoniadis et al., 2023c,a, Reardon et al., 2023, Zic et al., 2023, Xu et al., 2023]. These low-frequency GWs are generated as SMBHBs inspiral over cosmic timescales, providing compelling evidence for the hierarchical formation of massive galaxies and their central BHs.

1.2 Pulsars

1.2.1 The Discovery

Pulsars were first detected in 1967 by Jocelyn Bell Burnell and Anthony Hewish during a study of interplanetary scintillation at the Mullard Radio Astronomy Observatory. During their observations, they recorded periodic radio pulses occurring every 1.337 s, each with a pulse width of approximately 16 ms (see fig. 1.3). These mysterious signals were initially nicknamed "Little Green Man 1", humorously suggesting an extraterrestrial origin [Hewish et al., 1968]. Additional sources were soon discovered, and their consistent periodicity and apparent celestial origin indicated that the signals were not terrestrial or from within the solar system [Pilkington et al., 1968].

Initially, WDs were considered a possible source [Thorne and Ipser, 1968], but were quickly ruled out due to physical constraints. The short pulse duration implied an emitting region only a few hundred kilometers across, and the exceptional regularity pointed to an object with both extreme density and rotational stability characteristics inconsistent with WDs. Gold [1968] proposed that the pulses originated from NSs emitting beams of radiation along misaligned magnetic and rotational axes, producing the observed periodicity via a lighthouse-like effect. This model was strongly supported by the discovery of similar pulses from the Crab Nebula's supernova remnant [Staelin and Reifenstein, 1968, Comella et al., 1969], confirming pulsars as rapidly rotating NSs. The original source was later designated B1919+21 based on its celestial coordinates.

In 1974, Hewish received the Nobel Prize in Physics for his role in the discovery of pulsars. Although Bell Burnell was not included in the award, her critical role in the discovery has since been widely recognized; she was later honored with numerous accolades, including the 2018 Special Breakthrough Prize in Fundamental Physics.

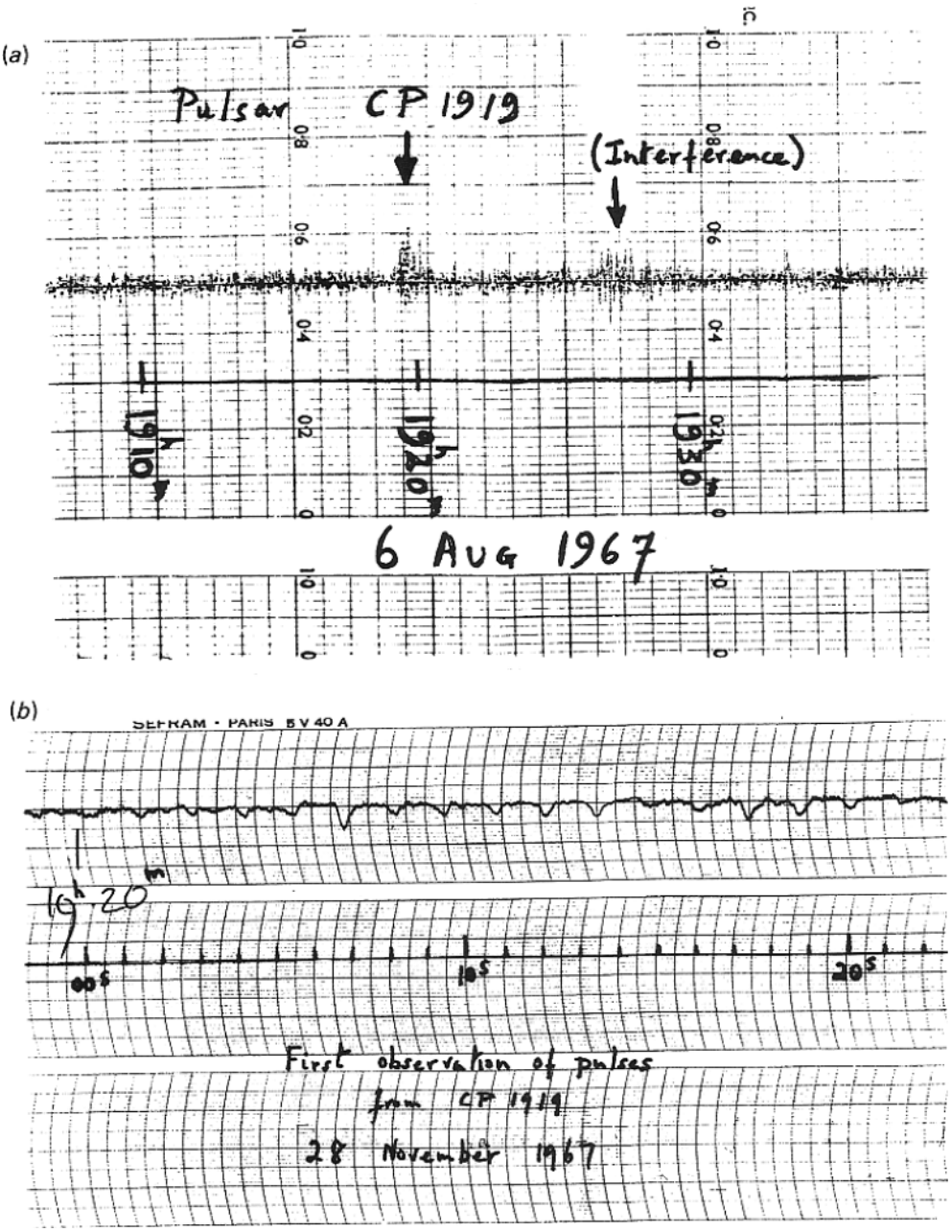

Figure 1.3: Pulsar B1919+21, also known as CP1919 (Cambridge Pulsar, located at right ascension $\alpha = 19^{\mathrm{h}}\ 19^{\mathrm{m}}$), was initially detected as a faint, noise-like signal on a scintillation survey chart—almost lost in background interference (top image). A later recording, taken at a higher chart speed (bottom image), revealed distinct, evenly spaced pulses occurring every 1.337 s. This demonstrated that what initially seemed like random noise was actually a pattern of regular pulses [Hewish et al., 1968]. Image credit: Jocelyn Bell Burnell and Antony Hewish.

1.2.2 Pulsar Properties

NSs are categorized into three main types—canonical pulsars, MSPs, and magnetars—primarily distinguished by their magnetic field strength (B)[1] and rotational period (P). Pulsars are rapidly rotating, highly magnetized NSs that emit beams of radiation from their magnetic poles. These beams, produced by magnetospheric particle acceleration, create periodic pulses when they sweep across the observer's line-of-sight—a geometry often referred to as the lighthouse model or magnetic dipole model [Gold, 1968, Pacini, 1968]. This model was further developed to explain spin-down and energy loss via magnetic dipole radiation [Goldreich and Julian, 1969, Taylor and Manchester, 1977] (see fig. 1.4). Although they are named for these pulses, the emission is continuous; the periodicity arises from the misalignment of the magnetic and rotational axes.

Canonical pulsars typically have magnetic field strengths of $B \sim 10^{12}$ G and P on the order of seconds. Their emission is powered by the gradual loss of rotational kinetic energy, which leads to a steady increase in P over time—a process known as pulsar braking [Goldreich and Julian, 1969, Lorimer and Kramer, 2012]. The rotational kinetic energy of a pulsar is given by

$$E = \frac{2\pi^2 I}{P^2}, \tag{1.6}$$

and its spin-down luminosity (energy loss rate) is

$$-\dot{E} = \frac{4\pi^2 I \dot{P}}{P^3}, \tag{1.7}$$

[1] In classical electromagnetism, the term 'magnetic field strength' typically refers to H (measured in $\frac{A}{m}$), while B is known as the magnetic flux density or magnetic induction (measured in Tesla or G). However, in astrophysics—particularly in discussions of NSs and pulsars—the term 'magnetic field strength' conventionally refers to B, as it directly governs magnetospheric physics, synchrotron radiation, and particle dynamics. In this work, we follow this astrophysical convention and use 'magnetic field strength' to denote B, while H is not explicitly considered.

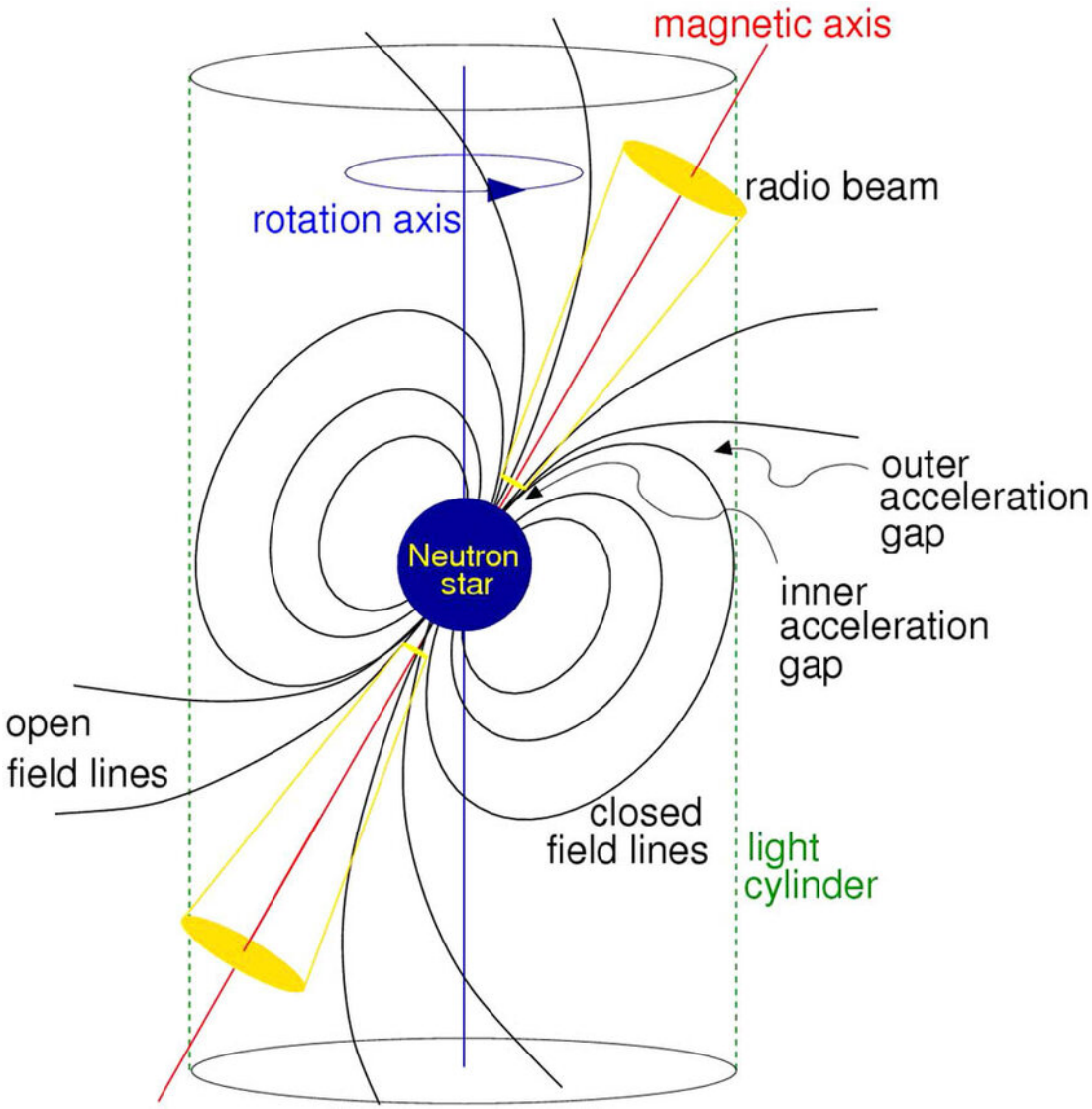

Figure 1.4: The lighthouse model. Particle cascades accelerate within the "gap" regions of the magnetosphere. These particles travel out-and-along the open magnetic field lines, emitting coherent radio emission. As the pulsar rotates, the beam of radiation sweeps across space, creating observable pulses due to the misalignment between the magnetic and rotational axes. Figure credit: [Lorimer and Kramer, 2012].

where I is the NS's moment of inertia. The magnetic field strength can be estimated by

$$B \gtrsim 3.2 \times 10^{19} P\dot{P}^{1/2} \quad (\mathrm{G}), \tag{1.8}$$

and the minimum mean density required to support a given rotation period is

$$\rho = \frac{3\pi}{GP^2}. \tag{1.9}$$

The characteristic age (τ) of a pulsar, a useful estimate of how long it has been spinning down since birth [Manchester and Taylor, 1977], is given by

$$\tau = \frac{P}{2\dot{P}}. \tag{1.10}$$

Pulsars emit radiation across the electromagnetic spectrum, most prominently in the radio band but often extending into optical, X-ray, and γ-ray wavelengths.These emissions are generally understood to originate from relativistic particles accelerated along curved magnetic field lines in the magnetosphere, producing synchrotron or curvature radiation [Ruderman and Sutherland, 1975]. Although the precise details remain debated, a widely accepted framework involves strong electric fields induced by the rotating magnetic dipole, which accelerate charged particles in so-called "gap" regions. Over time, pulsars slow down and may cross the so-called death line, beyond which their magnetospheres can no longer accelerate particles or sustain emission [Duncan and Thompson, 1992]. Pulsars with $P >$ a few seconds and $B < 10^{10}$ G typically become undetectable in this phase (see fig. 1.5). Occasionally, pulsars exhibit glitches—sudden increases in spin rate—believed to result from interactions between the crust and the internal neutron superfluid [Anderson and Itoh, 1975, Wang et al., 2012].

Histograms of P, $\dot{P}$, and B (see fig. 1.6) reveal two distinct pulsar populations:

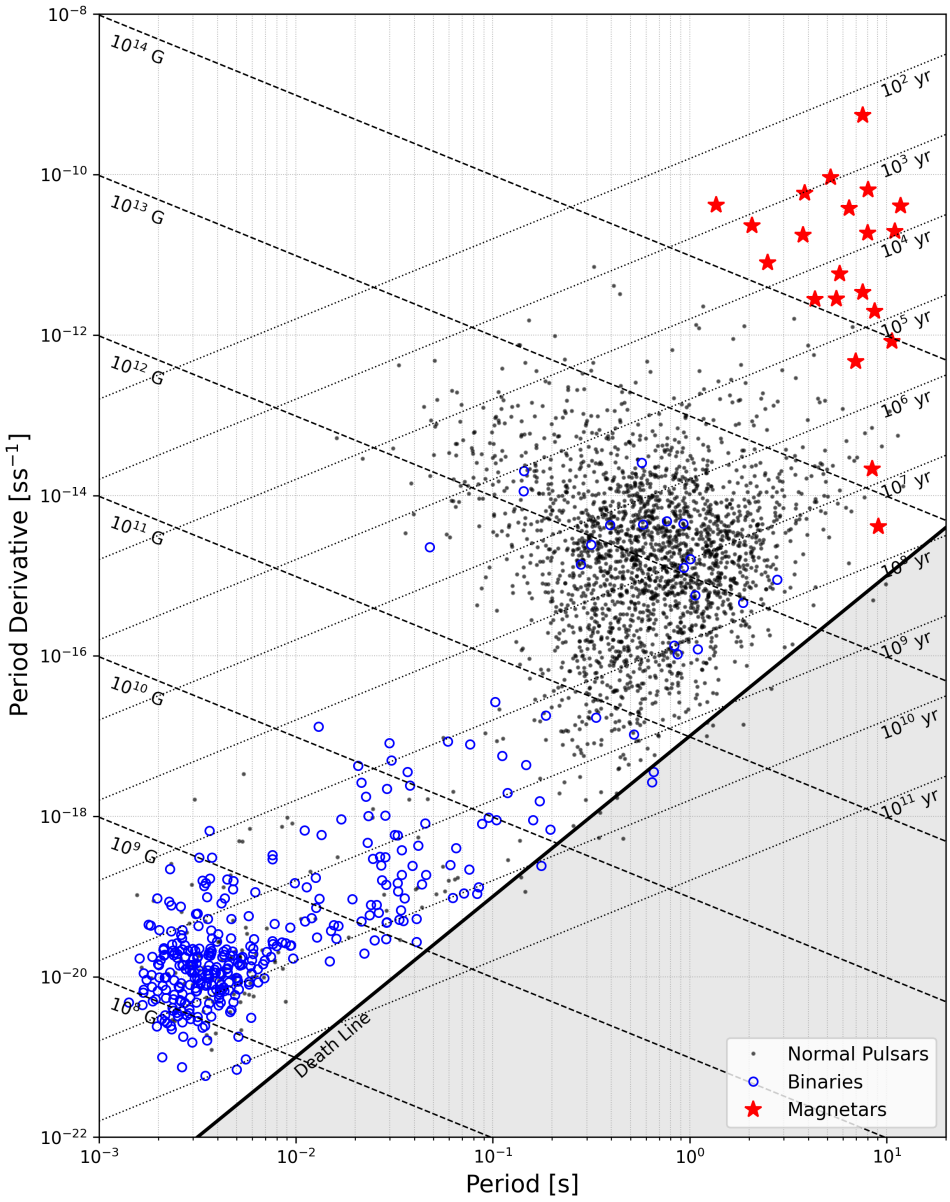

Figure 1.5: The P – $\dot{P}$ diagram, plotted using the latest data from the ATNF Pulsar Catalogue [Manchester et al., 2005], shows the logarithmic distribution of spin period (P_0, in seconds) versus period derivative (P_1, in ss^{-1}) for all known pulsars to date. Binary pulsars are indicated by blue circles. Two distinct populations are visible: the dense cluster of MSPs at low P and low $\dot{P}$, and the broader distribution of canonical pulsars with longer periods and higher spin-down rates. The sparse region in upper-right-most corner denotes the approximate location of magnetars (red stars), which have extremely high magnetic fields and emit primarily in X-rays and γ-rays rather than radio. The gray region under the "death line" is where a pulsar's radio emission ceases to be detectable.

canonical pulsars and MSPs. The magnetar population, visible in the P–$\dot{P}$ diagram (Figure 1.5), is too small to produce a discernible peak in the histograms.

MSPs form via accretion-induced spin-up in binary systems [Alpar et al., 1982, Radhakrishnan and Srinivasan, 1982, Bhattacharya and van den Heuvel, 1991]. As material from a companion star is accreted, angular momentum is transferred to the NS, reducing P to a few milliseconds. The first MSP, PSR B1937+21 (P = 1.558 ms), was discovered in 1982 [Backer et al., 1982]. To date, over 3000 pulsars have been identified [Manchester et al., 2005], ranging from PSR J0250+5854 (P = 23.5 s) [Tan et al., 2018] to the fastest-known PSR J1748−2446ad (P = 1.4 ms) [Hessels et al., 2006]. MSPs are incredibly stable rotators, rivaling atomic clocks over long timescales, and are central to high precision PTA experiments [Hobbs et al., 2012, Lorimer, 2008].

Magnetars, in contrast, are young NSs with extreme magnetic fields (B = 10^{14}–10^{15} G) [Duncan and Thompson, 1992, Thompson and Duncan, 1995, 1996]. These fields decay over time, releasing energy that powers high-energy emission in the form of Soft Gamma-ray Repeaters (SGRs) and Anomalous X-ray Pulsars (AXPs) [Kouveliotou et al., 1998, Mereghetti et al., 2015, Kaspi and Beloborodov, 2017]. Magnetic decay induces crustal fractures and magnetospheric activity that can lead to sporadic outbursts or, in extreme cases, giant flares releasing up to 10^{47} erg (10^{40} J)—briefly outshining the rest of the γ-ray sky.

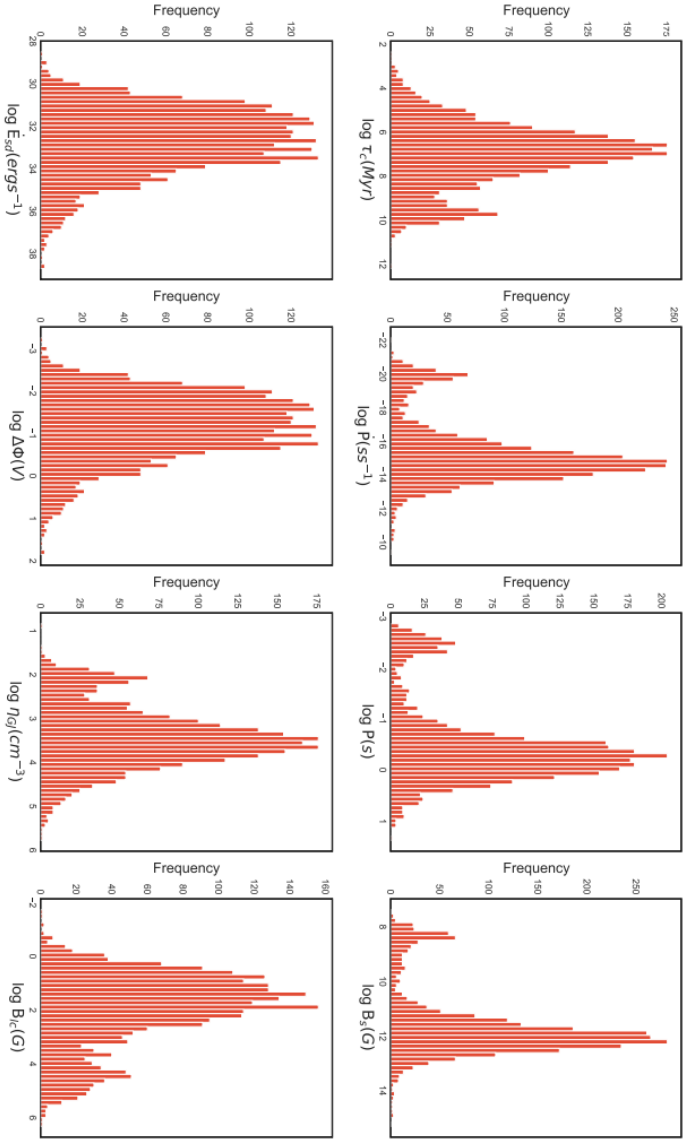

Figure 1.6: Logarithmic distributions of key pulsar variables essential for understanding their emission behavior and evolutionary state, illustrate the separation of millisecond and normal pulsars into distinct populations. These distributions exhibit two clear maxima, reflecting distinct populations based on intrinsic pulsar parameters. The spin period (P) and its time derivative ($\dot{P}$), the surface magnetic field strength (B_s), the magnetic field at the light cylinder ($B_{\rm lc}$), the spin-down luminosity ($\dot{E}$sd), the characteristic age (τ_c), the surface electric voltage ($\Delta\Phi$), and the Goldreich–Julian charge density (ηGJ) gives the expected density of magnetospheric plasma required to support co-rotation. These quantities help distinguish between pulsar populations and are essential for understanding their emission behavior and evolutionary state. Figure credit: [García et al., 2022].

1.3 Pulsar Timing

1.3.1 Timing Basics

Pulsar timing is a powerful tool for studying various phenomena, including the ISM [Cordes and Lazio, 2002, Keith et al., 2013, Coles et al., 2015], NS internal structure and stellar evolution dynamics [Anderson and Itoh, 1975, Link et al., 1999], GR [Kramer et al., 2006], nuclear matter densities [Demorest et al., 2010, Antoniadis et al., 2013, Özel and Freire, 2016, Fonseca et al., 2021, Riley et al., 2021], nuclear physics [Espinoza et al., 2011], exoplanets [Wolszczan and Frail, 1992, Wolszczan, 1994], and low-frequency GWs [Sazhin, 1978, Detweiler, 1979].

Pulsar timing is the process of measuring the ToAs of pulses at the telescope, using a predictive model to account for all known effects that influence those arrival times. While all pulsars can be timed, MSPs are particularly valuable for timing due to their exceptional rotational stability, which enables long-term, high-precision timing with sub-microsecond accuracy [Matsakis et al., 1997, Verbiest et al., 2009].

The timing model (see §1.3.2) describes the pulsar's spin parameters, astrometric position, proper motion, and—for binary systems—the orbital elements. It also accounts for delays caused by the ISM, such as dispersion measure (DM), and includes relativistic time delays both intrinsic to the pulsar system and due to the gravitational influence of bodies in the solar system. Corrections for the Earth's motion and the dynamics of the solar system are applied separately when converting observed arrival times to the reference frame of the Solar System Barycenter (SSB) [Hobbs et al., 2006].

Comparing observed pulse ToAs (t_{observed}) with those predicted by the timing model (t_{model}) yields the timing residual

$$\Delta t = t_{\text{observed}} - t_{\text{model}}, \tag{1.11}$$

where minimizing the residuals (Δt) refines the model parameters and improves predictive power.

Small deviations in residuals can signal a range of physical phenomena, including binary companions, glitches, timing noise, or the presence of GWs. Upon discovery, a pulsar's initial spin frequency, spin-down rate, sky position, and DM can be estimated, but these parameters become increasingly well-constrained through regular long-term monitoring [Edwards et al., 2006]. Inaccuracies in the timing model can manifest as systematic structures in the residuals (see fig. 1.7 for examples).

To improve the signal-to-noise ratio (S/N) of the observed pulsar signal—which can vary significantly from one pulse to the next—astronomers use a technique called "pulse folding". This process involves recording the radio signal as the pulsar's beam sweeps across the antenna, correcting for interstellar dispersion and the observatory's motion, and then coherently aligning and averaging many successive pulses. The resulting stable mean pulse profile has a significantly enhanced S/N, enabling precise ToA measurements [Lorimer, 2008].

In earlier studies, individual pulsars were used to constrain the strength (amplitude) of a potential stochastic GWB by setting upper limits [Kaspi et al., 1994]. However, this approach faces challenges because many pulsars emit faint, highly variable individual pulses that fluctuate in shape and intensity—variability that is intrinsic to the pulsar and not due to ISM effects [Cordes and Shannon, 2010]. Such pulse-to-pulse variability makes them unsuitable for the high-precision timing needed in PTAs. Nevertheless, in some cases, individual pulses are strong enough to study specific pulsar properties, such as jitter noise [Cordes and Downs, 1985], flux density variations [Cordes et al., 2004], and phase modulation phenomena like sub-pulse drifting [Drake and Craft, 1968, Hassall et al., 2013]. For PTA applications, however, stable timing relies on averaged pulse profiles, which reduce this variability and provide a consistent signal basis for precise ToA measurements [Lorimer and Kramer, 2012].

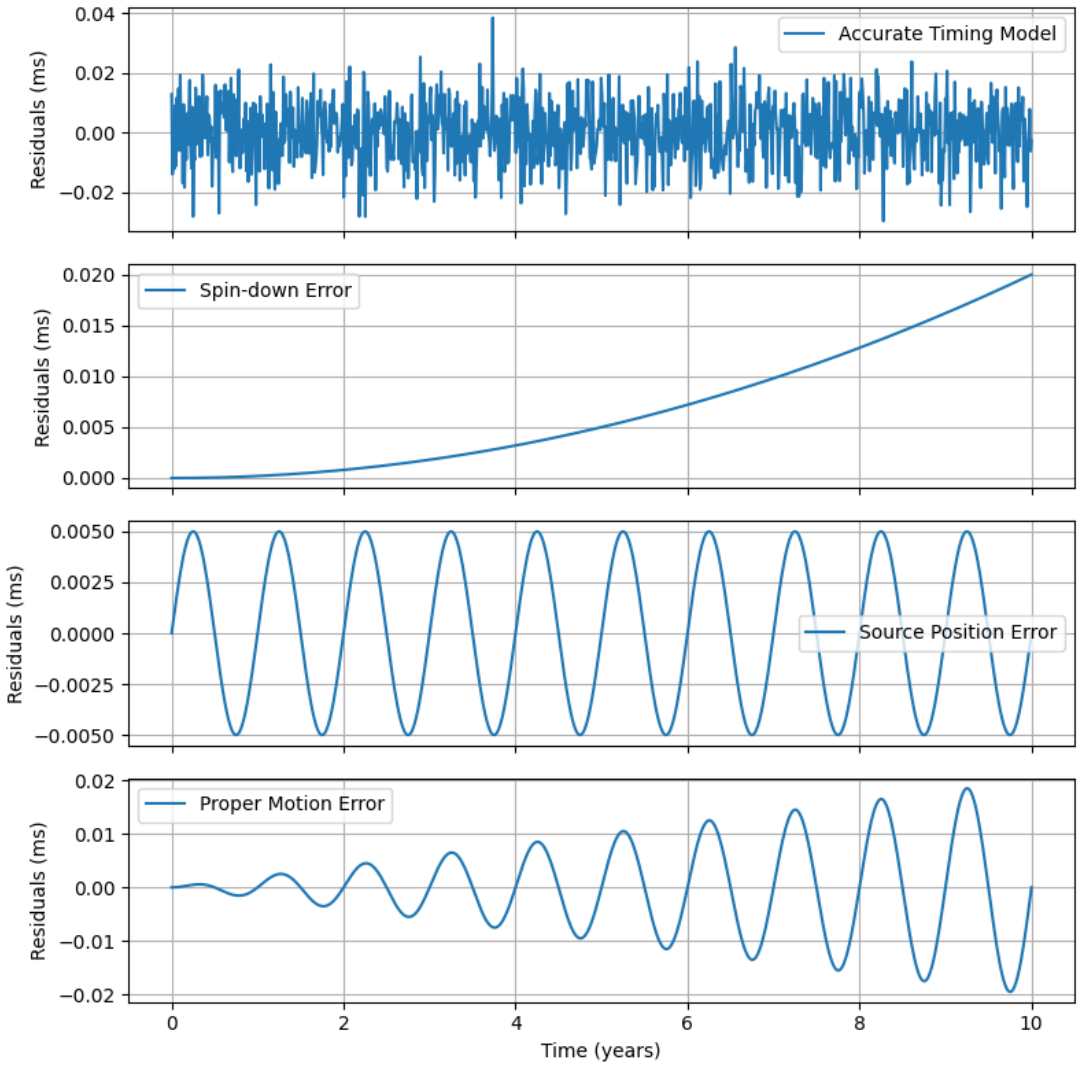

Figure 1.7: Illustrations of pulsar timing residuals exhibiting characteristic patterns caused by inaccuracies in the timing model parameters. From top to bottom: an ideal model yielding near-zero residuals; a spin-down error producing a quadratic trend; a position error generating sinusoidal residuals; and a proper motion error resulting in sinusoidal residuals with linearly increasing amplitude.

In addition to their utility for high-precision timing, pulsars are powerful tools for studying the magneto-ionic environments they reside in. Their integrated polarimetric pulse profiles—formed by averaging the Stokes parameters over many rotations—encode information about the pulsar's emission geometry and the intervening ISM's magnetic field and electron content [Helfand et al., 1975]. While these average profiles are generally stable, long-term polarimetric monitoring can reveal changes in emission modes [Miles et al., 2022] or nulling events [Backer, 1970], offering insight into the pulsar magnetosphere. These phenomena, which occur on timescales from minutes to months, are important considerations in extended timing campaigns.

1.3.2 Timing Model

A pulsar timing model must account for all known factors that influence pulse ToAs. The timing parameters are continuously refined to best fit the observed data. This iterative process employs techniques such as least-squares fitting and Bayesian inference to minimize the timing residuals [Press et al., 1992].

To accurately model ToAs, the observed topocentric arrival times (t_{topo}), measured at the telescope on Earth, must be converted to the nearly inertial SSB reference frame (t_{SSB}). This conversion includes various delays and corrections related to Earth's motion, the ISM, and relativistic effects. The pulsar timing equation expresses this transformation as

$$t_{\mathrm{SSB}} = t_{\mathrm{topo}} + \Delta_{\mathrm{clock}} - \Delta_{\mathrm{DM}} + \Delta_{\mathrm{R}_\odot} + \Delta_{\mathrm{S}_\odot} + \Delta_{\mathrm{E}_\odot} + \Delta_{\mathrm{R}_B} + \Delta_{\mathrm{S}_B} + \Delta_{\mathrm{E}_B}, \tag{1.12}$$

where Δ_{clock} corrects for differences between the observatory clock and terrestrial time standards, and Δ_{DM} is the dispersion delay from the frequency-dependent interaction of radio waves with free electrons in the ISM. The negative sign on Δ_{DM} reflects the convention in pulsar timing to subtract dispersion effects.

The terms $\Delta_{R_\odot}$, $\Delta_{S_\odot}$, and $\Delta_{E_\odot}$ represent, respectively, the Roemer delay (geometric light travel time across the Solar System), the Shapiro delay (gravitational time delay), and the Einstein delay (due to relativistic time dilation and redshift). The subscript $\odot$ denotes Solar System contributions.

If the pulsar is in a binary system, additional binary-induced corrections—Δ_{R_B}, Δ_{S_B}, and Δ_{E_B}—are required. The Shapiro delay (Δ_S) and Einstein delay (Δ_E), particularly in binaries, are essential for testing GR in the strong-field regime [Stairs, 2003].

Clock Corrections

In pulsar timing, several factors can introduce errors that impact either the measurement of pulse arrival times or the interpretation of those times in the timing model. Measurement uncertainties and propagation effects—such as interstellar scattering—can degrade the precision of the recorded ToA. In contrast, other sources of error, such as inaccuracies in the Solar System Ephemeris (SSE) [Champion et al., 2010] or instabilities in terrestrial time standards [Hobbs et al., 2012], do not alter the ToAs themselves but instead can introduce systematic errors into the timing analysis.

SSE and clock errors manifest in the timing residuals as spatially correlated noise, which can mimic or obscure the low-frequency GWB signal of interest [Hobbs et al., 2006, Tiburzi et al., 2016]. For example, an error in the terrestrial timescale introduces a monopolar correlation across all pulsars, uniformly shifting arrival times. In contrast, SSE errors often produce dipolar spatial correlations, arising from inaccuracies in planetary masses or orbital elements [Caballero et al., 2018, Guo et al., 2019].

To minimize timing errors from clock instabilities, pulsar signals are time-stamped using highly stable atomic clocks, such as hydrogen masers. These clocks provide excellent short-term stability but require long-term corrections to remain synchronized with standard time scales, such as Coordinated Universal Time (UTC) or International

Atomic Time (TAI). This correction is applied using

$$t_{\text{clock}} = t_{\text{observed}} + \Delta t_{\text{corr}}, \tag{1.13}$$

where Δt_{corr} accounts for long-term drift and ensures consistency of timing data across observatories [Petit and Tavella, 1996, Rodin, 2008, Hobbs et al., 2020].

Because both SSE and clock errors introduce correlated structure into PTA datasets, identifying and mitigating these effects is essential to distinguish true GW signatures from systematic noise in the residuals.

DM Corrections

As radio signals from pulsars traverse the ISM, they are subject to several propagation effects that can distort timing measurements. One of the most significant of these is dispersion, which arises from interactions between the radio waves and free electrons in the ionized ISM. As radio waves travel through the ionized ISM, they interact with free electrons, resulting in dispersion—a phenomenon where lower-frequency waves are delayed more than higher-frequency ones due to the frequency-dependent refractive index of the plasma (see fig. 1.8). This effect introduces a delay in pulse arrival times that must be accurately corrected in pulsar timing [Condon and Ransom, 2016].

The dispersion delay (Δ_{DM}) varies inversely with the square of the observing frequency and is given approximately by

$$\Delta_{\text{DM}} \approx 4.149 \times 10^3 \left(\frac{\text{DM}}{\text{pc cm}^{-3}}\right)\left(\frac{\nu}{\text{MHz}}\right)^{-2}. \tag{1.14}$$

The delay depends on the DM, which quantifies the total column density of free

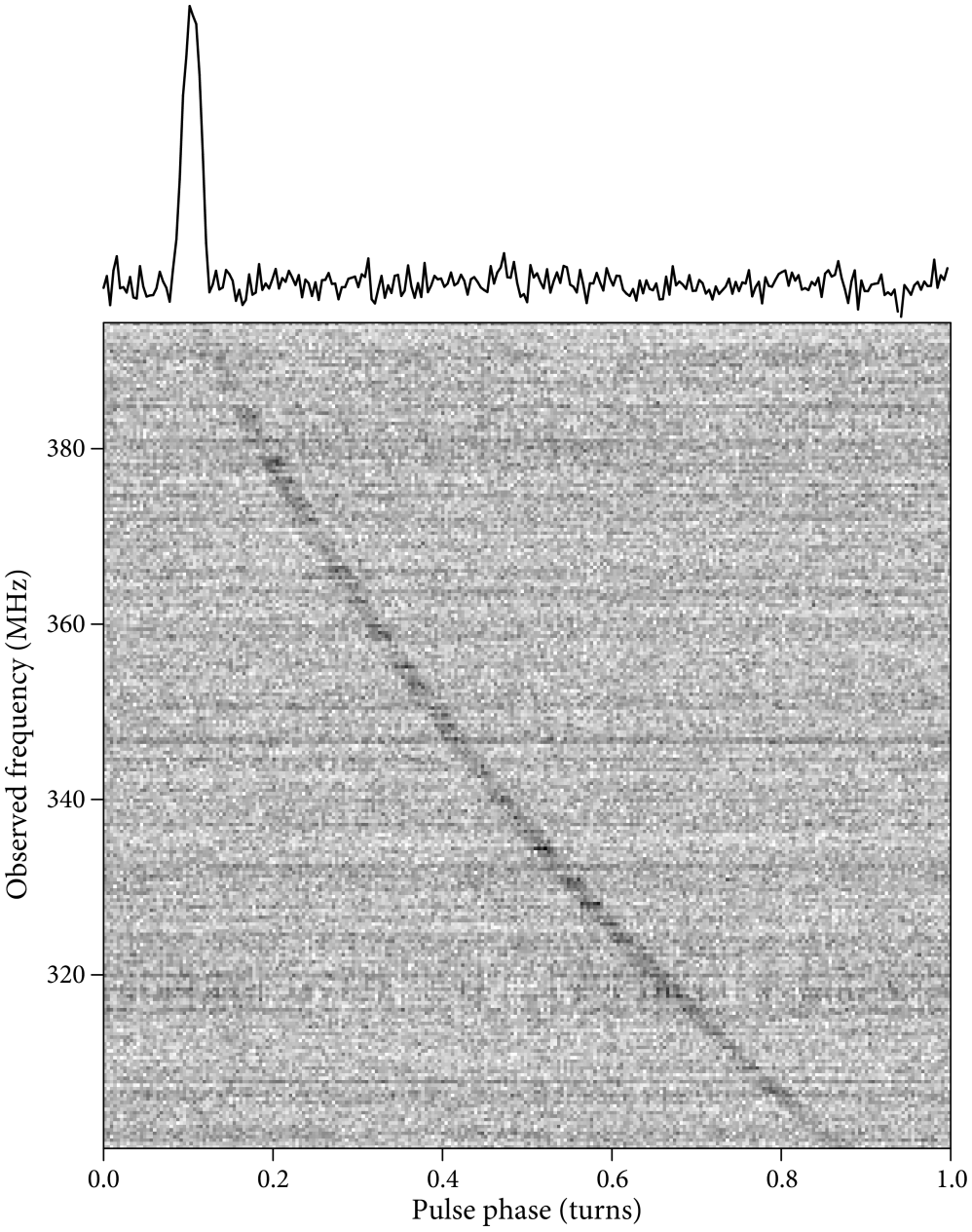

Figure 1.8: The figure illustrates the effect of interstellar dispersion on pulsar signals across a range of radio frequencies. Lower-frequency components are delayed more than higher-frequency ones due to the frequency-dependent refractive index of the ionized ISM, resulting in a characteristic sweep in arrival time. The top panel shows the de-dispersed pulse profile, where frequency channels have been aligned to remove this delay, producing a coherent signal across the band. Although the change in propagation speed due to dispersion is small, the resulting time delay can be substantial—typically on the order of milliseconds. Figure credit: [Condon and Ransom, 2016].

electrons between the pulsar and the observer [Manchester and Taylor, 1977]

$$\text{DM} = \int_0^d n_e, dl. \tag{1.15}$$

Here, n_e is the electron density, and dl is the path length.

Accurately measuring and correcting for DM is critical to ensure precise ToA measurements. Variations in the DM over time—due to changes in the ISM—can introduce low-frequency noise (red noise) in timing residuals, reducing the sensitivity of PTAs to nHz GWs [Keith et al., 2013].

Pulsar-Intrinsic Timing Noise

Pulsar-intrinsic "timing noise" refers to irregularities in the rotation of pulsars that cannot be attributed to external influences or measurement errors but are inherent to the pulsars themselves. This timing noise manifests as random, unpredictable deviations in the arrival times of individual pulses, superimposed on the (otherwise stable) spin-down rate of the pulsar. These irregularities are thought to result from complex internal processes within the NS, such as starquakes, crustal movements, or interactions between the crust and superfluid components [Liu et al., 2025].

Timing noise typically exhibits a "red" spectrum (see Section 2.4.3), meaning that its power increases at lower frequencies [Lentati et al., 2016, Parthasarathy et al., 2019]. This characteristic makes it challenging to distinguish intrinsic timing noise from other low-frequency signals in pulsar timing data, particularly those of interest in PTA experiments, such as a stochastic GWB, which is also expected to produce a common low-frequency red noise signal across multiple pulsars in the array [Verbiest et al., 2016]. Consequently, pulsar-intrinsic timing noise can mask or mimic a GW signal.

To accurately quantify this noise, various statistical methods—such as power spectral

density analysis and time-domain noise modeling—have been applied to try isolate these irregularities from other timing effects [Coles et al., 2011]. These models aim to disentangle pulsar intrinsic timing noise from other red noise sources, thereby increasing the sensitivity of PTAs to the GWB and enhancing their ability to characterize signals [Arzoumanian et al., 2020].

1.4 Pulsar Timing Arrays

1.4.1 Introduction

PTAs precisely monitor the ToAs from MSPs to detect subtle deviations caused by GWs. By creating a galactic-scale observatory, PTAs aim to study low-frequency (10^{-9}–10^{-7} Hz) GWs, particularly from a stochastic GWB produced by SMBHBs [Verbiest et al., 2016, Burke-Spolaor et al., 2019]. These ripples in the fabric of space and time, predicted by GR, carry information about their origins, the structure and early history of the universe, and the nature of gravity itself [Einstein, 1916].

The Hellings-Downs (HD) curve (see fig. 1.9) describes the angular correlation of timing residuals between pairs of pulsars in the presence of a stochastic GWB [Hellings and Downs, 1983]. As GWs pass through the galaxy, they induce correlated variations in the ToAs of different pulsars, creating a quadrupolar pattern that depends on the angular separation ($\zeta(\theta)$) of the pulsars, which is given by

$$\zeta(\theta) = \frac{3}{2}x\ln(x) - \frac{1}{4}x + \frac{1}{2} + \frac{1}{2}\delta(\theta), \tag{1.16}$$

where $x = \frac{1-\cos\theta}{2}$ and θ is the angle between the directions to two pulsars; the last term $\frac{1}{2}\delta(\theta)$ represents a Dirac delta function that picks out the case when the angular separation (θ) between two pulsars is zero. PTA sensitivity to these correlations depends on the number of pulsar pairs and their sky distribution [Siemens et al., 2013, Taylor et al., 2016]. An increase in the number of MSPs regularly observed over long timescales and improvements in timing model precision corresponds to an improved PTA sensitivity to GW detection. HD correlations are used to differentiate a GW signal from other noise sources, such as intrinsic pulsar noise or errors in the timing model. However, the expected correlation is challenging to detect as GW signals are weak by the time they reach Earth. One of the greatest challenges in detecting a stochastic GWB is

distinguishing the weak GW signal from various noise sources that also affect the timing residuals [Pol et al., 2021]. These include intrinsic pulsar noise, such as rotational irregularities (spin-noise) [Cordes and Shannon, 2010, Shannon and Cordes, 2010], and propagation effects through the ISM, such as dispersion and scattering [You et al., 2007, Hemberger and Stinebring, 2008, Keith et al., 2013]. Instrumental calibration effects can also mask or mimic the characteristic quadrupolar signature of a GWB, making detection more difficult [van Straten, 2006, 2013].

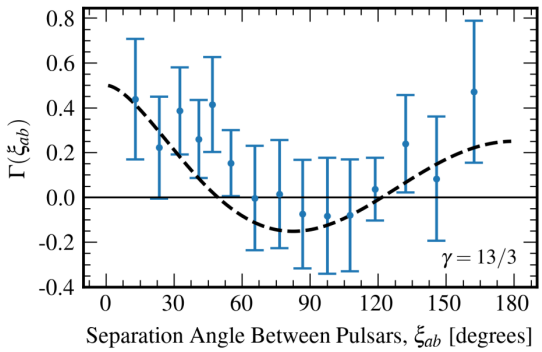

Figure 1.9: Average pairwise correlation in pulsar timing residuals as a function of angular separation, based on the NANOGrav 15-year dataset, is depicted in blue. The HD curve, representing the theoretical prediction for a GWB, is shown in black. The blue points and associated error bars represent optimally weighted averages of approximately 150 pulsar-pair correlations within each angular separation bin, accounting for the covariances between these correlations induced by the GWB. This figure illustrates how the observed data aligns with the expected HD curve. Figure credit: [Agazie et al., 2023b].

The characteristic strain, $h_c(f)$, quantifies the strength of a GW signal at different frequencies and is a commonly used measure in GW astronomy. A higher strain indicates a stronger GW signal, while the shape of the strain spectrum provides insight into the source population and its evolution. A schematic overview of the characteristic strain from various GW sources, spanning PTAs, space-based detectors, and ground-based observatories, is shown in fig. 1.10. This figure illustrates the frequency ranges and sensitivity limits of current and future detectors, highlighting the complementary nature of these efforts in covering the GW spectrum [Barack et al., 2019].

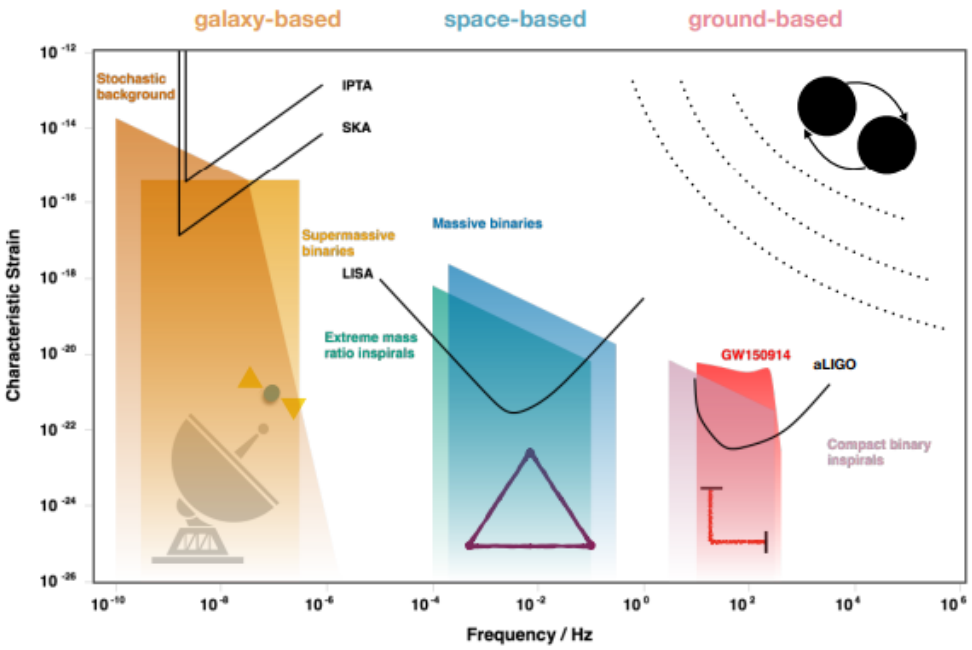

Figure 1.10: Schematic depiction of the characteristic strain due to anticipated GW sources as a function of frequency between galaxy-, space- and ground-based detectors [Barack et al., 2019].

For a stochastic GWB from SMBHBs, the characteristic strain follows a power-law of the form

$$h_c(f) = A\left(\frac{f}{\mathrm{yr}^{-1}}\right)^{\alpha}, \tag{1.17}$$

where A is the strain amplitude at the reference frequency of 1 yr^{-1}, and $\alpha = -2/3$ for circular, GW-driven SMBHBs, corresponding to a spectral index of $\gamma = 13/3$ in the power spectral density.

The power spectral density, $S(f)$, of the timing residuals induced by a stochastic GWB is also modeled as a power-law, given by

$$S(f) = \frac{A^2}{12\pi^2}\left(\frac{f}{f_{\mathrm{yr}}}\right)^{-\gamma} \mathrm{yr}^3, \tag{1.18}$$

where f is the GW frequency in Hz (or cycles per year), A is the amplitude as before, and γ is the spectral index.

For SMBHBs emitting GWs as they inspiral, $\gamma = 13/3$ [Phinney, 2001]. This value is derived under the assumption that the binaries are in circular orbits and evolve solely due to GW emission. Other astrophysical sources predict steeper spectra: for instance, $\gamma = 5$ for a primordial GWB [Grishchuk, 2005], and $\gamma = 16/3$ for cosmic strings [Damour and Vilenkin, 2005]. However, the cosmic string spectrum may vary across the PTA frequency band, so a single power-law may not fully capture its shape [Sanidas et al., 2012].

The complementary relationship between PTAs, future space-based observatories like the Laser Interferometer Space Antenna (LISA; [Amaro-Seoane et al., 2017]), and ground-based detectors like LIGO [Aasi et al., 2015] and Virgo [Acernese et al., 2015] allows for the exploration of GWs across a wide range of frequencies. While PTAs are sensitive to nHz GWs from SMBHBs and cosmic strings, LISA will probe

mid-frequency GWs from intermediate-mass BHs, and LIGO and Virgo focus on high-frequency GWs from stellar-mass BH and NS mergers, offering a multi-scale view of the universe's gravitational landscape [Sazhin, 1978, Detweiler, 1979].

1.4.2 Collaborations

The International Pulsar Timing Array (IPTA; [Hobbs et al., 2010, Antoniadis et al., 2022]) is a collaborative global effort, integrating data and resources from several national PTAs: the North American (NANOGrav; [McLaughlin, 2013]), European (EPTA; [Kramer and Champion, 2013]), Australian (PPTA; [Manchester et al., 2013]), Chinese (CPTA; [Lee, 2016, Xu et al., 2023]), Indian (InPTA; [Joshi et al., 2018, Tarafdar et al., 2022]), and South African (MPTA; [Bailes et al., 2020, Miles et al., 2023]). By sharing data across multiple observatories and incorporating diverse timing models, the IPTA enhances its sensitivity and sky coverage, allowing for a more comprehensive search for GWs. This collaborative approach increases the likelihood of detecting weak signals from a stochastic GWB, as well as providing more robust constraints on their properties [Hobbs et al., 2010, Manchester et al., 2013, Verbiest et al., 2016, Perera et al., 2019]. By 2019, the galactic distribution of IPTA pulsars (see fig. 1.11) incorporated high-precision timing data from 65 MSPs [Perera et al., 2019]. However, the total number of MSPs monitored by the IPTA has been increasing over the years. Recent estimates suggest that the IPTA now regularly observes nearly 100 MSPs (see e.g., `https://ipta4gw.org/`).

1.4.3 Indirect Evidence

GR was first confirmed through its explanation of the anomalous perihelion advance of Mercury's orbit—a longstanding discrepancy that Newtonian mechanics could not resolve [Will, 2014]. This early success demonstrated GR's predictive power in the

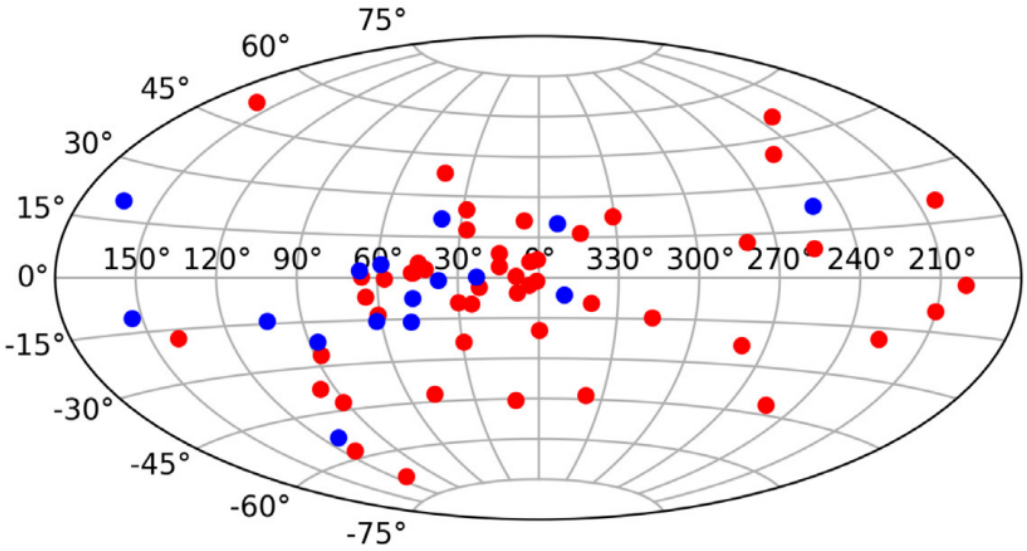

Figure 1.11: The galactic distribution of 65 pulsars from the latest IPTA data release. It includes 49 pulsars from the IPTA's first data release (marked as red dots) and introduces 16 new pulsars (marked as blue dots) not previously featured. The vertical axis represents Galactic latitude in degrees, while the horizontal axis represents Galactic longitude in degrees, with the Galactic Centre at the origin and longitude increasing leftward. Figure credit: [Perera et al., 2019].

relatively weak gravitational fields of the Solar System.

While Mercury's orbit provided a test in a weak-field regime, more extreme environments are needed to probe GR under strong gravitational fields. Binary neutron star systems, such as PSR B1913+16, serve as ideal laboratories for such tests as the gravitational potential is high and spacetime curvature is significant. Precise pulse ToA measurements revealed a gradual decay in the orbital period [Taylor and Weisberg, 1982], consistent with the energy loss expected from GW emission as predicted by GR (see fig. 1.12).

The observed rate of decay matched GR's predictions with striking precision, offering robust evidence for the theory's validity in strong-field conditions [Taylor, 1992, Weisberg and Taylor, 2005]. Over more than 30 years, the orbital period shortened by just 2.3 milliseconds, yet pulsar timing was precise enough to constrain deviations from GR to within 0.3% [Weisberg et al., 2010]. More recent measurements by Weisberg and Huang [2016] refined this further, finding the ratio of observed to predicted orbital decay to be 0.9983±0.0016—indicating a deviation of only 0.17%. This indirect confirmation of GWs provided compelling support for GR and earned Russell Hulse and Joseph Taylor the 1993 Nobel Prize in Physics.

Further tests of GR in strong-field regimes, particularly those involving GWs, have been enabled by observations of compact object binaries. A particularly notable example is the discovery of a $2M_\odot$ pulsar in a 2.5-hour orbit with a $0.2M_\odot$ WD companion [Antoniadis et al., 2013]. The observed orbital decay in this system closely matched GR's predictions, extending previous GW tests beyond double NS systems. This is especially significant because many alternative theories of gravity predict deviations from GR in asymmetric systems like NS–WD binaries, where the gravitational binding energies differ substantially. Agreement with GR in such a system thus places stringent constraints on possible deviations. Furthermore, the presence of a $2M_\odot$ NS provides critical insights into the equation of state (EOS) of ultra-dense matter. EOS models

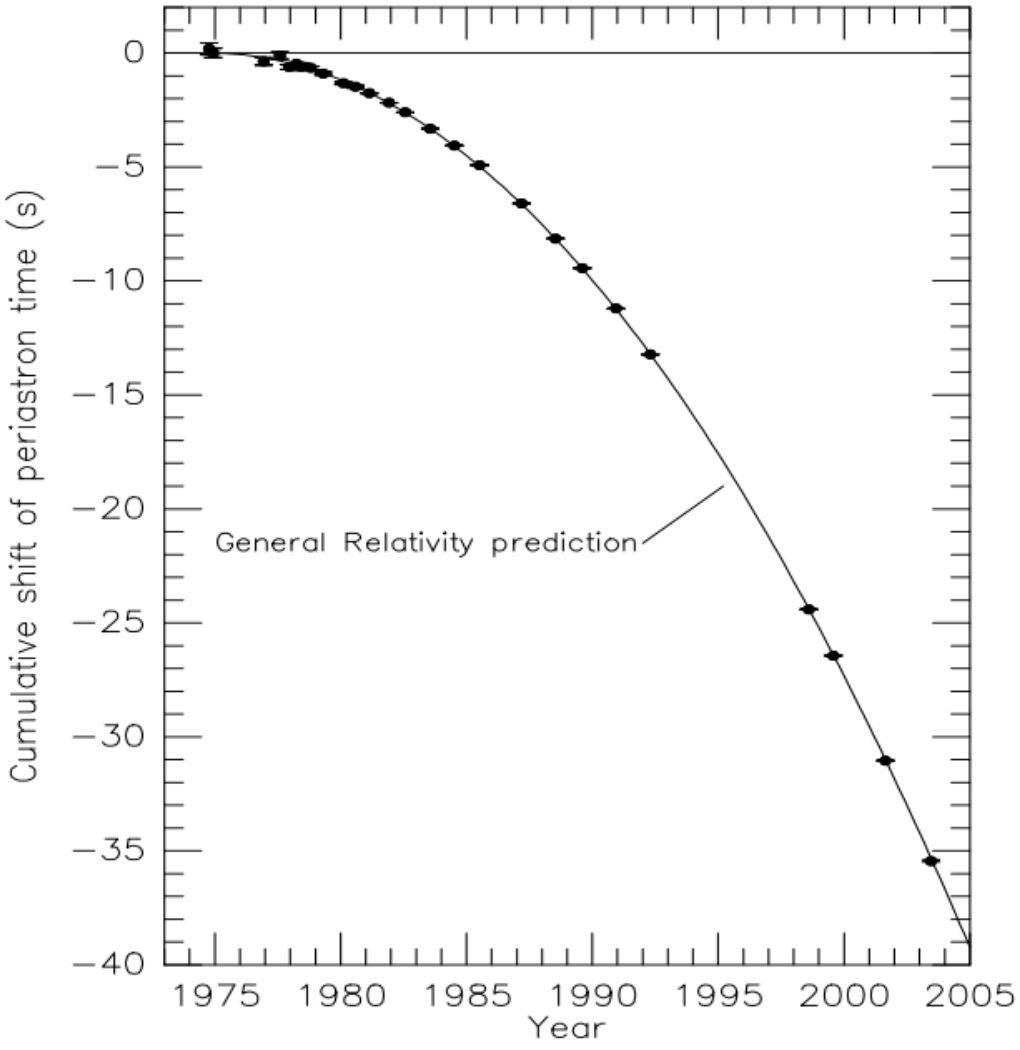

Figure 1.12: The orbital decay of PSR B1913+16. The data points are the observed change in the epoch of periastron with time, matched perfectly to the theoretical line predicted by GR. Figure credit: [Weisberg and Taylor, 2005].

predicting maximum NS masses below this value are ruled out, helping to narrow the range of viable descriptions of dense nuclear matter [Lattimer and Prakash, 2004, Stairs et al., 2006, Demorest et al., 2010, Freire et al., 2012, Archibald et al., 2018, Voisin et al., 2020].

1.4.4 Recent Progress

Detecting the stochastic GWB directly with PTAs presents significant challenges, requiring long-term, high-precision monitoring. For example, achieving the necessary sensitivity may demand monthly timing of at least 20 MSPs over 20 years, with RMS timing residuals of about 100 ns [Jenet et al., 2005, Liu et al., 2020]. Despite these challenges, even non-detections yield meaningful astrophysical insights by placing upper limits on the GWB amplitude, thereby constraining the demographics and dynamics of SMBHB populations, including their merger rates and orbital separations [Sesana, 2016, Burke-Spolaor et al., 2019].

For instance, the PPTA set the first such upper limit, placing $A_{\rm GWB} < 1.0 \times 10^{-15}$ (95% confidence) at $f = 1$ yr^{-1}, based on 11 years of timing data from 24 MSPs [Shannon et al., 2015]. That same year, NANOGrav and the EPTA reported similar limits of 1.5×10^{-15} and 3×10^{-15}, respectively [Arzoumanian et al., 2015a, Lentati et al., 2015]. These upper limits prompted revisions to SMBHB merger rate predictions and refinements to BH–host galaxy scaling relations, especially the BH bulge mass relation [Simon and Burke-Spolaor, 2016].

The EPTA's first data release [Desvignes et al., 2016] was based on 42 of the most reliable pulsars Subsequent analysis using 24 years of high-precision timing data for 6 of these MSPs did not find the characteristic HD correlations expected from a GWB, but it confirmed the presence of a common uncorrelated red noise process, improving constraints on its amplitude and spectral properties [Chen et al., 2021]. This discovery

aligns with NANOGrav's 12.5-year dataset [Arzoumanian et al., 2020], and the PPTA's [Goncharov et al., 2021a], and IPTA's second data releases [Antoniadis et al., 2022]. Potential sources of this noise include unmodeled SSE errors [Arzoumanian et al., 2018, Vallisneri et al., 2020], pulsar timing noise, and ISM effects, all of which could introduce uncorrelated noise between pulsars or contribute to the common-spectrum process [Guo et al., 2019, Zic et al., 2022]. Methods for mitigating such errors were developed to improve PTA sensitivity to GWs [Hazboun et al., 2020, Pol et al., 2021, Johnson et al., 2022].

The most recent PTA data releases have independently reported evidence of a stochastic signal exhibiting HD correlations at a significance level of 2-–4σ, marking a major milestone in the search for the GWB [Agazie et al., 2024, 2023b, Antoniadis et al., 2023c,a, Reardon et al., 2023, Zic et al., 2023, Xu et al., 2023]. As PTA sensitivity continues to improve, future observations may provide deeper insights into this stochastic background and enable the detection of continuous GWs from individual SMBHBs.

Chapter 2

Technical Introduction

This chapter focuses on the challenges of achieving high-precision pulsar timing in the presence of instrumental polarization distortions, and presents advanced calibration and timing techniques developed to mitigate these effects. We explore how improved polarimetric calibration and arrival time estimation methods can enhance the sensitivity of PTA experiments. Several techniques—such as Matrix Template Matching (MTM), and Measurement Equation Template Matching (METM)—are introduced here and discussed in more detail in Sections 2.2.2, and 2.3.3, respectively.

Early studies of the nearest and brightest MSP, PSR J0437−4715 [Johnston et al., 1993, Navarro et al., 1997], highlighted key challenges in achieving the timing precision needed for PTA experiments. One major issue was the significant timing errors caused by instrumental polarization artifacts [Sandhu et al., 1997, Vivekanand et al., 1998, Jenet et al., 2005], which degrade the accuracy of ToA estimates. To address these errors, the polarimetric invariant profile technique was developed, improving timing accuracy over traditional total intensity profiles by mitigating the effects of instrumental polarization [Britton, 2000]. This technique played an important role in early high-precision timing studies, enabling novel tests of GR, such as the detection of annual-orbital parallax [van Straten et al., 2001]. Despite its advantages, the invariant profile

method has limitations which complicate its application in some cases. First, the S/N of the invariant profile is lower than that of the total intensity, and it drops to zero for fully polarized sources. Second, the noise in the invariant profile is neither normally distributed or homoscedastic with respect to pulse longitude. Therefore, while the invariant profile mitigates polarization artifacts, it is insufficient to fully address timing errors, as instrumental distortions—especially in the total intensity profile—continue to cause significant timing errors that are often correlated among multiple pulsars [van Straten, 2013]. As a result, precise polarimetry is essential for achieving the level of accuracy required for PTA experiments [Rogers, 2020].

The Matrix Template Matching (MTM; [van Straten, 2006]) technique was developed to overcome these challenges. Using full-polarization observations of PSR J0437−4715, MTM primarily estimates ToAs with high precision and can also be used to derive calibration solutions for very bright pulsars, correcting for time-varying instrumental effects, such as the parallactic rotation of the receiver, which can introduce systematic errors in ToA estimates. MTM has led to significant advances, including the detection of Shapiro delay and orbital precession. MTM faces limitations when applied to pulsars with lower flux densities, such as PSR J1022+1001, as the calibration solutions derived from these observations are often not precise enough to fully correct for instrumental distortions [van Straten, 2013]. However, MTM can still be successfully used as an arrival time estimation technique for such pulsars, reliably deriving ToAs despite its calibration challenges. To address the limitations of MTM, the Measurement Equation Template Matching (METM; [van Straten, 2013]) technique was developed, building upon MTM while incorporating elements from the Measurement Equation Method (MEM; [van Straten, 2004]). Unlike MEM, which requires additional observations of sources with known circular polarization, METM can be applied without such auxiliary data, making it more flexible and effective in correcting for time-varying instrumental distortions. METM provides more accurate calibration

by modeling time-varying instrumental responses more effectively.

By improving instrumental calibration accuracy and reducing timing errors, these methods can significantly advance the precision of pulsar timing, as shown in Chapter 3, published as Rogers et al. [2024].

2.1 Polarization

Polarization refers to the orientation of transverse electromagnetic waves, specifically the direction in which the electric field vector oscillates. In pulsar astronomy, understanding polarization properties is essential for probing the Galactic magnetic field structure [Han et al., 2006, 2018], pulsar emission mechanisms [Backer et al., 1976, Everett and Weisberg, 2001], and the intervening ISM through which the electromagnetic waves travel [e.g., Rickett, 1990]. Radio pulsar emission is often highly polarized, typically exhibiting a combination of linear and circular polarization. For linear polarization, the electric field oscillates in a single plane, while for circular polarization, the field rotates in a helical pattern as the wave propagates (see fig. 2.1).

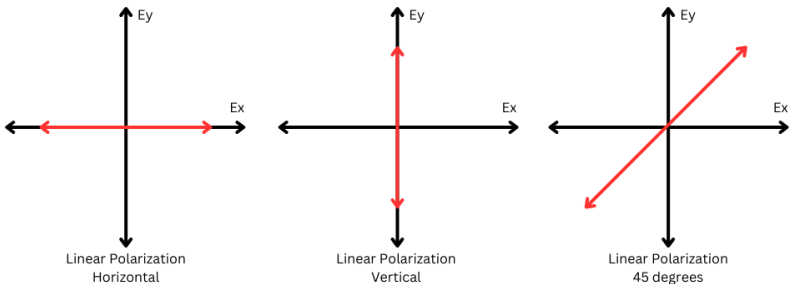

Figure 2.1: This diagram illustrates various states of linear polarization: Linear polarization aligned with the celestial North oscillates along the x-axis, while linear polarization aligned with the celestial East oscillates along the y-axis. Linear 45-degree polarization combines equal amplitudes of North and East components. Left-hand circular polarization rotates counter-clockwise, and right-hand circular polarization rotates clockwise as seen by an observer looking toward the source. Right-handed elliptical polarization traces an elliptical path, demonstrating the diverse orientations of electric field oscillations in coherent electromagnetic waves. For more details on the reference frame, see van Straten et al. [2010].

Accurate polarization calibration plays a crucial role in pulsar timing because it corrects for instrumental polarization artifacts that can introduce systematic timing errors. These artifacts can distort pulse profiles in a frequency-dependent manner, producing effects that resemble dispersion and potentially biasing estimates of DM

and pulse arrival times. Proper calibration ensures these distortions are minimized, improving the reliability of timing measurements. While Faraday rotation is generally negligible for pulsar timing at most radio frequencies, it remains important for studying the ISM and refining polarization measurements [van Straten, 2013].

To quantify the polarization state of pulsar emissions, radio telescopes detect the electric field of incoming radio waves and use specialized receivers to measure orthogonal polarization components, allowing the calculation of the four Stokes parameters (I, Q, U, and V) [Chandrasekhar, 1950]. These parameters describe the intensity and polarization characteristics of the signal. For receivers that sample linearly polarized components (commonly denoted as E_x and E_y), the Stokes parameters are calculated as

$$I = E_x E_x^* + E_y E_y^*, \tag{2.1}$$

$$Q = E_x E_x^* - E_y E_y^*, \tag{2.2}$$

$$U = 2\,\mathrm{Re}(E_x^* E_y), \tag{2.3}$$

$$V = 2\,\mathrm{Im}(E_x^* E_y), \tag{2.4}$$

where E_x and E_y are the complex-valued analytic representations of the electric field components in the x and y directions, respectively, and E_x^* and E_y^* represent their complex conjugates.

In contrast, circularly polarized feeds (i.e., left and right circular polarization, E_L and E_R) use a different basis, and the definitions of the Stokes parameters are accordingly adapted. However, both representations are mathematically equivalent and transformable through appropriate coordinate transformations (see Hamaker et al. 1996 for a detailed treatment of polarization bases).

The Stokes parameters describe different aspects of the polarization state:

- I: Total intensity of the emission.

- Q: Difference in intensity between horizontally and vertically polarized components (linear polarization).
- U: Difference in intensity between two diagonally polarized components.
- V: Intensity of circular polarization. Positive values represent right-hand (clockwise) circular polarization, following the IAU 1974 convention. (Note that this is opposite to the IEEE convention, often used by pulsar astronomers [e.g., van Straten et al., 2010], where positive V corresponds to left-hand circular polarization.)

The total linear polarization is given by $\sqrt{Q^2 + U^2}$, and the total polarized flux (including both linear and circular components) is

$$P = \sqrt{Q^2 + U^2 + V^2}, \tag{2.5}$$

where P represents the magnitude of the polarized flux.

2.1.1 Position Angle

Polarization in pulsar emission provides critical insights into the geometry of the magnetic field and the pulsar emission mechanism. One key quantity used to describe linear polarization is the polarization position angle (ψ), which represents the orientation of the electric field vector in the plane of the sky. It is defined as

$$\psi = \frac{1}{2} \tan^{-1}\left(\frac{U}{Q}\right), \tag{2.6}$$

where Q and U are the Stokes parameters describing linear polarization. In the context of pulsars, ψ reflects the projected direction of the pulsar's magnetic field as the pulsar rotates.

An important observational feature in pulsar polarization is the presence of orthogonal polarization mode jumps, where the position angle abruptly shifts by approximately 90 degrees. These jumps are believed to arise from emission propagating through distinct magnetospheric modes with different polarization characteristics. Both orthogonal [Backer et al., 1976, Stairs et al., 1999] and non-orthogonal [Backer and Rankin, 1980, Navarro et al., 1997] jumps are observed, and they introduce complexity into interpreting ψ curves.

The polarization properties of MSPs often resemble those of young pulsars: both tend to show high degrees of linear polarization and exhibit complex ψ behavior, including abrupt jumps and rapid swings. These polarization features are essential for understanding the magnetic field structure and emission processes [Philippov and Kramer, 2022, Mitra et al., 2024].

The Rotating Vector Model (RVM) [Radhakrishnan and Cooke, 1969] provides a geometric framework to interpret the variation of ψ across pulse phase ϕ as a projection of the rotating dipolar magnetic field onto the plane of the sky. The RVM predicts a characteristic S-shaped curve given by

$$\tan(\psi - \psi_0) = \frac{\sin\alpha \sin(\phi - \phi_0)}{\sin(\alpha + \beta)\cos\alpha - \cos(\alpha + \beta)\sin\alpha\cos(\phi - \phi_0)}, \tag{2.7}$$

where ψ_0 is the PA at the magnetic axis, α is the angle between the magnetic and rotation axes, and β is the impact parameter (i.e., the observer's closest approach to the magnetic axis).

However, real observations often show significant deviations from the ideal RVM prediction, including multiple orthogonal jumps, non-dipolar field structures, and rapid PA swings [Manchester et al., 1975, Backer and Rankin, 1980, Stinebring et al., 1984, Edwards, 2004]. In addition, reversals in circular polarization handedness are frequently observed near the pulse center [Rankin, 1983, Navarro et al., 1997, Xilouris et al., 1998],

complicating the connection between PA and emission geometry. While fitting the RVM to high-quality data can still yield useful estimates of α and β, the method is sensitive to systematic effects and often underestimates parameter uncertainties [Everett and Weisberg, 2001].

To improve upon this, Blaskiewicz et al. [1991] extended the RVM by including first-order special relativistic effects, such as aberration and retardation, without incorporating general relativistic (gravitational) corrections. These effects predict that the observed PA curve should lag behind the total intensity profile due to the forward bending of magnetic field lines in the co-rotating frame. This lag offers a more physically realistic view of how relativistic motion and magnetic geometry shape the observed polarization.

2.1.2 Faraday Rotation

As polarized radio waves from pulsars travel through the magnetized plasma of the ISM, they experience Faraday rotation, which causes the plane of linear polarization to rotate. This effect is frequency-dependent and serves as a useful probe of the ISM's magnetic field and free electron content. The change in ψ ($\Delta\psi$) due to Faraday rotation is given by

$$\Delta\psi = \mathrm{RM}\ \lambda^2, \tag{2.8}$$

where λ is the wavelength in meters, and RM is the rotation measure quantifying the amount of Faraday rotation. RM is defined as

$$\mathrm{RM} = 0.812 \int_0^d n_e B_{\parallel}\, dl, \tag{2.9}$$

where n_e is the electron density in cm^{-3}, $B_{\parallel}$ is the magnetic field component along the line-of-sight in μG, and d is the distance to the pulsar in parsecs. The coefficient 0.812

includes the necessary conversion constants to bridge centimeter-gram-second (CGS) units in equation (2.6) with International System of Units (SI) units in equation (2.5).

Although RM depends on both electron density and magnetic field strength, it does not independently constrain n_e along the line-of-sight. However, when used alongside the DM (see Equation 1.15), one can estimate the average line-of-sight magnetic field weighted by electron density as

$$\langle B_{\parallel} \rangle = \frac{\mathrm{RM}}{0.812 \cdot \mathrm{DM}}. \tag{2.10}$$

Thus, RM is particularly useful for constraining the structure and orientation of the Galactic magnetic field, rather than directly probing electron density alone [Han et al., 2006, 2018].

Faraday rotation also plays a crucial role in large-scale studies of the Galactic magnetic field (see fig. 2.2). Observations of pulsar polarization yield RM values that trace the line-of-sight component of the Milky Way's diffuse magnetic field [Rand and Kulkarni, 1989, Rand and Lyne, 1994, Haverkorn et al., 2006]. These measurements have revealed large-scale magnetic field patterns, including counterclockwise fields in the Galactic spiral arms and clockwise fields in the inter-arm regions (as viewed from the north Galactic pole) [Han et al., 2006, 2018]. They also support efforts to model the three-dimensional structure of the Galactic magnetic field (e.g., [Sobey et al., 2019]).

2.1.3 Instrumental Effects

Instrumental effects can significantly influence polarization measurements, introducing systematic errors and noise into ToA estimates [Hotan et al., 2005, van Straten, 2006, 2013]. Radio telescopes detect orthogonal components of the electric field vector, but imperfections in this detection such as feed cross-coupling (also known as polarization leakage), can lead to mixing between polarization states. This results in inaccurate

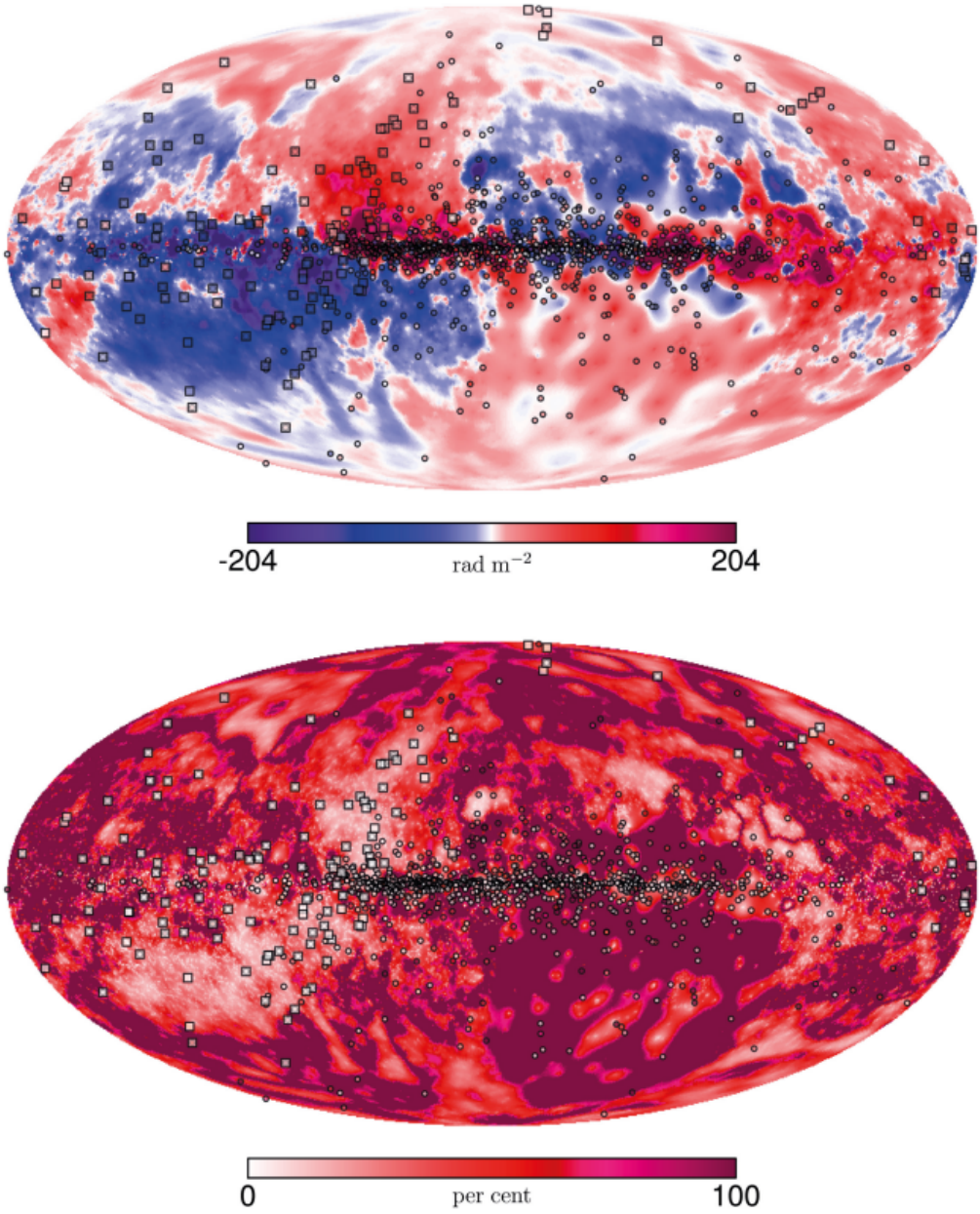

Figure 2.2: Upper: The RM sky is shown in Galactic coordinates using a Mollweide projection, with the center at $l, b = 0\,\mathrm{deg}$. The background represents the Galactic RM signal from extragalactic sources. Circles mark 1133 RMs from the pulsar catalog, while squares show 137 new RMs from LOFAR. All data use the same color scale, capped at ±204 rad m^2, with reds/pinks showing magnetic fields pointing toward Earth and blues/purples showing fields pointing away. Lower: Percentage uncertainties for the measurements above are displayed using matching markers and a color scale, capped at 100%. Figure credit: [Sobey et al., 2019].

Stokes parameter measurements and mischaracterization of linear and circular polarization. Differences in the gain and phase responses of orthogonally polarized receptors can also distort measurements of the position angle ψ [Foster et al., 2015]. Furthermore, frequency-dependent variations in receiver sensitivity and phase response across wide bandwidths can introduce additional distortions [Manchester et al., 1973, Dai et al., 2015].

To mitigate these instrumental effects, polarization calibration procedures are employed. These use observations of known, polarized reference sources to characterize and correct the system response. This calibration accounts for imperfections in the receiving system, such as cross-coupling and unequal gain between polarization channels. Regular calibration observations are essential for tracking temporal variations in the instrument's behavior and maintaining accurate polarization measurements [van Straten, 2006, 2013].

The system's effect on the polarization signal can be described using two mathematical frameworks: the Jones matrix, which operates on the electric field vector, and the Mueller matrix, which operates on the Stokes vector. The Mueller matrix is a 4×4 real-valued matrix that describes how an optical system transforms the input Stokes parameters into observed values. In contrast, the Jones matrix J is a 2×2 complex matrix that models how the system transforms the electric field components directly

$$\mathbf{E}' = J\mathbf{E}, \tag{2.11}$$

where $\mathbf{E}$ is the true incident electric field, and $\mathbf{E}'$ is the measured field after passing through the system.

For a realistic, imperfect receiver, the Jones matrix can be expressed as

$$J = \begin{pmatrix} 1 & \epsilon_1 e^{i\phi_1} \\ \epsilon_2 e^{-i\phi_2} & 1 \end{pmatrix}. \tag{2.12}$$

Here, ϵ_1 and ϵ_2 represent the magnitudes of feed cross-coupling, and ϕ_1 and ϕ_2 are their respective phases. The matrix elements are retained to first order in ϵ_1 and ϵ_2, assuming that the imperfections are small. The off-diagonal terms represent the cross-coupling between the two polarizations, which can arise due to factors such as misalignment or non-orthogonality of the feed elements Heiles et al. [2001].

To estimate and correct these instrumental parameters, observations of bright, highly polarized pulsars across a wide range of parallactic angles are used [van Straten, 2004]. As the parallactic angle changes, the sky-projected orientation of the feed rotates, which modulates the response of the telescope to the pulsar's known polarization. By modeling these variations, the cross-coupling parameters can be inferred and used to compute the Jones matrix, which is then used to calibrate other pulsar observations.

These calibration steps are crucial for accurate timing, as systematic timing errors caused by polarization calibration imperfections are often most evident in the ToA residuals as a function of parallactic angle. This effect is illustrated in fig. 2.3, where observations of PSR J0437−4715 show large ToA variations over a single observing session. As the parallactic angle changes during the observation, the telescope's orientation with respect to the pulsar's polarization evolves. If the instrumental response is not perfectly calibrated, this rotation leads to measurable, systematic timing errors—often exceeding the estimated ToA uncertainties.

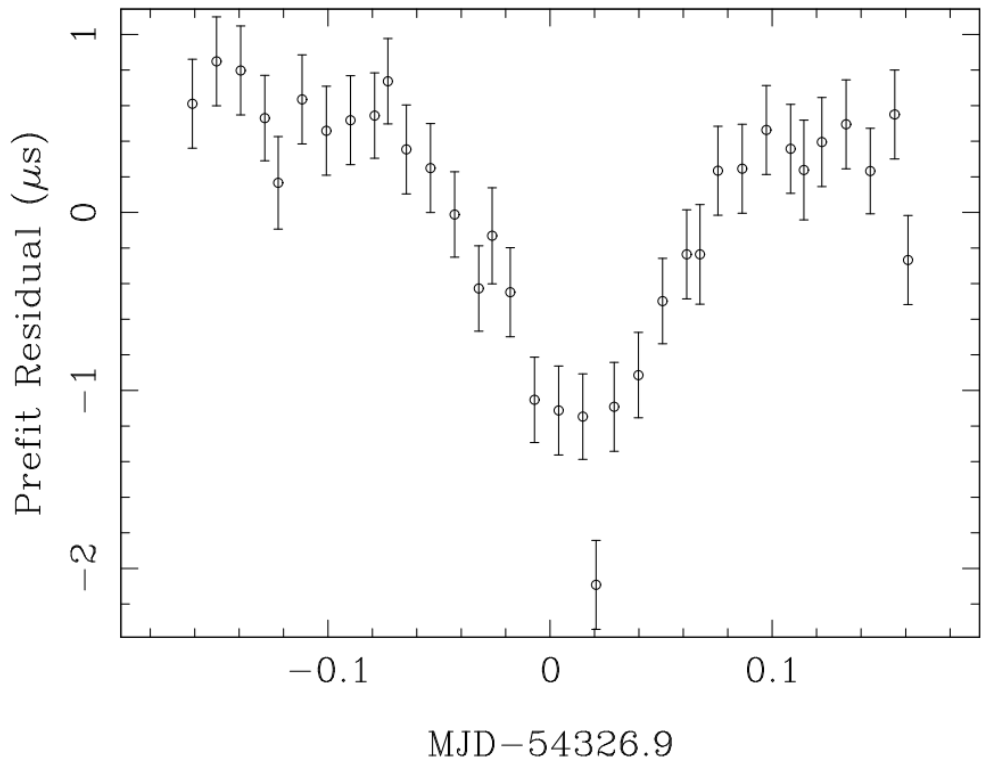

Figure 2.3: Systematic timing errors in a single day of uncalibrated observations of PSR J0437−4715. The variations correlate with the changing parallactic angle of the telescope. As the receiver rotates relative to the sky over time, imperfections in its polarization response (such as cross-coupling) project differently onto the incoming signal. This leads to a modulation in ToA measurements with parallactic angle, producing systematic errors nearly an order of magnitude larger than the nominal ToA uncertainty (~250 ns). Figure credit: [van Straten, 2013].

2.2 Arrival Time Estimation

Pulsar timing analysis relies on precise measurements of pulse ToAs, which are derived from the observed radio signal after it has passed through the telescope system. The process of ToA generation typically involves the following steps:

1. reception of the pulsar signal by the telescope,
2. digitization and channelization of the raw voltage data,
3. dedispersion to remove frequency-dependent dispersion delays caused by the ISM,
4. averaging over many pulses to produce a stable mean pulse profile,
5. polarization calibration to correct for instrumental effects, and
6. cross-correlation with a high S/N template to determine the ToA.

The resulting ToAs are then compared to timing models, producing residuals that reflect astrophysical, instrumental, or propagation-induced discrepancies.

However, this process is affected by noise and propagation effects (see Section 2.4) such as ISM dispersion, scattering, and instrumental noise, all of which distort the signal and complicate ToA estimation [van Straten, 2013]. To mitigate these distortions, high S/N templates are constructed from averaged pulse profiles and serve as references for matching. These templates help minimize deviations between observed pulses and expected profiles, improving the accuracy of the ToA measurement (see Sections 2.2.1 and 2.2.2 for details on template matching methods).

In wide-band pulsar timing, template matching faces additional challenges due to frequency-dependent variations in pulse shapes. These arise from both intrinsic emission changes and propagation effects, such as scintillation [Rickett, 1990, Cordes

and Rickett, 1998] and temporal evolution of DM [Liu et al., 2014]. Such variations distort profiles across different frequency channels and reduce ToA accuracy [Liu et al., 2011, Keith et al., 2013].

Historically, several methods have been developed to counter these effects. Gaussian interpolation has been applied to low S/N profiles [Krishnamohan and Downs, 1983, Kramer et al., 1994, Hotan et al., 2005], principal component analysis (PCA) has been used to model pulse phase jitter [Osłowski et al., 2011], and full-Stokes-based timing methods leverage polarization information to improve timing precision [van Straten, 2006]. More recent techniques use two-dimensional templates across time and frequency to jointly estimate ToAs and DM, accounting for profile evolution [Liu et al., 2014, Pennucci et al., 2014]. However, these methods often lack robust strategies for building high-fidelity wideband templates.

2.2.1 Scalar Template Matching

Scalar Template Matching (STM; [Taylor, 1992]) is the traditional method for ToA estimation. It operates by cross-correlating the observed pulse profile with a template, using only the total intensity component (Stokes I). The cross-correlation function is given by

$$C(\tau) = \int S(t)T(t+\tau)\,dt, \tag{2.13}$$

where $S(t)$ is the observed profile, $T(t)$ is the template, and τ is the timing residual at time t.

This approach assumes a stable pulse shape across observations, an assumption that can lead to biases in the presence of profile variability. Calibration is essential for STM accuracy. Instrumental effects are typically corrected using the Ideal Feed Assumption (IFA) calibration method, which determines parameters such as system gain, differential gain, and differential phase from observations of a pulsed calibration source (e.g., a

noise diode) (described in more detail in Section 2.3.1). Additionally, flux calibration relies on the assumption that a reference quasar's flux is known. However, if the pulsar's emission characteristics vary over time, the assumption that the pulse profile remains stable can lead to inaccuracies in the ToA estimates [van Straten, 2006].

Despite these limitations, STM remains widely used in the PTA community due to its computational simplicity, making it suitable for processing large datasets. STM is advantageous in scenarios where full polarimetric data is unavailable.

2.2.2 Matrix Template Matching

Matrix Template Matching (MTM) extends STM by incorporating all four Stokes parameters (I, Q, U, and V) thereby using full polarimetric information. This allows MTM to correct for polarimetric calibration errors and instrumental distortions (described as linear transformations of the electric field) through a model based on the Jones matrix formalism.

The relationship between the observed polarization profile $\rho'(\phi_n)$ and the reference template $\rho_0(\phi_n)$ is described by

$$\rho'(\phi_n) = J\rho_0(\phi_n - \varphi)J^\dagger + \rho_{DC} + \rho_N(\phi_n), \tag{2.14}$$

where ϕ_n is the pulse phase, φ the phase shift, ρ_N the system noise, and ρ_{DC} accounts for any remaining discrepancy between the two profiles (i.e., representing any systematic offset that is independent of pulse phase). The polarimetric transformation J is a Jones matrix characterizing instrumental response [van Straten, 2006].

The polarization state is represented by the 2×2 coherency matrix $\rho = \langle e \otimes e^\dagger \rangle$, decomposed using Pauli matrices:

$$\rho = \frac{1}{2}(S_0\sigma_0 + \mathbf{S} \cdot \boldsymbol{\sigma}), \tag{2.15}$$

where S_0 is total intensity, $\mathbf{S}$ is the polarization vector (S_1, S_2, S_3), and $\boldsymbol{\sigma}$ are the Pauli matrices [Britton, 2000].

In the Fourier domain, this relationship becomes

$$\rho'(\nu_m) = J\rho_0(\nu_m)J^\dagger \exp(-i2\pi\nu_m\varphi) + \rho_N(\nu_m), \tag{2.16}$$

and a least-squares fit minimizes the following merit function:

$$\chi^2 = \frac{1}{{\sigma_k}^2} \sum_{m=1}^{N} \sum_{k=0}^{3} \left| S'_k(\nu_m) - \mathrm{tr}[\sigma_k \rho'(\nu_m)] \right|^2, \tag{2.17}$$

which is typically solved using the Levenberg–Marquardt method [Press et al., 1992].

Although MTM introduces six additional degrees of freedom compared to STM—corresponding to the parameters of the Jones matrix—this added complexity is justified. These parameters enable precise modeling and correction of instrumental distortions, significantly reducing systematic timing errors. The method benefits particularly from pulsars with strong and stable polarization signals. In cases where the polarization vector varies significantly across the pulse phase, MTM can better leverage this variation to distinguish between intrinsic pulse features and calibration errors, thus improving timing precision [van Straten, 2006].

Empirical studies demonstrate MTM's advantages. For example, Graikou et al. [2017] observed a 15.5% reduction in timing residuals for PSR J1933−6211. Wang et al. [2024a] reported jitter noise reductions of 6.7–39.6% and white noise decreases of 0.19–13.4% across 7 of 8 pulsars observed with FAST. MTM has also shown significant noise reduction and improved ToA precision in pulsars observed by the Nançay Radio Telescope, becoming the preferred method for extracting ToAs [Guillemot et al., 2023]. While STM is strongly impacted by instrumental distortions, which can introduce systematic timing errors, MTM effectively resolves these errors and is expected

to outperform conventional methods in most cases, allowing full calibration of the instrumental response from a single observation [Rogers et al., 2024].

2.3 Instrumental Calibration

2.3.1 Ideal Feed Assumption

Pulsar profiles are often calibrated using the Ideal Feed Assumption (IFA; [Lorimer and Kramer, 2012]), which simplifies the model response of a radio telescope's feed system. The IFA assumes that the system responds "ideally" to incoming electromagnetic waves, meaning it introduces no cross-polarization leakage. In this idealization, the orthogonal polarization channels are assumed to be perfectly isolated, with no cross-coupling, and to be illuminated by an artificial reference source (such as a noise diode) that induces identical responses (in amplitude and phase) in each receptor [Caleb et al., 2019]. The assumption is that any deviations from this ideal response are negligible or can be treated as minor perturbations.

Under the IFA, the Jones matrix representing the telescope's polarimetric response is a diagonal matrix with unity elements, indicating no mixing between polarization channels. This greatly simplifies both the calibration and the analysis process. However, real-world telescope systems rarely adhere perfectly to this idealization. Imperfections such as feed misalignment, cross-coupling effects, and errors in the calibration process (e.g., incorrect estimation of differential gain and phase due to non-ideal coupling of the noise diode) can cause deviations from the ideal response. While differential gain and phase between polarization channels are accounted for in the ideal response, inaccuracies in their estimation during calibration can result in significant deviations. These distortions, if uncorrected, can introduce systematic errors into the pulsar profiles used for generating ToAs, thereby affecting timing precision [van Straten, 2006].

2.3.2 Measurement Equation Modeling

For PTAs, achieving nanosecond-level precision in ToA measurements depends heavily on accurate instrumental calibration. One approach to polarimetric calibration is Measurement Equation Modeling (MEM) [van Straten, 2004], a technique that models the full polarimetric response of a radio telescope by relating the observed data to the true sky signal through a series of transformations. These transformations account for instrumental distortions—such as cross-coupling and gain imbalance—as well as propagation effects from the Earth's ionosphere and the ISM. MEM uses observations of strongly polarized pulsars over a wide range of parallactic angles to constrain the system's response, using observations of a reference source, like the noise diode, to provide first estimates of the ideal feed parameters. All model parameters are then refined through optimization procedures such as least-squares fitting, minimizing discrepancies between the observed data and the model [van Straten, 2004].

During this modeling process, the instrumental response is parameterized following the formalism introduced by Britton [2000], which expresses how a non-ideal receiver alters the incoming polarized signal. However, to ensure the model remains well-constrained, certain degenerate parameters—identified in Appendix B of van Straten [2004]—are fixed to zero. These include the differential ellipticity between the two receptors ($\delta\chi$), which causes mixing between Stokes I and V, and the rotation of the receptor feed about the line-of-sight (σ_θ), which mixes Stokes Q and U. Setting these values to zero implies that the receptors have equal and opposite ellipticities and that the receiver orientation is constant during the observation. Additionally, the unknown polarization of the calibration signal from the noise diode is described using a normalized Stokes vector $\hat{C} = (C_1, C_2, C_3)/C_0$, where C_0 is the total intensity of the noise diode and the components correspond to Stokes Q, U, and V, respectively. These assumptions and parameterizations enable a stable solution for the polarimetric

response, even in the presence of imperfect or incomplete calibration data.

This modeling framework has been shown to significantly improve timing precision. For instance, Manchester et al. [2013] applied MEM to Parkes radio telescope observations of nine pulsars and found substantial reductions in both root-mean-square (RMS) and chi-square values derived from post-fit timing residuals, compared to uncalibrated profiles.

2.3.3 Measurement Equation Template Matching

METM is an advanced calibration technique used to match observations of a reference pulsar to a well-calibrated template profile. This method enables highly precise solutions of the instrumental response across different epochs, effectively characterizing the telescope's polarimetric response [van Straten, 2013].

A key strength of METM lies in its ability to model complex polarization effects and track instrumental variations over time. Unlike conventional methods such as the IFA, METM employs a template-based, iterative approach to improve calibration. The central idea is to build a detailed model of the expected pulsar signal that incorporates all known instrumental and propagation effects, such as Faraday rotation, polarization cross-coupling, and gain imbalance, and then iteratively refine this model to match the observed data [van Straten, 2004, 2006].

The fitting process involves minimizing the chi-squared merit function, similar to MTM, where the differences between observed and modeled Stokes parameters are minimized in the Fourier domain [van Straten, 2006]. Optimization is carried out using nonlinear least-squares techniques such as the Levenberg–Marquardt algorithm [Press et al., 1992]. Each instrumental effect (e.g., gain, phase, coupling) is represented by distinct parameters within the model, and while they are all jointly fit, their impact on the residuals may differ in magnitude. The minimization process weights all deviations

according to the noise variance in the data, meaning that stronger or better-measured components contribute more to the fit. This weighting ensures that dominant systematic effects are accurately corrected without being overwhelmed by lower S/N features [van Straten, 2006, 2013].

A bright, well-calibrated pulsar with stable and well-characterized polarization, such as PSR J0437−4715, is often used as a reference source. Over multiple iterations, METM refines the calibration model by minimizing residuals between the observed data and the predicted signal, ultimately generating a time-dependent solution for the telescope's response matrix [van Straten, 2013].

2.4 Noise Contributions

In addition to instrumental calibration and ToA estimation, accurate noise modeling is critical for achieving high-precision pulsar timing. Pulsar timing data are affected by various sources of noise that must be effectively modeled and mitigated. These noise sources include:

- Radio Frequency Interference (RFI): can lead to false detections of pulsar emissions, and distort the pulse profile, particularly in the case of impulsive RFI bursts on timescales shorter than the pulse period [Kocz et al., 2010, Nita and Gary, 2010].
- White noise: random, uncorrelated measurement fluctuations.
- Red noise: correlated low-frequency variations, which can introduce significant timing inaccuracies over long periods.
- DM noise: arises from the variable dispersion of radio waves through the ionized ISM, making precise DM determination and mitigation strategies essential [Keith et al., 2013, Lee et al., 2014, Jones et al., 2017].

Addressing and correcting for these noise sources is key to achieving the sensitivity needed in PTAs to detect the stochastic GWB.

2.4.1 Radio Frequency Interference

RFI typically originates from man-made sources, including communication and radar systems, as well as various electronic devices. It is a significant source of noise in radio astronomy, posing substantial challenges for accurate data collection and analysis. In pulsar timing, RFI mitigation is critical for preserving timing precision and maintaining a high S/N, as interference can significantly impact measurement accuracy.

Radio telescopes are often tuned to avoid known RFI-contaminated frequencies, and bandpass filters are used to exclude these problematic bands (see e.g., [Kerr et al., 2020]). However, RFI can still infiltrate observations, despite these precautions. Traditional RFI mitigation techniques rely on identifying and removing RFI-contaminated data using statistical methods that detect outliers, primarily in the time domain [Lazarus et al., 2016, 2020]. These methods operate on the assumption that RFI signals exhibit distinct statistical characteristics compared to genuine astrophysical signals.

Several statistical techniques, commonly used for automated RFI detection and flagging, include:

- Median Absolute Deviation (MAD): Calculates the median of the absolute deviations of data points from the median of the entire dataset. Points exceeding a certain threshold, typically 3–5 times the MAD, are flagged as potentially contaminated by RFI.

- Z-scores: Represents how many standard deviations a data point lies from the mean. Data points with high absolute Z-scores are considered outliers and likely contaminated by RFI.

- Interquartile Range (IQR): This approach identifies potential outliers by examining data points that fall outside the range defined by $Q1 - 1.5 \times$ IQR (lower whisker) and $Q3 + 1.5 \times$ IQR (upper whisker).

- Chi-squared test: Assesses whether the distribution of timing residuals deviates significantly from a normal distribution. Significant deviations can indicate the presence of non-Gian noise, potentially caused by RFI.

A combination of these can be applied to enhance the robustness of RFI detection. However, careful consideration is required when setting thresholds for flagging outliers:

thresholds that are too high may miss RFI contamination, while those that are too low risk eliminating genuine pulsar signals.

For practical use, the `paz` tool from the `PSRCHIVE` software suite [Hotan et al., 2004] provides automated methods for removing RFI. It can zap frequency channels or time sub-integrations based on user-defined or statistical criteria. For instance, users may choose to zap channels with persistently low S/N or with known contamination from persistent RFI sources (e.g., those near mobile communication bands). The interactive tool `pazi` allows manual inspection and removal of remaining RFI based on visual features such as bright horizontal (frequency) or vertical (time) stripes in the data.

In this work, RFI mitigation was further enhanced through the use of advanced pipelines such as `CoastGuard` [Lazarus et al., 2020] and/or `MeerGuard` [Reardon, 2021]—for advanced RFI detection and removal in pulsar timing data—providing an additional layer of precision in identifying and flagging RFI, ensuring that only high-quality, uncontaminated data are used in our analyses. These methods are discussed in more detail in Section 2.5.2.

2.4.2 White Noise

White noise is characterized by equal power across all frequencies within a given bandwidth, leading to a flat power spectral density

$$S(f) = \frac{\sigma^2}{\Delta f}, \tag{2.18}$$

where $S(f)$ is the power spectral density, σ^2 is the noise variance, and Δf is the bandwidth [Lentati et al., 2015, Tiburzi et al., 2016]. On short timescales, pulsar timing residuals are primarily dominated by white noise, which includes contributions from radiometer noise, jitter noise, and scintillation noise [Cordes and Shannon, 2010, Liu et al., 2012, Shannon et al., 2014, Lam et al., 2019].

Jitter noise, caused by intrinsic pulse-to-pulse variability, affects all pulsars [Cordes and Downs, 1985]. Scintillation noise results from stochastic broadening of the pulse due to a finite number of scintles—diffraction-limited patches in the turbulent ISM that scatter the pulsar signal—within the observing bandwidth. The finite number of scintles introduces variability in the observed pulse shape, which contributes to scintillation noise. This effect is frequency-dependent and varies with observing conditions [Cordes and Shannon, 2010].

In high S/N data, jitter noise can become the dominant noise source. Studies have quantified its effect on timing precision. For example, Osłowski et al. [2011] found that jitter limits the timing precision of PSR J0437−4715 to approximately 30 ns/hr of integration. Similarly, Shannon et al. [2014] reported that PSR J1909−3744 exhibits very low jitter noise (~10 ns/hr) due to its exceptionally stable pulse profile. More recently, Lam et al. [2019] confirmed the presence of jitter noise in 43 MSPs observed by NANOGrav, demonstrating its frequency dependence. Additionally, Parthasarathy et al. [2021] measured jitter in 29 pulsars from the MeerKAT project, with PSR J2241−5236 showing the lowest jitter at ~4 ns/hr.

In pulsar timing models, white noise is often parameterized using EFAC, EQUAD, and ECORR [Chalumeau et al., 2022]:

- EFAC scales the ToA measurement error bars to account for inaccuracies in the estimation process [Taylor, 1992].

- EQUAD adds an additional white noise term in quadrature to capture extra noise sources such as spin noise or pulse phase jitter [Cordes and Downs, 1985, Liu et al., 2011, van Haasteren et al., 2011, Shannon et al., 2014]. Its interpretation depends on the integration time of the ToAs: longer integrations average over more pulses, which reduces jitter contributions, so shorter integrations may require a higher EQUAD to reflect unresolved variability [Lentati et al., 2015].

- ECORR models correlated white noise (phase jitter) across different frequencies within the same epoch [Arzoumanian et al., 2015b].

EFAC (E_f) and EQUAD (E_q) are applied to the ToA uncertainties using the model

$$\sigma_{\text{new}} = \sqrt{E_q^2 + E_f^2 \sigma_{\text{old}}^2}, \tag{2.19}$$

where σ_{old} is the original measurement uncertainty for the ToA, and σ_{new} is the modified uncertainty incorporating both EFAC and EQUAD.

2.4.3 Red Noise

Red noise, also known as timing noise or spin noise, refers to temporally correlated noise that affects timing residuals over long timescales. This noise is believed to originate from a combination of intrinsic pulsar processes, ISM effects, and long-term instrumental systematics. It is characterized by a power spectral density that increases at lower frequencies,

$$S(f) \propto \frac{A}{f^\gamma}, \tag{2.20}$$

where A is the amplitude, $\gamma \geq 0$ is the spectral index, and f is the frequency. A higher γ means more power is present at lower frequencies, consistent with the long-timescale correlations typical of red noise [Lentati et al., 2015, Tiburzi et al., 2016].

Several mechanisms can contribute to red noise:

- Magnetospheric instabilities can introduce long-term fluctuations in the pulsar's spin-down rate ($\dot{\nu}$), leading to correlated variations in the timing residuals [Lyne et al., 2010, Ferdman et al., 2015].

- Glitches, which are sudden increases in a pulsar's spin frequency, are often followed by a recovery phase that can last months to years. These post-glitch relaxations can introduce long-term deviations from the timing model, contributing

to red noise [Espinoza et al., 2011, Lower et al., 2020].

- Scattering and plasma turbulence in the ISM can cause variations in the signal arrival times across long timescales, especially due to changes in the distribution of electron density along the line-of-sight [Hemberger and Stinebring, 2008, Cordes and Shannon, 2010].

- Clock errors and inaccuracies in SSB corrections can also introduce red noise into pulsar timing data [Caballero et al., 2018, Hobbs et al., 2020].

MSPs generally exhibit lower levels of red noise than younger, slower pulsars. This is largely attributed to their highly stable rotation rates and relatively weak magnetic fields, which are thought to reduce the impact of magnetospheric fluctuations and spin irregularities [Verbiest et al., 2009, Shannon and Cordes, 2010]. While pulsar age does influence spin stability, magnetic field strength and rotational energy loss rate are often more directly linked to the observed red noise levels [Cordes and Shannon, 2010].

However, red noise is still detectable in some MSPs, particularly in long-term datasets where high-precision timing is essential [Alam et al., 2021b, Goncharov et al., 2021b]. Due to its correlated nature, red noise can be difficult to distinguish from astrophysical signals such as GWs, since both can manifest as low-frequency trends in timing residuals [Stinebring et al., 1990, van Haasteren et al., 2009, Tiburzi et al., 2016].

2.4.4 Dispersion Noise

Dispersion noise (or DM noise) arises from variations in the dispersion of radio waves as they propagate through the ionized ISM [Backer et al., 1993, You et al., 2007, Lam et al., 2016]. These variations are caused by changes in the electron density along the line-of-sight, leading to frequency-dependent delays in pulse arrival times. The

dispersive delay scales with the square of the wavelength (λ^2), meaning that lower-frequency signals are delayed more as they traverse the ISM. This effect introduces uncertainties in pulsar timing, especially in wide-band observations where accurate correction of frequency-dependent delays is essential.

Dispersion and other propagation effects (such as scattering) can also modify the observed pulse shape. This complicates timing analysis, as the average pulse profile is a combination of both intrinsic pulsar emission features and ISM-induced distortions. Intrinsic features (such as the number, width, and relative amplitude of pulse components) are stable in the pulsar's rest frame but often vary with observing frequency due to emission physics. Propagation effects, on the other hand, distort the pulse profile as it travels through the ISM. For instance, interstellar scattering causes asymmetric pulse broadening, particularly at low frequencies, while unresolved dispersion smearing across frequency channels or finite filter bandwidths can lead to temporal smearing of the pulse [Kramer et al., 2006, Lentati et al., 2014, 2017]. The extent of these effects depends on both the properties of the ISM and the frequency resolution and channelization of the observing instrument.

DM noise includes both red and white components and does not always exhibit long-term correlations. Its variability depends on the spatial and temporal structure of the ISM: in some lines of sight, it changes gradually over months, while in others, it fluctuates rapidly due to small-scale turbulence [Lam et al., 2016, Jones et al., 2017]. Because of this variability, DM noise can mask or mimic other types of timing noise, including intrinsic spin noise or GWs.

To address these challenges, several techniques have been developed to model and correct for DM variations:

- **Delta DM estimation:** This method involves estimating time-variable changes in DM by comparing timing residuals across multiple observing frequencies. In

addition to fitting for frequency-dependent delays, modern approaches also incorporate pulse profile shape variations, which are used as additional information to constrain DM changes [Lentati et al., 2017]. For example, since dispersion and scattering alter the pulse profile differently at different frequencies, modeling the evolving profile shape over time can help isolate dispersive delays from intrinsic shape changes. Wideband timing methods, such as those described by Pennucci 2019 and Luo et al. 2021 simultaneously estimate pulse arrival times and DM while allowing the profile shape to vary with frequency, making the analysis less sensitive to amplitude modulation caused by scintillation.

- **Bayesian Inference:** Probabilistic frameworks, such as those based on Bayesian inference, have been used to jointly estimate DM variations along with other noise components. These models often treat DM as a stochastic process with a red noise spectrum and allow for uncertainty quantification and marginalization over model parameters. This approach helps separate DM noise from other low-frequency signals such as spin noise or potential GW signals [Lentati et al., 2015].

Together, these techniques enable more precise tracking of time-variable DMs, which is critical for reducing timing residuals and enhancing the sensitivity of PTAs to low-frequency GW signals.

2.5 Software Tools

2.5.1 PSRCHIVE

PSRCHIVE is an open-source software suite designed for the analysis of pulsar data [Hotan et al., 2004]. It offers a wide array of tools for processing, manipulating, visualizing, and analyzing radio pulsar observations. The suite is instrumental in tasks such as:

- Data reduction, including RFI mitigation, DM correction, and polarimetric calibration.
- Pulse profile analysis, enabling alignment, averaging, and measurement of properties like flux density, polarization, and pulse width.
- Timing analyses, such as extracting ToAs from pulse profiles and generating ToA files compatible with timing software like TEMPO2.
- Visualization of pulse profiles, dynamic spectra, and other relevant data products [van Straten et al., 2012].
- Polarimetric calibration [van Straten, 2004, Ord et al., 2004, van Straten, 2013, Rogers et al., 2024].
- Arrival time estimation [Taylor, 1992, Hotan et al., 2005, van Straten, 2006, Rogers et al., 2024].
- Faraday rotation measure determination [Han et al., 2006, Noutsos et al., 2008, Caleb et al., 2019].
- Fourth-order electric field moment propagation [van Straten, 2009].
- Statistical analysis of profile variability [Demorest, 2007, Osłowski et al., 2011].

- ISM studies through pulsar scintillation [Rickett, 1990, Cordes and Rickett, 1998, Nguyen et al., 2022].
- Exoplanet detection [Bartnik and Fonseca, 2023].

2.5.2 CoastGuard

The automated pipeline CoastGuard was developed to efficiently reduce and analyze pulsar timing data for the EPTA project. It is a Python-based tool built on the PSRCHIVE library and was specifically designed to identify and mitigate RFI in pulsar observations [Lazarus et al., 2016].

CoastGuard processes raw pulsar data through initial cleaning steps that address formatting issues and remove obvious sources of noise. It then applies up to four RFI-mitigation algorithms in sequence to detect and flag contaminated data [Lazarus et al., 2020]:

1. "rcvrstd" removes frequency channels that fall outside the usable band of the receiver's sensitivity (i.e., in regions where the bandpass sharply rolls off and the receiver response becomes unreliable) or are known to be persistently contaminated. These bad channels are defined in advance for each receiver.

2. "surgical" operates on folded pulsar data cubes, which are three-dimensional arrays of pulse profiles organized by pulse phase, frequency channel, and time sub-integration. Each cube contains the averaged pulse shape for many rotations of the pulsar, enabling high-S/N profiles while retaining frequency and time resolution. The algorithm detects and flags RFI-affected profiles by fitting the integrated pulse profile (i.e., the mean pulse shape across the observation) using a least-squares method. To avoid bias from the pulsar signal, the fitting is performed on the residuals outside the on-pulse region. RFI contamination is identified using

four statistical metrics:

- Standard deviation
- Mean
- Range
- Maximum amplitude of the Fourier transform of mean-subtracted residuals

These metrics are sensitive to a range of RFI types, including narrowband noise, sudden dropouts, and brief periodic bursts. For each metric, a matrix of values is computed for each time–frequency bin (i.e., each sub-integration and channel). Long-term trends and bandpass variations in these matrices are removed using piecewise quadratic fits. The rescaled matrices are then searched for outliers, defined as values more than five standard deviations ($> 5\sigma$) from the median of their respective row or column. Any pulse profile flagged as an outlier by at least two metrics is down-weighted (zero-weighted) in subsequent analysis.

3. "bandwagon" removes sub-integrations and frequency channels that have an excessive fraction of masked or flagged data, under the assumption that they are likely dominated by RFI.

4. "hotbins" targets localized bursts of RFI in the off-pulse region. It replaces outlier phase bins with locally generated Gaussian noise, preserving the overall noise characteristics without introducing artificial structure.

A variant of this pipeline, MeerGuard, was developed for the MeerTime project. It is adapted to handle the wide-bandwidth data typical of MeerKAT observations and incorporates frequency-dependent pulse templates to improve RFI excision and timing precision [Reardon, 2021].

2.5.3 Tempo2

TEMPO2 is an advanced pulsar timing analysis software package developed to provide accurate and robust timing solutions, particularly suited for PTA data. It was designed to overcome limitations of its predecessor, TEMPO, and offers a more versatile framework for modeling pulsar timing data with high precision. TEMPO2 accounts for a wide range of astrophysical effects and instrumental delays, allowing for detailed modeling of pulsar parameters and timing behavior [Edwards et al., 2006, Hobbs et al., 2006].

To perform a timing analysis using TEMPO2, two key input files are required:

- A .tim file, which contains the ToAs of pulsar signals. Each ToA entry includes:
  - The observing frequency
  - The Modified Julian Date (MJD) of the observation
  - The telescope identifier
  - The measured ToA value and its uncertainty.
- A .par file, or timing model (ephemeris), which provides the initial estimates of the pulsar's physical and orbital parameters. These include:
  - Astrometric parameters: such as right ascension, declination, and proper motion
  - Spin parameters: such as the spin frequency and its derivatives
  - Binary parameters (if applicable): such as orbital period, eccentricity, and projected semi-major axis.

With these files, TEMPO2 constructs an initial timing model by fitting the ToAs to these parameters. This fitting process minimizes the timing residuals using a weighted least-squares algorithm [Press et al., 1992]. The fit quality is quantified using the

chi-squared statistic

$$\chi^2 = \sum_{i=1}^{N} \left(\frac{R_i}{\sigma_i} \right)^2 , \tag{2.21}$$

where N is the number of data points, σ_i is the uncertainty of the i^{th} ToA, and R_i is the post-fit residual for the i^{th} data point. As more data are recorded, the timing model parameters can be measured to higher precision.

Residual plots indicate the accuracy of the timing model and any unmodeled effects may be identified if significant deviations are observed. In such cases, the model can be refined by adjusting or adding parameters, or modeling the red noise, as described in the following section.

Applications of TEMPO2 extend beyond PTAs. It has been used in:

- Stringent tests of GR and alternative theories of gravity by comparing observed relativistic effects with theoretical predictions [Kramer et al., 2006, Antoniadis et al., 2013].
- Measuring NS masses, which contribute to understanding the NS EOS and the behavior of matter at extreme densities [Demorest et al., 2010, Fonseca et al., 2021].
- Correcting for dispersion and scattering effects of the ISM, helping to map the distribution of free electrons and turbulence in the Galaxy [Keith et al., 2013, Jones et al., 2017].
- Measuring pulsar proper motions, contributing to understanding the structure and motion of the Milky Way, tracing the dynamics of the Galactic disk and halo [Han et al., 2018, Sobey et al., 2019].

2.5.4 TempoNest

TEMPONEST is an advanced Bayesian software package that significantly enhances the analysis of pulsar timing data by jointly estimating both the non-linear timing solution and a range of stochastic parameters, such as red spin noise and DM variations [Lentati et al., 2014]. It supports both traditional power-law noise models and a model-independent approach, which parameterize noise power at specific frequencies. Studies utilizing TEMPONEST (e.g., [Desvignes et al., 2016, Verbiest et al., 2016, Reardon et al., 2016, Xu et al., 2023]) have demonstrated that conventional linear timing models often underestimate uncertainties, sometimes by an order of magnitude, particularly in high-precision datasets. By allowing Bayesian model selection, TEMPONEST can distinguish between different timing and noise models, showing, for example, that spin noise and DM variations in pulsar B1937+21 are best described by power-law models. Neglecting these stochastic processes can lead to unreliable uncertainty estimates and affect the robustness of scientific conclusions [Lentati et al., 2014, 2015].

TEMPONEST is designed as a plug-in to TEMPO2, integrating its pulsar timing capabilities with the nested sampling algorithm. Nested sampling, first introduced by Skilling [2004], is a Monte Carlo method designed for the efficient calculation of evidence, while also producing posterior distributions as a by-product. The MultiNest algorithm [Feroz and Hobson, 2008, Feroz et al., 2009] is a powerful Bayesian framework that allows for robust quantification of noise model parameters and their uncertainties, while also providing a means for model comparison. TEMPONEST extends this approach to handle posterior distributions with multiple modes (i.e., situations where the data suggests more than one plausible set of model parameters) or large degeneracies (i.e., when different combinations of model parameters produce similar timing residuals, making it difficult to distinguish between them). Examples of such degeneracies in pulsar timing analyses include the trade-offs between the DM and other

noise components like red noise [Lentati et al., 2016].

In addition to the standard ToA and ephemeris files used in TEMPO2, TEMPONEST requires a configuration file that specifies settings for the MultiNest algorithm. These include the number of live points, which determines how many points are sampled and tracked during the search of the parameter space, the convergence criteria for stopping the sampling process, and the prior distributions for noise model parameters.

Bayesian inference provides a systematic approach to estimating model parameters (θ) given the data (D), using Bayes' theorem

$$P(\theta|D) = \frac{L(\theta|D)p(\theta)}{Z}, \tag{2.22}$$

where $P(\theta|D)$ is the posterior probability distribution, $L(\theta|D)$ is the likelihood, $p(\theta)$ is the prior, and Z is the Bayesian evidence. The evidence plays a crucial role in model selection, favoring simpler models unless a more complex model provides a significantly better fit to the data. This is known as Occam's razor: a simpler model with a compact parameter space is preferred unless the additional complexity provides substantial explanatory power [Lentati et al., 2015].

2.6 Research Questions

Pulsar signals are highly polarized, which presents challenges for PTA experiments due to instrumental distortions such as differential gain variations and parallactic rotation of the receiver. These distortions affect the polarization properties of observed signals, introducing systematic timing errors that can undermine the sensitivity of PTA experiments [van Straten, 2006]. For example, many pulsars in the PPTA dataset experience timing errors caused by uncalibrated instrumental polarization artifacts, leading to correlated errors across multiple pulsars [van Straten, 2013].

2.6.1 Research Question 1

How can high-fidelity polarization calibration reduce systematic timing errors, and to what extent could this improve the robustness of GWB detection by PTAs?

Enhanced instrumental calibration is critical for improving GW detection. It also refines pulsar timing precision, enabling precise measurements of parameters such as the secular variation of the projected semi-major axis and Shapiro delay in PSR J1022+1001 [van Straten, 2013].

2.6.2 Research Question 2

Which additional PPTA pulsars could benefit from advanced calibration techniques to achieve sub-μs timing precision, and what new astrophysical parameters might this reveal?

Several pulsars in the PPTA already achieve sub-μs residuals, such as PSR J1909−3744 and PSR J0437−4715 [Reardon et al., 2016, Lentati et al., 2016], but the extent to which others could reach similar precision through calibration improvements remains unclear. Identifying additional pulsars that could reach similar precision through advanced calibration techniques is key for optimizing the array's sensitivity

and scientific return. This question also motivates quantifying the number of pulsars that fall short due to calibration-limited performance.

2.6.3 Research Question 3

To what extent can improved calibration techniques:

1. **mitigate red noise arising from instrumental effects and pulsar spin irregularities, and**

2. **reduce white noise by enhancing the accuracy of ToA estimation?**

Red noise in pulsar timing, caused by intrinsic pulsar spin irregularities, DM variations, or long-term instrumental instabilities, remains a significant challenge for PTAs [Verbiest et al., 2009, Alam et al., 2021b, Goncharov et al., 2021b]. Advanced instrumental calibration could help distinguish between astrophysical effects and instrumental distortions, mitigating red noise [van Straten, 2013].

2.6.4 Research Question 4

Can improved calibration techniques enhance the modeling of noise sources in wide-bandwidth data, leading to better timing precision and stronger constraints on GW signals?

The MeerKAT radio telescope, part of the MeerTime Large Survey Project [Bailes et al., 2016], has already demonstrated significant progress in pulsar timing precision, as shown by the MPTA's first data release, which achieved timing residuals better than 1 μs for 67 pulsars [Miles et al., 2023]. MPTA's potential has been demonstrated in various studies, such as those investigating jitter noise in MSPs [Parthasarathy et al., 2021], conducting a comprehensive census of MSPs visible to MeerKAT [Spiewak et al., 2022], and discovering mode-changing in one of the most precisely timed MSPs

[Miles et al., 2022]. These advancements in timing precision provide a glimpse into the future capabilities of the Square Kilometer Array (SKA; [Dewdney et al., 2009]).

2.6.5 Research Question 5

Could reducing systematic noise through improved calibration enable the detection of more elusive low-frequency GW sources, such as individual SMBHBs?

Beyond detecting the stochastic GWB [Agazie et al., 2024, 2023b, Antoniadis et al., 2023c,a, Reardon et al., 2023, Zic et al., 2023, Xu et al., 2023], PTAs may eventually reach the sensitivity needed to detect continuous GW sources or burst events from exotic objects [Jenet et al., 2004, Corbin and Cornish, 2010, Ellis, 2013, Taylor and Gair, 2013, Huerta et al., 2015, Zhu et al., 2015b, Babak et al., 2016, Mingarelli et al., 2017]. Achieving such sensitivity requires minimizing systematic errors, particularly in polarization calibration and ToA estimation—both strongly influenced by instrumental distortions.

Chapter 3

Manuscript 1

This chapter is based on work published in The Astrophysical Journal (vol. 973, no. 2, Art. no. 94, 2024). It demonstrates the impact of state-of-the-art instrumental calibration techniques on the precision of arrival times obtained from 9.6 years of observations of MSPs using the Murriyang 64-m CSIRO Parkes Radio Telescope. Our study focuses on 21-cm observations of 25 high-priority pulsars that are regularly observed as part of the Parkes Pulsar Timing Array (PPTA) project, including those predicted to be the most susceptible to calibration errors. We employ Measurement Equation Template Matching (METM) for instrumental calibration and Matrix Template Matching (MTM) for arrival time estimation, resulting in significantly improved timing residuals with up to a sixfold reduction in white noise compared to arrival times estimated using Scalar Template Matching and conventional calibration based on the Ideal Feed Assumption. The median relative reduction in white noise is 33%, and the maximum absolute reduction is 4.5 μs. For PSR J0437−4715, METM and MTM reduce the best-fit power-law amplitude (2.7 σ) and spectral index (1.7 σ) of the red noise in the arrival time residuals, which can be tentatively interpreted as mitigation of $1/f$ noise due to otherwise unmodeled steps in polarimetric response—sudden changes or discontinuities in the instrumental response to the polarization of incoming pulsar signals, which have not been accounted for

in the timing model. These findings demonstrate the potential to directly enhance the sensitivity of PTA experiments through more accurate methods of instrumental calibration and arrival time estimation.

3.1 Introduction

PTAs are invaluable tools for detecting spatially correlated signal fluctuations at low frequencies, spanning from nHz to μHz [Sazhin, 1978, Detweiler, 1979, Hellings and Downs, 1983]. Within this frequency band, the dominant anticipated signal is the stochastic gravitational-wave background (GWB) generated by a cosmic population of inspiralling SMBHBs [Sesana et al., 2004, Burke-Spolaor et al., 2019]. Additional speculative sources of GWs in the nHz range encompass cosmic strings [Siemens et al., 2007, Blanco-Pillado et al., 2018], phase transitions [Caprini et al., 2010, Kobakhidze et al., 2017, Xue et al., 2021], and a primordial GWB originating from quantum fluctuations of the gravitational field during the early universe, amplified by inflation [Grishchuk, 1975, Lasky et al., 2016].

The GWB is expected to manifest as a common red noise process, characterized by a similar spectral signature, in all pulsars within the array [Phinney, 2001]. Detection of spatially correlated signals in the ToAs of multiple pulsars [Rajagopal and Romani, 1995], with the quadrupolar signature (HD correlation) initially proposed by Hellings and Downs [1983], provide compelling evidence of a stochastic GWB detection [Agazie et al., 2023b]. Over the past decade, PTA collaborations have steadily improved the sensitivity of their data sets for GW searches, progressively reducing the upper limits on the stochastic GWB amplitude [van Haasteren et al., 2011, Demorest et al., 2013, Shannon et al., 2013b, Arzoumanian et al., 2014, Lentati et al., 2015, Shannon et al., 2015, Arzoumanian et al., 2016, Verbiest et al., 2016, Arzoumanian et al., 2018, Perera et al., 2018, Alam et al., 2021b,a], and working towards identifying individual GW

sources [Yardley et al., 2010, Zhu et al., 2014, Babak et al., 2016, Aggarwal et al., 2019].

Beyond GWs, various astrophysical processes can introduce red noise that is unique to each pulsar [Coles et al., 2011, van Haasteren and Levin, 2013, Lentati et al., 2014]. These include intrinsic spin noise [Shannon and Cordes, 2010, Melatos and Link, 2014, Lam et al., 2017], magnetospheric torque variations [Lyne et al., 2010], variable dispersion [Keith et al., 2013, Jones et al., 2017] and multi-path propagation effects in the interstellar medium (ISM) [Hemberger and Stinebring, 2008, Cordes and Shannon, 2010, Dolch et al., 2021], and the presence of undetected objects in orbit around pulsars [Shannon et al., 2013a].

The IPTA collaboration, composed of various PTA projects, is dedicated to the pursuit of a common goal: the detection of nHz-frequency GWs [Hobbs et al., 2010, Perera et al., 2019, Verbiest et al., 2016]. Currently, the IPTA encompasses four PTA members: the EPTA [Kramer and Champion, 2013, Desvignes et al., 2016], the InPTA [Joshi et al., 2018, Susobhanan et al., 2020], NANOGrav [McLaughlin, 2013, Arzoumanian et al., 2018, Cordes and McLaughlin, 2019, Ransom et al., 2019], and the PPTA [Manchester et al., 2013, Reardon et al., 2016, Kerr et al., 2020]. Furthermore, efforts are underway to establish the CPTA, leveraging the Five-hundred-meter Aperture Spherical Telescope [FAST; Lee, 2016, Hobbs et al., 2019]. Other scientific initiatives, such as the MPTA in South Africa [Bailes et al., 2016], and the Canadian Hydrogen Intensity Mapping Experiment (CHIME) pulsar collaboration in Canada [Ng, 2018], are poised to contribute to the IPTA's collaborative endeavours. An essential addition to this list is the γ-ray pulsar timing array (Fermi PTA), which offers an independent probe of the GWB and stands as the sole means of confirming radio PTA results [Ajello et al., 2022].

In 2020 and 2021, significant advancements were made in our understanding of PTAs. The NANOGrav 12.5-year data set [NG12.5; Arzoumanian et al., 2020], EPTA

second data release [EPTA DR2; Chen et al., 2021], and PPTA second data release [PPTA DR2; Goncharov et al., 2021b] all revealed a common uncorrelated red noise (CURN) process within their data sets, marking a crucial discovery. However, these studies failed to conclusively confirm or refute the presence of hypothetical HD correlations.

This revelation gained further support through an analysis of the second data release from the IPTA [IPTA DR2; Perera et al., 2019], which consolidated historical data from EPTA, NANOGrav, and PPTA, and confirmed the existence of a CURN process [Antoniadis et al., 2022]. However, independent analysis of PPTA DR2 by Goncharov et al. [2021b] shed light on the potential misinterpretation of noise without a statistically identical spectrum between pulsars as a common red process.

PTAs demonstrate sensitivity not only to the quadrupolar correlation of GWs [Taylor et al., 2016, Burke-Spolaor et al., 2019] but also to various other correlated signals. These can include monopolar correlation due to terrestrial time standards errors [Hobbs et al., 2012, 2020], and dipolar correlation stemming from errors in the SSE model [Champion et al., 2010, Caballero et al., 2018]. Incorrect modeling of these sources may introduce red noise into timing residuals, potentially compromising GW detection sensitivity [Tiburzi et al., 2016]. While NG12.5 ruled out monopolar and dipolar spatially correlated signals [Arzoumanian et al., 2020], the analysis of timing residuals in NG12.5, EPTA DR2 and PPTA DR2 do not yield statistical support for quadrupolar spatial correlation [Arzoumanian et al., 2020, Chen et al., 2021, Goncharov et al., 2021b].

The most recent GWB search papers by the EPTA [Antoniadis et al., 2023c], NANOGrav [Agazie et al., 2024], and PPTA [Reardon et al., 2023] present analyses of their latest data releases: EPTA second data release [EPTA DR2new+; Antoniadis et al., 2023c], NANOGrav 15-year data set [NG15; Agazie et al., 2023a], and PPTA third data release [PPTA DR3; Zic et al., 2023]. These papers unveil evidence for an

HD-correlated GWB with varying levels of significance, with estimated probabilities of false alarm rates at 3σ, 3-4σ and 2σ, respectively. A comparison of these studies showcases consistent measurements of nHz GWB parameters, even with diverse data modeling approaches, demonstrating agreement within 1σ. The coherence of pulsar noise parameters in the majority of analyzed pulsars and the standardization of noise models reconcile modeling disparities, refining constraints on GWB amplitude and HD correlations. This advancement provides a robust foundation for IPTA's Data Release 3 by extending data sets to encompass additional pulsars [Agazie et al., 2024]. Concurrently, the CPTA also reported similar findings on the HD-correlated GWB [Xu et al., 2023], aligning with the broader consensus from other PTA projects.

The sensitivity of PTA experiments is founded upon the accuracy and precision with which arrival times can be estimated. Therefore, it remains important to study and quantify the extent to which PTA sensitivity may be limited by unmodeled instrumental artifacts and calibration errors. Instrumental polarization can distort pulse profiles, leading to correlated errors in the ToAs of each pulsar that can mimic signals associated with a stochastic GWB [van Straten, 2013, Lentati et al., 2016]. Consequently, polarimetric calibration is crucial for minimizing systematic timing errors [van Straten, 2006, Guillemot et al., 2023], which are most readily observed as dramatic variations of arrival time residuals as a function of parallactic angle [e.g. Figure 1 of van Straten, 2013]. Various methods, including enhanced arrival time estimation [Hotan et al., 2005, van Straten, 2006], instrumental calibration [Jenet and Anderson, 1998, van Straten, 2004], and radio frequency interference (RFI) mitigation [Lazarus et al., 2016, 2020, Reardon, 2021], have been developed to quantify and mitigate sources of systematic error, thereby enhancing the precision and accuracy of ToA estimates.

For most pulsars, modest instrumental distortion can induce systematic timing errors of the order of 100 ns [van Straten, 2013], significantly hindering efforts to detect the stochastic GWB [Jenet et al., 2005] (see §2.1.3). In this study, we investigate

instrumental distortion of arrival times estimated for the 25 high-priority MSPs regularly observed for the PPTA project, which includes pulsars with great potential for improvement by addressing calibration errors [van Straten, 2013].

The paper's structure is as follows: we describe the data set in §3.2, detail our methods in §3.3, present our results in §3.4, and conclude with a discussion of our findings and prospects for future research in §3.5.

3.2 Observations

The observations analyzed in this study were carried out using the Murriyang 64-m radio telescope at Parkes. Our analysis focuses on a subset of the data from PPTA DR2, which provides precise arrival times for 26 MSPs. (PSR J1732−5049 was excluded from this research as it was recently removed from the PPTA's high-priority list.) DR2 spans a 14-year period, with an observational cadence of approximately three weeks, and includes observations from various radio frequency bands (10-cm, 20-cm, 40/50-cm) and backend instruments (CASPSR, CPSR2, PDFBs, WBCORR) [Kerr et al., 2020]. Notably, DR2 yielded the lowest root-mean-square (RMS) timing residuals for each pulsar up to the point of our analysis, which precedes PPTA DR3.

The selected subset of PPTA DR2 comprises observations conducted between MJDs 55409 and 58933 (from 1 August 2010 to 25 March 2020) at 1400 MHz (corresponding to the 20-cm band observations) employing the H-OH and 21-cm Multibeam receivers and CASPSR backend. Although CASPSR was also used to observe in the 10-cm (~ 3100 MHz) and 40/50-cm (~ 700 MHz) bands, our analysis focuses solely on the 20-cm band observations due to the limited availability of 10-cm data and the significant RFI contamination in the 40/50-cm band [Parthasarathy et al., 2019]. Please refer to Table 3.1 for more details about the observations of each pulsar.

Pulsar (JNAME)	P (ms)	O_{ToA}	N_{ToA}	Span (yr)	MJD Range (start – finish)
PSR J0437−4715	5.76	882	700	8.210	55409 – 58933
PSR J0613−0200	3.06	238	221	8.773	55427 – 58752
PSR J0711−6830	5.49	349	333	9.565	55427 – 58932
PSR J1017−7156	2.34	353	333	8.764	55472 – 58749
PSR J1022+1001	16.45	241	222	8.172	55426 – 58410
PSR J1024−0719	5.16	138	127	9.098	55426 – 58749
PSR J1045−4509	7.47	187	177	9.051	55444 – 58749
PSR J1125−6014	2.63	150	141	8.865	55694 – 58932
PSR J1446−4701	2.19	170	145	8.913	55677 – 58932
PSR J1545−4550	3.58	133	123	6.621	56513 – 58931
PSR J1600−3053	3.60	189	174	9.551	55444 – 58932
PSR J1603−7202	14.84	222	212	9.095	55427 – 58749
PSR J1643−1224	4.63	167	155	9.057	55445 – 58753
PSR J1713+0747	4.57	256	246	9.059	55444 – 58753
PSR J1730−2304	8.12	186	165	9.598	55427 – 58932
PSR J1744−1134	4.07	253	237	9.057	55445 – 58753
PSR J1824−2452A	3.05	87	80	8.923	55493 – 58752
PSR J1832−0836	2.72	78	72	6.804	56447 – 58932
PSR J1857+0943	5.36	138	127	9.515	55457 – 58932
PSR J1909−3744	2.95	374	344	8.926	55444 – 58752
PSR J1939+2134	1.56	153	142	7.823	55472 – 58329
PSR J2124−3358	4.93	227	221	9.474	55472 – 58933
PSR J2129−5721	3.73	255	238	9.516	55457 – 58933
PSR J2145−0750	16.05	224	211	9.474	55471 – 58932
PSR J2241−5236	2.19	399	329	9.644	55410 – 58933

Table 3.1: Observational characteristics of 25 high-priority PPTA pulsars, including J2000.0 coordinates (JNAME), spin period (P) in milliseconds, observed ToAs (O_{ToA}), remaining ToAs after outlier rejection (N_{ToA}), observation time span (in years), and corresponding modified Julian date (MJD) range. Note that for PSR J1022+1001, ToAs from August 15th to 30th each year were excluded in consideration of solar conjunction.

3.3 Methods

The following sections describe the two methods of polarimetric calibration and the two methods of arrival time estimation that are compared in this work.

3.3.1 Polarimetric Calibration

To establish a baseline for comparing the impact of calibration techniques, data are calibrated using an estimate of the polarimetric response of the observing system based on an approximation known as the *Ideal Feed Assumption* [IFA; Lorimer and Kramer, 2012] (see §2.3.1). The IFA calibration model includes the assumptions that the receptors are perfectly orthogonally polarized and that the reference source (e.g., a pulsed noise diode coupled to the receptors) is 100% linearly polarized, illuminating both receptors equally and in-phase [Caleb et al., 2019]. The IFA is an incomplete description of the instrumental response, and, for some systems, calibration based on the IFA results in significant systematic variations of the total intensity profile and arrival time distortions. Therefore, for comparison in this study, the data are also calibrated using *Measurement Equation Template Matching* [METM; van Straten, 2013]. METM uses a single well-calibrated observation of a pulsar with a high S/N as a polarized reference source, one or more uncalibrated observations of the same pulsar, and (optionally), observations of an amplitude-modulated reference source.

For this study, PSR J0437−4715 is used as the polarized reference source, and its template profile is derived from multiple MEM solutions. MEM (see §2.3.2) uses uncalibrated observations of a pulsar observed at multiple parallactic angles and an amplitude-modulated reference source. We employ the polarimetric calibration pipeline (PSRPL)[1] to perform both MEM and METM on multiple data sets. Following RFI

[1] http://psrchive.sourceforge.net/manuals/psrpl/

excision using MEERGUARD[2], the Meertime extension of COASTGUARD[3] [Lazarus et al., 2016, 2020], we generate five-minute sub-integrations of PSR J0437−4715 and two-minute sub-integrations of noise diode observations. Separate calibrator models are produced for each data set.

During the MEM stage, eq. (19) of Britton [2000] is used to parameterize the unknown response of the non-ideal receiver, and the degenerate model parameters described in appendix B of van Straten [2004] are set to zero. The degenerate model parameters include the difference in the receptor ellipticities, δ_χ, which mixes Stokes I and Stokes V, and the rotation of the receiver about the line-of-sight, σ_θ, which mixes Stokes Q and Stokes U. By setting these parameters to zero, the receptors are assumed to have equal (and opposite) ellipticities, and the rotation of the receiver about the line-of-sight is assumed to be zero. The unknown polarization of the non-ideal noise diode signal is parameterized by the three components of the normalized Stokes polarization vector, $\hat{\boldsymbol{C}} = (\hat{C}_1, \hat{C}_2, \hat{C}_3) = (C_1, C_2, C_3)/C_0$, where C_0 is the total intensity of the noise diode and, for linearly polarized receptors, C_1, C_2, and C_3 correspond to Stokes Q, U, and V of the noise diode (see §2.3.2)

From the dataset, 66 MEM solutions were generated. Of these, 52 were selected as the most robust, having a weighted mean reduced χ^2 (averaged over all frequency channels) between 0.85 and 1.05. These selected solutions were then ranked based on the product of several range-normalized attributes. Given the minimum and maximum values, $x_{\min}$ and $x_{\max}$, of some attribute x, and the value of that attribute derived from the i^{th} solution x_i, the (dimensionless) range-normalized attribute,

$$\hat{x}_i = \frac{x_i - x\min}{x_{\max} - x_{\min}} \tag{3.1}$$

lies on the interval $[0, 1]$. This normalization gives equal weight to each of the attributes

[2]https://github.com/danielreardon/MeerGuard
[3]https://github.com/plazar/coast_guard

included in the rank metric, which is a function of the integration length of the session, the S/N of the integrated average profile, the weighted mean reduced χ^2, the median uncertainties of the estimated values of δ_θ (the difference in receptor orientations) and σ_χ (the receptor ellipticities), and the fraction of the band that was lost to RFI. Based on these attributes, the MEM solution derived from the observing session recorded on 2014 April 15 is ranked as the best, and the calibrated total profile observed on this day is selected as the reference profile.

The 51 other MEM-calibrated total profiles are matched to this reference profile using Matrix Template Matching [MTM; van Straten, 2006], then the reference profile and matched totals are integrated to form a template profile with an integration length of 160 hours, shown in Figure 3.1. Between pulse phase ~ 0.9 and 0.13, the polarized flux appears to be greater than the total intensity, which is not physically possible. This artifact of imperfect baseline removal may indicate that radiation from this pulsar is received at all times; therefore, there is no off-pulse region of pulse phase, and each of the four Stokes parameters is offset by an arbitrary amount. This baseline artifact does not affect arrival time estimates, which are calculated using only the non-zero spin harmonics of the Fourier transform of each pulse profile. Although PSR J0437−4715 is the brightest pulsar with the highest precision in the PPTA, it is also exceptionally susceptible to calibration errors, primarily owing to the transition between orthogonally polarized modes in the middle of its main pulse.

This template profile is used as the polarized reference source in the following stage of METM analysis, during which eq. (19) of Britton [2000] is used to parameterize the receiver and all model parameters are varied.

A total of 296 robust METM solutions are selected. This number results from applying Tukey's fence thresholds (see §3.3.2) to various quality attributes, including the median reduced χ^2 across all frequency channels, the median uncertainties of the estimated δ_θ and σ_χ, and the normalized Stokes parameters $\hat{C}_1$ and $\hat{C}_2$. Solutions

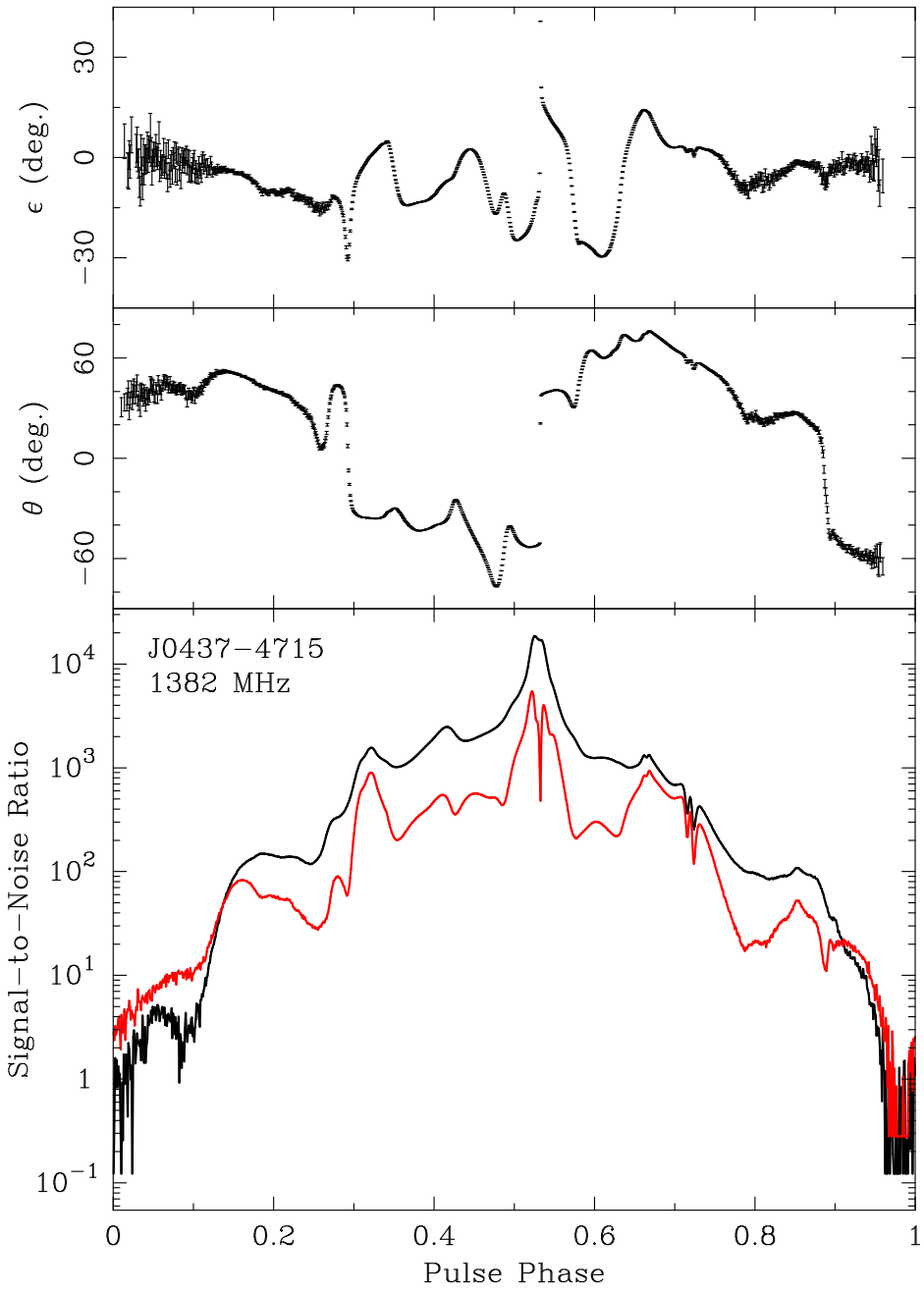

Figure 3.1: Average polarization of PSR J0437−4715, plotted on a logarithmic scale as a function of pulse phase using polar coordinates: orientation, θ, ellipticity, ϵ, and polarized intensity plotted in red below the total intensity. Flux densities are normalized by the standard deviation of the off-pulse total intensity phase bins. Calibrated using MEM and used as the template for METM, this profile is integrated from 160 hours of observations that span 9.6 years and 400 MHz of bandwidth centred at 1382 MHz.

that pass these criteria and have a sufficiently low fraction of the band lost to RFI are considered robust.

In this analysis, variation of ionospheric Faraday rotation is not included in the METM model; therefore, for each METM solution, the variation of the best-fit estimate of σ_θ with radio frequency is used to derive an estimate of the average change in ionospheric Faraday rotation on that day, relative to 2014 April 15. After excluding outliers, the ionospheric Faraday rotation measure differences (ΔRM shown in Figure 3.2) vary between -3.3 and $+2.7$ rad m^{-2} over the 9.6 years spanned by robust METM solutions. The predominantly day-to-night variation of ionospheric total electron content is observed as annual variations in the derived ionospheric ΔRM estimates owing to the annual drift between solar time and the sidereal times at which PSR J0437−4715 is observed. The observed peak in ionospheric ΔRM around MJD 56750 (2014 March/April) is near the peak in solar magnetic activity cycle 24. These estimates of ionospheric RM

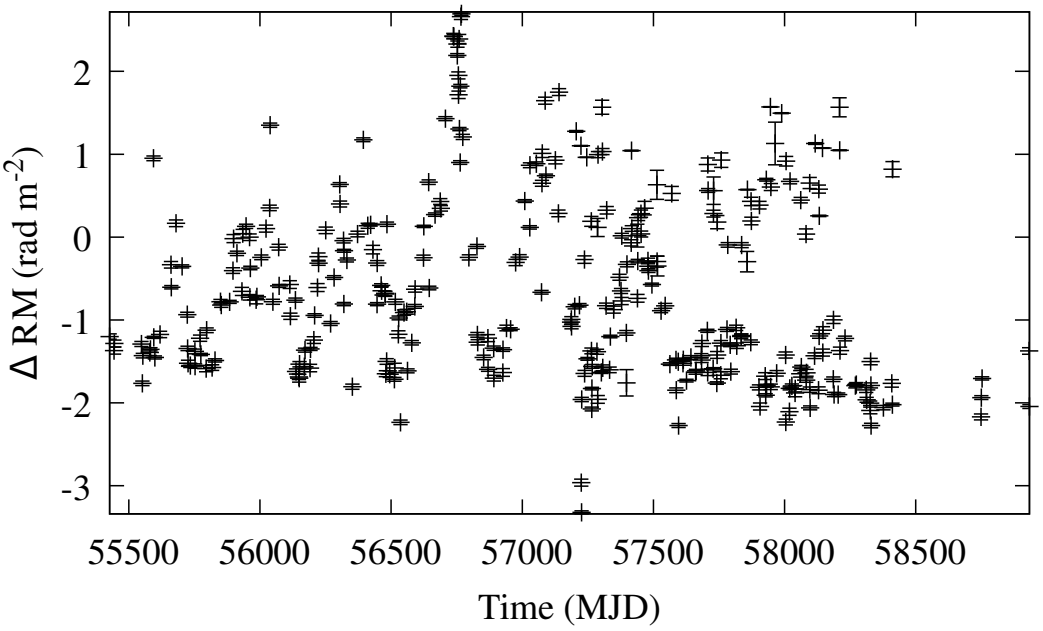

Figure 3.2: Temporal variation of average daily ionospheric contribution to Faraday rotation, measured with respect to the ionosphere on 2014 April 15 (MJD 56762). Most of the error bars, which denote the 1-σ uncertainty of the RM estimate, are too small to be distinguished from the data point.

are used to correct the estimates of σ_θ in each METM solution.

To reduce the noise in the estimated model parameters and interpolate across gaps in both time and radio frequency, seven of the METM model parameters (σ_θ, σ_χ, δ_θ, δ_χ, $\hat{C}_1$, $\hat{C}_2$, and $\hat{C}_3$) are smoothed using two-dimensional penalized splines [Eilers and Marx, 1996, Grimstad et al., 2015]. The optimal smoothing factor is determined using an iterative search algorithm. For each trial smoothing factor, the average goodness-of-fit is evaluated over four iterations of Monte Carlo cross-validation, also known as repeated random sub-sampling validation. On each of the four iterations, the smoothing spline is fit to a randomly selected half of the parameter estimates, and the other half of the estimates are used to validate the goodness-of-fit of the spline. The smoothing splines fit to the best estimates of $\hat{\boldsymbol{C}}$ are shown in Figure 3.3. We speculate that the apparent over-polarization of the noise diode, which starts around MJD 57000, is of unknown instrumental origin. In future work, it might prove useful to model instrumental impurity using a depolarizing Mueller matrix [Lu and Chipman, 1996] and include this model in the calibration solution.

Given an observation of the artificial noise source, the components of $\hat{\boldsymbol{C}}$ predicted by the smoothing splines are used to derive estimates of the absolute gain G, differential gain γ, and differential phase ϕ of the instrument as described in Ord et al. [2004][4]. These are combined with the values of σ_θ, σ_χ, δ_θ, and δ_χ predicted by the associated smoothing splines to fully describe the polarimetric response of the instrument at any epoch and radio frequency spanned by the splines.

The critical steps detailed above are outlined here:

1. Prepare Data

    - Collect observations of the polarized reference source and its calibrators to create MEM sessions, ensuring that each session has good parallactic angle

[4]Only $\hat{\boldsymbol{C}}$ is required to determine G, γ, and ϕ because the METM model is configured to include the reference source in the signal chain after the front-end component described by σ_θ, σ_χ, δ_θ, and δ_χ.

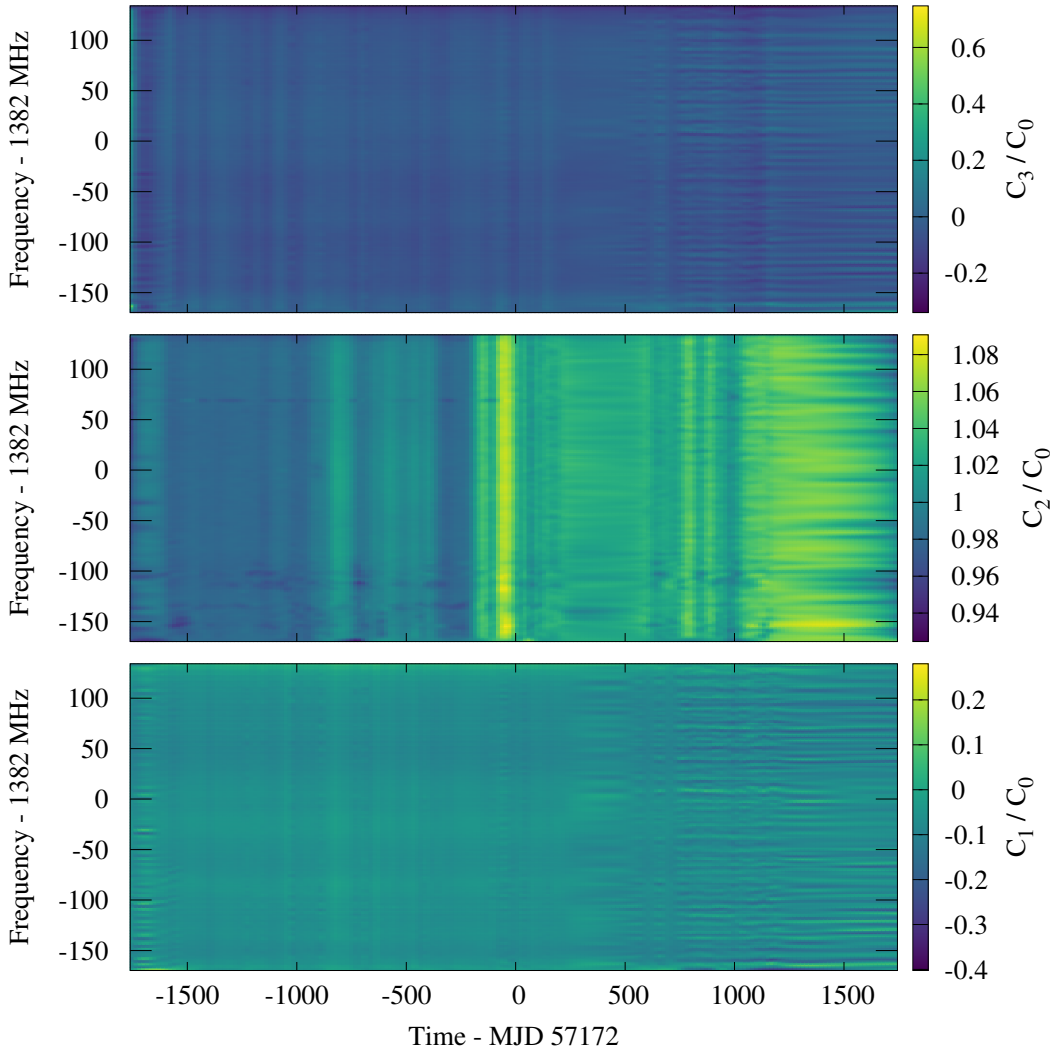

Figure 3.3: Two-dimensional smoothing splines fit to the best estimates of the normalized polarization vector of the artificial noise source; each component is plotted as a function of time and frequency. This figure shows results for the $MULT_1$ (21cm) receiver; other receivers, such as H-OH, exhibit small but noticeable differences.

coverage and sufficient S/N for accurate analysis.

2. Produce Calibrator Models

   - Produce MEM calibrator model solutions.
   - Create template archives for METM analysis.
   - Produce METM calibrator model solutions.
   - Correct ionospheric Faraday rotation.
   - Produce spline-smoothed METM solutions.

3. Calibrate Pulsar Data

   - Apply calibration solutions to pulsar observations.

After completing these steps, arrival times are computed as described in the following section. A more detailed outline of the PSRCHIVE commands used for both polarimetric calibration and arrival time estimation is provided in Appendix 3.7.3.

3.3.2 Arrival Time Estimation and Analysis

Arrival times are estimated using both conventional *Scalar Template Matching* [STM; Taylor, 1992] (see §2.2.1) and *Matrix Template Matching* [MTM; van Straten, 2006] (see §2.2.2). MTM quadruples the number of observational constraints while introducing only six degrees of freedom. For 23 out of 25 pulsars in our analysis, arrival time estimates derived from the polarization profile (using MTM) are expected to have greater precision than those derived from the total intensity profile alone (using STM), as indicated by the theoretical relative ToA uncertainty between MTM and STM ($\hat{\sigma}_\varphi$ in Table 3.2; see van Straten 2013 for a detailed explanation). Table 3.2 also shows the predicted timing error for a 1% calibration error [τ_β; van Straten, 2013] and the timing precision achieved by PPTA DR2 [σ_τ; Kerr et al., 2020]. For a given MSP, the potential

Table 3.2: Relative Arrival Time Uncertainties for Each Pulsar. Columns, from left to right, include J2000.0 coordinates (JNAME), predicted timing error for a 1% calibration error (τ_β), PPTA DR2 timing precision [σ_τ, Kerr et al., 2020], fraction of PPTA DR2 timing residuals that could be due to predicted calibration error [τ_β/σ_τ, van Straten, 2013], theoretical relative ToA uncertainty between MTM and STM template matching algorithms ($\hat{\sigma}_\varphi$), and the ratio between uncertainties in arrival times derived from the invariant interval and total intensity ($\hat{\sigma}_{\tilde{\varphi}}$). For PSR J0437−4715, PPTA DR2 timing precision is acheived by timing the invariant profile [Britton, 2000].

Pulsar (JNAME)	τ_β (ns)	σ_τ (ns)	τ_β/σ_τ	$\hat{\sigma}_\varphi$	$\hat{\sigma}_{\tilde{\varphi}}$
PSR J0437−4715	205	116	1.77	0.82	1.43
PSR J0613−0200	59	1018	0.06	0.95	1.49
PSR J0711−6830	73	979	0.07	0.89	1.53
PSR J1017−7156	74	635	0.12	0.92	1.58
PSR J1022+1001	278	1555	0.18	0.73	1.67
PSR J1024−0719	33	1023	0.03	0.73	2.20
PSR J1045−4509	338	2570	0.13	0.87	1.50
PSR J1125−6014	8	1510	0.005	0.94	1.30
PSR J1446−4701	85	1359	0.08	0.96	1.33
PSR J1545−4550	66	808	0.08	0.84	1.74
PSR J1600−3053	119	572	0.21	0.88	1.39
PSR J1603−7202	143	1316	0.11	0.84	1.56
PSR J1643−1224	269	2248	0.12	0.92	1.39
PSR J1713+0747	5	287	0.02	0.86	1.57
PSR J1730−2304	196	1322	0.15	0.74	1.69
PSR J1744−1134	108	385	0.28	1.59	6.98
PSR J1824−2452A	20	2628	0.008	0.84	4.01
PSR J1832−0836	17	563	0.03	0.95	1.44
PSR J1857+0943	121	1208	0.10	0.92	1.43
PSR J1909−3744	22	152	0.15	0.83	1.52
PSR J1939+2134	44	586	0.08	0.92	1.49
PSR J2124−3358	115	2551	0.05	0.85	1.45
PSR J2129−5721	225	964	0.23	1.08	1.61
PSR J2145−0750	147	995	0.15	0.95	1.45
PSR J2241−5236	21	334	0.06	0.98	1.36

significance of systematic timing errors due to inaccurate instrumental calibration is characterised by τ_β/σ_τ (column 4).

The predicted values of relative uncertainty $\hat{\sigma}_\varphi$ are based on analysis of spectral content in the phase-resolved average profiles of all four Stokes parameters and additional (white) radiometer noise. However, over sufficiently long timescales, pulse arrival time residuals exhibit (red) timing noise, and it is necessary to model and remove this red noise before the white noise content of residuals can be quantified and compared. In principle, the systematic timing errors induced by polarization distortions could also induce red noise, such as the $1/f$ noise produced by unmodeled steps in instrumental response. Therefore, it is also interesting to quantify and compare the red noise content of pulsar timing residuals.

In this study, we analyze both the white and red noise components of timing residuals using TEMPO2 [Edwards et al., 2006, Hobbs et al., 2006][5] and TEMPONEST [Lentati et al., 2014][6].

TEMPO2 (see §2.5.3) is employed to fit the timing model to the observed ToAs by minimizing the timing residuals. TEMPONEST (see §2.5.4) utilizes the multi-modal nested sampling algorithm MULTINEST [Feroz et al., 2009][7] to explore the parameter space of the non-linear pulsar timing model. Simultaneously, it determines a red noise model and two time-independent white noise modifiers:

- Error Scale Factor (EFAC): This accounts for any errors that are proportional to the estimated uncertainty (including potential miscalibrated radiometer noise in the system). It modifies each ToA uncertainty by a constant scale factor E_f.

- Error Added in Quadrature (EQUAD): This compensates for additional white noise by adding a constant E_q in quadrature to each ToA uncertainty [Lentati

[5] https://www.atnf.csiro.au/research/pulsar/tempo2/
[6] https://github.com/LindleyLentati/TempoNest
[7] https://github.com/farhanferoz/MultiNest

Table 3.3: Prior ranges on white and red noise model parameters, comprising the dimensionless base-10 logarithms of the error scale factor $\hat{E}_{f,10} = \log_{10}(E_f)$, the error added in quadrature $\hat{E}_{q,10} = \log_{10}(E_q/\mathrm{s})$, and the red-noise amplitude $\hat{A}_{\mathrm{red},10} = \log_{10}(A_{\mathrm{red}}/\mathrm{yr}^{3/2})$; and the power-law spectral index β.

Parameter	Prior Range	Type
$\hat{E}_{f,10} = \log_{10}(E_f)$	(-1,1)	log-uniform
$\hat{E}_{q,10} = \log_{10}(E_q/\mathrm{s})$	(-9,-5)	log-uniform
$\hat{A}_{\mathrm{red},10} = \log_{10}(A_{\mathrm{red}}/\mathrm{yr}^{3/2})$	(-18,-10)	log-uniform
β	(0,7)	log-uniform

et al., 2014].

The total ToA uncertainty is therefore obtained by adjusting the uncertainty σ_τ as follows:

$$\sigma'_\tau = \sqrt{E_q^2 + E_f^2 \sigma_\tau^2} \tag{3.2}$$

EFAC and EQUAD values are typically applied to all ToAs in a pulsar timing data set and adjusted iteratively until the fitted model's reduced χ^2 reaches unity [Shannon et al., 2014].

TEMPONEST models red noise using a power-law spectrum characterized by an amplitude (A_{red}) and spectral index γ:

$$S(f) = \frac{A_{\mathrm{red}}^2}{12\pi^2} \left(\frac{f}{f_{\mathrm{yr}}} \right)^{-\gamma} \tag{3.3}$$

where f_{yr} is a reference frequency of 1 cycle per year, and the amplitude A_{red} is in units of $\mathrm{yr}^{3/2}$ [Lentati et al., 2014, Parthasarathy et al., 2019]. The prior ranges for the red noise and additional white noise parameters used in our analysis are detailed in Table 3.3. Note that TEMPONEST is configured to sample the spectrum using 120 Fourier coefficients.

Outliers in pulsar timing measurements bias both timing model and noise model parameter estimates and reduce the accuracy of estimated parameter uncertainties

[Vallisneri and van Haasteren, 2017]. To address this challenge, we employ robust and automated outlier removal techniques. An initial outlier rejection involves removing any instances of ToAs with error equal to 0 and performing a 5-sigma outlier removal on both the relative error for each residual (residual divided by uncertainty) and ToA goodness-of-fit. We then run TEMPO2 with the initial (slightly corrupted) TEMPONEST red-noise model, producing whitened residuals that are corrupted by some remaining outliers. These remaining outliers are removed using Tukey's Fence [Tukey, 1977], a robust statistical method for outlier detection and removal [Morello et al., 2019], which is used to enhance timing accuracy. This approach typically flags only a small portion (around 5%) of the data as outliers and has been shown to improve timing accuracy by a factor of two for many pulsars [Lower et al., 2020]. Tukey's Fence defines a "reasonable" range based on the interquartile range (IQR), which is the difference between the 75^{th} percentile (Q3) and the 25^{th} percentile (Q1) of the data set. The range extends from Q1 - q*IQR to Q3 + q*IQR, where q is a parameter. While a common choice for q is 1.5, it can be adjusted according to specific analysis requirements, determining the stringency of the outlier cutoff. We used a less stringent cutoff value of q=2 for our analysis.

Following the application of Tukey's Fence to each MSP, we update the best-fit model by re-running TEMPONEST to generate a red noise model that is not corrupted by outliers. The impact of this outlier rejection step is summarized in Table 3.4, which lists the initial and final number of ToAs retained for each method. PSR J0437−4715 and PSR J2241−5721 are exceptions. An additional 5-sigma removal was performed on the relative error for each residual to catch a few outliers missed by Tukey's Fence for these pulsars. A final run of TEMPO2 with the final TempoNest red-noise model produces whitened residuals for each calibration and ToA estimation method combination. By comparing the red and white noise model parameters, we aim to evaluate whether advanced techniques like METM and MTM, which better account for instrumental

Table 3.4: The number of initial ToAs obtained for each method, and $N_{\rm toas}$, the final number of ToAs used across all methods after the outlier rejection has been applied.

Pulsar	METM-MTM	IFA-MTM	METM-STM	IFA-STM	$N_{\rm toas}$
PSR J0437−4715	883	857	923	951	700
PSR J0613−0200	239	240	240	248	221
PSR J0711−6830	350	351	351	355	333
PSR J1017−7156	354	356	355	366	333
PSR J1022+1001	232	232	231	232	215
PSR J1024−0719	139	139	140	142	127
PSR J1045−4509	188	190	190	194	177
PSR J1125−6014	151	150	151	156	141
PSR J1446−4701	171	171	171	175	145
PSR J1545−4550	134	134	137	153	123
PSR J1600−3053	190	190	185	188	174
PSR J1603−7202	223	223	222	228	212
PSR J1643−1224	168	170	171	172	155
PSR 1713+0747	257	258	258	264	246
PSR J1730−2304	187	187	187	188	165
PSR J1744−1134	254	252	256	259	237
PSR J1824−2452	88	88	88	90	80
PSR J1832−0836	79	79	79	82	72
PSR J1857+0943	139	139	139	141	127
PSR J1909−3744	375	374	379	392	344
PSR J1939+2134	154	154	154	156	142
PSR J2124−3358	228	228	228	231	221
PSR J2129−5721	256	257	256	263	238
PSR J2145−0750	225	225	225	230	211
PSR J2241−5236	400	414	401	421	329

calibration errors, can enhance the experimental sensitivity of PTAs over extended periods compared to conventional methods like IFA and STM.

3.4 Results

In this section, we present the results of our analysis, comparing advanced polarimetric calibration [METM; van Straten, 2013] and arrival time estimation [MTM; van Straten, 2006] methods with conventional approaches (IFA and STM). We applied

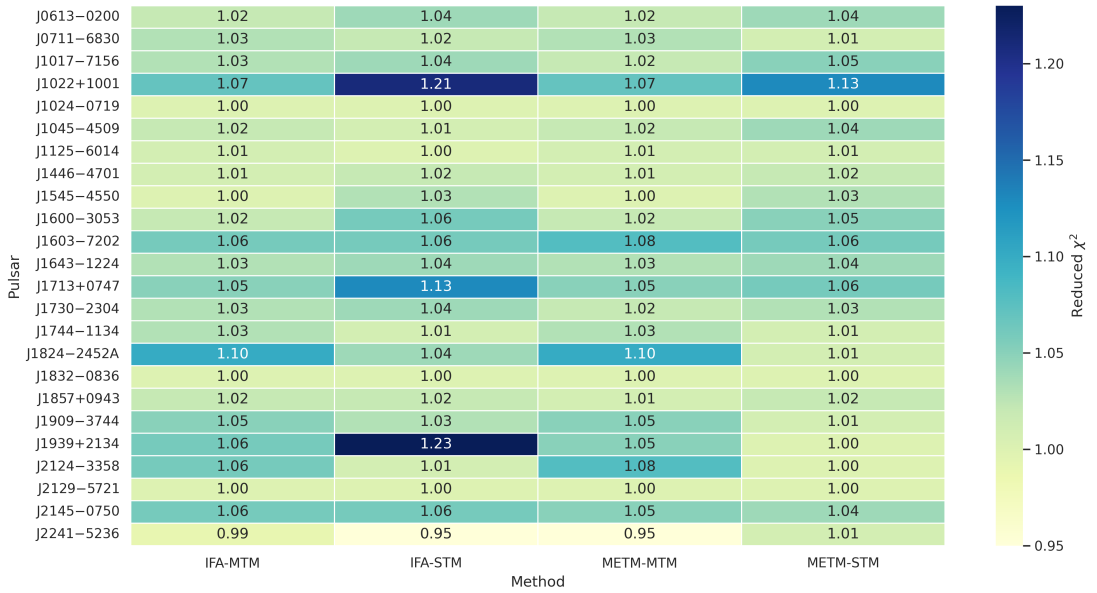

Figure 3.4: The reduced χ^2 heat map illustrates the median goodness-of-fit over all arrival times obtained for each pulsar. PSR J0437−4715 is excluded owing to exceptionally large values of 2.34, 7.77 2.04, and 2.61 for the IFA-MTM, IFA-STM, METM-MTM, and METM-STM methods, respectively.

these techniques to 25 high-priority pulsars regularly observed as part of the PPTA project, resulting in four distinct data sets (IFA-MTM, METM-MTM, IFA-STM, and METM-STM).

The quality of the arrival time estimation procedure is summarised in Figure 3.4, which presents a heat map of the median arrival time goodness-of-fit for each pulsar. Goodness-of-fit is characterised by the reduced χ^2 of the fit between the observed pulse profile and the template pulse profile. Large values of the reduced χ^2 may indicate that the template pulse profile is not an accurate representation of the average pulse profile, or that the observed pulse profiles vary by more than what would be expected due to radiometer noise alone; e.g. owing to additional pulsar self-noise known as jitter [Cordes and Downs, 1985, Osłowski et al., 2011].

The results of modelling the arrival time estimates are presented in Table 3.5, which lists, for each pulsar and each combination of methods, the number of ToAs, the

weighted standard deviations of the post-fit residuals output by TEMPO2 and the noise model parameters obtained through TEMPONEST.

Table 3.5: Noise statistics and noise model parameters for each timing data set. Columns, from left to right, include each pulsar's J2000.0 coordinates (JNAME); the calibration-ToA estimation method; the number of TOAs, $N_{\rm toas}$; the uncertainty-weighted standard deviation of the post-fit timing residuals σ_τ, and whitened timing residuals $\sigma_{\tau,\rm wh}$; and the maximum likelihood estimates of the noise model parameters, comprising the dimensionless base-10 logarithms of the error scale factor $\hat{E}_{f,10} = \log_{10}(E_f)$, the error added in quadrature $\hat{E}_{q,10} = \log_{10}(E_q/\rm s)$, and the red-noise amplitude $\hat{A}_{\rm red,10} = \log_{10}(A_{\rm red}/\rm yr^{3/2})$; and the power-law spectral index β. Values in parentheses are the 1σ uncertainty in the last digit quoted.

Pulsar	Method	$N_{\rm toas}$	$\frac{\sigma_\tau}{\mu\rm s}$	$\frac{\sigma_{\tau,\rm wh}}{\mu\rm s}$	$\hat{E}_{f,10}$	$\hat{E}_{q,10}$	$\hat{A}_{\rm red,10}$	β
PSR J0437−4715	METM-MTM	700	0.584	0.100	0.60(5)	-7.02(2)	-13.48(7)	3.0(4)
	IFA-MTM	700	0.653	0.103	0.64(5)	-7.02(2)	-13.47(7)	3.1(4)
	METM-STM	700	0.680	0.231	0.6(1)	-6.64(1)	-13.5(1)	3.1(7)
	IFA-STM	700	0.947	0.663	0.3(4)	-6.17(1)	-13.1(1)	2.0(5)
PSR J0613−0200	METM-MTM	221	0.661	0.583	0.04(3)	-7.0(4)	-15(1)	4(2)
	IFA-MTM	221	0.648	0.583	0.04(3)	-7.0(4)	-16(1)	4(2)
	METM-STM	221	1.111	1.083	0.22(6)	-6.3(3)	-16(1)	3(2)
	IFA-STM	221	1.200	1.117	0.22(7)	-6.3(3)	-16(1)	3(2)
PSR J0711−6830	METM-MTM	333	0.816	0.754	-0.02(2)	-6.6(3)	-14(1)	2(2)
	IFA-MTM	333	0.805	0.722	-0.01(2)	-6.8(3)	-13.8(8)	2(2)
	METM-STM	333	0.925	0.842	0.02(2)	-6.7(4)	-13.6(9)	2(2)
	IFA-STM	333	1.069	0.972	0.04(2)	-6.6(3)	-14.0(7)	4(2)
PSR J1017−7156	METM-MTM	333	1.704	0.223	-0.09(2)	-7.4(4)	-12.88(6)	2.7(4)
	IFA-MTM	333	1.726	0.221	-0.09(2)	-7.4(4)	-12.89(5)	2.7(4)
	METM-STM	333	1.751	0.294	0.14(2)	-7.3(4)	-12.90(6)	2.9(5)
	IFA-STM	333	1.800	0.312	0.15(2)	-7.2(4)	-12.90(6)	2.9(5)
PSR J1022+1001	METM-MTM	215	0.857	0.833	0.00(5)	-6.19(4)	-16(1)	3(2)
	IFA-MTM	215	0.875	0.864	0.01(5)	-6.17(4)	-16(1)	3(2)
	METM-STM	215	1.341	1.281	0.07(4)	-6.00(4)	-15(1)	3(2)
	IFA-STM	215	1.619	1.619	0.04(5)	-5.88(4)	-16(1)	3(2)
PSR J1024−0719	METM-MTM	127	0.739	0.654	0.05(3)	-6.9(4)	-15(1)	4(2)
	IFA-MTM	127	0.787	0.721	0.07(3)	-6.8(4)	-15(1)	4(2)
	METM-STM	127	1.088	1.078	0.11(3)	-6.9(5)	-16(1)	3(2)
	IFA-STM	127	1.095	1.081	0.12(3)	-6.9(5)	-16(1)	3(2)

Pulsar	Method	$N_{\rm toas}$	$\frac{\sigma_\tau}{\mu s}$	$\frac{\sigma_{\tau,\rm wh}}{\mu s}$	$\hat{E}_{f,10}$	$\hat{E}_{q,10}$	$\hat{A}_{\rm red,10}$	β
PSR J1045−4509	METM-MTM	177	4.025	1.280	-0.07(5)	-6.5(5)	-12.46(9)	2.6(5)
	IFA-MTM	177	4.689	1.311	-0.06(4)	-6.5(4)	-12.44(9)	2.6(5)
	METM-STM	177	7.010	4.364	-0.3(3)	-5.34(4)	-12.5(2)	2.7(9)
	IFA-STM	177	5.739	4.702	0.3(1)	-5.4(1)	-12.5(4)	2(1)
PSR J1125−6014	METM-MTM	141	1.939	0.833	0.0(1)	-6.06(5)	-12.9(1)	2.8(7)
	IFA-MTM	141	1.919	0.836	0.0(1)	-6.07(5)	-12.8(1)	2.6(6)
	METM-STM	141	2.030	0.844	0.0(1)	-6.08(5)	-12.8(1)	2.8(7)
	IFA-STM	141	1.993	0.833	0.0(1)	-6.08(5)	-12.8(1)	2.7(6)
PSR J1446−4701	METM-MTM	145	1.747	1.318	-0.01(7)	-6.00(9)	-15(1)	3(2)
	IFA-MTM	145	1.605	1.345	0.04(6)	-6.0(1)	-15(1)	3(2)
	METM-STM	145	2.132	1.978	0.34(7)	-5.8(1)	-16(1)	3(2)
	IFA-STM	145	2.247	2.227	0.33(8)	-5.8(1)	-16(1)	3(2)
PSR J1545−4550	METM-MTM	123	0.594	0.429	-0.1(1)	-6.9(4)	-13.3(2)	3(1)
	IFA-MTM	123	0.603	0.434	0.06(7)	-6.9(4)	-13.3(2)	3(1)
	METM-STM	123	1.068	0.776	0.13(9)	-6.6(4)	-13.2(3)	3(1)
	IFA-STM	123	1.052	0.785	0.12(9)	-6.5(4)	-13.1(3)	3(1)
PSR J1600−3053	METM-MTM	174	1.828	0.230	-0.04(6)	-7.0(4)	-13.3(2)	2.9(6)
	IFA-MTM	174	1.748	0.221	0.05(5)	-7.2(4)	-13.2(1)	2.7(5)
	METM-STM	174	1.757	0.311	0.08(6)	-7.1(4)	-14.0(5)	5(1)
	IFA-STM	174	2.100	0.341	0.10(7)	-6.9(3)	-14.1(5)	5(1)
PSR J1603−3053	METM-MTM	212	0.783	0.497	0.01(3)	-7.2(4)	-13.3(2)	2.6(8)
	IFA-MTM	212	0.819	0.504	0.01(3)	-7.2(4)	-13.3(2)	2.8(9)
	METM-STM	212	0.877	0.593	0.00(3)	-7.1(4)	-13.2(2)	2.6(8)
	IFA-STM	212	0.961	0.747	0.06(3)	-6.8(4)	-13.4(3)	3(1)
PSR J1643−1224	METM-MTM	155	2.481	0.452	-0.12(6)	-6.8(4)	-12.65(7)	2.0(3)
	IFA-MTM	155	2.153	0.438	-0.14(7)	-6.7(4)	-12.64(6)	1.9(3)
	METM-STM	155	2.282	1.087	0.26(4)	-6.6(4)	-12.8(2)	2.6(7)
	IFA-STM	155	2.133	1.039	0.24(4)	-6.6(4)	-12.8(2)	2.4(7)
PSR J1713+0747	METM-MTM	246	0.234	0.201	-0.08(5)	-6.76(3)	-13.6(1)	1.5(6)
	IFA-MTM	246	0.232	0.204	-0.07(6)	-6.75(3)	-13.6(1)	1.5(6)
	METM-STM	246	0.252	0.216	-0.04(6)	-6.72(3)	-13.6(1)	1.6(6)
	IFA-STM	246	0.247	0.215	-0.01(6)	-6.72(3)	-13.6(1)	1.5(6)
PSR J1730−2304	METM-MTM	165	0.935	0.668	0.11(3)	-7.1(4)	-13.7(4)	3(1)
	IFA-MTM	165	0.865	0.664	0.11(3)	-7.2(4)	-13.7(4)	3(1)
	METM-STM	165	1.460	0.963	0.11(3)	-6.9(5)	-13.5(4)	3(1)

Pulsar	Method	$N_{\rm toas}$	$\frac{\sigma_\tau}{\mu s}$	$\frac{\sigma_{\tau,\rm wh}}{\mu s}$	$\hat{E}_{f,10}$	$\hat{E}_{q,10}$	$\hat{A}_{\rm red,10}$	β
	IFA-STM	165	1.488	1.171	0.14(4)	-6.4(4)	-13.7(8)	4(1)
PSR J1744−1134	METM-MTM	237	0.426	0.306	0.02(3)	-6.8(2)	-13.5(4)	2(1)
	IFA-MTM	237	0.438	0.311	0.04(3)	-6.9(2)	-13.5(4)	2(1)
	METM-STM	237	0.442	0.301	-0.09(4)	-6.63(5)	-13.6(4)	2(1)
	IFA-STM	237	1.034	0.682	-0.13(6)	-6.21(3)	-14.5(6)	5(2)
PSR J1824−2452A	METM-MTM	80	16.467	0.537	0.1(4)	-6.2(2)	-12.4(1)	3.5(6)
	IFA-MTM	80	15.780	0.507	0.0(4)	-6.2(2)	-12.3(1)	3.3(7)
	METM-STM	80	16.445	0.551	0.2(3)	-6.3(2)	-12.4(1)	3.6(6)
	IFA-STM	80	16.148	0.510	-0.1(4)	-6.2(2)	-12.4(1)	3.5(7)
PSR J1832−0836	METM-MTM	72	2.485	0.597	-0.02(6)	-6.8(4)	-14.1(4)	6(1)
	IFA-MTM	72	2.066	0.645	0.03(5)	-6.8(4)	-14.0(4)	5(1)
	METM-STM	72	1.605	0.929	0.1(1)	-6.4(4)	-13.9(5)	5(1)
	IFA-STM	72	1.593	0.809	0.0(2)	-6.3(4)	-13.0(5)	3(2)
PSR J1857+0943	METM-MTM	127	1.288	0.573	-0.06(5)	-6.8(4)	-13.9(4)	4(1)
	IFA-MTM	127	1.255	0.597	-0.04(5)	-6.8(4)	-13.8(4)	4(1)
	METM-STM	127	1.335	0.849	0.02(6)	-6.6(4)	-13.8(4)	4(1)
	IFA-STM	127	1.532	0.889	0.04(6)	-6.5(4)	-13.9(4)	4(1)
PSR J1909−3744	METM-MTM	344	0.518	0.200	-0.10(6)	-6.73(3)	-14.0(2)	3.7(8)
	IFA-MTM	344	0.512	0.204	-0.11(7)	-6.72(3)	-14.0(2)	3.7(8)
	METM-STM	344	0.530	0.204	-0.08(6)	-6.72(3)	-14.0(3)	3.6(9)
	IFA-STM	344	0.540	0.204	-0.13(7)	-6.72(3)	-14.0(3)	3.8(9)
PSR J1939+2134	METM-MTM	142	1.121	0.101	0.4(2)	-7.0(2)	-12.94(6)	2.5(3)
	IFA-MTM	142	1.126	0.101	0.4(2)	-7.0(2)	-12.95(6)	2.5(3)
	METM-STM	142	1.117	0.104	0.1(3)	-6.93(7)	-12.98(6)	2.7(3)
	IFA-STM	142	1.173	0.104	0.6(1)	-7.3(3)	-12.96(6)	2.5(3)
PSR J2124−3358	METM-MTM	221	1.341	1.320	-0.01(2)	-6.9(5)	-16(1)	3(2)
	IFA-MTM	221	1.275	1.272	-0.02(2)	-6.9(5)	-16(1)	3(2)
	METM-STM	221	2.936	2.983	0.37(2)	-6.4(5)	-16(1)	3(2)
	IFA-STM	221	2.920	2.886	0.38(3)	-6.4(5)	-16(1)	3(2)
PSR J2129−5721	METM-MTM	238	1.131	0.914	0.01(3)	-6.7(4)	-14.7(6)	5(1)
	IFA-MTM	238	1.162	0.911	0.00(3)	-6.7(4)	-14.4(6)	5(1)
	METM-STM	238	1.301	1.151	0.17(2)	-6.9(4)	-15(1)	4(2)
	IFA-STM	238	1.336	1.194	0.17(2)	-6.9(4)	-14.4(7)	5(2)
PSR J2145−0750	METM-MTM	211	0.592	0.531	0.00(3)	-6.51(7)	-16(1)	4(2)
	IFA-MTM	211	0.581	0.531	0.02(3)	-6.51(7)	-15(1)	4(2)
	METM-STM	211	0.832	0.602	0.00(3)	-6.41(6)	-14.6(8)	4(2)

Pulsar	Method	$N_{\rm toas}$	$\frac{\sigma_\tau}{\mu s}$	$\frac{\sigma_{\tau,\rm wh}}{\mu s}$	$\hat{E}_{f,10}$	$\hat{E}_{q,10}$	$\hat{A}_{\rm red,10}$	β
	IFA-STM	211	0.810	0.684	0.03(4)	-6.32(7)	-15(1)	4(2)
PSR J2241−5236	METM-MTM	329	0.251	0.214	0.14(4)	-6.80(6)	-13.9(4)	3(1)
	IFA-MTM	329	0.255	0.217	0.13(5)	-6.80(6)	-14.0(5)	3(1)
	METM-STM	329	0.254	0.215	0.15(3)	-6.87(6)	-14.0(3)	3(1)
	IFA-STM	329	0.269	0.229	0.14(4)	-6.80(5)	-13.9(3)	3(1)

The parameters that characterise the white noise of each pulsar are summarised in Table 3.6, which compares the minimum, median, and maximum values of E_f, E_q, and the uncertainty-weighted standard deviation of the whitened (red noise removed) post-fit timing residuals, $\sigma_{\tau,\rm wh}$, for the four data sets. Notably, IFA-STM has the largest median values of E_f and E_q; therefore, it serves as the baseline for model comparison in this study. Table 3.7 compares the best-fit E_q estimates of the IFA-STM and METM-MTM

Table 3.6: Minimum, median, and maximum values of the error scale factor E_f, error added in quadrature E_q, and uncertainty-weighted standard deviation of the whitened post-fit timing residuals $\sigma_{\tau,\rm wh}$, for each combination of calibration and arrival time estimation methods.

Model	E_f			E_q (μs)			$\sigma_{\tau,\rm wh}$ (μs)		
	Min	Med	Max	Min	Med	Max	Min	Med	Max
METM-MTM	0.77	1.02	4.02	0.04	0.16	0.99	0.10	0.54	1.32
IFA-MTM	0.72	1.07	4.34	0.04	0.15	0.95	0.10	0.51	1.35
METM-STM	0.53	1.27	4.21	0.05	0.23	4.61	0.10	0.84	4.36
IFA-STM	0.75	1.30	4.13	0.05	0.33	3.85	0.10	0.81	4.70

data sets for those seven pulsars with statistically significant differences.

The IFA-STM and METM-MTM data sets are further compared in Table 3.8, which lists $\sigma_{\tau,\rm wh}$ for each pulsar. For each pulsar, column 4 lists the white-noise quotient

$$Q = \frac{\sigma_{\tau,\rm wh}\{\text{METM-MTM}\}}{\sigma_{\tau,\rm wh}\{\text{IFA-STM}\}} \tag{3.4}$$

that is used to define the percentage improvement, $(1 - Q) \times 100\%$. METM-MTM

Table 3.7: Pulsars with statistically significant different estimates of error added in quadrature, E_q. The best-fit estimates of E_q derived from the IFA-STM and METM-MTM data sets are shown in columns 2 and 3, and the quadrature differences between them are listed in column 4. Values in parentheses are the 1σ uncertainty in the last digit quoted.

Pulsar (JNAME)	E_q (μs)		ΔE_q (μs)
	IFA-STM	METM-MTM	
PSR J0437−4715	0.67(2)	0.095(4)	0.67(2)
PSR J1022+1001	1.3(1)	0.64(7)	1.1(1)
PSR J1045−4509	4(1)	0.3(3)	4(1)
PSR J1446−4701	1.7(4)	1.0(2)	1.4(4)
PSR J1713+0747	0.19(1)	0.17(1)	0.08(2)
PSR J1744−1134	0.62(4)	0.15(6)	0.60(7)
PSR J2145−0750	0.48(8)	0.31(5)	0.37(9)

yields significant reductions in $\mathrm{rms}_{\mathrm{white}}$; a similar result was found for three pulsars observed with the Nançay Radio Telescope [Guillemot et al., 2023]. For the MSPs in our sample, the median reduction in white noise is 33%, and the maximum reduction of 85% (an impressive factor of 6.6) is observed for PSR J0437−4715. For this pulsar, we plot the noise model parameter distributions derived from each data set in Figure 3.5 and compare the amplitude spectra of the residuals in Figure 3.6.

Finally, Figure 3.7 depicts the improvement in timing precision for each pulsar by comparing the $\sigma_{\tau,\mathrm{wh}}$ values from PPTA DR2 with those derived in this study using METM-MTM and IFA-STM. As discussed in more detail in §3.5.7, this visual comparison should be treated as indicative because there are significant differences between the 21-cm data included in the PPTA DR2 analysis and the subset of data analyzed in this work.

3.5 Discussion

Comparing METM and MTM with conventional methods, we observe a significant reduction in white noise in pulse arrival times across all pulsars in our sample. This

Table 3.8: Comparison of uncertainty-weighted standard deviations of whitened post-fit timing residuals, $\sigma_{\tau,\mathrm{wh}}$. Estimates of $\sigma_{\tau,\mathrm{wh}}$ for the IFA-STM and METM-MTM methods are listed in columns 2 and 3, and the white-noise quotient, Q defined by equation (3.4) is listed in column 4.

Pulsar (JNAME)	$\sigma_{\tau,\mathrm{wh}}$ (ns) IFA-STM	METM-MTM	Q
PSR J0437−4715	663	100	0.15
PSR J0613−0200	1117	583	0.52
PSR J0711−6830	972	754	0.78
PSR J1017−7156	312	223	0.71
PSR J1022+1001	1630	839	0.51
PSR J1024−0719	1081	654	0.60
PSR J1045−4509	4702	1280	0.27
PSR J1125−6014	833	833	1.00
PSR J1446−4701	2227	1318	0.59
PSR J1545−4550	785	429	0.55
PSR J1600−3053	341	230	0.67
PSR J1603−7202	747	497	0.67
PSR J1643−1224	1039	452	0.43
PSR J1713+0747	215	201	0.93
PSR J1730−2304	1171	668	0.57
PSR J1744−1134	682	306	0.45
PSR J1824−2452A	510	537	1.05
PSR J1832−0836	809	597	0.74
PSR J1857+0943	889	573	0.64
PSR J1909−3744	204	200	0.98
PSR J1939+2134	104	101	0.97
PSR J2124−3358	2886	1320	0.46
PSR J2129−5721	1194	914	0.77
PSR J2145−0750	684	513	0.75
PSR J2241−5236	229	214	0.93

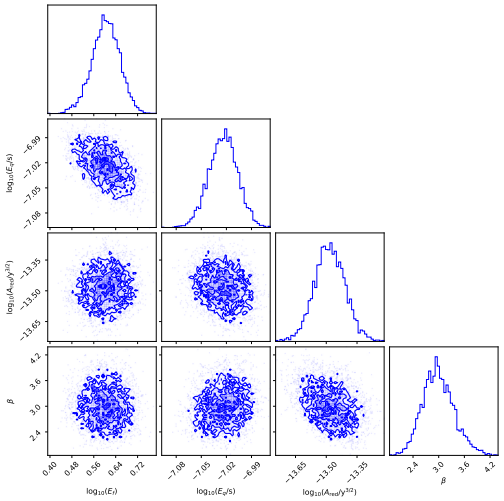

(a) METM-MTM

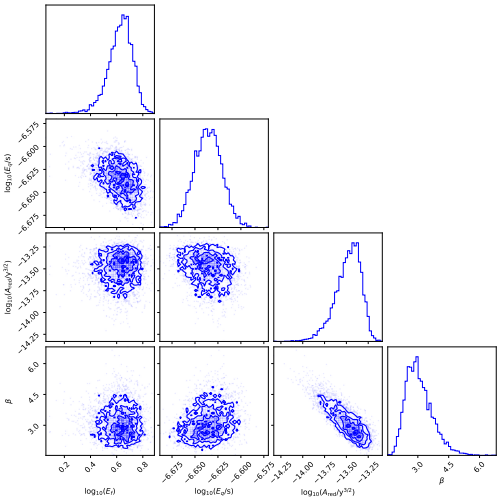

(b) METM-STM

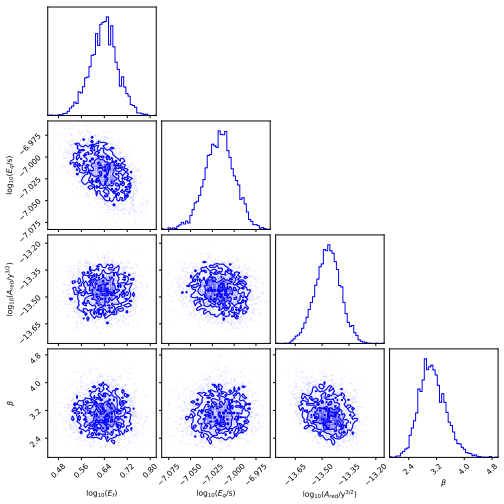

(c) IFA-MTM

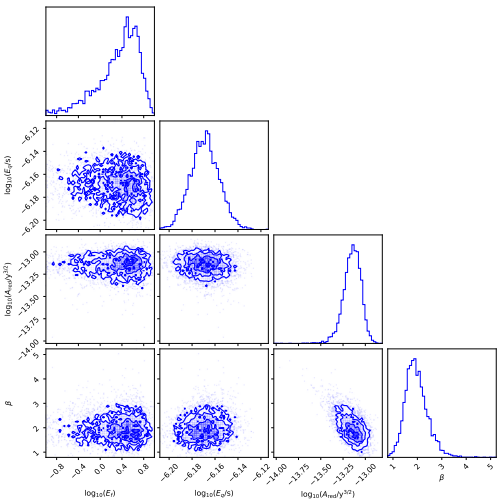

(d) IFA-STM

Figure 3.5: Noise model parameter distributions for PSR J0437−4715. The two-dimensional posterior surfaces and one-dimensional marginal distributions for red and white noise parameters are derived from the MULTINEST chains generated by TEMPONEST during joint parameter space exploration [Lentati et al., 2014].

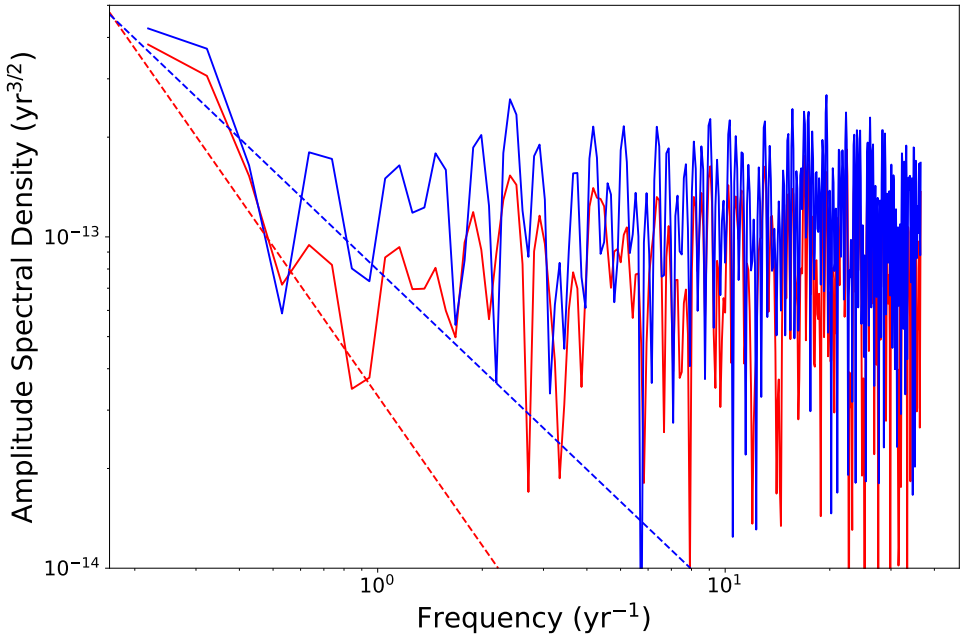

Figure 3.6: Amplitude spectra of the post-fit residuals of PSR J0437−4715 for the METM-MTM (red) and IFA-STM (blue) data sets. The best-fit red noise models output by TEMPONEST for each data set are indicated by dashed lines with matching colours.

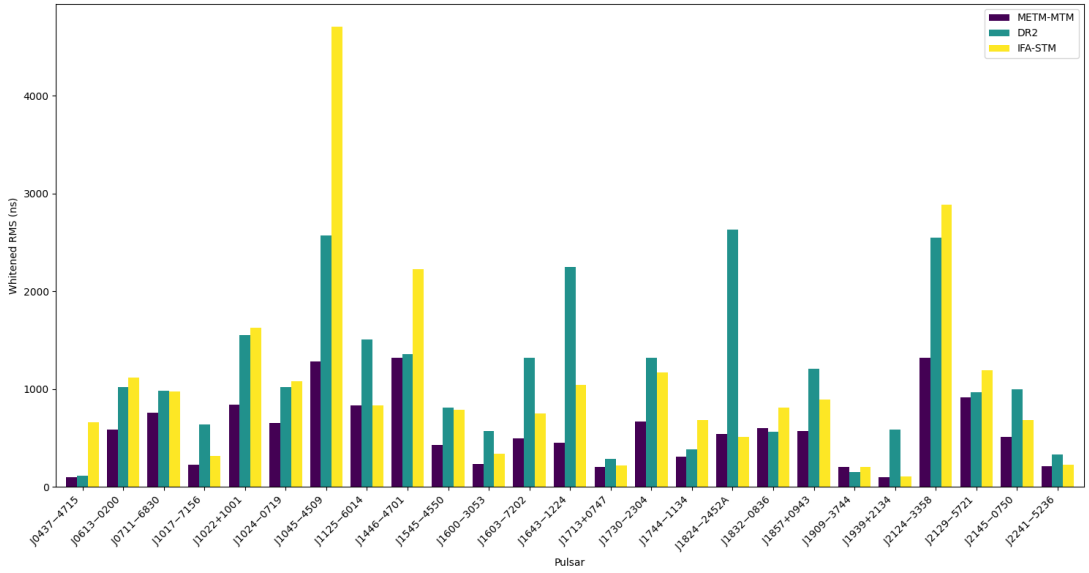

Figure 3.7: Comparison of DR2, METM-MTM, and IFA-STM $\sigma_{\tau,\mathrm{wh}}$ for all pulsars. Each bar represents the $\sigma_{\tau,\mathrm{wh}}$ value obtained using METM-MTM (blue), DR2 (green), and IFA-STM (yellow) for a specific pulsar. Note that DR2 uses the invariant interval [Britton, 2000] for PSR J0437−4715.

is evident from the significantly smaller uncertainty-weighted standard deviations of whitened post-fit timing residuals for METM-MTM compared to IFA-STM (up to 6.6 times smaller; see Table 3.8 and Table 3.5). For the majority of PPTA pulsars, the reduction in white noise achieved with METM-MTM exceeds the predicted relative ToA uncertainty between MTM and STM algorithms ($\hat{\sigma}_{\varphi}$, see Table 3.2). This includes pulsars like PSR J1744−1134 and PSR J2129−5721, for which MTM is predicted to perform worse than STM, because the phase shift becomes difficult to separate owing to the covariance between the phase shift and unknown Jones matrix model parameters. MTM still produces more precise timing results in practice. These results indicate that MTM is able to mitigate the impact of polarization calibration errors, which contribute additional white noise to STM-derived arrival times.

Further supporting this interpretation, the smallest improvements are achieved for pulsars with low susceptibility to calibration error as characterised by τ_{β} (see Table 3.2), such as PSR J1125−6014, PSR J1713+0747, PSR J1909+3744, PSR J1939−2134, PSR J1824−2452A, and PSR J2241−5236 (see Table 3.8). Similarly, for pulsars that are highly susceptible to calibration error, such as PSR J0437−4715, PSR J1022+1001, PSR J1045−4509, and PSR J1643−1224, METM-MTM significantly reduces $\sigma_{\tau,\mathrm{wh}}$. The largest reduction in $\sigma_{\tau,\mathrm{wh}}$, with a quadrature difference of 4.5 μs between IFA-STM and METM-MTM data sets, is observed for PSR J1045−4509. This pulsar also has the greatest susceptibility to calibration error τ_{β}.

The whitened residuals include a contribution from pulsar-intrinsic jitter, which is not separately accounted in our noise analysis. The white noise induced by jitter is statistically independent of the radiometer noise that dominates the error of each arrival time estimate; therefore, jitter increases E_q. Jitter noise varies with pulse phase and, when the sub-pulse structures that cause jitter are broader than the pulse phase bins used to resolve the average profile, jitter noise is correlated between phase bins. That is, jitter causes the noise in each phase bin to no longer be independent and identically

distributed, a fundamental assumption on which the STM and MTM algorithms are based. Therefore, jitter inflates the reduced χ^2 of each template-matching fit and causes underestimation of arrival time error, which in turn increases E_f. In summary, pulsar-intrinsic jitter impacts on the ToA goodness-of-fit, the error scale factor E_f and the error added in quadrature E_q. These useful metrics are discussed in the following three sections.

3.5.1 Time-of-Arrival Goodness-of-Fit

The template-matching reduced χ^2 heat map (see Figure 3.4) presents the median goodness-of-fit for arrival times derived from each pulsar in our study. PSR J0437−4715 was left out of the analysis because its timing data is dominated by jitter, leading to irregularities in the pulse arrival times that are much larger than the expected measurement uncertainties. This mismatch causes the model fit to look artificially bad (with very high reduced χ^2), even though the timing model is still valid.

Calibration errors are expected to increase the reduced χ^2 of each ToA estimate. Therefore, MTM is expected to yield lower reduced χ^2 values than yielded by STM. This is observed for several of the pulsars in our data set; most notably, PSR J1022+1001, renowned for its temporal profile variations [Kramer et al., 1999, Ramachandran and Kramer, 2003, Hotan et al., 2004], has one of the two highest reduced χ^2 values for IFA-STM. This high value is significantly reduced when using MTM. Similarly, for PSR J1939+2134 and PSR J1713+0747, MTM yields lower reduced χ^2 values than STM. Notable exceptions include PSR J1824−2452A and PSR J2124−3358, for which MTM increases the median reduced χ^2. This warrants further explanation, which is currently only speculative. These pulsars may demonstrate greater intrinsic variability in Stokes Q, U, and V than in Stokes I, possibly due to switching between orthogonally polarized modes. The variability might also originate in the ISM or ionosphere; for

example, uncorrected Faraday rotation variations [e.g. Yan et al., 2011] could lead to bandwidth depolarization, a transformation that cannot be represented by a Jones matrix and therefore cannot be modeled by MTM. A more quantitative investigation is beyond the scope of this paper, and presents an opportunity for future research.

3.5.2 Error Scale Factor

When ToA uncertainties accurately reflect the white noise content of arrival time estimates, E_f is expected to be close to unity (i.e., $\log_{10}(E_f) \sim 0$). Values of $E_f > 1$ may suggest that the algorithm for arrival time estimation systematically underestimates ToA uncertainty. Alternatively, it could result from additional noise sources with amplitudes that are proportional to that of the radiometer noise in the integrated pulse profile.

The interpretation of E_f aligns with two main results. Firstly, E_f appears to indicate that STM underestimates the uncertainty, as evidenced by the median E_f around 1.3 for STM compared to around 1.0 for MTM (see Table 3.6). However, for some pulsars, E_f is dominated by jitter; for instance, PSR J0437−4715 has the highest E_f value of approximately 4 for each model (For IFA-STM, E_f is $\sim 2 \pm 3$ which is poorly constrained and consistent with 4.). This pulsar displays the lowest METM-MTM whitened noise ($\sigma_{\tau,\mathrm{wh}} \sim 100$ ns) in our data set; it also has the highest level of self-noise (dominated by pulse phase jitter) relative to the radiometer noise [Osłowski et al., 2011, Parthasarathy et al., 2021].

Although jitter dominates E_f for some pulsars, the error factor remains a valuable diagnostic measure. For example, our initial analysis of E_f highlighted errors in both the Phase Gradient Shift (PGS) algorithm (the default STM algorithm when estimating arrival times using PSRCHIVE tools like PAT) and the PSRCHIVE implementation of MTM. After correcting these errors, as described in Appendix 3.7.1, there were no

statistically significant differences between the E_f values derived from IFA-calibrated and METM-calibrated data for a given pulsar and arrival time estimation algorithm.

3.5.3 Error Added in Quadrature

Error added in quadrature, E_q, characterises any additional sources of unaccounted white noise with amplitudes that are uncorrelated with that of the radiometer noise estimated from the off-pulse baseline. When ToA uncertainties accurately reflect the noise content of arrival time estimates, $E_q \to 0$ and $\log_{10}(E_q) \to -\infty$; therefore, larger E_q values indicate greater unaccounted uncertainty in TOA measurements.

Out of all of the E_q estimates listed in Table 3.5, we compare those derived from the IFA-STM and METM-MTM data sets and list the seven pulsars with statistically significant differences in Table 3.7. Most notably, METM-MTM has reduced E_q for PSR J1045−4509 by an order of magnitude. This pulsar also has the greatest reduction in $\sigma_{\tau,\mathrm{wh}}$ and the largest susceptibility to calibration error as characterised by τ_β. It is also interesting to find PSR J1744−1134 in this subset. For this pulsar, the theoretical uncertainty for MTM-derived arrival times is predicted to be 1.6 times greater than that of STM-derived arrival times; it is one of only two pulsars for which $\hat{\sigma}_\varphi > 1$ (see Table 3.2). However, PSR J1744−1134 also has the second-largest susceptibility to calibration error relative to timing precision ($\tau_\beta/\sigma_\tau \sim 0.28$ in Table 3.2).

Across the entire set of pulsars, the median E_q for IFA-STM is 330 ns, which is approximately two times the median E_q of 160 ns for METM-MTM (see Table 3.6), and there is moderate correlation between ΔE_q and τ_β (Pearson correlation coefficient $r \sim 0.58$). There is also very high correlation between ΔE_q and the differences in the weighted standard deviations of the whitened residuals, $\Delta\sigma_{\tau,\mathrm{wh}}$ ($r \sim 0.92$), and moderate correlation between τ_β and $\Delta\sigma_{\tau,\mathrm{wh}}$ ($r \sim 0.63$). However, it should be noted that the correlations between these variables are reduced when PSR J1045−4509 is

omitted from the data set. In this case, the correlation between ΔE_q and τ_β is low ($r \sim 0.37$), the correlation between ΔE_q and $\Delta\sigma_{\tau,\mathrm{wh}}$ is moderate ($r \sim 0.60$), and the correlation between $\Delta\sigma_{\tau,\mathrm{wh}}$ and τ_β is low ($r \sim 0.45$).

As both E_q and $\sigma_{\tau,\mathrm{wh}}$ are significantly reduced by METM-MTM and both are correlated with τ_β, we conclude that polarization calibration errors contribute significantly to the additional white noise in pulsar timing data.

3.5.4 Red Noise

For most of the PPTA pulsars, the results in Table 3.5 show no significant differences in red noise model parameters across the four data sets considered. The IFA-STM and METM-STM data sets for PSR J1600−3053 and the IFA-STM data set for PSR J1744−1134 appear to have marginally smaller red noise amplitudes and marginally steeper spectra; however, the noise model parameter distribution plots included in Appendix 3.7.2 (Figure 3.8 and Figure 3.9) clearly show that, in these three cases, the red noise amplitude and spectral index are both highly covariant and poorly constrained. Therefore, these results are omitted from further consideration.

In contrast, for PSR J0437−4715, the best-fit red noise model for the IFA-STM data set has a significantly larger amplitude (2.7 σ difference) and marginally smaller spectral index (1.7 σ difference) than those derived from the other three data sets. Figure 3.5 verifies that the red noise model parameters are well constrained and only moderately covariant in the IFA-STM and METM-STM data sets. Both the larger red noise amplitude and smaller spectral index (β = 2) derived from the IFA-STM data set are consistent with the presence of additional $1/f$ noise in the amplitude spectrum of these data. It is equally likely that additional white noise in the IFA-STM data biases the red noise model parameters.

Figure 3.6 plots the amplitude spectra of the METM-MTM and IFA-STM post-fit residuals for PSR J0437−4715 (computed before subtracting the best-fit red noise model). The amplitude spectral density is the square root of the power spectral density (PSD); therefore, a PSD characterized by a power law with a spectral index of β, as defined in equation 3.3, corresponds to a power-law amplitude spectrum with a spectral index of $\beta' = \beta/2$. The steeper power-law spectrum with slope $\beta' = 3/2$ that best fits the METM-MTM data is either buried under additional red noise with slope $\beta' = 1$ in the IFA-STM data or buried under additional white noise at key frequencies around yr^{-1} that constrain the slope of the spectrum.

It may be possible to differentiate between these two equally probable interpretations by analyzing data that span more time and radio frequencies [e.g. Zic et al., 2023]. Observing at multiple radio frequencies helps to distinguish between these scenarios by enabling the separation of chromatic noise sources—such as DM variations and interstellar scattering, which scale with observing frequency—from achromatic processes. For example, DM-induced timing noise follows a characteristic frequency dependence (typically $\propto \nu^{-2}$), allowing interstellar contributions to be isolated through multi-frequency modeling [Cordes and Shannon, 2010, Lam et al., 2018]. In contrast, frequency-independent excess red noise would be more consistent with intrinsic pulsar processes or a GWB. Additional insight may also be gained by searching for the inter-pulsar correlated systematic timing error induced by polarimetric distortion [van Straten, 2013]. This systematic error is a function of the polarized emission from each pulsar, and is independent of the angular separation between them. Therefore, instrumental distortion adversely impacts on the sensitivity of a PTA experiment to all moments (monopolar, dipolar, and quadrupolar) in a multipole expansion of residual timing delays.

3.5.5 Impact of METM

In the interest of better understanding which of the two techniques – METM or MTM – has the greatest impact on pulsar timing experiments, this section compares four statistical measures (ToA goodness-of-fit, error scale factor, error added in quadrature, and weighted standard deviation of whitened residuals) for the two calibration methods (METM and IFA) and the following section compares these quantities for the two arrival time estimation methods (MTM and STM).

The information in Figure 3.4 and its caption can be used to compare the goodness-of-fit of arrival times computed after calibration using either METM or IFA. First, when comparing IFA-STM with METM-STM (columns 3 and 5), four pulsars stand out as having exceptionally high values of median reduced χ^2 in the IFA-STM data set: PSR J0437−4715, PSR J1022+1001, PSR J1713+0747, and PSR J1939+2134. For each of these pulsars, METM significantly improves the STM goodness-of-fit. When comparing IFA-MTM with METM-MTM (columns 2 and 4), a similar reduction in reduced χ^2 is observed only for PSR J0437−4715. That is, METM generally has little impact on ToA goodness-of-fit when MTM is used.

In Table 3.6, comparison of the median values of E_f for METM-STM and IFA-STM (bottom two rows) and the median values of E_f for METM-MTM and IFA-MTM (top two rows) shows that METM only marginally reduces the error scale factor for both template matching techniques. For arrival times derived using STM, the median value of E_q drops by 30% from 0.33 μs (IFA) to 0.23 μs (METM). For MTM-derived ToAs, there is negligible difference in the median E_q for IFA and METM. In summary, METM generally has minimal impact on white noise model parameters when MTM is used.

Although METM significantly reduces the $\sigma_{\tau,\mathrm{wh}}$ of STM-derived arrival times for a number of pulsars in Table 3.5 (e.g., PSR J0437−4715, PSR J1022+1001, PSR J1603−3053, and PSR J1744−1134), there are also some pulsars for which METM

increases $\sigma_{\tau,\mathrm{wh}}$ (e.g., PSR J1832−0836 and PSR J2124−3358). The increase in $\sigma_{\tau,\mathrm{wh}}$ for these pulsars corresponds with large EFAC values reported in column 6 of Table 3.5, indicating that the ToA uncertainties are relatively high compared to other pulsars in the dataset. Consequently, the median values of $\sigma_{\tau,\mathrm{wh}}$ listed in Table 3.6 show that, with respect to IFA, METM slightly increases the median value of $\sigma_{\tau,\mathrm{wh}}$ by about 30 ns for arrival times derived using either template matching method. When comparing $\sigma_{\tau,\mathrm{wh}}$ of MTM-derived arrival times of each pulsar, the differences between METM and IFA are very small.

In summary, METM has negligible impact on TOAs derived using MTM, and only minimal impact on TOAs derived using STM. METM improves the STM goodness-of-fit and reduces the $\sigma_{\tau,\mathrm{wh}}$ of STM-derived arrival times for a small number of pulsars. For the STM-derived arrival times of all pulsars, METM reduces the median value of E_q by 100 ns, but also increases the median value of $\sigma_{\tau,\mathrm{wh}}$ by 30 ns.

3.5.6 Impact of MTM

As done in the previous section, the information in Figure 3.4 (and its caption) is used to compare the goodness-of-fit of arrival times computed using either MTM or STM. We start by comparing IFA-MTM with IFA-STM (columns 2 and 3). For each of the four previously-identified pulsars with exceptionally high values of IFA-STM median reduced χ^2 (PSR J0437−4715, PSR J1022+1001, PSR J1713+0747, and PSR J1939+2134), MTM significantly improves the goodness-of-fit. For PSR J0437−4715 and PSR J1022+1001, the improvement due to MTM is greater than the improvement due to METM. For PSR J1939+2134, the opposite is observed. When comparing METM-MTM with METM-STM (columns 4 and 5), the reduced χ^2 values for MTM and STM are similar (difference less than 0.05%) for most pulsars except PSR J0437−4715, PSR J1022+1001, and PSR J2241−5236, for which MTM achieves a

better fit than STM; and PSR J1824−2452A, PSR J1939+2134, and PSR J2124−3358, for which STM achieves a better fit than MTM. Overall, the differences between MTM and STM ToA goodness-of-fit are greatest in the IFA-calibrated data set.

In Table 3.6, comparison of the median values of E_f for METM-MTM and METM-STM (rows 1 and 3) and the median values of E_f for IFA-MTM and IFA-STM (rows 2 and 4) shows that MTM significantly reduces the error scale factor for both calibration techniques. For data calibrated using METM, the median value of E_q drops by 30% from 0.23 μs (STM) to 0.16 μs (MTM). For IFA-calibrated data, the median value of E_q drops by 55% from 0.33 μs (STM) to 0.15 μs (MTM). In general, MTM significantly reduces the median values of both white noise model parameters regardless of which calibration technique is used. MTM also significantly reduces the maximum values of E_q for both calibration methods (from 3.85 μs to 0.95 μs for IFA; and from 4.61 μs to 0.99 μs for METM).

A similar trend is observed in the weighted standard deviations of the whitened residuals. For both calibration techniques, MTM reduces the median value of $\sigma_{\tau,\mathrm{wh}}$ by 0.3 μs and the maximum value of $\sigma_{\tau,\mathrm{wh}}$ by 3 μs.

In summary, MTM has significant impact on TOAs derived from data using either calibration technique. For data calibrated using either IFA or METM, MTM improves the ToA goodness-of-fit, reduces the median E_f, and reduces both the median and maximum values of E_q and $\sigma_{\tau,\mathrm{wh}}$.

3.5.7 Comparison with PPTA DR2

The values of $\sigma_{\tau,\mathrm{wh}}$ derived in this work are compared with those reported for PPTA DR2 in Figure 3.7. Although this visual comparison may usefully indicate those pulsars for which improved techniques can be expected to have greatest impact, some caution and consideration is required when interpreting this plot. First, the PPTA

DR2 20-cm data span longer periods of time and include observations made using a variety of instrumental backends, each of which may require the inclusion of jumps to model unknown time delays. In contrast, our analysis focuses on only one backend. Second, the PPTA DR2 data were calibrated using Measurement Equation Modeling [MEM; van Straten, 2004] and therefore the IFA-STM results presented in this work are expected to have greater values of $\sigma_{\tau,\mathrm{wh}}$ than those reported for PPTA DR2. This is particularly true for PSR J1045−4509 and PSR J1446−4701. Furthermore, for PPTA DR2, PSR J0437−4715 was timed using the polarimetric invariant profile [Britton, 2000], which greatly mitigates the impact of polarization calibration errors [van Straten et al., 2001]. Consequently, for this pulsar, $\sigma_{\tau,\mathrm{wh}}$ for IFA-STM is significantly greater than that of PPTA DR2. Keeping in mind the above caveats, Figure 3.7 shows that METM-MTM yields better timing precision than PPTA DR2 for 23 of the 25 pulsars studied. The two exceptions are PSR J1832−0836 and PSR J1909−3744, pulsars that have low susceptibility to calibration error as characterised by τ_β.

3.6 Conclusion

Compared to conventional approaches for polarization calibration and arrival time estimation, the use of MTM [van Straten, 2006] significantly reduces white noise in pulse arrival times. When combined with METM [van Straten, 2013], further improvements may be observed, although in the case of PSR J0437−4715, the additional impact of METM appears marginal relative to the substantial gains already achieved by MTM alone. This combination also reduces the best-fit amplitude of red noise in the timing residuals for this pulsar, either by mitigating additional red noise or by improving the accuracy of red-noise model parameter estimates through a reduction in white-noise-induced bias.

In this work, we evaluated the impact of METM and MTM on timing precision

using four different quantities: the ToA goodness-of-fit, error scale factor E_f, error added in quadrature E_q, and the weighted standard deviation of the whitened post-fit residuals $\sigma_{\tau,\mathrm{wh}}$. We found that, with respect to the baseline IFA-STM data set, both METM and MTM improve the ToA goodness-of-fit; however, METM generally has little impact when MTM is used. A similar pattern is observed in fig. 16 of Guillemot et al. [2023].

Whereas METM only marginally reduces the median error scale factor, MTM significantly decreases the median value of E_f. In general, this indicates that the STM algorithm used in this work typically under-estimates arrival time uncertainty; however, for PSR J0437−4715, E_f is dominated by jitter for both template-matching techniques. We also found that both METM and MTM significantly reduce the error added in quadrature; however, the median value of E_q differs very little between METM and IFA when MTM is used. In contrast, MTM significantly decreases both the median and maximum values of E_q for both METM and IFA calibration methods. Finally, METM was shown to marginally increase the median value of $\sigma_{\tau,\mathrm{wh}}$, whereas MTM significantly decreases both the median and maximum values of $\sigma_{\tau,\mathrm{wh}}$. (As expected, changes in E_q and $\sigma_{\tau,\mathrm{wh}}$ are highly correlated.)

In summary, MTM significantly improves arrival time precision, regardless of the calibration technique used. This demonstrates that, as long as the calibration is accurate enough to minimize bandwidth depolarization, MTM can effectively model and correct for any remaining calibration errors. Bandwidth depolarization can distort the pulse's polarization profile if not properly accounted for, reducing the accuracy of timing measurements. Therefore, to ensure MTM performs optimally, it's essential to minimize depolarization across the observing band. We recommend using MTM for most pulsars in every PTA experiment. Depending on the instrument, achieving sufficiently well-calibrated observations may necessitate use of either MEM or METM.

Increased arrival time precision has the potential to enhance our ability to detect

errors in SSEs [Vallisneri et al., 2020] and terrestrial time models [Hobbs et al., 2020], facilitate new or more accurate measurements of pulsar properties [e.g. van Straten, 2013], and increase PTA sensitivity to the stochastic GWB. Therefore, MTM should be adopted and utilized for all future IPTA data releases.

3.7 Appendix

3.7.1 Arrival time uncertainty corrections

Scalar Template Matching Correction

The PSRCHIVE software used for this study includes two different algorithms for estimating the phase shift between a high-S/N template profile and an observed profile by cross-correlation in the Fourier domain [Taylor, 1992, hereafter T92]. The Phase Gradient Shift (PGS) algorithm uses the Van Wijngaarden–Dekker–Brent method [Brent, 1973] to find the phase shift τ that minimizes an objective χ^2 merit function, then uses the curvature, $\partial^2\chi^2/\partial\tau^2$, to calculate the theoretical uncertainty of τ. The Fourier domain with Markov Chain Monte Carlo (FDM) method minimizes the same objective merit function using the Levenberg-Marquardt algorithm, then optionally uses Markov Chain Monte-Carlo (MCMC) to sample the distribution of τ and calculate its uncertainty. The matrix template matching (MTM) algorithm also uses the curvature of χ^2 to compute arrival time uncertainty; therefore, in this work, we experimentally compare MTM and STM using the PGS implementation.

Both MTM and PGS are expected to underestimate uncertainty at low S/N, as demonstrated for the PGS algorithm through simulations [appendix A of Hotan et al., 2005], mathematical proof [appendix B of Arzoumanian et al., 2015a], and comparative analysis of experimental data [Wang et al., 2022]. However, the original implementation of PGS also overestimates arrival time uncertainty when the fit between the template and observation is poor. This unexpected result is most obvious when analyzing the PSR J0437−4715 timing residuals. For arrival times estimated using the original PGS implementation, the best-fit estimate of the E_f noise model parameter increased from ~ 1.8 for IFA-calibrated data to ~ 5.9 for METM-calibrated data.

The apparent increase in uncertainty is an artifact of the original PGS implementation, which computes the formal error of the phase shift based on the incorrect assumption that the reduced χ^2 is unity. This is equivalent to assuming that the noise in the post-fit residual profile is equivalent to the radiometer noise in each harmonic (σ in eqs. [A 6] through [A 11] of T92). This assumption breaks down when the observed profile is not a good match to the template, as

is the case when the total intensity is significantly distorted by residual calibration errors.

Poor template-matching fits in the IFA-calibrated data are expected to increase χ^2; however, owing to the incorrect definition of σ in the original PGS implementation, they also artificially inflate the derived arrival time uncertainty (σ_τ, defined by eq. [A 10] of T92). In contrast, METM calibration significantly reduces distortions to the total intensity profile, and thereby improves the scalar template-matching fit and reduces the arrival time uncertainties yielded by PGS. Consequently, a larger value of E_f is required to account for things like pulsar-intrinsic jitter in the METM-calibrated data. Though smaller, a similar inflation of E_f was also observed for PSR J1022+1001, which is also highly susceptible to polarization calibration errors [van Straten, 2013].

The erroneous assumption that the reduced χ^2 equals unity was made optional in the PSRCHIVE software (on 2023 July 4) and this assumption was disabled before reproducing the results and analysis presented in this paper.

Matrix Template Matching Correction

During our initial analysis of the best-fit noise model parameters produced by TEMPONEST, we found that all arrival times estimated using MTM had a median E_f of 0.7, indicating that this algorithm systematically *overestimates* arrival time uncertainty by a factor of approximately $\sqrt{2}$. To better understand the origin of this erroneous scale factor, we revisited both the derivation and the implementation of the equations that define the uncertainty of the best-fit MTM phase shift, first presented in § 3.2 of van Straten [2006, hereafter S06]. Here, the covariance matrix that defines the formal uncertainties of the MTM model parameters is given by $\mathbf{C} = \boldsymbol{\alpha}^{-1}$, where $\boldsymbol{\alpha}$ is the curvature matrix defined by eq. (14) of S06. This relationship between $\boldsymbol{\alpha}$ and $\mathbf{C}$ follows eq. (15.5.15) of Numerical Recipes [Press et al., 1992, hereafter NR], and the definition of $\boldsymbol{\alpha}$ is based on eqs. (15.5.8) and (15.5.11) of NR. (In particular, following the discussion in § 15.5 of NR, the term containing a second derivative has been dropped.) Compared to eq. (15.5.11) of NR, eq. (14) of S06 includes an extra factor of 2; however, this factor of 2 was missing in the PSRCHIVE implementation of the calculation. Erroneously dividing $\boldsymbol{\alpha}$ by 2 is equivalent to

multiplying $\mathbf{C}$ by 2 and inflating the MTM arrival time uncertainty by $\sqrt{2}$.

A similar factor of 2 error appeared in the PSRCHIVE calculation of the gradient vector, $\boldsymbol{\beta}$, which is also defined by eq. (15.5.8) of NR. Therefore, for future reference, a complete derivation of both $\boldsymbol{\beta}$ and $\boldsymbol{\alpha}$ is provided here, beginning with the merit function defined by eq. (10) of S06,

$$\chi^2 = \sum_{m=1}^{N/2} \sum_{k=0}^{3} |S_{m,k} - \mathrm{tr}[\boldsymbol{\sigma}_k \, \boldsymbol{\rho}'_m]|^2 \varsigma_k^{-2}. \tag{3.5}$$

In this equation, $S_{m,k}$ are the complex-valued Fourier transforms of the average pulse profiles of the observed Stokes parameters, as a function of pulsar spin harmonic m and Stokes parameter index k, $\boldsymbol{\rho}'_m$ is the model coherency matrix for harmonic m, $\boldsymbol{\sigma}_k$ are the Hermitian basis matrices, and $\mathrm{tr}[\mathbf{A}]$ is the trace of matrix $\mathbf{A}$. Define the observed coherency matrix at harmonic m,

$$\boldsymbol{\rho}_m = \frac{1}{2} \sum_{k=0}^{3} S_{m,k} \boldsymbol{\sigma}_k, \tag{3.6}$$

such that $S_{m,k} = \mathrm{tr}[\boldsymbol{\sigma}_k \, \boldsymbol{\rho}_m]$, then use the linearity of the matrix trace and the transitivity of matrix multiplication to express the difference between observed and model Stokes parameters for harmonic m,

$$D_{m,k} = \mathrm{tr}[\boldsymbol{\sigma}_k \, (\boldsymbol{\rho}_m - \boldsymbol{\rho}'_m)]. \tag{3.7}$$

Assuming that the noise in each Stokes parameter is equal, let $\varsigma_k = \varsigma$. The first partial derivative of χ^2 with respect to model parameter η_r is then

$$\frac{\partial \chi^2}{\partial \eta_r} = -\frac{2}{\varsigma^2} \sum_{m=1}^{N/2} \sum_{k=0}^{3} \mathrm{Re}\left[D_{m,k} \mathrm{tr}\left(\boldsymbol{\sigma}_k \, \frac{\partial \boldsymbol{\rho}'_m}{\partial \eta_r} \right)^* \right]. \tag{3.8}$$

Because $\mathrm{tr}(\boldsymbol{\sigma}_k \, \boldsymbol{\rho})^* = \mathrm{tr}(\boldsymbol{\sigma}_k \, \boldsymbol{\rho}^\dagger)$ and both the trace of a matrix and the real part of a complex number are linear,

$$\frac{\partial \chi^2}{\partial \eta_r} = -\frac{2}{\varsigma^2} \sum_{m=1}^{N/2} \mathrm{Re}\,\mathrm{tr}\left[\sum_{k=0}^{3} D_{m,k} \boldsymbol{\sigma}_k \, \frac{\partial \boldsymbol{\rho}'^\dagger_m}{\partial \eta_r} \right]. \tag{3.9}$$

Combining the definitions of the coherency matrix and the Stokes parameters yields

$$\boldsymbol{\rho} = \frac{1}{2} \sum_{k=0}^{3} \mathrm{tr}(\boldsymbol{\sigma}_k \, \boldsymbol{\rho}) \boldsymbol{\sigma}_k; \tag{3.10}$$

therefore,

$$\sum_{k=0}^{3} D_{m,k}\boldsymbol{\sigma}_k = 2(\boldsymbol{\rho}_m - \boldsymbol{\rho}'_m) \tag{3.11}$$

and

$$\beta_r \equiv -\frac{1}{2}\frac{\partial\chi^2}{\partial\eta_r} = \frac{2}{\varsigma^2}\sum_{m=1}^{N/2} \mathrm{Re}\,\mathrm{tr}\left[(\boldsymbol{\rho}_m - \boldsymbol{\rho}'_m)\frac{\partial\boldsymbol{\rho}'^{\dagger}_m}{\partial\eta_r}\right]. \tag{3.12}$$

Taking the partial derivative of $-\beta_r$ with respect to model parameter η_s (and dropping the term containing a second derivative) yields

$$\alpha_{rs} \equiv \frac{1}{2}\frac{\partial^2\chi^2}{\partial\eta_r\partial\eta_s} = \frac{2}{\varsigma^2}\sum_{m=1}^{N/2} \mathrm{Re}\,\mathrm{tr}\left[\frac{\partial\boldsymbol{\rho}'^{\dagger}_m}{\partial\eta_r}\frac{\partial\boldsymbol{\rho}'_m}{\partial\eta_s}\right]. \tag{3.13}$$

which is equivalent to eq. (14) of S06. Both β_r and α_{rs} include a factor of 2 that was missing in the PSRCHIVE adaptation of the Levenberg-Marquardt algorithm to complex-valued matrices. This error was corrected (on 2023 July 9) before reproducing the results and analysis presented in this paper.

3.7.2 Rejected Red-Noise Models

When comparing the four methods applied to each pulsar in Table 3.5, there are slight differences in the best-fit red noise model parameters that mostly fall within the estimated uncertainties. Exceptions include three data sets (PSR J1600−3053 IFA-STM and METM-STM, and PSR J1744−1134 IFA-STM) that exhibit marginally smaller red noise amplitudes and steeper spectra; however, the following plots show that these parameters are highly covariant and poorly constrained in these three cases. Consequently, these minor differences are not further considered.

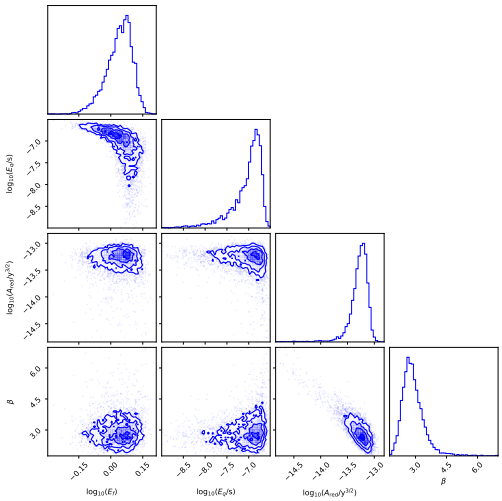

(a) METM-MTM

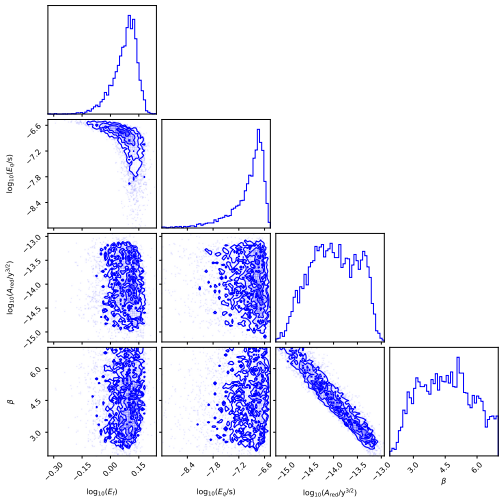

(b) METM-STM

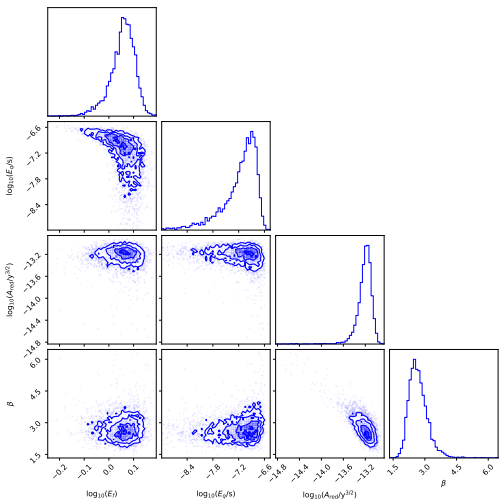

(c) IFA-MTM

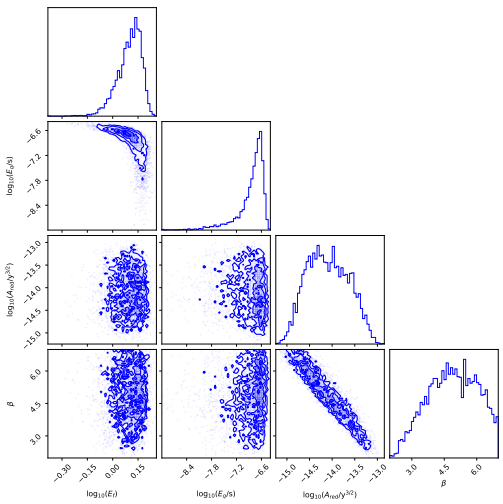

(d) IFA-STM

Figure 3.8: Noise Model Parameter Distributions for PSR J1600−3053. See Figure 3.5 for information.

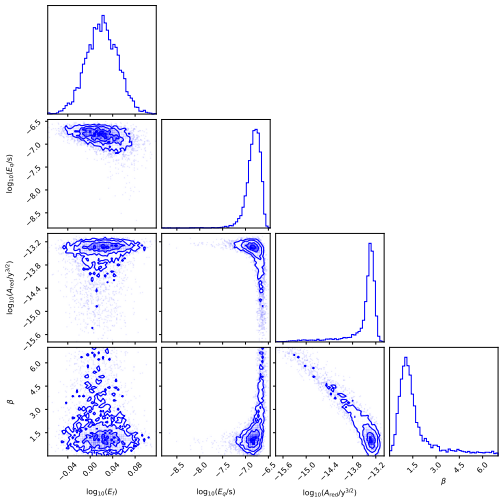

(a) METM-MTM

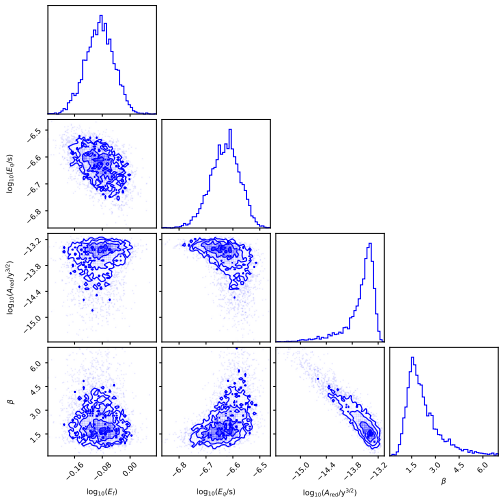

(b) METM-STM

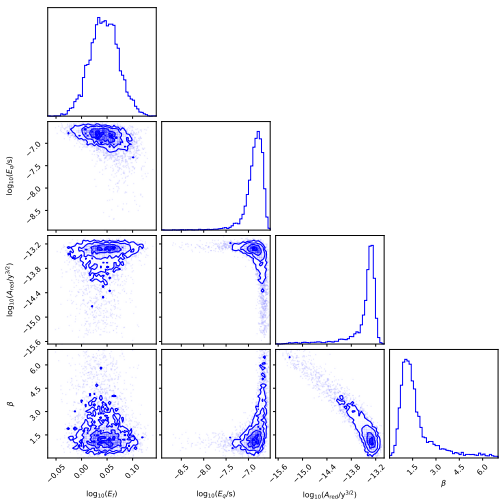

(c) IFA-MTM

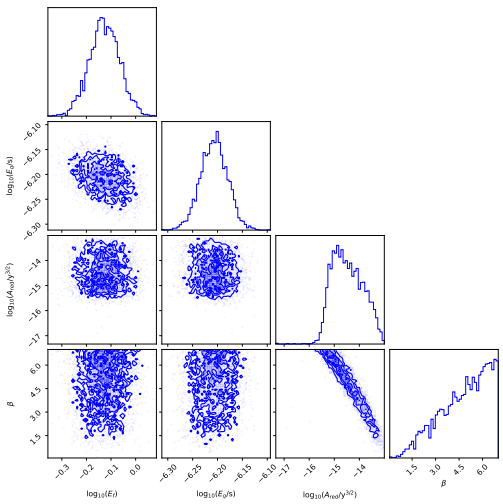

(d) IFA-STM

Figure 3.9: Noise Model Parameter Distributions for PSR J1744−1134. See Figure 3.5 for information.

3.7.3 Calibration Steps

To help others integrate MEM, METM, and MTM into existing pipelines, this appendix provides a more detailed description of the commands used for polarimetric calibration.

Produce MEM Solutions

Inputs:

1. Uncalibrated observations of the reference pulsar (e.g., PSR J0437−4715 at Parkes), divided into long sessions, where each session spans at most one day (horizon to horizon) and includes a minimum of 2 hours of observations; and

2. Uncalibrated observations of the square-wave amplitude-modulated noise diode (CAL) observed prior to each pulsar observation.

Steps:

Assuming that the CAL observations are listed in a single flat ASCII file named `database.txt` (as produced by pac) and that the pulsar observations for a single session are listed in a file named `session.ls`, the following steps are performed for each session:

A. Calibrate the data using the ideal feed assumption and produce a time-integrated total named `choose.ar`, which is later passed to pcm for use when choosing the phase bins to include in the MEM fit.

```
pac -P -O pac_out -d database.txt -M session.ls
psradd -T -o choose.ar pac_out/*.calibP
```

B. Run pcm in MEM mode.

```
pcm $args -c choose.ar -d database.txt -M session.ls
```

where `$args` includes the following command-line options:

`-m bri00e19`	use Equation (19) of Britton 2000 to model the instrumental response
`-k`	assume that the receptors have equal ellipticities
`-Q`	model the noise diode as coupled after the orthomode transducer
`-s`	normalize Stokes parameters by the phase-integrated invariant interval
`-n 64`	use 64 phase bins as model constraints
`-a 0`	disable the phase-alignment check
`-K 3.0`	reject outliers when computing CAL levels
`-step 3.0`	detect and model steps in instrumental response
`-X 2.0`	mask channels with $\chi^2/N_{\rm free} > 2.0$
`-N`	do not unload calibrated data files

Outputs:

1. `pcm.fits` - the best-fit parameters that describe the model of the instrumental response and the polarization of the noise diode (CAL)

2. `total.ar` - the calibrated time-integrated full-polarization average pulse profile for this session.

The `pcm.fits` files should be reviewed, and solutions with any obvious model-fitting problems, errors, or poorly constrained model parameters should be discarded.

Create METM Template Profile

Inputs:

1. The `total.ar` files produced for each MEM session.

Steps:

A. Choose the best MEM solution (criteria described in the paper) and rename its `total.ar` file to `chosen.ar`.

B. Model and eliminate any temporal variations (e.g. changes in instrumental response, ionospheric Faraday rotation, etc.) before further integrating in time. For each `total.ar`

```
pcm -t8 -n 128 -S chosen.ar -out total.mtm total.ar
```

C. Integrate the calibrated `total.calib` files output by pcm and the `chosen.ar` template.

```
psradd -T -o pulsar.std chosen.ar */total.calib \
       -j "weight snr fscrunch=1" -phath 0.003
```

Outputs:

1. `pulsar.std` - the template to be used for METM

Produce METM Solutions

Inputs:

1. `pulsar.std` - the high S/N, well-calibrated, full-polarization average profile of the reference pulsar
2. Uncalibrated observations of the reference pulsar (e.g., PSR J0437−4715 at Parkes), divided into short sessions that include a minimum of 1 hour of observations; and
3. Uncalibrated observations of the square-wave amplitude-modulated noise diode (CAL) observed prior to each pulsar observation.

Steps:

Assuming that the CAL observations are listed in a single flat ASCII file named `database.txt` (as produced by pac) and that the pulsar observations for a single short session are listed in a file named `session.ls`, the following step is performed for each session:

```
pcm -S pulsar.std -d database.txt -M session.ls $args
```

where `$args` includes the following command-line options:

`-m bri00e19`	use Equation (19) of Britton 2000 to model the instrumental response
`-Q`	model the noise diode as coupled after the orthomode transducer
`-s`	normalize Stokes parameters by the phase-integrated invariant interval
`-n 200`	use 200 harmonics as model constraints
`-K 3.0`	reject outliers when computing CAL levels
`-step 3.0`	detect and model steps in instrumental response
`-X 2.0`	mask channels with $\chi^2/N_{\rm free} > 2.0$

Outputs:

1. `pcm.fits` - the best-fit parameters that describe the model of the instrumental response and the polarization of the noise diode (CAL); and
2. `total.ar` - the calibrated time-integrated full-polarization average pulse profile for this session.

The `pcm.fits` files should be reviewed, and solutions with any obvious model-fitting problems, errors, or poorly constrained model parameters should be discarded.

Correct Ionospheric Faraday Rotation

Inputs:

1. All of the solutions contained in `pcm.fits` files produced using METM

Steps: Estimate the ionospheric rotation measure contribution and subtract it from each session.

```
pcmrm pcm.fits
```

Outputs:

1. `pcm.rms` - the `pcm.fits` solution with σ_θ corrected for ionospheric Faraday rotation

Smooth METM solutions

Inputs:

1. `file.ls` - the listing of the `pcm.rmc` files corrected for ionospheric Faraday rotation using `pcmrm`.

Steps: Spline-smooth the METM solutions using Monte-Carlo cross-validation.

```
smint -p1 -cross -cross-m 4 -cross-f 0.5 -cross-iqr 0 -M files.ls
```

Where the following command-line options specify

`-p1`	the initial guess for the penalized spline smoothing factor
`-cross`	find the optimal spline smoothing factor using Monte-Carlo cross-validation
`-cross-m 4`	the number of cross-validation iterations
`-cross-f 0.5`	the fraction of data used to validate the best-fit spline on each iteration
`-cross-iqr 0`	disables outlier excision using the uncertainty-weighted inter-quartile range
`-M files.ls`	list of `pcm.fits` files (corrected for ionospheric Faraday rotation)

Outputs:

1. `smint.fits` - the spline-smoothed calibrator solution
2. `cal_stokes_fit*.eps`
3. `pcal_fit_*.eps`

The postscript files plot the spectrum for each of the smoothed model parameters; each page shows the data extracted from one of the input `pcm.fits` files (black points with error bars) and the spline fit to the data at this epoch (red line).

Calibrate the Pulsar Data

Inputs:

1. `metm_database.txt` - database of spline-smoothed METM calibrator solutions
2. `cal_database.txt` - database of CAL files.
3. `fluxcal_database.txt` - database of FLUXCAL files.
4. `uncalibrated.ls` - a list of the pulsar observations to be calibrated

Steps: Perform METM calibration.

```
pac $args -M uncalibrated.ls \
    -d cal_database.txt -d fluxcal_database.txt -d metm_database.txt
```

where `$args` includes the following command-line options:

`-K 3.0`	reject outliers when computing calibrator levels
`-g`	frequency-average the data to match the number of channels of the calibrator
`-m b`	use only calibrators observed before the pulsar
`-S`	use the complete Reception model
`-e cmetm`	extension added to output filenames

Outputs:

1. calibrated pulsar observations with a new extension, `*.cmetm`

Produce Arrival Time Estimates

Inputs:

1. calibrated pulsar observations listed in a text file named `calibrated.ls`
2. a well-calibrated template profile (e.g. the calibrated observation with the highest S/N)

Steps:

A. Time- and Frequency-average the profile data.

```
pam -TF -e TF -M calibrated.ls
```

B. Produce the MTM arrival-time estimates in a `.tim` file.

```
pat -Fpcs pulsar.std -f tempo2 -C gof *.TF > mtm.tim
```

Outputs:

1. `mtm.tim` - TEMPO2-formatted file of arrival time estimates produced by MTM.

Chapter 4

Manuscript 2

This chapter is based on work currently in preparation for submission to the Astrophysical Journal. It evaluates the precision of pulse arrival time estimates derived from 4.5 years of MSP observations conducted with the MeerKAT Radio Telescope as part of the MeerKAT Pulsar Timing Array [MPTA; Miles et al., 2023] project. We compare three techniques for ToA estimation: (1) Matrix Template Matching [MTM; van Straten, 2006] and (2) Scalar Template Matching [STM; Taylor, 1992] both using the same high S/N profiles as templates, and (3) MPTA$_{\mathrm{T}}$, the Fourier domain Monte Carlo (FDM) method employed in the MPTA timing analysis pipeline, using frequency-dependent templates generated by PULSEPORTRAITURE [Pennucci, 2019].

Analyzing the data from 75 high-priority MPTA pulsars, we find that MTM slightly outperforms MPTA$_{\mathrm{T}}$ in 18 cases (24%) despite using a more sophisticated method of arrival time estimation. MTM outperforms STM in 59 cases (79%), consistent with previous studies (e.g., [Rogers et al., 2024]) showing that ToA estimates derived from polarization profiles (using MTM) tend to have greater precision than those derived from total intensity profiles alone (using STM). Across most pulsars, MPTA$_{\mathrm{T}}$ achieves lower average whitened root-mean-squared (RMS) residuals than both MTM and STM, likely due to PULSEPORTRAITURE's robust handling of frequency-dependent pulse

shape evolution in MPTA$_{\rm T}$'s template construction. Residual polarization calibration errors—unmodeled by MTM—may also contribute to its underperformance relative to MPTA$_{\rm T}$.

While MTM demonstrates the ability to improve timing precision, outperforming STM, its performance was limited compared to MPTA$_{\rm T}$. Because the same dataset and calibration procedures were used across all methods, these findings emphasize that differences in template construction, particularly the use of frequency-dependent templates, play a key role in achieving high-precision timing across wideband datasets. Nevertheless, the results highlight MTM's potential as a complementary approach to existing methods. Future work integrating frequency-dependent templates from PULSEPORTRAITURE with MTM could further enhance timing precision, which is critical for GW detection efforts and broader astrophysical research.

4.1 Introduction

MSPs are NSs that have been spun up to exceptionally high rotation rates through the accretion of matter from a companion star in a binary system. They are also characterized by long-term rotational stability, making them ideal for precision timing applications. Their precise periodic radio emissions enable tests of GR [Taylor and Weisberg, 1982, Kramer et al., 2006, Freire et al., 2012, Archibald et al., 2018, Kramer et al., 2021a], alternate gravity theories [Zhu et al., 2015a, Voisin et al., 2020], and refinement of terrestrial time standards [Petit and Tavella, 1996, Hobbs et al., 2020]. Additionally, MSP timing contributes to exoplanet discovery [Wolszczan and Frail, 1992, Wolszczan, 1994], constraints on the nuclear matter EOS [Demorest et al., 2010, Antoniadis et al., 2013, Özel and Freire, 2016, Cromartie et al., 2020, Miller et al., 2021, Riley et al., 2021], and the search for GWs [Hellings and Downs, 1983, Foster and Backer, 1990, Miles et al., 2023]. Insights into NS interiors [Antonopoulou et al.,

2018], magnetospheric dynamics [Dyks and Rudak, 2015, Ilie et al., 2019], and Galactic structure [Noutsos et al., 2008, Yao et al., 2017] further highlight their importance.

PTAs leverage the exceptional timing precision of MSPs to detect GWs from sources such as SMBHBs [Rajagopal and Romani, 1995, Jaffe and Backer, 2003, Wyithe and Loeb, 2003, Sesana et al., 2004, Kocsis and Sesana, 2011, Roedig et al., 2012, Taylor et al., 2017], as well as from potential cosmological sources like cosmic strings or phase transitions [Kibble, 1976, Ölmez et al., 2010, Sanidas et al., 2012, Lentati et al., 2015, Arzoumanian et al., 2018, Grishchuk, 2005]. A key requirement for this is the ability to measure pulse arrival times with sub-microsecond precision—better than one part in 10^4 of the pulse period [van Straten et al., 2001]. Combined with long-term monitoring of a spatially distributed array of MSPs, this precision enables the detection of correlated timing deviations indicative of passing GWs [Hellings and Downs, 1983].

Whereas previous studies focused on placing rigorous upper limits on the energy density of the stochastic GWB [Lentati et al., 2015, Shannon et al., 2015, Aggarwal et al., 2019, Perera et al., 2019], current efforts are directed toward detecting the expected HD correlations [Hellings and Downs, 1983], a definitive signature of the GWB.

Recently, multiple PTAs—including the EPTA [Desvignes et al., 2016], NANOGrav [McLaughlin, 2013], the PPTA [Manchester, 2008], and InPTA [Tarafdar et al., 2022]—have reported evidence consistent with the HD spatial correlation, providing strong indications of a GWB signal [Agazie et al., 2023b, Antoniadis et al., 2023b, Reardon et al., 2023]. While the reported significance of the spatial correlation varies between ~2–4σ, falling short of a definitive detection, these findings underscore the importance of precise noise modeling and advanced ToA estimation techniques for robust GW detection.

The MPTA [Miles et al., 2023], operating under the MeerTime collaboration [Bailes et al., 2016], contributes significantly to international GW detection efforts through its role in the IPTA [Hobbs et al., 2010]). The MPTA focuses on high-precision timing

of MSPs selected for their rotational stability and well-characterized timing behavior. Located in South Africa's Northern Cape Province [Dewdney et al., 2009], the MPTA's 64-dish array enhances Southern Hemisphere pulsar sky coverage and is projected to contribute approximately half of the IPTA's overall sensitivity to GWs in coming years [Spiewak et al., 2022].

This paper examines 4.5 years of MPTA observations of high-priority MSPs, chosen for their exceptional timing stability. Using MTM [van Straten, 2006] for ToA estimation, we assess its performance against both STM and the Fourier Domain Monte Carlo (FDM) algorithm used in the MPTA pipeline. The MPTA uses the FDM algorithm with total intensity, frequency-dependent templates generated by PULSEPORTRAITURE [Pennucci, 2019]; this configuration is referred to throughout as $\mathrm{MPTA_T}$. STM is applied to total intensity, high S/N templates using the "pat" tool with the "-A FDM" option, while MTM is applied to high S/N full-polarization templates.

Following this introduction, Section 4.2 outlines the dataset, Section 4.3 details the analysis methodology, Section 4.4 presents results, and Section 4.5 discusses implications and future directions.

4.2 Observations

We analyzed 4.5 years of MPTA observations, spanning Modified Julian Dates (MJD) 58526 to 60155 (12 February 2019 to 29 July 2023). The dataset includes 83 MSPs regularly monitored by the MPTA, selected based on their rotational stability and low timing noise.

Observations were performed using the MeerKAT L-band receiver (856–1712 MHz) and the Pulsar Timing User Supplied Equipment (PTUSE) backend [Bailes et al., 2020]. PTUSE performs real-time coherent de-dispersion and folding, recording data with 1024 phase bins and 1024 frequency channels.

Initial data processing was carried out with the Python-based MEERPIPE pipeline, which includes polarization calibration using Jones matrices provided by SARAO [Serylak et al., 2021]. Radio frequency interference (RFI) was mitigated using MEERGUARD [Reardon, 2021], a customized version of COASTGUARD [Lazarus et al., 2016], specifically developed for the MeerTime project.

After cleaning, the data were integrated offline to 32 frequency channels, one sub-integration, and four Stokes parameters (i.e., full polarization). This frequency resolution was chosen to balance time and computational efficiency with sensitivity to frequency-dependent effects, while preserving sufficient spectral detail for MTM analysis.

From each observation, we extracted 32 ToAs (one per sub-band) using both MTM and STM approaches, enabling direct comparison with the MPTA ToAs. For STM, we applied the "pat" tool with the "-A FDM" option to high S/N, total intensity templates. MTM was applied to high S/N, full-polarization templates.

To enable a controlled comparison, we aligned our analysis with the MPTA dataset, using the publicly available 4.5-year ToA set based on the $\mathrm{MPTA_T}$ configuration (total intensity, frequency-dependent templates, FDM). ToAs absent from that dataset were excluded from our sample.

Although the MPTA nominally covers the same time span, timing baselines ranged from 2 to 4.5 years across the pulsars due to varying observation cadences and start times. Additionally, discrepancies in ToA counts arose for several pulsars because the MPTA timing dataset included extra ToAs not present in the public repository. We later found these resulted from longer observations acquired during the relativistic binary campaign [Kramer et al., 2021b], for which the MPTA team applied PSRPSPLIT to divide data into shorter sub-integrations. This approach helps model fast-varying relativistic effects (e.g., Shapiro delay). Our analysis did not incorporate such splitting, leading to minor differences in timing results (see Table 4.1), particularly for PSRs

J0614−3329, J1435−6100, J1732−5049, J1757−5322, and J2129−5721, where MTM's whitened RMS residuals differ from MPTA$_{\rm T}$ by over 1μs (see Table 4.8, Appendix). These pulsars should be reprocessed in future work using matched time resolution.

In addition to these differences, the MTM algorithm automatically flagged and excluded certain frequency channels during the ToA estimation process for a few pulsars, based on internal signal-quality metrics (e.g., low S/N or poor fit convergence). These flagged channels led to slight variations in ToA counts (see Table 4.2). For the remaining pulsars, we achieved a strict 1-to-1 match in ToA counts between our MTM outputs and the MPTA$_{\rm T}$ dataset.

4.3 Methods

4.3.1 Template Creation

Our standardized profiles ("templates") were created by selecting the observation with the highest S/N as the initial standard. Additional observations were S/N-weighted (e.g., more weight assigned to observations with higher S/N) and combined with the reference template using the PSRADD tool. Only real, observational data were used in template construction. This approach was chosen to preserve the true pulse morphology and polarization structure, consistent with previous high-precision timing work (e.g., [van Straten, 2004, Osłowski et al., 2013]).

4.3.2 ToA Estimation

Matrix Template Matching [MTM; van Straten, 2006] was used to estimate ToAs from full-Stokes profiles. MTM operates in the Fourier domain, fitting the observed polarization profile to a high-S/N template by adjusting phase and instrumental polarization parameters to maximize the likelihood of the match. Unlike Standard Template

PSR Name	Method	Span (yr)	NToAs
J0614−3329	MPTA	4.28	3499
J0614−3329	MTM	4.28	2739
J0955−6150	MPTA	4.35	6167
J0955−6150	MTM	4.35	3299
J1101−6424	MPTA	4.33	3963
J1101−6424	MTM	4.33	3405
J1435−6100	MPTA	4.38	3976
J1435−6100	MTM	4.38	3377
J1525−5545	MPTA	3.63	9504
J1525−5545	MTM	3.63	3040
J1545−4550	MPTA	4.33	4905
J1545−4550	MTM	4.33	3374
J1629−6902	MPTA	4.40	3106
J1629−6902	MTM	4.40	3080
J1732−5049	MPTA	4.46	4442
J1732−5049	MTM	4.46	3190
J1757−5322	MPTA	4.19	3323
J1757−5322	MTM	4.19	3259
J1811−2405	MPTA	4.33	6290
J1811−2405	MTM	4.33	5170
J1902−5105	MPTA	4.27	3438
J1902−5105	MTM	4.27	3246
J1909−3744	MPTA	4.46	7199
J1909−3744	MTM	4.46	7171
J1933−6211	MPTA	4.38	2937
J1933−6211	MTM	4.38	2601
J2129−5721	MPTA	4.31	3039
J2129−5721	MTM	4.31	2880

Table 4.1: The data span and number of ToAs for pulsars with discrepancies between the MPTA and MTM datasets arising from longer observations being split into shorter sub-integrations using PSRPSPLIT.

PSR Name	Method	Span (yr)	NToAs
J0030+0451	STM	3.73	2880
J0030+0451	MTM	3.73	2847
J0101−6422	STM	3.82	1430
J0101−6422	MTM	3.82	1398
J0125−2327	STM	4.25	3170
J0125−2327	MTM	4.25	3138
J1455−3330	STM	4.29	2448
J1455−3330	MTM	4.29	2447
J1732−5049	STM	4.46	3191
J1732−5049	MTM	4.46	3190
J1744−1134	STM	4.27	2957
J1744−1134	MTM	4.27	2956
J1804−2717	STM	3.14	1569
J1804−2717	MTM	3.14	1567
J1804−2858	STM	3.96	2167
J1804−2858	MTM	3.96	2163
J1843−1113	STM	4.27	2886
J1843−1113	MTM	4.27	2885
J1843−1448	STM	4.25	1969
J1843−1448	MTM	4.25	1968

Table 4.2: Data span and number of ToAs for pulsars with discrepancies due to MTM flagging channels as invalid.

Matching (STM), which uses only the total intensity (Stokes I), MTM incorporates all four Stokes parameters. This allows it to better account for pulse shape variations and calibration imperfections, often leading to improved timing precision. A detailed description of the MTM implementation in our analysis is provided in §2.2.2.

4.3.3 Noise Modeling

Pulsar timing residuals are affected by various noise processes, modeled as white noise (e.g., instrumental uncertainties and measurement errors), red noise (e.g., long-term rotational irregularities), and DM noise (e.g., temporal and spatial variations in the ISM).

White Noise

To accurately characterize timing uncertainties, we model several sources of white noise that affect pulsar timing residuals. These noise components help account for deviations not captured by ToA measurement errors alone and are crucial for obtaining reliable parameter estimates in timing models.

Standard white noise parameters include:

- EFAC, a multiplicative factor applied to reported ToA uncertainties (typically accounting for radiometer noise);
- EQUAD, an added term in quadrature to capture excess system noise (e.g., instrumental effects);
- ECORR, which models perfectly correlated noise between simultaneous sub-band ToAs, such as that introduced by pulse phase jitter.

In this work, we adopt SECORR [Bailes et al., 2020], a time-dependent variant of ECORR used by the MPTA. This model incorporates the integration time T of each

observation:

$$\sigma_{ij}^2 = \delta_{ij}\,\sigma_{\mathrm{SECORR,hr}}^2 \sqrt{\frac{3600\,\mathrm{s}}{T}}, \tag{4.1}$$

where σ^2 is the variance, δ_{ij} is the Kronecker delta function, and $\sigma_{\mathrm{SECORR,hr}}^2$ is the SECORR amplitude scaled to a 1-hour integration. This formulation captures the expected reduction in jitter noise with longer observation times (scaling as $T^{-1/2}$) and aligns with ECORR-like models used in NANOGrav [Arzoumanian et al., 2018, Alam et al., 2021b].

In our analysis, individual ToAs are extracted from ~5-minute observations (~300 s), so the $T^{-1/2}$ scaling in SECORR increases the modeled noise relative to the 1-hour reference. This appropriately captures the contribution of pulse phase jitter, which is known to dominate at short integration times [Shannon et al., 2014, Lam et al., 2019]. While the templates used were constructed from long integrations (>20,000 s), this only affects the template quality, not the per-ToA noise model. Therefore, SECORR remains essential to account for stochastic, broadband noise arising from intrinsic pulse variability [Rickett, 1975, Taylor et al., 1975, Liu et al., 2011, Osłowski et al., 2011].

Achromatic Red Noise

Achromatic red noise, attributed to NS rotational irregularities [Shannon and Cordes, 2010], is modeled with a power-law spectrum

$$S(f) = \frac{A^2}{12\pi^2}\left(\frac{f}{f_{\mathrm{yr}}}\right)^{-\gamma}, \tag{4.2}$$

where A is the amplitude, γ is the spectral index, and $f_{\mathrm{yr}} = 1\,\mathrm{yr}^{-1}$.

DM Noise

The wide bandwidth and high S/N ratio of MeerKAT enable accurate DM estimation using TEMPO2 [Hobbs et al., 2006, Johnston et al., 2020].

Variations in DM over time (referred to as DM noise) arise primarily owing to relative motion between the pulsar and Earth, as the line-of-sight path changes more rapidly than the large-scale structure of the ISM. These fluctuations are modeled as a power-law process in time, with an amplitude that scales as λ^2, where λ is the observing wavelength [Keith et al., 2013, Jones et al., 2017]. This wavelength dependence reflects the stronger impact of DM variations at lower frequencies, consistent with the ν^{-2} scaling of dispersive delays (see §2.4.4).

Prior Ranges

We modeled noise using the Bayesian inference package TEMPONEST [Lentati et al., 2014], which is widely used in PTA analyses [Lam et al., 2017, Goncharov et al., 2021b, Chalumeau et al., 2022]. For our analysis, we adopted a configuration with 1000 live points and a target sampling efficiency of 0.1—settings commonly used in PTA studies to ensure a balance between computational cost and thorough exploration of the parameter space.

In this nested sampling framework, live points refer to the number of concurrent samples used to explore the posterior distribution, influencing the resolution of parameter estimation. The target sampling efficiency determines the fraction of accepted proposals during sampling, with lower values favoring precision over speed.

Our noise model includes priors (see Table 4.3) for white noise (EFAC, EQUAD, SECORR), achromatic red noise ($\log_{10}\mathrm{Ared}$, $\gamma\mathrm{red}$), and chromatic DM noise ($\log_{10}\mathrm{ADM}$, $\gamma\mathrm{DM}$).

Table 4.3: Prior ranges for noise parameters.

Parameter	Prior Range
White Noise Parameters	
$\log_{10}$ EFAC	$[-1, 1.5]$
$\log_{10}$ EQUAD	$[-10, -5]$
$\log_{10}$ SECORR	$[-10, -5]$
Red Noise Parameters	
$\log_{10} A_{\rm red}$	$[-18, -10]$
$\gamma_{\rm red}$	$[0, 7]$
DM Noise Parameters	
$\log_{10} A_{\rm DM}$	$[-18, -10]$
$\gamma_{\rm DM}$	$[0, 7]$

Table 4.4: Models compared to determine the most probable representation of the noise processes in each pulsar.

M_N	EFAC+EQUAD	SECORR	Red	DM
M_1	✓	-	-	-
M_2	✓	✓	-	-
M_3	✓	-	✓	-
M_4	✓	-	-	✓
M_5	✓	✓	✓	-
M_6	✓	✓	-	✓
M_7	✓	✓	✓	✓
M_8	✓	-	✓	✓

Model Selection

Following the approach adopted in the MPTA's 4.5-year analysis [Miles et al., 2025], we tested eight predefined noise models (labeled M_N, where N ranges from 1 to 8; see Table 4.4) for each method. These models incorporate different combinations of white, red, and DM noise terms. The best-fit model was selected based on the highest Nested Importance Sampling (NIS) value reported by TEMPONEST.

4.4 Results

This section presents the results of our analysis, comparing MTM and STM ToA estimation methods (both using the same high S/N templates) and the MPTA_{T} FDM approach (using frequency-dependent templates).

Table 4.8 (Appendix) summarizes the timing results for each pulsar and method. It includes the weighted root-mean-square (RMS) values for both the pre-fit RMS residuals (Full) and whitened RMS residuals (White) reported by TEMPO2. Noise model parameters derived using TEMPONEST are listed alongside the Nested Importance Sampling (NIS) metric used for model comparison.

To cross-validate our TEMPONEST-based results, we also compare them with those reported by the MPTA's 4.5-year analysis [Miles et al., 2025], hereafter referred to as MPTA_{E}, which derives noise models using ENTERPRISE—a Bayesian pulsar timing software package that facilitates flexible modeling of noise processes and GW signals, widely adopted across the PTA community [Ellis et al., 2019].

Note that PSRs J1125−5825 and J1732−5049 exhibit extremely large pre-fit RMS residuals of $\sim 900\mu$s when using the STM method. After noise whitening, the RMS residuals increase further (to ~ 950 and $\sim 2000\mu$s, respectively), indicating instability or failure in the STM-derived timing solution for these cases. For PSRs J1455−3330 and J2150−0326, TEMPO2 was unable to converge to a valid timing solution under the STM method, despite all methods starting from the same initial timing model. These four pulsars are therefore excluded from the following results and discussion.

PSRs J1804−2858, J1825−0319, and J1843−1448 exhibit unusually large whitened RMS residuals ($> 10\mu$s) for one or more ToA estimation methods, which significantly skewed summary plots and statistical comparisons, making interpretation difficult. To ensure a fair and interpretable comparison across methods, these pulsars were excluded from the plots, tables, and aggregated statistics. This excluded group also includes

PSR J0437−4715, one of the closest, brightest, and most precisely timed pulsars. For this source, a notably large EFAC value of 7 was obtained—likely a consequence of MeerKAT's high sensitivity, which amplifies the influence of jitter noise. This may cause EFAC to increase to account for unmodeled noise or underestimated ToA uncertainties [Miles et al., 2025]. For completeness, noise parameters and timing statistics for these eight excluded pulsars are presented in Table 4.9 in the appendix.

Our analysis shows that among the 75 pulsars included in the comparison, MTM achieved lower whitened RMS residuals than $\mathrm{MPTA_T}$ in 18 cases (24%).

4.4.1 Whitened RMS

Figure 4.1 presents a comparison of whitened RMS residuals across all three ToA estimation methods (MTM, STM, and $\mathrm{MPTA_T}$), highlighting the 18 pulsars where MTM yields improved timing precision compared to $\mathrm{MPTA_T}$. In some cases, the improvement is marginal (e.g., <1% for PSRs J1421−4409 and J1737−0811), while for others, such as PSR J1022+1001, the reduction reaches 30%.

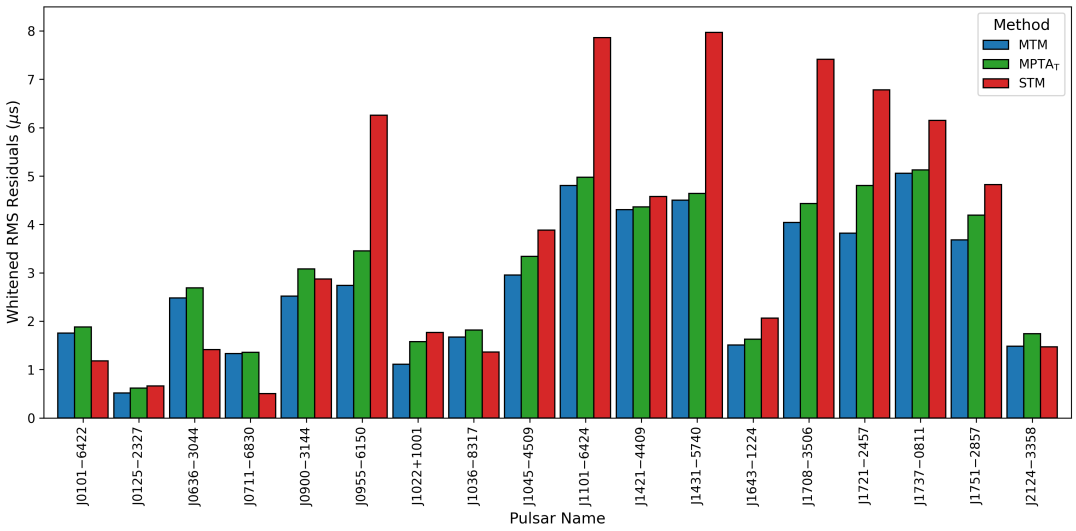

Figure 4.1: Comparison of whitened RMS residuals across all three ToA estimation methods (MTM, STM, and $\mathrm{MPTA_T}$), highlighting the 18 pulsars where MTM yields lower residuals than $\mathrm{MPTA_T}$.

A subset of pulsars exhibit unexpectedly better performance under the STM method compared to both MTM and MPTA$_{\mathrm{T}}$. As shown in Figure 4.2, PSRs J0030+0451, J0636−3044, J0711−6830, J1036−8317, and J2124−3358 report notably lower whitened RMS residuals when analyzed using STM. Additional cases with similar behavior include PSRs J0101−6422, J2222−0137, J2236−5527, J2322+2057, and J2322−2650. For these pulsars, STM also produces substantially lower pre-fit RMS residuals, suggesting a closer initial match to the profile data despite its simpler approach. The reasons for this unexpected performance remain unclear. It may be related to the noise characteristics or profile morphology of these sources, and we plan to investigate these cases further in future work.

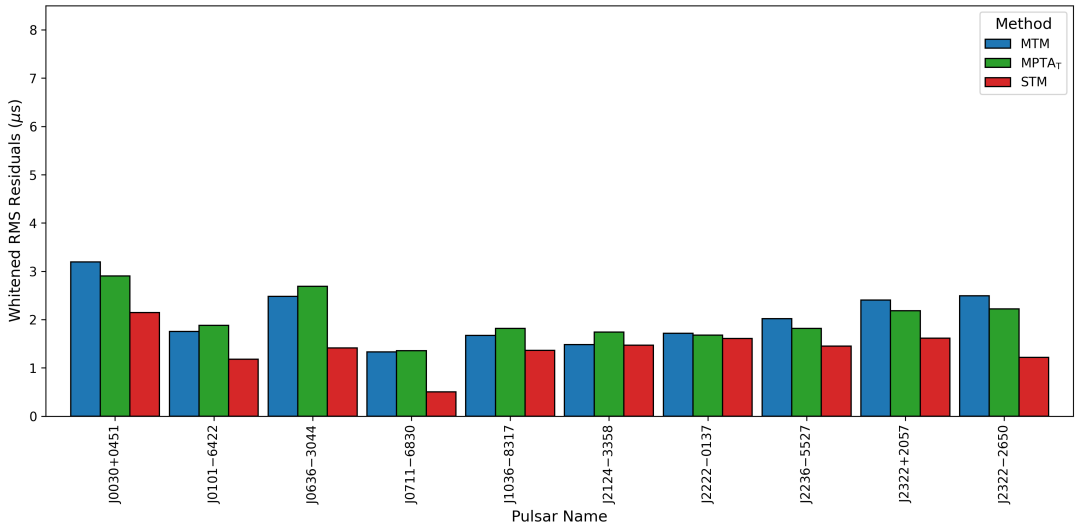

Figure 4.2: Bar plot of whitened RMS residuals for pulsars where STM outperformed both MTM and MPTA$_{\mathrm{T}}$.

To compare the distribution of whitened RMS residuals, Figure 4.3 presents the density distribution for all three methods. The MTM and STM methods show broader distributions and higher variability, which may reflect greater sensitivity to template fidelity and profile structure. In contrast, the MPTA$_{\mathrm{T}}$ method uses frequency-resolved templates generated with PULSEPORTRAITURE [Pennucci, 2019], which explicitly models profile evolution across frequency. This capability is expected to improve

the alignment of pulse profiles across sub-bands, particularly in the presence of DM variations, although we do not directly quantify its impact on DM correction in this work.

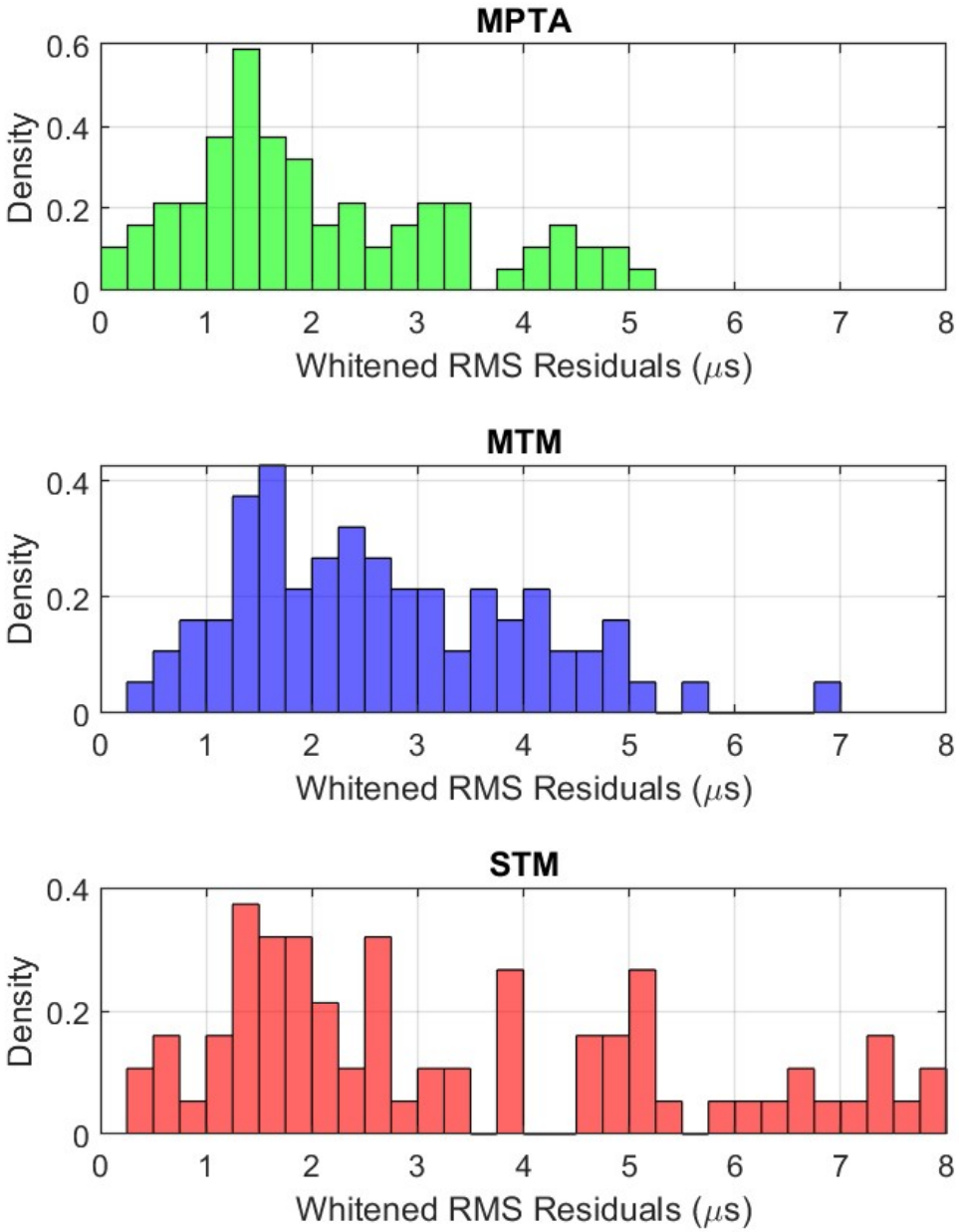

Figure 4.3: Density distribution of whitened RMS residuals for each method.

4.4.2 Noise Model Analysis

To better understand the white noise behavior across methods, Figures 4.4–4.7 show the reported EFAC and EQUAD values alongside the whitened RMS residuals for each pulsar. Comparisons are made between MTM and $\mathrm{MPTA_T}$ (EFAC and EQUAD in Figures 4.4 and 4.6), and between MTM and STM (Figures 4.5 and 4.7).

Overall, $\mathrm{MPTA_T}$ achieves EFAC values close to 1 and EQUAD values near zero for most pulsars, indicating a well-calibrated white noise model. In contrast, MTM and STM generally report larger EFAC and EQUAD values, particularly in cases where they underperform relative to $\mathrm{MPTA_T}$. The STM method, in particular, exhibits a broader EQUAD distribution, suggesting greater variability or unmodeled noise.

These elevated EFAC and EQUAD values in the MTM and STM results suggest the presence of additional white noise components in the data. This could arise from mismatches between the high-S/N templates and the actual observations (e.g., if the template fails to fully represent profile evolution or pulse shape variability across frequency or time). Inaccuracies due to residual polarization calibration errors could also contribute to this increased noise.

The correlation matrices for noise parameters, shown in Figures 4.8, 4.9, and 4.10 show the pairwise correlations between noise model parameters across the analyzed pulsar population (excluding the small number of pulsars omitted from the main results as described earlier; see Appendix 4.9).

For $\mathrm{MPTA_T}$, no strong correlations are observed between most parameters, except for a moderate anti-correlation between EFAC and EQUAD, also visible in STM. This anti-correlation is weaker for MTM, possibly indicating that MTM better captures unmodeled white noise, reducing the need for EFAC and EQUAD to trade off against each other. STM also shows a strong positive correlation between EQUAD and whitened RMS residuals. This may reflect increased levels of unmodeled noise in STM, or a

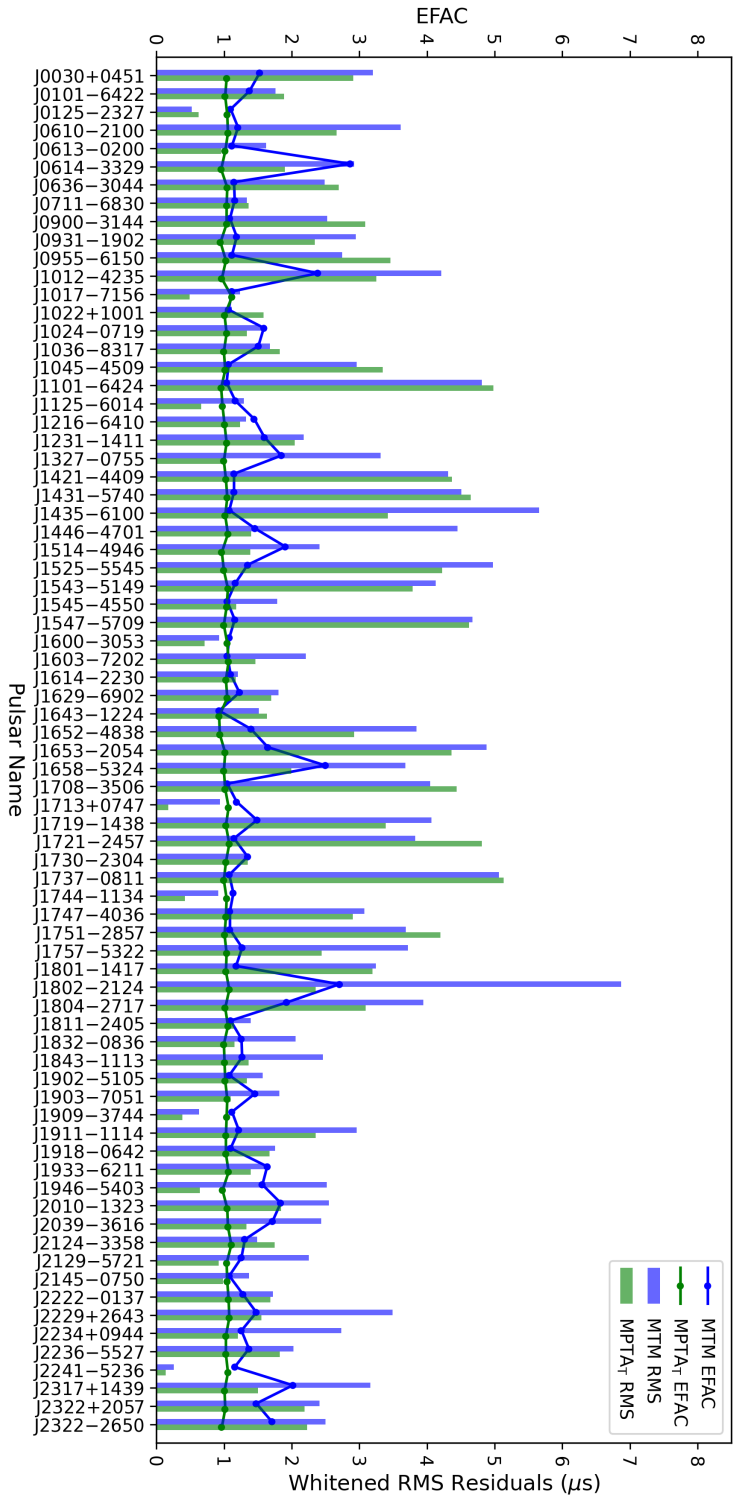

Figure 4.4: Plot of each pulsar's reported EFAC (dots) and whitened RMS residuals (bars) for MTM (blue) and MPTA$_{\mathrm{T}}$ (green).

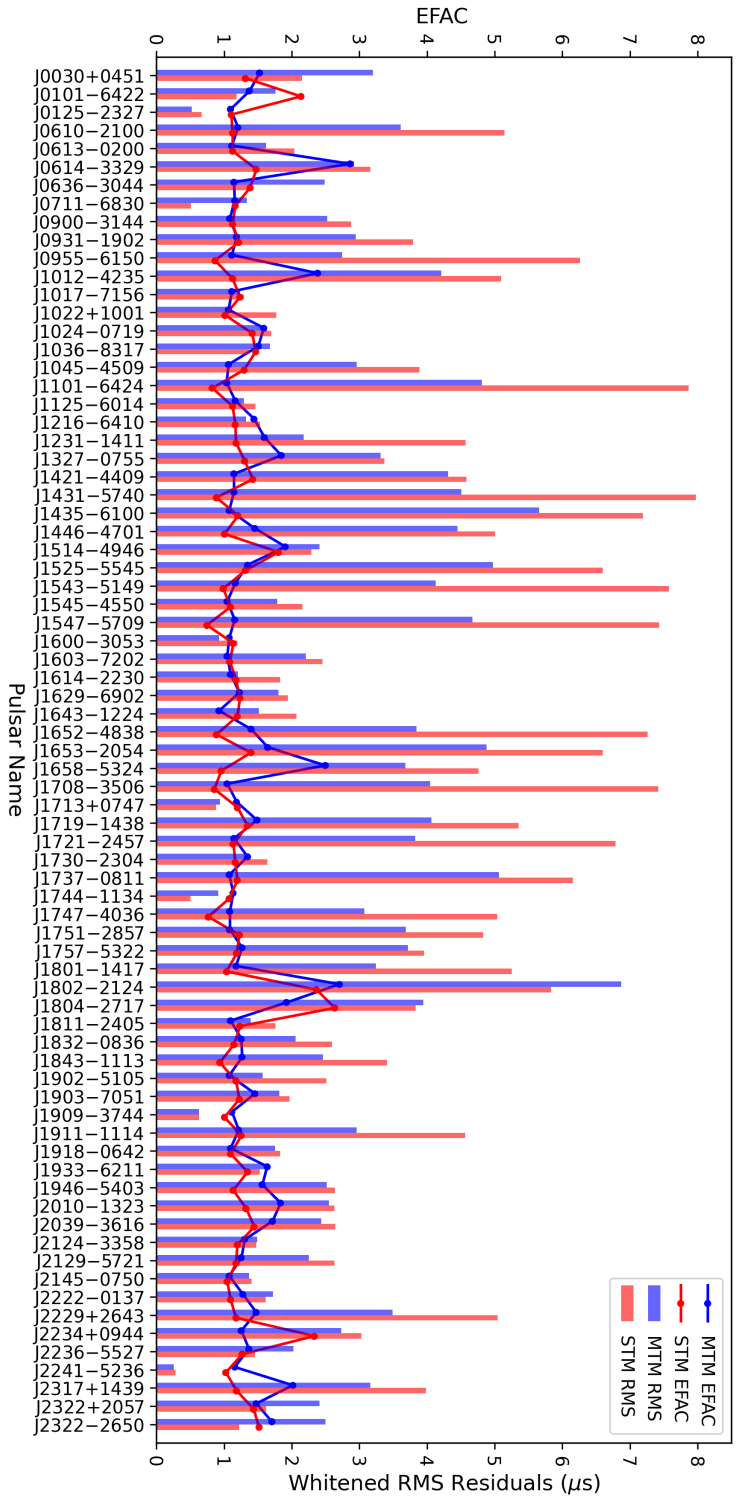

Figure 4.5: Plot of each pulsar's reported EFAC (dots) and whitened RMS residuals (bars) for MTM (blue) and STM (red).

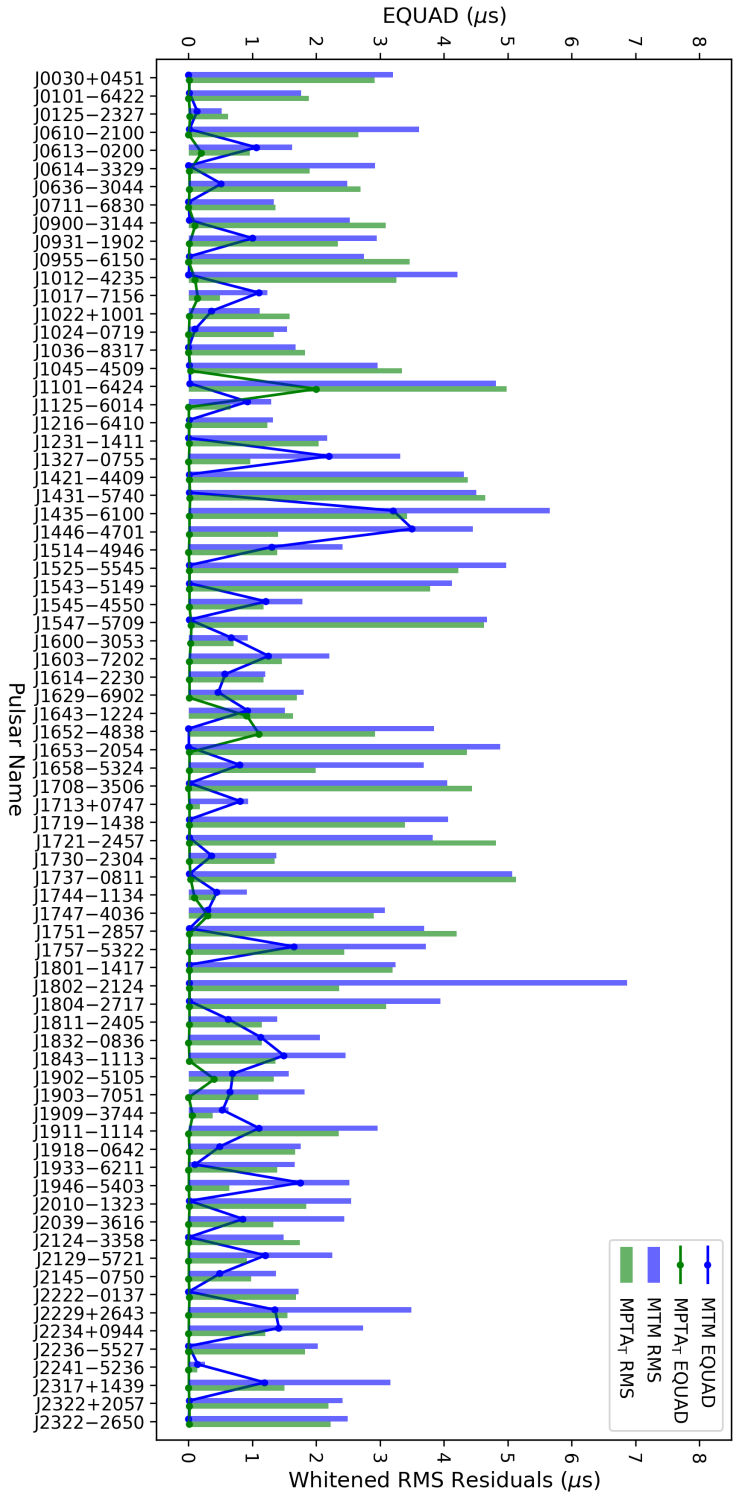

Figure 4.6: Plot of each pulsar's reported EQUAD (dots) and whitened RMS residuals (bars) for MTM (blue) and MPTA$_{\mathrm{T}}$ (green).

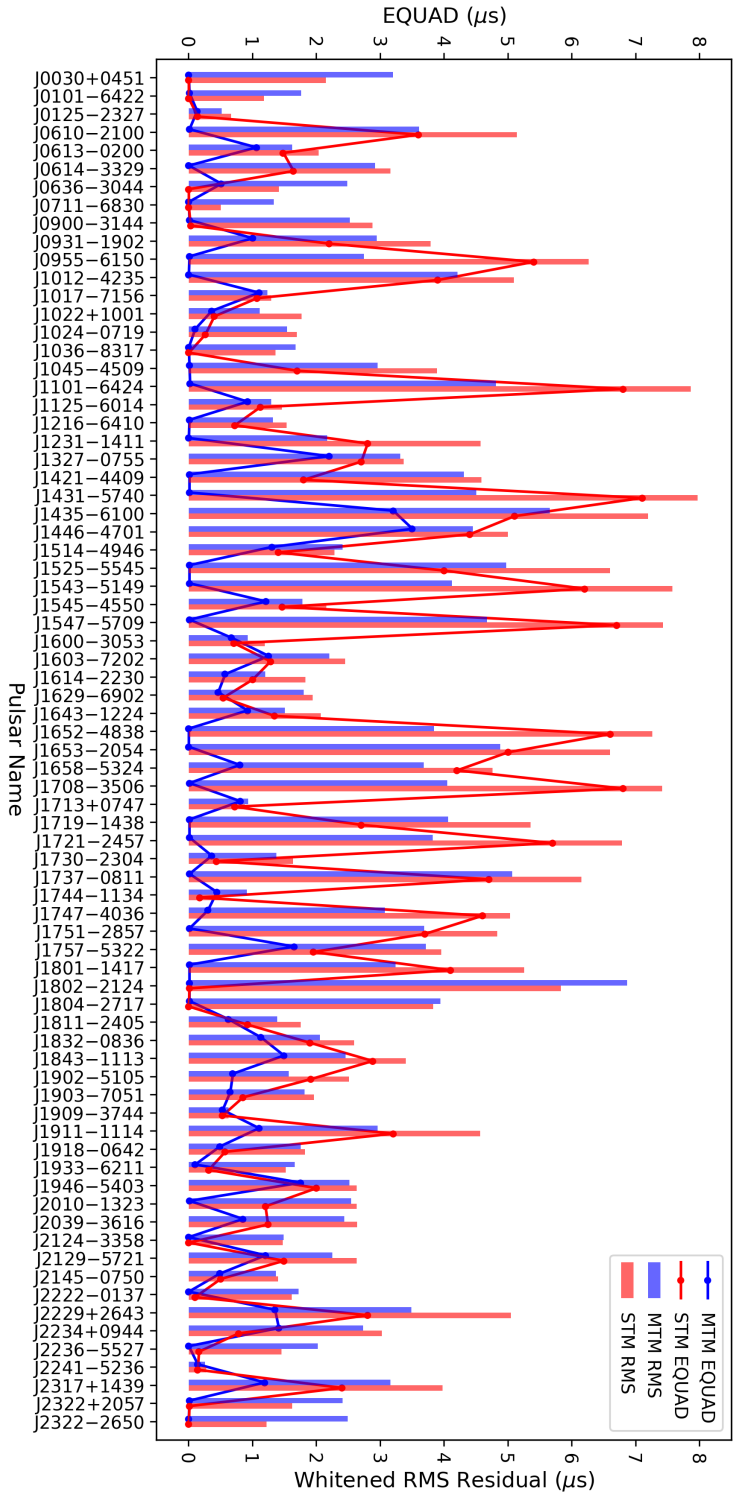

Figure 4.7: Plot of each pulsar's reported EQUAD (dots) and whitened RMS residuals (bars) for MTM (blue) and STM (green).

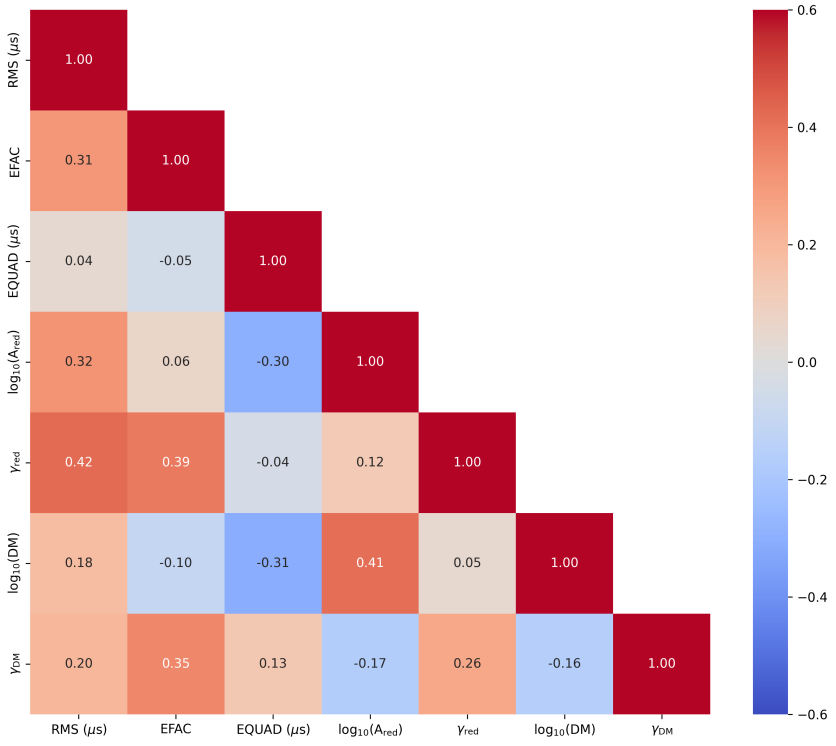

Figure 4.8: Correlation matrix of noise parameters for the MTM method.

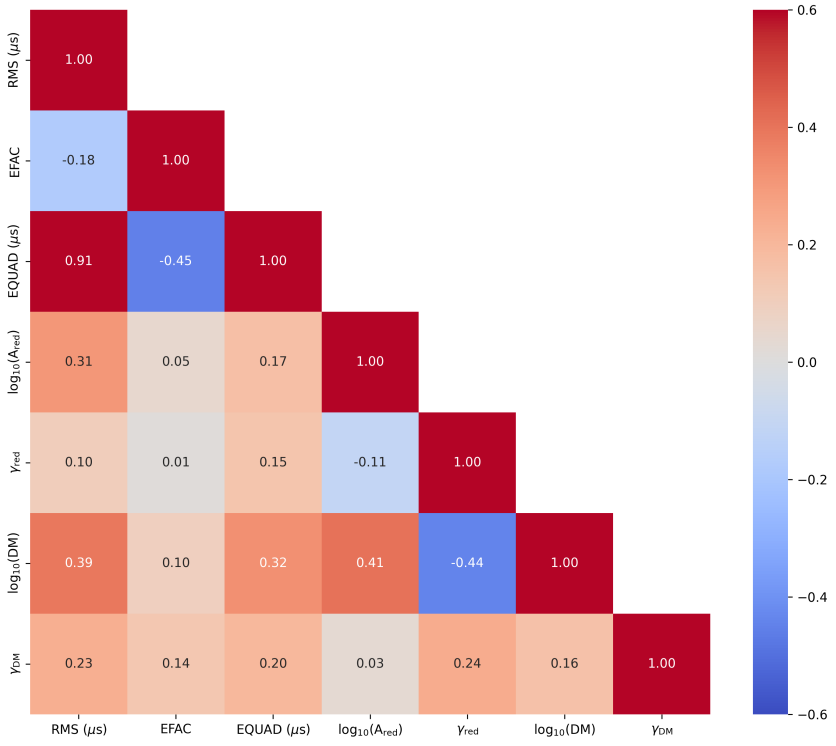

Figure 4.9: Correlation matrix of noise parameters for the STM method.

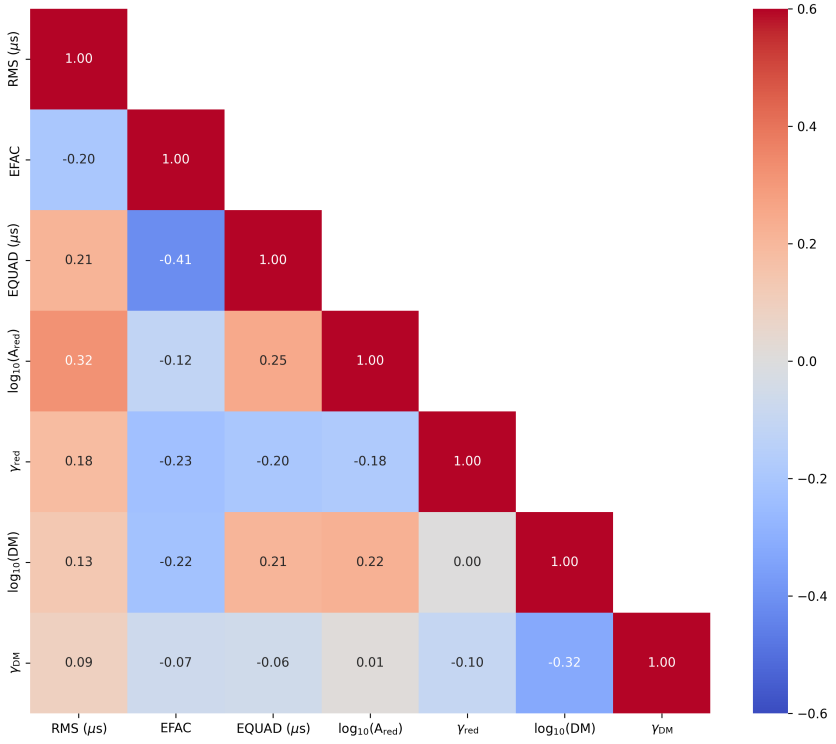

Figure 4.10: Correlation matrix of noise parameters for the MPTA$_{\mathrm{T}}$ method (excluding omitted pulsars).

poorer match between its templates and the true pulse profiles, leading to a larger EQUAD to account for excess variance.

STM additionally exhibits a moderate anti-correlation between $\log_{10}(\mathrm{DM})$ and γ_{red}, which may indicate a tendency to attribute long-timescale variability to DM noise rather than red noise. For several pulsars (e.g., J0030+0451, J0101−6422, J1653−2054, J2317−1439, and J2322−2650; see Table 4.8), STM favors higher $\log_{10}(\mathrm{DM})$ values, while MTM and MPTA$_{\mathrm{T}}$ either show no such preference or instead prefer red noise contributions. STM also shows moderate correlations between $\log 10(\mathrm{DM})$ and both $\log_{10}(A_{\mathrm{red}})$ and whitened RMS residuals, supporting the possibility that it is more sensitive to degeneracies between these noise components, potentially due to limitations in noise modeling or template fidelity.

Both STM and MTM show moderate correlation between $\log_{10}(A_{\mathrm{red}})$ and $\log_{10}(A_{\mathrm{DM}})$, suggesting that for some pulsars, it may be difficult to disentangle chromatic DM noise from achromatic red noise. In contrast, MPTA$_{\mathrm{T}}$ uses frequency-dependent templates generated with PULSEPORTRAITURE, which help to better model dispersive delays across the observing band (see §4.3.3 and §1.3.2). This likely explains the weaker correlation observed in the MPTA$_{\mathrm{T}}$ results. For MTM, a moderate correlation is also seen between γ_{red} and both EFAC and the whitened RMS residuals. While this may suggest greater sensitivity to the spectral slope of red noise, it should not be interpreted as causal. These trends could arise from differences in how unmodeled noise is absorbed into EFAC or residuals depending on the ToA estimation method and template characteristics.

A more detailed comparison of the DM noise terms across methods—particularly $\log_{10}(A_{\mathrm{DM}})$ and γ_{DM}—may further clarify these differences. These parameters are reported for each pulsar in the appendix (Table 4.8), allowing direct comparison of how DM noise is modeled under each approach.

4.5 Discussion

This study provides a comprehensive performance evaluation of noise models derived using TEMPONEST [Lentati et al., 2014], comparing three primary methods for ToA estimation:

1. MTM with high-S/N profiles as templates,
2. STM using the same high-S/N templates as MTM, and
3. MPTA$_{\rm T}$, which uses frequency-dependent templates generated by PULSEPORTRAITURE.

Tables 4.5 and 4.6 present summary statistics for the pre-fit and whitened RMS residuals (excluding pulsars omitted from the main analysis; see Appendix 4.9). MPTA$_{\rm T}$ demonstrates the best overall performance, achieving the lowest mean and standard deviation of whitened RMS residuals. The likely explanation for this is its use of frequency-dependent templates, which better model pulse profile evolution across the wide ~ 900 MHz bandwidth used for MeerKAT L-band observations. While Jones matrices are applied for polarization calibration, they correct instrumental effects but do not capture intrinsic pulse evolution. The PULSEPORTRAITURE-generated templates account for this frequency-dependent evolution, mitigating errors that could otherwise propagate into ToA estimates and affect noise modeling. This is particularly important given that the MeerKAT L-band bandwidth is roughly 50% larger than that used in typical PTA experiments, making two-dimensional (frequency and phase) modeling essential.

In theory, STM and MPTA$_{\rm T}$ should produce comparable results—they use the same underlying data and differ only in template construction. However, for most pulsars, STM results in larger residuals and elevated EQUAD values compared to MPTA$_{\rm T}$. This suggests that the high-S/N templates used by STM are insufficient to model

Metric	MPTA_T	MTM	STM
Mean	2.3	2.9	3.7
Std Dev	1.4	1.4	2.3
Min	0.17	0.27	0.29
Max	6.31	7.08	9.36

Table 4.5: Pre-fit RMS Residuals (μs)

Metric	MPTA_T	MTM	STM
Mean	2.1	2.7	3.4
Std Dev	1.3	1.4	2.1
Min	0.13	0.25	0.27
Max	5.12	6.86	7.97

Table 4.6: Whitened RMS Residuals (μs)

profile evolution, especially over wide bandwidths. While such templates preserve integrated pulse shape, they cannot accommodate frequency-dependent changes in pulse morphology, leading to increased white noise contributions in the timing residuals. In contrast, MPTA_T's frequency-dependent templates effectively track pulse evolution and improve sensitivity to dispersive delays, which in turn reduces apparent DM noise. The observed differences between STM and MPTA_T emphasize the critical role of template design in achieving high-precision wideband timing.

Among the 75 pulsars analyzed, MTM produced improved whitened RMS residuals compared to STM in 65 cases (87%), and outperformed MPTA_T in 18 cases (24%). That MTM generally outperforms STM is consistent with previous findings (e.g., Rogers et al. 2024), reflecting the benefits of using MTM. However, MPTA_T still delivers better results in the majority of cases, indicating limitations in MTM's reliance on high-S/N templates for this analysis. MTM's broader distribution of whitened RMS residuals (Figure 4.3) reflects increased variability across the pulsar population, although the average reductions in timing residuals (Table 4.7) are similar to those of MPTA_T. This suggests that the excess noise in MTM is primarily white in nature. In a few pulsars,

application of the noise model resulted in increased whitened RMS residuals (by 20–140 ns), possibly due to inadequate modeling or imperfections in the timing solution.

Metric	**MPTA$_{\rm T}$**	**MTM**	**STM**
Mean	0.2	0.2	0.3
Min	-0.14	-0.02	-0.08
Max	1.67	1.72	1.51

Table 4.7: Reduction: pre-fit RMS residuals - whitened RMS residuals (μs).

Both MTM and STM show elevated whitened RMS residuals and EQUAD values, suggesting the presence of additional unmodeled white noise. This could arise from a combination of calibration errors, intrinsic pulsar variability (such as jitter), or mismatches between the templates and the observed data. While it's difficult to isolate the exact source of this excess noise, correlations between noise parameters point to complex dependencies. For example, MTM shows a stronger relationship between $\gamma_{\rm red}$ and EFAC, as well as with whitened residuals, potentially indicating that MTM is more responsive to the spectral characteristics of red noise. In contrast, the larger EQUAD values seen in STM may reflect broader mismatches due to its inability to model frequency-dependent pulse profile evolution.

While MTM does not match the overall performance of MPTA$_{\rm T}$, it consistently outperforms STM in most cases. As a ToA estimation method, MTM makes use of full polarization information and high-S/N templates to deliver more precise ToAs than STM. However, the use of frequency-averaged templates can limit its effectiveness in wideband data, such as that from MeerKAT, where pulse profiles evolve significantly with frequency. The elevated white noise parameters observed in MTM results are likely due to unmodeled frequency-dependent effects, not deficiencies in the method itself. In contrast, MPTA$_{\rm T}$ incorporates frequency-dependent templates that better account for such evolution, leading to improved timing precision. Future work applying a combined use of MTM and frequency-dependent templates may leverage the strengths of both

approaches for enhanced timing performance.

4.6 Conclusion

This study provides a comparative evaluation of MTM, STM, and MPTA$_{\rm T}$ methods for pulsar timing, highlighting their strengths and limitations across a dataset of 75 high-priority pulsars regularly observed as part of the MeerTime project. While MTM achieved improved whitened residuals in 18 pulsars (24%) over MPTA$_{\rm T}$, these cases represent a minority. The overall performance of MTM, with higher mean whitened RMS residuals (2.7 μs vs. 3.1 μs for MPTA$_{\rm T}$) and a slightly broader spread in the data (standard deviation of 1.4 μs compared to 1.3 μs), underscores its limitations relative to the frequency-dependent template approach used by MPTA$_{\rm T}$.

Despite these differences, MTM and MPTA$_{\rm T}$ achieved comparable reductions in residuals on a per-pulsar basis, suggesting that the additional noise present in MTM results is predominantly white rather than red. This is supported by the consistently higher EFAC and EQUAD values observed in both MTM and STM, which point to the presence of unmodeled white or systematic noise—possibly arising from residual polarization calibration errors or the limitations of using high-S/N, frequency-averaged templates. By contrast, MPTA$_{\rm T}$'s use of frequency-dependent templates from PULSE-PORTRAITURE appears to better model pulse shape evolution across wide bandwidths, and, when combined with MCMC-derived uncertainty estimates, likely results in more accurate ToAs and uncertainty characterization. The elevated white noise parameters observed in MTM may also reflect the challenges of working with full-polarization data, which, while offering richer information, is more susceptible to calibration imperfections than total intensity profiles alone. These calibration issues, and their potential contribution to systematic noise in MTM and STM, were not fully explored in earlier chapters and merit closer investigation.

Future analyses should examine the polarization calibration pipeline used in MeerTime and its influence on MTM performance. Additionally, applying a combined use of MTM and frequency-dependent templates from PULSEPORTRAITURE in future work may overcome the limitations identified here, offering a pathway to improved timing precision for future pulsar timing studies and advancing the precision of the IPTA.

4.7 Appendix

4.7.1 Noise Model Results

Table 4.8: Included in this table for each pulsar (PSR Name) are the analysis method used (Method) and the noise characteristics of the pulsar's timing residuals. Specifically, we provide the pre-fit RMS of the timing residuals (Full, μs) and the equivalent post-fit RMS after subtracting the maximum-likelihood realization of the noise processes (White, μs). The table also includes the noise model identifier (M_N) and key noise parameters: the EFAC (EF), EQUAD (EQ, μs), and SECORR (EC, μs) values, which describe the scaling of TOA uncertainties, additional white noise, and epoch-dependent correlated noise, respectively. For parameters characterizing time-correlated noise processes, such as the amplitude and spectral index of the red noise ($\log_{10} A_{red}$, γ_{red} and DM variations ($\log_{10} A_{DM}$, γ_{DM}, we report the median reported values and associated uncertainties. Finally, the NIS is provided as a measure of the goodness-of-fit for each method and model. Values marked with a dash ("-") indicate that the corresponding parameter was not applicable or not constrained for that pulsar.

PSR Name	Method	M_N	Full	White	EF	EQ	EC	$\log_{10} A_{red}$	γ_{red}	$\log_{10} A_{DM}$	γ_{DM}	NIS
J0030+0451	$MPTA_E$	1	2.829	-	1.03	0.36	-	-	-	-	-	-
J0030+0451	$MPTA_T$	2	2.905	2.905	1.03(1)	0.01(3)	0.01(3)	-	-	-	-	3.40E+04
J0030+0451	MTM	1	3.193	3.193	1.52(2)	0.00(1)	-	-	-	-	-	3.36E+04
J0030+0451	STM	4	2.176	2.148	1.31(2)	0.00(1)	-	-	-	-11.6(9)	2.6(9)	3.43E+04
J0101−6422	$MPTA_E$	1	1.878	-	0.99	-	-	-	-	-	-	-
J0101−6422	$MPTA_T$	1	1.878	1.878	1.01(2)	0.00(1)	-	-	-	-	-	1.72E+04
J0101−6422	MTM	1	1.756	1.756	1.37(3)	0.01(2)	-	-	-	-	-	1.71E+04
J0101−6422	STM	4	1.297	1.179	2.13(4)	0.00(0)	-	-	-	-11.0(1)	2.0(6)	1.70E+04
J0125−2327	$MPTA_E$	6	0.654	-	1.04	0.10	0.17	-	-	-13.34	1.64	-
J0125−2327	$MPTA_T$	8	0.711	0.617	1.04(2)	0.02(3)	-	-14(1)	0.9(8)	-11.9(2)	3(1)	4.16E+04
J0125−2327	MTM	8	0.612	0.512	1.09(2)	0.13(2)	-	-15(2)	2(1)	-11.8(2)	2(1)	4.20E+04
J0125−2327	STM	8	0.762	0.633	1.10(2)	0.14(2)	-	-14(2)	2(1)	-11.7(1)	2.3(7)	4.14E+04
J0610−2100	$MPTA_E$	4	2.720	-	1.05	-	-	-	-	-13.00	1.98	-
J0610−2100	$MPTA_T$	4	2.720	2.654	1.05(1)	0.00(1)	-	-	-	-11.4(1)	2.0(4)	3.25E+04
J0610−2100	MTM	4	3.706	3.605	1.20(2)	0.01(4)	-	-	-	-10.9(1)	3.5(7)	3.19E+04
J0610−2100	STM	4	5.458	5.137	1.12(3)	3.6(1)	-	-	-	-10.6(1)	3.3(5)	3.15E+04
J0613−0200	$MPTA_E$	4	0.992	-	1.02	0.23	-	-	-	-14.06	5.96	-
J0613−0200	$MPTA_T$	6	1.042	0.952	1.01(2)	0.2(2)	0.00(1)	-	-	-11.68(9)	2.9(6)	3.96E+04
J0613−0200	MTM	4	1.670	1.617	1.11(3)	1.06(3)	-	-	-	-12.0(3)	3.8(9)	3.88E+04
J0613−0200	STM	4	2.120	2.032	1.12(4)	1.48(5)	-	-	-	-11.16(9)	4.3(7)	3.80E+04
J0614−3329	$MPTA_E$	4	1.922	-	0.95	-	-	-	-	-13.46	2.35	-
J0614−3329	$MPTA_T$	4	1.926	1.893	0.95(1)	0.01(1)	-	-	-	-11.7(1)	2.3(7)	4.25E+04
J0614−3329	MTM	4	2.989	2.915	2.86(4)	0.00(1)	-	-	-	-10.95(9)	4.2(7)	3.20E+04
J0614−3329	STM	4	3.341	3.157	1.47(4)	1.64(9)	-	-	-	-10.79(8)	4.4(7)	3.20E+04
J0636−3044	$MPTA_E$	4	3.067	-	1.04	-	-	-	-	-13.51	1.50	-
J0636−3044	$MPTA_T$	1	3.150	2.690	1.04(2)	0.01(3)	-	-	-	-	-	2.56E+04
J0636−3044	MTM	4	2.509	2.480	1.14(2)	0.51(9)	-	-	-	-13(2)	3(1)	2.60E+04
J0636−3044	STM	8	1.614	1.413	1.38(2)	0.00(0)	-	-14(2)	4(1)	-10.80(9)	3.8(8)	2.53E+04
J0711−6830	$MPTA_E$	1	1.372	-	1.03	-	-	-	-	-	-	-
J0711−6830	$MPTA_T$	6	1.372	1.356	1.03(1)	0.00(1)	0.03(5)	-	-	-14(2)	3(2)	3.37E+04
J0711−6830	MTM	4	1.349	1.330	1.15(2)	0.00(0)	-	-	-	-12.1(2)	2(1)	3.39E+04
J0711−6830	STM	6	0.501	0.500	1.16(2)	0.00(0)	0.02(3)	-	-	-13(2)	3(2)	3.34E+04

PSR Name	Method	M_N	Full	White	EF	EQ	EC	$\log_{10} A_{red}$	γ_{red}	$\log_{10} A_{DM}$	γ_{DM}	NIS
J0900−3144	$MPTA_E$	3	4.379	-	1.06	-	0.91	-12.57	1.35	-	-	-
J0900−3144	$MPTA_T$	8	4.436	3.082	1.03(3)	0.1(2)	-	-12.20(9)	2.6(4)	-10.86(8)	1.8(2)	3.92E+04
J0900−3144	MTM	8	4.038	2.519	1.08(1)	0.01(2)	-	-12.25(9)	2.8(5)	-10.87(7)	1.8(2)	3.97E+04
J0900−3144	STM	8	4.133	2.872	1.12(2)	0.03(8)	-	-12.4(1)	3.0(5)	-10.66(7)	2.0(2)	3.93E+04
J0931−1902	$MPTA_E$	1	2.335	-	0.94	-	-	-	-	-	-	-
J0931−1902	$MPTA_T$	1	2.335	2.335	0.94(2)	0.01(1)	-	-	-	-	-	2.25E+04
J0931−1902	MTM	4	2.956	2.939	1.18(2)	1.0(1)	-	-	-	-14(2)	4(2)	2.25E+04
J0931−1902	STM	6	4.174	3.787	1.21(4)	2.2(1)	0.01(2)	-	-	-10.63(9)	2.9(5)	2.19E+04
J0955−6150	$MPTA_E$	4	3.672	-	1.02	0.60	-	-	-	-12.74	2.08	-
J0955−6150	$MPTA_T$	4	3.746	3.454	1.02(1)	0.0(1)	-	-	-	-11.10(8)	2.2(3)	7.22E+04
J0955−6150	MTM	4	3.111	2.739	1.11(1)	0.01(1)	-	-	-	-11.03(9)	2.7(5)	3.89E+04
J0955−6150	STM	8	6.783	6.260	0.86(3)	5.4(1)	-	-13(2)	2(1)	-10.7(1)	4.2(8)	3.74E+04
J1012−4235	$MPTA_E$	4	3.258	-	0.95	0.60	-	-	-	-13.86	1.68	-
J1012−4235	$MPTA_T$	4	3.375	3.246	0.96(2)	0.1(2)	-	-	-	-11.5(2)	3.1(9)	3.43E+04
J1012−4235	MTM	4	4.468	4.203	2.38(3)	0.00(1)	-	-	-	-10.54(8)	4.2(7)	3.36E+04
J1012−4235	STM	6	5.404	5.089	1.12(4)	3.9(1)	0.01(1)	-	-	-10.63(9)	4.0(7)	3.33E+04
J1017−7156	$MPTA_E$	5	0.909	-	1.10	0.14	0.21	-13.28	1.63	-	-	-
J1017−7156	$MPTA_T$	8	0.943	0.485	1.11(2)	0.14(4)	-	-13.2(1)	1.6(3)	-11.30(7)	1.9(2)	4.53E+04
J1017−7156	MTM	8	1.477	1.229	1.11(6)	1.10(2)	-	-16(2)	3(2)	-11.34(8)	2.2(2)	4.31E+04
J1017−7156	STM	8	1.527	1.288	1.23(5)	1.07(2)	-	-15(2)	3(1)	-11.32(8)	2.3(2)	4.29E+04
J1022+1001	$MPTA_E$	6	1.387	-	1.00	-	1.37	-	-	-13.11	0.83	-
J1022+1001	$MPTA_T$	6	1.431	1.575	1.00(1)	0.01(2)	0.45(5)	-	-	-11.3(1)	0.7(3)	3.67E+04
J1022+1001	MTM	6	1.340	1.109	1.06(2)	0.36(2)	0.27(3)	-	-	-11.3(1)	0.8(3)	3.75E+04
J1022+1001	STM	6	1.689	1.767	1.01(2)	0.40(3)	0.44(4)	-	-	-11.3(1)	0.7(3)	3.64E+04
J1024−0719	$MPTA_E$	6	1.337	-	1.03	-	0.14	-	-	-14.51	5.98	-
J1024−0719	$MPTA_T$	4	1.337	1.332	1.03(1)	0.00(1)	-	-	-	-12.4(4)	4(1)	3.36E+04
J1024−0719	MTM	4	1.543	1.536	1.58(2)	0.1(1)	-	-	-	-12.4(4)	5(1)	3.36E+04
J1024−0719	STM	4	1.708	1.693	1.41(2)	0.26(4)	-	-	-	-12.1(3)	4(1)	3.30E+04
J1036−8317	$MPTA_E$	4	1.848	-	1.00	-	-	-	-	-13.46	1.63	-
J1036−8317	$MPTA_T$	8	1.848	1.817	0.99(2)	0.00(1)	-	-15(2)	3(2)	-13(2)	3(1)	2.50E+04
J1036−8317	MTM	8	1.854	1.669	1.50(3)	0.00(1)	-	-14(2)	3(1)	-11.09(9)	1.2(3)	2.51E+04
J1036−8317	STM	8	1.953	1.359	1.46(2)	0.00(1)	-	-12.8(4)	1.7(7)	-10.73(8)	0.9(2)	2.47E+04
J1045−4509	$MPTA_E$	4	4.961	-	1.01	0.66	-	-	-	-12.33	2.33	-
J1045−4509	$MPTA_T$	4	5.007	3.338	1.01(2)	0.03(9)	-	-	-	-10.69(7)	2.4(2)	3.81E+04
J1045−4509	MTM	4	4.676	2.956	1.06(1)	0.01(2)	-	-	-	-10.71(7)	2.5(2)	3.85E+04
J1045−4509	STM	8	4.942	3.885	1.29(3)	1.7(1)	-	-12.3(1)	2.1(4)	-10.50(9)	3.1(4)	3.76E+04
J1101−6424	$MPTA_E$	4	4.985	-	0.94	1.88	-	-	-	-12.70	1.96	-
J1101−6424	$MPTA_T$	4	5.093	4.976	0.95(3)	2(1)	-	-	-	-11.1(1)	2.3(5)	4.27E+04
J1101−6424	MTM	4	4.901	4.807	1.03(2)	0.02(7)	-	-	-	-11.1(1)	2.6(6)	3.94E+04
J1101−6424	STM	4	7.892	7.860	0.82(4)	6.8(1)	-	-	-	-10.7(1)	2.8(6)	3.80E+04
J1125−6014	$MPTA_E$	6	1.338	-	0.97	-	0.17	-	-	-13.19	4.41	-
J1125−6014	$MPTA_T$	6	1.345	0.656	0.97(2)	0.00(1)	0.04(1)	-	-	-11.47(9)	4.1(7)	3.54E+04
J1125−6014	MTM	4	1.762	1.287	1.16(4)	0.92(3)	-	-	-	-11.41(9)	4.0(7)	3.40E+04
J1125−6014	STM	6	1.964	1.458	1.12(5)	1.12(4)	0.01(1)	-	-	-11.32(9)	3.5(6)	3.37E+04
J1216−6410	$MPTA_E$	4	1.328	-	0.99	-	-	-	-	-13.17	2.53	-
J1216−6410	$MPTA_T$	8	1.328	1.232	1.00(1)	0.00(1)	-	-15(2)	4(1)	-11.53(9)	2.7(5)	4.20E+04
J1216−6410	MTM	8	1.617	1.316	1.44(2)	0.01(1)	-	-13.1(3)	3.0(9)	-10.79(7)	3.2(4)	4.18E+04

PSR Name	Method	M_N	Full	White	EF	EQ	EC	$\log_{10} A_{red}$	γ_{red}	$\log_{10} A_{DM}$	γ_{DM}	NIS
J1216−6410	STM	8	1.754	1.527	1.16(3)	0.72(6)	-	-13.0(2)	3.1(9)	-10.89(7)	2.7(3)	4.13E+04
J1231−1411	$MPTA_E$	1	2.000	-	1.04	-	-	-	-	-	-	-
J1231−1411	$MPTA_T$	4	2.053	2.035	1.03(2)	0.01(1)	-	-	-	-14(3)	2(2)	2.50E+04
J1231−1411	MTM	4	2.180	2.168	1.59(2)	0.00(1)	-	-	-	-13(2)	3(2)	2.52E+04
J1231−1411	STM	1	4.588	4.566	1.17(4)	2.8(1)	-	-	-	-	-	2.43E+04
J1327−0755	$MPTA_E$	1	1.243	-	0.99	-	-	-	-	-	-	-
J1327−0755	$MPTA_T$	5	1.244	0.964	0.99(3)	0.00(1)	0.1(2)	-15(2)	2(2)	-	-	9.70E+03
J1327−0755	MTM	6	3.453	3.310	1.84(9)	2.2(1)	0.1(3)	-	-	-15(3)	3(2)	9.25E+03
J1327−0755	STM	6	3.975	3.362	1.3(1)	2.7(1)	0.6(3)	-	-	-12(2)	3(1)	9.25E+03
J1421−4409	$MPTA_E$	4	4.317	-	1.03	-	-	-	-	-13.32	2.25	-
J1421−4409	$MPTA_T$	4	4.399	4.363	1.02(1)	0.01(4)	-	-	-	-11.8(3)	3(1)	3.43E+04
J1421−4409	MTM	4	4.393	4.305	1.14(1)	0.01(2)	-	-	-	-11.0(1)	3.2(7)	3.43E+04
J1421−4409	STM	4	5.270	4.580	1.42(4)	1.8(3)	-	-	-	-10.36(7)	2.8(4)	3.37E+04
J1431−5740	$MPTA_E$	8	6.242	-	1.03	-	-	-12.52	2.63	-12.20	2.32	-
J1431−5740	$MPTA_T$	8	6.306	4.639	1.04(2)	0.02(6)	-	-12.3(1)	2.7(6)	-10.49(8)	2.6(3)	3.63E+04
J1431−5740	MTM	8	5.915	4.503	1.14(2)	0.01(1)	-	-12.3(2)	2.6(5)	-10.48(8)	2.6(3)	3.64E+04
J1431−5740	STM	8	9.356	7.967	0.88(4)	7.1(1)	-	-12.4(2)	3.4(8)	-10.31(7)	3.1(4)	3.49E+04
J1435−6100	$MPTA_E$	4	3.430	-	1.01	-	-	-	-	-13.22	1.43	-
J1435−6100	$MPTA_T$	4	3.470	3.415	1.01(1)	0.01(4)	-	-	-	-11.5(1)	1.2(3)	4.71E+04
J1435−6100	MTM	1	5.655	5.651	1.07(3)	3.2(2)	-	-	-	-	-	3.87E+04
J1435−6100	STM	1	7.229	7.189	1.20(5)	5.1(2)	-	-	-	-	-	3.79E+04
J1446−4701	$MPTA_E$	2	1.390	-	1.05	-	0.23	-	-	-	-	-
J1446−4701	$MPTA_T$	2	1.395	1.395	1.05(2)	0.01(1)	0.05(4)	-	-	-	-	2.75E+04
J1446−4701	MTM	1	4.472	4.447	1.45(7)	3.5(1)	-	-	-	-	-	2.58E+04
J1446−4701	STM	1	5.333	4.998	1.00(6)	4.4(1)	-	-	-	-	-	2.55E+04
J1514−4946	$MPTA_E$	1	1.481	-	0.97	-	-	-	-	-	-	-
J1514−4946	$MPTA_T$	1	1.481	1.380	0.96(3)	0.00(1)	-	-	-	-	-	8.76E+03
J1514−4946	MTM	8	2.630	2.405	1.90(8)	1.3(1)	-	-16(2)	3(2)	-10.9(1)	3.1(8)	8.56E+03
J1514−4946	STM	7	3.794	2.281	1.8(1)	1.4(2)	0.00(1)	-12.7(4)	4(1)	-10.28(9)	3.8(6)	8.49E+03
J1525−5545	$MPTA_E$	6	4.630	-	0.99	-	1.53	-	-	-12.38	2.23	-
J1525−5545	$MPTA_T$	7	4.646	4.218	0.99(1)	0.01(3)	0.9(5)	-12.6(3)	3(1)	-10.59(6)	1.4(2)	1.12E+05
J1525−5545	MTM	7	5.817	4.969	1.34(2)	0.01(2)	0.1(3)	-12.1(3)	2.5(8)	-10.19(9)	2.1(2)	3.49E+04
J1525−5545	STM	7	7.393	6.593	1.31(5)	4.0(2)	0.0(1)	-12.0(8)	2.3(6)	-10.22(9)	2.1(3)	3.41E+05
J1543−5149	$MPTA_E$	4	3.792	-	1.05	-	-	-	-	-13.58	2.35	-
J1543−5149	$MPTA_T$	4	3.792	3.781	1.05(1)	0.01(1)	-	-	-	-15(3)	3(2)	3.09E+04
J1543−5149	MTM	4	4.133	4.119	1.16(2)	0.01(1)	-	-	-	-14(3)	3(2)	3.08E+04
J1543−5149	STM	1	7.660	7.571	0.98(4)	6.2(1)	-	-	-	-	-	2.99E+04
J1545−4550	$MPTA_E$	6	1.184	-	1.03	-	0.19	-	-	-13.21	1.61	-
J1545−4550	$MPTA_T$	6	1.192	1.170	1.03(1)	0.01(1)	0.04(4)	-	-	-11.6(2)	2.3(9)	6.31E+04
J1545−4550	MTM	6	1.822	1.780	1.04(3)	1.21(4)	0.00(0)	-	-	-11.7(3)	3(1)	4.24E+04
J1545−4550	STM	4	2.240	2.154	1.09(3)	1.46(5)	-	-	-	-11.4(1)	2.5(7)	4.17E+04
J1547−5709	$MPTA_E$	4	4.712	-	0.99	-	-	-	-	-13.21	1.21	-
J1547−5709	$MPTA_T$	8	4.772	4.618	0.99(2)	0.0(1)	-	-12.8(5)	3(1)	-15(3)	3(2)	3.32E+04
J1547−5709	MTM	4	4.966	4.668	1.15(2)	0.01(2)	-	-	-	-10.53(8)	3.8(5)	3.32E+04
J1547−5709	STM	4	8.016	7.424	0.74(4)	6.7(1)	-	-	-	-10.27(8)	3.7(5)	3.21E+04
J1600−3053	$MPTA_E$	4	0.850	-	1.01	0.15	-	-	-	-13.26	3.03	-
J1600−3053	$MPTA_T$	7	0.865	0.704	1.04(3)	0.03(7)	0.01(2)	-13(1)	2.5(9)	-11.40(7)	2.4(3)	4.20E+04

PSR Name	Method	M_N	Full	White	EF	EQ	EC	$\log_{10} A_{red}$	γ_{red}	$\log_{10} A_{DM}$	γ_{DM}	NIS
J1600−3053	MTM	4	1.099	0.920	1.07(4)	0.67(3)	-	-	-	-11.45(8)	2.6(3)	4.11E+04
J1600−3053	STM	4	1.195	1.188	1.13(4)	0.71(3)	-	-	-	-11.41(9)	2.6(3)	4.07E+04
J1603−7202	$MPTA_E$	6	1.524	-	1.06	-	0.82	-	-	-13.21	0.85	-
J1603−7202	$MPTA_T$	6	1.524	1.456	1.06(1)	0.01(1)	0.21(2)	-	-	-11.50(9)	1.2(3)	3.82E+04
J1603−7202	MTM	6	2.225	2.199	1.04(2)	1.25(4)	0.16(2)	-	-	-11.9(4)	3(1)	3.80E+04
J1603−7202	STM	6	2.505	2.446	1.08(2)	1.28(5)	0.19(3)	-	-	-12(1)	3(1)	3.75E+04
J1614−2230	$MPTA_E$	4	1.671	-	1.02	-	-	-	-	-13.15	2.32	-
J1614−2230	$MPTA_T$	4	1.681	1.167	1.02(1)	0.01(1)	-	-	-	-11.3(1)	0.4(2)	3.84E+04
J1614−2230	MTM	4	1.775	1.199	1.09(2)	0.57(4)	-	-	-	-11.3(1)	0.4(2)	3.87E+04
J1614−2230	STM	6	2.227	1.882	1.17(3)	1.00(5)	0.18(8)	-	-	-11.2(1)	0.6(2)	3.76E+04
J1629−6902	$MPTA_E$	6	1.637	-	1.04	0.29	0.21	-	-	-14.87	5.31	-
J1629−6902	$MPTA_T$	6	1.697	1.692	1.04(2)	0.01(4)	0.04(4)	-	-	-15(2)	3(2)	3.83E+04
J1629−6902	MTM	5	1.800	1.795	1.22(2)	0.46(8)	0.03(4)	-16(2)	3(2)	-	-	3.80E+04
J1629−6902	STM	4	2.012	1.936	1.23(2)	0.54(6)	-	-	-	-11.05(8)	4.4(7)	3.75E+04
J1643−1224	$MPTA_E$	6	2.145	-	0.97	0.74	0.49	-	-	-12.68	2.11	-
J1643−1224	$MPTA_T$	7	2.149	1.628	0.92(3)	0.91(6)	0.11(5)	-12.5(1)	2.9(6)	-10.77(8)	2.7(3)	4.00E+04
J1643−1224	MTM	7	1.978	1.504	0.92(3)	0.92(5)	0.07(6)	-12.5(1)	2.8(5)	-10.76(8)	3.0(4)	4.03E+04
J1643−1224	STM	8	2.625	2.064	1.19(5)	1.34(7)	-	-12.4(1)	2.8(5)	-10.61(8)	3.0(3)	3.93E+04
J1652−4838	$MPTA_E$	5	3.559	-	0.94	1.12	0.74	-12.62	1.68	-	-	-
J1652−4838	$MPTA_T$	8	3.633	2.913	0.93(3)	1.1(5)	-	-12.7(2)	2(1)	-10.83(8)	1.5(2)	3.76E+04
J1652−4838	MTM	8	4.397	3.839	1.39(2)	0.00(1)	-	-12.5(2)	2.8(7)	-10.8(1)	1.6(3)	3.66E+04
J1652−4838	STM	8	7.983	7.256	0.88(4)	6.6(1)	-	-12.8(7)	4(1)	-10.7(1)	1.2(3)	3.50E+04
J1653−2054	$MPTA_E$	4	5.023	-	1.01	-	-	-	-	-12.47	1.75	-
J1653−2054	$MPTA_T$	4	5.023	4.353	1.01(1)	0.01(1)	-	-	-	-10.79(8)	1.7(2)	3.07E+04
J1653−2054	MTM	4	5.395	4.876	1.64(2)	0.00(1)	-	-	-	-10.62(8)	2.3(3)	3.07E+04
J1653−2054	STM	8	7.290	6.595	1.39(5)	5.0(2)	-	-12.5(6)	3(1)	-10.37(8)	2.8(4)	2.99E+04
J1658−5324	$MPTA_E$	1	2.089	-	0.99	-	-	-	-	-	-	-
J1658−5324	$MPTA_T$	1	2.089	1.985	0.99(2)	0.01(1)	-	-	-	-	-	1.40E+04
J1658−5324	MTM	1	3.680	3.676	2.49(5)	0.8(2)	-	-	-	-	-	1.35E+04
J1658−5324	STM	8	5.205	4.756	0.99(7)	4.2(1)	-	-16(2)	3(2)	-12(2)	2(1)	1.34E+04
J1708−3506	$MPTA_E$	4	4.567	-	1.03	1.53	-	-	-	-12.72	1.31	-
J1708−3506	$MPTA_T$	8	4.608	4.431	1.01(4)	0.0(1)	-	-15(2)	3(2)	-11.2(2)	1.1(3)	2.91E+04
J1708−3506	MTM	4	4.216	4.042	1.04(2)	0.01(3)	-	-	-	-10.9(1)	1.8(3)	2.93E+04
J1708−3506	STM	6	7.749	7.411	0.83(6)	6.8(1)	0.00(1)	-	-	-10.4(1)	3.7(7)	2.79E+04
J1713+0747	$MPTA_E$	1	0.165	-	1.07	0.14	-	-	-	-	-	-
J1713+0747	$MPTA_T$	6	0.179	0.170	1.06(2)	0.01(1)	0.03(1)	-	-	-14(2)	1(2)	1.79E+04
J1713+0747	MTM	1	0.943	0.930	1.18(8)	0.81(2)	-	-	-	-	-	1.67E+04
J1713+0747	STM	1	0.959	0.878	1.19(7)	0.72(2)	-	-	-	-	-	1.67E+04
J1719−1438	$MPTA_E$	4	3.385	-	1.03	-	-	-	-	-13.33	2.69	-
J1719−1438	$MPTA_T$	4	3.428	3.380	1.02(1)	0.01(2)	-	-	-	-11.7(2)	3.2(9)	3.05E+04
J1719−1438	MTM	4	4.122	4.059	1.48(2)	0.01(2)	-	-	-	-11.2(3)	3.3(9)	3.02E+04
J1719−1438	STM	4	5.673	5.350	1.34(4)	2.7(2)	-	-	-	-10.52(8)	4.5(7)	2.96E+04
J1721−2457	$MPTA_E$	4	4.929	-	1.07	-	-	-	-	-13.00	5.05	-
J1721−2457	$MPTA_T$	7	4.929	4.807	1.07(2)	0.01(2)	0.1(2)	-15(2)	3(2)	-11.4(3)	4(1)	2.43E+04
J1721−2457	MTM	8	3.970	3.818	1.14(2)	0.01(1)	-	-16(2)	3(2)	-11.1(1)	2.2(6)	2.48E+04
J1721−2457	STM	6	7.421	6.779	1.13(5)	5.7(1)	0.01(1)	-	-	-10.32(9)	3.4(6)	2.37E+04
J1730−2304	$MPTA_E$	6	1.443	-	1.02	-	0.39	-	-	-13.24	1.44	-

PSR Name	Method	M_N	Full	White	EF	EQ	EC	$\log_{10} A_{red}$	γ_{red}	$\log_{10} A_{DM}$	γ_{DM}	NIS
J1730−2304	$MPTA_T$	6	1.478	1.341	1.02(1)	0.01(1)	0.03(6)	-	-	-11.44(9)	1.4(3)	3.73E+04
J1730−2304	MTM	4	1.480	1.370	1.34(2)	0.36(4)	-	-	-	-11.48(9)	1.3(2)	3.76E+04
J1730−2304	STM	4	1.765	1.632	1.16(2)	0.43(4)	-	-	-	-11.39(9)	1.3(2)	3.69E+04
J1737−0811	$MPTA_E$	4	5.332	-	1.00	-	-	-	-	-12.74	2.06	-
J1737−0811	$MPTA_T$	4	5.414	5.124	0.99(2)	0.03(9)	-	-	-	-11.05(9)	1.9(4)	3.73E+04
J1737−0811	MTM	8	5.331	5.060	1.07(1)	0.01(3)	-	-16(2)	3(2)	-11.2(3)	3(1)	3.74E+04
J1737−0811	STM	8	6.766	6.148	1.19(4)	4.7(1)	-	-14(2)	3(1)	-10.31(8)	4.1(6)	3.67E+04
J1744−1134	$MPTA_E$	2	0.397	-	1.03	0.09	0.26	-	-	-	-	-
J1744−1134	$MPTA_T$	6	0.450	0.415	1.03(2)	0.09(1)	0.06(1)	-	-	-12.0(1)	1.3(4)	3.97E+04
J1744−1134	MTM	6	0.929	0.908	1.13(2)	0.44(1)	0.04(2)	-	-	-14(2)	3(1)	3.80E+04
J1744−1134	STM	6	0.528	0.494	1.07(2)	0.17(1)	0.06(1)	-	-	-12.0(2)	1.1(4)	3.95E+04
J1747−4036	$MPTA_E$	8	3.297	-	1.04	0.49	-	-12.72	2.86	-12.99	0.96	-
J1747−4036	$MPTA_T$	8	3.364	2.896	1.02(3)	0.3(7)	-	-12.4(1)	3.2(6)	-10.73(7)	2.2(2)	3.74E+04
J1747−4036	MTM	8	3.497	3.068	1.08(3)	0.3(7)	-	-12.4(1)	3.6(8)	-10.69(7)	2.3(2)	3.72E+04
J1747−4036	STM	8	5.396	5.031	0.76(4)	4.60(8)	-	-12.5(2)	3.3(9)	-10.71(8)	2.3(3)	3.59E+04
J1751−2857	$MPTA_E$	4	4.445	-	1.00	-	-	-	-	-12.78	2.39	-
J1751−2857	$MPTA_T$	8	4.480	4.192	1.00(1)	0.01(4)	-	-13.2(7)	4(1)	-11.1(1)	2.5(8)	3.46E+04
J1751−2857	MTM	8	3.971	3.681	1.08(2)	0.01(3)	-	-13.1(2)	4(1)	-11.1(1)	2.5(7)	3.50E+04
J1751−2857	STM	8	5.945	4.826	1.22(5)	3.7(1)	-	-12.2(2)	3.4(7)	-10.17(7)	3.2(3)	3.41E+04
J1757−5322	$MPTA_E$	2	2.412	-	1.03	-	0.32	-	-	-	-	-
J1757−5322	$MPTA_T$	2	2.436	2.437	1.03(1)	0.01(2)	0.11(6)	-	-	-	-	3.93E+04
J1757−5322	MTM	4	3.760	3.713	1.26(2)	1.65(8)	-	-	-	-15(3)	3(2)	3.79E+04
J1757−5322	STM	4	4.116	3.953	1.18(2)	1.95(9)	-	-	-	-11.5(3)	0.7(4)	3.76E+04
J1801−1417	$MPTA_E$	8	3.275	-	1.01	-	-	-12.92	3.26	-13.10	2.35	-
J1801−1417	$MPTA_T$	8	3.275	3.189	1.02(1)	0.01(2)	-	-14(2)	3(1)	-15(3)	3(2)	3.65E+04
J1801−1417	MTM	4	3.386	3.236	1.17(2)	0.01(1)	-	-	-	-10.84(8)	3.8(6)	3.65E+04
J1801−1417	STM	4	5.616	5.247	1.03(3)	4.1(1)	-	-	-	-10.49(8)	3.8(5)	3.53E+04
J1802−2124	$MPTA_E$	6	2.998	-	1.05	-	1.01	-	-	-12.47	2.72	-
J1802−2124	$MPTA_T$	7	3.009	2.350	1.07(2)	0.01(4)	0.1(2)	-12.4(1)	2.6(8)	-10.75(8)	2.0(3)	3.73E+04
J1802−2124	MTM	8	7.078	6.861	2.70(4)	0.01(1)	-	-12.7(6)	4(1)	-10.8(1)	2.9(6)	3.40E+04
J1802−2124	STM	8	6.069	5.827	2.36(3)	0.01(1)	-	-13(2)	3(1)	-10.9(4)	2.2(6)	3.44E+04
J1804−2717	$MPTA_E$	2	3.036	-	1.01	-	0.82	-	-	-	-	-
J1804−2717	$MPTA_T$	2	3.050	3.086	1.01(2)	0.01(1)	0.26(5)	-	-	-	-	1.78E+04
J1804−2717	MTM	6	3.988	3.936	1.92(4)	0.01(2)	0.03(7)	-	-	-14(3)	3(2)	1.75E+04
J1804−2717	STM	4	4.038	3.824	2.63(5)	0.00(1)	-	-	-	-10.05(1)	4.6(8)	1.65E+04
J1811−2405	$MPTA_E$	6	1.387	-	1.04	0.23	-	-	-	-13.12	2.47	-
J1811−2405	$MPTA_T$	4	1.405	1.141	1.05(1)	0.01(3)	-	-	-	-11.23(7)	1.1(1)	8.15E+04
J1811−2405	MTM	6	1.633	1.386	1.09(2)	0.62(3)	0.05(7)	-	-	-11.13(8)	1.6(3)	6.62E+04
J1811−2405	STM	7	1.934	1.751	1.23(3)	0.92(5)	0.05(8)	-13.1(9)	1.8(8)	-10.98(9)	2.1(3)	6.50E+04
J1832−0836	$MPTA_E$	4	1.510	-	0.98	-	-	-	-	-12.83	2.25	-
J1832−0836	$MPTA_T$	8	1.510	1.145	0.99(2)	0.00(1)	-	-13.8(8)	4(1)	-11.20(9)	2.3(3)	2.46E+04
J1832−0836	MTM	4	2.265	2.049	1.25(3)	1.13(6)	-	-	-	-11.04(9)	3.5(7)	2.41E+04
J1832−0836	STM	4	3.150	2.588	1.14(4)	1.90(7)	-	-	-	-10.87(8)	2.4(4)	2.37E+04
J1843−1113	$MPTA_E$	4	1.623	-	1.01	-	-	-	-	-12.94	2.70	-
J1843−1113	$MPTA_T$	4	1.658	1.356	1.00(1)	0.01(2)	-	-	-	-11.28(8)	2.7(4)	3.65E+04
J1843−1113	MTM	4	2.667	2.452	1.26(3)	1.49(6)	-	-	-	-11.2(1)	3.6(7)	3.54E+04
J1843−1113	STM	4	3.795	3.399	0.93(4)	2.88(6)	-	-	-	-11.3(1)	2.6(8)	3.46E+04

PSR Name	Method	M_N	Full	White	EF	EQ	EC	$\log_{10} A_{red}$	γ_{red}	$\log_{10} A_{DM}$	γ_{DM}	NIS
J1902−5105	$MPTA_E$	4	1.382	-	1.06	-	-	-	-	-13.29	1.51	-
J1902−5105	$MPTA_T$	8	1.451	1.328	1.01(2)	0.40(8)	-	-16(2)	3(2)	-11.50(9)	1.5(2)	4.35E+04
J1902−5105	MTM	4	1.664	1.565	1.07(2)	0.69(5)	-	-	-	-11.51(8)	1.7(2)	4.08E+04
J1902−5105	STM	6	2.537	2.507	1.17(4)	1.91(4)	0.00(0)	-	-	-10.88(8)	4.4(6)	3.98E+04
J1903−7051	$MPTA_E$	6	1.102	-	1.04	-	0.11	-	-	-13.86	2.21	-
J1903−7051	$MPTA_T$	6	1.102	1.089	1.04(1)	0.00(1)	0.01(2)	-	-	-12.0(3)	3(1)	3.55E+04
J1903−7051	MTM	2	1.817	1.812	1.45(2)	0.65(4)	0.00(1)	-	-	-	-	3.51E+04
J1903−7051	STM	6	2.005	1.959	1.22(2)	0.85(5)	0.00(1)	-	-	-13(3)	3(1)	3.47E+04
J1909−3744	$MPTA_E$	6	0.257	-	1.04	0.07	0.07	-	-	-13.60	2.04	-
J1909−3744	$MPTA_T$	7	0.310	0.375	1.03(1)	0.06(0)	0.02(0)	-13.9(2)	3(1)	-11.69(7)	2.0(2)	1.05E+05
J1909−3744	MTM	4	0.677	0.622	1.11(2)	0.53(1)	-	-	-	-11.63(8)	2.4(3)	9.78E+04
J1909−3744	STM	4	0.684	0.621	1.00(2)	0.53(1)	0.00(0)	-	-	-11.64(8)	2.3(3)	9.79E+04
J1911−1114	$MPTA_E$	1	2.402	-	1.02	-	-	-	-	-	-	-
J1911−1114	$MPTA_T$	4	2.402	2.346	1.02(2)	0.00(1)	-	-	-	-11.4(1)	2.9(8)	2.13E+04
J1911−1114	MTM	4	3.001	2.956	1.21(3)	1.1(1)	-	-	-	-11.5(4)	3.4(9)	2.12E+04
J1911−1114	STM	4	4.899	4.558	1.25(5)	3.2(1)	-	-	-	-10.6(1)	4.1(8)	2.06E+04
J1918−0642	$MPTA_E$	2	1.665	-	1.02	-	0.29	-	-	-	-	-
J1918−0642	$MPTA_T$	6	1.682	1.663	1.02(1)	0.01(2)	0.07(4)	-	-	-12.1(5)	3(1)	3.87E+04
J1918−0642	MTM	4	1.786	1.749	1.09(2)	0.49(9)	-	-	-	-11.7(1)	1.7(5)	3.87E+04
J1918−0642	STM	6	1.888	1.820	1.09(2)	0.57(6)	0.01(1)	-	-	-11.0(1)	4.0(8)	3.85E+04
J1933−6211	$MPTA_E$	6	1.409	-	1.05	-	0.26	-	-	-13.35	2.05	-
J1933−6211	$MPTA_T$	4	1.409	1.385	1.06(1)	0.00(1)	-	-	-	-11.9(1)	1.2(5)	3.50E+04
J1933−6211	MTM	8	1.674	1.660	1.63(2)	0.1(2)	-	-15(2)	4(2)	-15(3)	3(2)	3.10E+04
J1933−6211	STM	6	1.568	1.519	1.34(2)	1.31(5)	0.01(3)	-	-	-11.5(2)	1.5(6)	3.06E+04
J1946−5403	$MPTA_E$	1	0.637	-	0.97	-	-	-	-	-	-	-
J1946−5403	$MPTA_T$	2	0.637	0.638	0.97(2)	0.00(0)	0.01(2)	-	-	-	-	2.32E+04
J1946−5403	MTM	1	2.612	2.513	1.56(5)	1.75(6)	-	-	-	-	-	2.21E+04
J1946−5403	STM	1	3.066	2.629	1.13(5)	2.00(7)	-	-	-	-	-	2.20E+04
J2010−1323	$MPTA_E$	1	1.839	-	1.03	-	-	-	-	-	-	-
J2010−1323	$MPTA_T$	4	1.854	1.835	1.04(1)	0.01(2)	-	-	-	-13(2)	2(1)	3.83E+04
J2010−1323	MTM	4	2.607	2.541	1.83(2)	0.01(4)	-	-	-	-11.04(9)	4.0(7)	3.75E+04
J2010−1323	STM	4	2.709	2.625	1.32(3)	1.20(8)	-	-	-	-10.98(8)	4.6(7)	3.74E+04
J2039−3616	$MPTA_E$	1	1.303	-	1.06	-	-	-	-	-	-	-
J2039−3616	$MPTA_T$	1	1.321	1.321	1.05(2)	0.00(1)	-	-	-	-	-	2.30E+04
J2039−3616	MTM	4	2.461	2.430	1.71(3)	0.85(7)	-	-	-	-16(2)	3(2)	2.26E+04
J2039−3616	STM	8	2.885	2.636	1.44(3)	1.24(9)	-	-15(2)	3(2)	-11.0(1)	2.4(7)	2.22E+04
J2124−3358	$MPTA_E$	2	1.739	-	1.10	-	0.23	-	-	-	-	-
J2124−3358	$MPTA_T$	2	1.739	1.740	1.10(1)	0.00(1)	0.07(2)	-	-	-	-	3.80E+04
J2124−3358	MTM	4	1.496	1.482	1.30(2)	0.00(0)	-	-	-	-13(2)	2(1)	3.87E+04
J2124−3358	STM	4	1.492	1.468	1.19(2)	0.00(0)	-	-	-	-11.6(2)	2.4(6)	3.83E+04
J2129−5721	$MPTA_E$	1	0.961	-	1.03	-	-	-	-	-	-	-
J2129−5721	$MPTA_T$	8	0.961	0.910	1.03(1)	0.00(0)	-	-15(2)	4(1)	-11.9(3)	1.7(6)	3.73E+04
J2129−5721	MTM	4	2.326	2.248	1.25(2)	1.20(4)	-	-	-	-12.4(3)	4(1)	3.48E+04
J2129−5721	STM	8	2.946	2.628	1.17(2)	1.49(5)	-	-13.8(6)	5(1)	-16(2)	3(2)	3.42E+04
J2145−0750	$MPTA_E$	2	1.133	-	1.04	-	0.82	-	-	-	-	-
J2145−0750	$MPTA_T$	6	1.134	0.978	1.04(1)	0.00(0)	0.21(2)	-	-	-11.5(1)	1.1(3)	3.70E+04
J2145−0750	MTM	6	1.512	1.360	1.07(2)	0.49(2)	0.20(2)	-	-	-11.6(2)	1.1(5)	3.67E+04

PSR Name	Method	M_N	Full	White	EF	EQ	EC	$\log_{10} A_{red}$	γ_{red}	$\log_{10} A_{DM}$	γ_{DM}	NIS
J2145−0750	STM	6	1.572	1.398	1.04(2)	0.50(3)	0.21(3)	-	-	-11.6(2)	1.2(5)	3.66E+04
J2222−0137	$MPTA_E$	2	1.591	-	1.06	-	0.91	-	-	-	-	-
J2222−0137	$MPTA_T$	6	1.646	1.676	1.06(1)	0.01(1)	0.26(3)	-	-	-12(1)	3(1)	3.61E+04
J2222−0137	MTM	6	1.699	1.715	1.27(2)	0.00(1)	0.22(2)	-	-	-12(1)	3(1)	3.60E+04
J2222−0137	STM	6	1.574	1.608	1.09(2)	0.1(1)	0.27(3)	-	-	-11.8(3)	3(1)	3.60E+04
J2229+2643	$MPTA_E$	4	1.550	-	1.07	-	-	-	-	-13.73	3.70	-
J2229+2643	$MPTA_T$	4	1.550	1.543	1.07(2)	0.00(1)	-	-	-	-15(3)	3(2)	2.41E+04
J2229+2643	MTM	2	3.511	3.481	1.47(3)	1.35(8)	0.01(2)	-	-	-	-	2.39E+04
J2229+2643	STM	2	5.426	5.039	1.17(3)	2.8(1)	0.0(2)	-	-	-	-	2.34E+04
J2234+0944	$MPTA_E$	3	1.253	-	1.02	-	-	-12.86	2.11	-	-	-
J2234+0944	$MPTA_T$	8	1.261	1.195	1.02(2)	0.00(1)	-	-12.9(4)	2.1(5)	-13(2)	4(1)	2.85E+04
J2234+0944	MTM	4	2.824	2.725	1.25(3)	1.41(6)	-	-	-	-11.4(1)	2.5(6)	2.80E+04
J2234+0944	STM	4	3.240	3.022	2.33(4)	0.78(6)	-	-	-	-11.0(1)	3.4(8)	2.66E+04
J2236−5527	$MPTA_E$	5	1.818	-	1.01	-	0.74	-12.85	1.32	-	-	-
J2236−5527	$MPTA_T$	6	1.818	1.821	1.02(2)	0.00(1)	0.6(3)	-	-	-16(2)	3(2)	1.85E+04
J2236−5527	MTM	1	2.016	2.016	1.36(2)	0.00(1)	-	-	-	-	-	1.85E+04
J2236−5527	STM	4	1.510	1.447	1.26(2)	0.16(5)	-	-	-	-11.3(2)	1.3(6)	1.83E+04
J2241−5236	$MPTA_E$	1	0.168	-	1.05	-	-	-	-	-	-	-
J2241−5236	$MPTA_T$	8	0.172	0.129	1.05(1)	0.00(0)	-	-16(2)	3(1)	-12.08(9)	2.2(3)	4.87E+04
J2241−5236	MTM	4	0.269	0.251	1.15(2)	0.14(0)	-	-	-	-11.98(9)	2.7(4)	4.85E+04
J2241−5236	STM	4	0.287	0.273	1.02(2)	0.14(0)	-	-	-	-11.99(9)	2.8(5)	4.81E+04
J2317+1439	$MPTA_E$	8	1.532	-	1.00	-	-	-13.45	3.51	-13.91	3.50	-
J2317+1439	$MPTA_T$	3	1.532	1.494	1.00(2)	0.00(1)	-	-13.3(2)	4(1)	-	-	2.32E+04
J2317+1439	MTM	3	3.211	3.155	2.01(4)	1.19(8)	-	-13(1)	3(1)	-	-	2.26E+04
J2317+1439	STM	4	4.379	3.974	1.18(3)	2.4(1)	-	-	-	-15(3)	3(2)	2.24E+04
J2322+2057	$MPTA_E$	1	2.030	-	1.02	0.36	-	-	-	-	-	-
J2322+2057	$MPTA_T$	1	2.185	2.185	1.01(2)	0.01(3)	-	-	-	-	-	2.07E+04
J2322+2057	MTM	4	2.439	2.406	1.47(3)	0.01(2)	-	-	-	-14(3)	3(1)	2.05E+04
J2322+2057	STM	6	1.736	1.614	1.43(3)	0.01(3)	0.00(1)	-	-	-10.9(1)	3.6(7)	2.04E+04
J2322−2650	$MPTA_E$	1	2.185	-	0.95	-	-	-	-	-	-	-
J2322−2650	$MPTA_T$	1	2.219	2.219	0.96(2)	0.01(1)	-	-	-	-	-	2.36E+04
J2322−2650	MTM	1	2.490	2.490	1.70(3)	0.00(1)	-	-	-	-	-	2.36E+04
J2322−2650	STM	4	1.280	1.218	1.51(3)	0.00(0)	-	-	-	-11.0(1)	3.2(8)	2.36E+04

4.7.2 Outliers

Table 4.9: Included in this table for each pulsar (PSR Name) are the analysis method used (Method) and the noise characteristics of the pulsar's timing residuals. Specifically, we provide the pre-fit RMS of the timing residuals (Full, μs) and the equivalent post-fit RMS after subtracting the maximum-likelihood realization of the noise processes (White, μs). The table also includes the noise model identifier (M_N) and key noise parameters: the EFAC (EF), EQUAD (EQ, μs), and SECORR (EC, μs) values, which describe the scaling of TOA uncertainties, additional white noise, and epoch-dependent correlated noise, respectively. For parameters characterizing time-correlated noise processes, such as the amplitude and spectral index of the red noise ($\log_{10} A_{red}$, γ_{red} and DM variations ($\log_{10} A_{DM}$, γ_{DM}, we report the median reported values and associated uncertainties. Finally, the NIS is provided as a measure of the goodness-of-fit for each method and model. Values marked with a dash ("-") indicate that the corresponding parameter was not applicable or not constrained for that pulsar.

PSR Name	Method	M_N	Full	White	EF	EQ	EC	$\log_{10} A_{red}$	γ_{red}	$\log_{10} A_{DM}$	γ_{DM}	NIS
J0437−4715	$MPTA_E$	6	0.233	-	1.20	-	0.21	-	-	-13.10	1.16	-
J0437−4715	$MPTA_T$	6	0.233	0.195	1.23(2)	0.00(0)	0.06(0)	-	-	-11.96(6)	1.0(2)	5.63E+04
J0437−4715	MTM	8	0.383	0.310	7.0(6)	0.28(1)	-	-13.7(2)	0.8(3)	-12.0(1)	3.1(6)	5.04E+04
J0437−4715	STM	6	0.389	0.350	2.8(3)	0.22(2)	0.05(0)	-	-	-11.87(9)	2.9(6)	5.04E+04
J1125−5825	$MPTA_E$	4	3.282	3.290	0.93	0.66	-	-	-	-12.78	2.85	-
J1125−5825	$MPTA_T$	4	3.313	2.549	0.93(2)	0.02(6)	-	-	-	-11.07(7)	2.7(4)	3.93E+04
J1125−5825	MTM	4	3.473	2.783	0.97(1)	0.01(2)	-	-	-	-11.13(9)	3.4(5)	3.91E+04
J1125−5825	STM	7	-	-	31.6(0)	10.0(0)	9.2(4)	-10.19(4)	0.13(2)	-10.00(0)	0.0(0)	-4.02E+05
J1455−3330	$MPTA_E$	3	1.875	-	1.00	-	-	-14.25	5.06	-	-	-
J1455−3330	$MPTA_T$	5	1.876	1.869	1.01(1)	0.00(1)	0.03(7)	-14(2)	3(1)	-	-	2.85E+04
J1455−3330	MTM	2	2.303	2.312	1.62(2)	0.00(1)	0.16(4)	-	-	-	-	2.83E+04
J1455−3330	STM	7	-	-	1.20(2)	0.01(2)	0.0(1)	-10.02(1)	0.03(3)	-13(3)	1(2)	2.76E+04
J1732−5049	$MPTA_E$	1	1.838	-	1.04	-	-	-	-	-	-	-
J1732−5049	$MPTA_T$	4	1.974	1.960	1.04(1)	0.02(4)	-	-	-	-12(1)	1.7(7)	5.27E+04
J1732−5049	MTM	4	3.551	3.522	1.16(2)	1.58(8)	-	-	-	-14(3)	3(1)	3.70E+04
J1732−5049	STM	7	-	-	9.5(1)	0.01(1)	0.0(1)	-10.01(0)	0.01(1)	-10.9(3)	0.9(6)	3.00E+04
J1804−2858	$MPTA_E$	8	9.952	-	1.07	-	-	-11.88	2.16	-11.47	3.96	-
J1804−2858	$MPTA_T$	8	9.952	5.092	1.10(2)	0.01(2)	-	-11.6(1)	2.9(4)	-10.03(2)	2.7(2)	2.47E+04
J1804−2858	MTM	8	24.916	19.732	2.11(6)	0.0(2)	-	-11.9(3)	4.0(9)	-10.02(2)	3.0(4)	2.21E+04
J1804−2858	STM	8	32.149	25.768	26.2(6)	9.97(3)	-	-11.5(2)	3.1(7)	-10.02(1)	1.7(1)	2.06E+04
J1825−0319	$MPTA_E$	1	4.623	-	1.02	-	0.28	-	-	-	-	-
J1825−0319	$MPTA_T$	4	4.639	4.639	1.02(2)	0.01(3)	-	-	-	-10.72(8)	2.2(2)	3.56E+04
J1825−0319	MTM	4	11.039	11.039	1.05(1)	0.01(1)	-	-	-	-10.49(8)	2.8(3)	3.62E+04
J1825−0319	STM	8	8.572	8.572	0.92(5)	6.8(6)	-	-11.8(1)	3.2(5)	-10.15(7)	2.9(3)	3.39E+04
J1843−1448	$MPTA_E$	4	15.370	-	0.96	6.56	-	-	-	-12.93	3.64	-
J1843−1448	$MPTA_T$	4	15.705	15.629	0.97(5)	4(7)	-	-	-	-14(3)	3(2)	2.06E+04
J1843−1448	MTM	4	14.058	13.997	1.06(2)	0.02(5)	-	-	-	-13(2)	4(1)	2.08E+04
J1843−1448	STM	4	16.218	11.653	2.8(3)	8.9(7)	-	-14(3)	3(1)	-10.01(1)	2.8(4)	2.07E+04
J2150−0326	$MPTA_E$	1	1.460	-	1.03	-	-	-	-	-	-	-
J2150−0326	$MPTA_T$	4	1.460	1.384	1.03(2)	0.00(1)	-	-	-	-11.5(1)	1.2(3)	2.53E+04
J2150−0326	MTM	6	2.835	2.790	1.20(3)	1.30(8)	0.05(9)	-	-	-12.0(3)	5(1)	2.48E+04
J2150−0326	STM	6	-	-	1.19(4)	2.1(1)	0.00(1)	-	-	-11.3(2)	1.5(6)	2.44E+04

Chapter 5

Results and Discussion

5.1 Introduction

MSPs are highly precise galactic clocks whose exceptional long-term stability enables a wide range of scientific investigations [Alpar et al., 1982, Lorimer, 2008]. PTAs utilize networks of regularly monitored MSPs to detect low-frequency (nHz) GWs, predicted to arise from a stochastic GWB generated by the mergers of a cosmic population of SMBHBs [Verbiest et al., 2016, Burke-Spolaor et al., 2019]. By offering a unique observational window into the universe, PTAs have the potential to reveal new insights into the most powerful forces shaping its evolution.

The potential for PTA projects to detect the subtle timing deviations caused by low-frequency GWs, relies on achieving extraordinary precision in measuring the arrival times of pulsar signals. However, attaining such precision presents significant challenges, including the need to mitigate instrumental calibration errors, account for frequency-dependent pulse evolution, and address various noise sources that can obscure or mimic GW signals. Among these, systematic timing errors—particularly those arising from instrumental distortions and polarization artifacts—remain a persistent issue, limiting the sensitivity of PTA experiments and the reliability of their findings.

This chapter discusses the key findings and broader implications of the results presented in this thesis, in particular, in Chapters 3 and 4, which focus on the Parkes and MeerKAT PTAs, respectively. These studies investigate the application of advanced instrumental calibration and ToA estimation methods to reduce systematic errors and enhance timing precision. These advancements not only increase the sensitivity of PTAs towards detecting the stochastic GWB, but also pave the way for identifying individual GW sources and uncovering other astrophysical phenomena, impacting the field of GW astronomy and pulsar science.

5.2 Polarization Calibration

Pulsar signals are intrinsically polarized, which makes them particularly susceptible to instrumental effects such as differential gain variations and parallactic rotation of the receiver. These effects distort the polarization properties of observed signals, resulting in systematic timing errors that pose a significant limitation to the detection of both the stochastic GWB and individual GW sources. Systematic timing errors from uncalibrated polarization artifacts can mimic correlations across pulsars, which can be misinterpreted as evidence of a GWB, directly impacting the sensitivity and robustness of PTA experiments [van Straten, 2006, 2013].

Polarization calibration has historically been limited by simplified models, such as the IFA [Lorimer and Kramer, 2012], which can fail to account for the complexities of real-world systems. Systematic timing errors in the PPTA dataset introduced timing residuals that were often misinterpreted, exhibiting spectral properties similar to astrophysical noise. This issue was particularly evident in PSR J0437−4715, where unmodeled steps in the polarimetric response produced spurious signals resembling red noise (see chapter 3). Unmodeled red noise has the potential to induce false positive GW detections [Tiburzi et al., 2016]. Such challenges underscore the critical need for

advanced calibration techniques capable of accurately isolating and correcting for these instrumental effects.

The advanced polarization calibration method, METM [van Straten, 2013] has demonstrated its potential to mitigate these distortions effectively. By modeling the full polarimetric response of the telescope, METM has achieved an almost threefold reduction in white noise for PSR J0437−4715 and significantly reduced systematic timing errors across several high-priority pulsars in the PPTA dataset, including those most impacted by calibration errors [Rogers et al., 2024].

As outlined in chapter 3, these improvements for mitigating systematic errors can enhance the robustness of PTA experiments and increase the likelihood of detecting genuine GW signals. Advanced polarization calibration techniques such as METM offer a clear pathway to improving PTA sensitivity and reliability in detecting both stochastic and individual GW signals.

5.3 Timing Precision

In this thesis, chapters 3 and 4 highlight significant progress in achieving better timing precision through advanced calibration techniques and ToA estimation methods. In the PPTA dataset, the combined use of METM and MTM [Rogers et al., 2024] reduced white noise by a median of 33% across the majority of pulsars, with reductions of up to 4.5 μs, outperforming conventional methods like IFA and STM [Taylor, 1992]. Similarly, in the MPTA dataset, MTM further demonstrated its potential by improving timing precision for 77% of pulsars, achieving a median reduction in white noise of 28% compared to STM and reductions of up to 3.4 μs for specific pulsars [Rogers et al., 2025].

Further, in Chapter 4, comparing MTM and STM results to those derived using the MPTA's (see [Miles et al., 2023]) combined use of Fourier Domain Monte Carlo

(FDM) and PULSEPORTRAITURE [Pennucci, 2019] revealed unexpected discrepancies. As STM and FDM employ essentially the same ToA estimation algorithm, equivalent results were anticipated between the two methods. However, MPTA achieved superior precision, likely due to the use of frequency-dependent templates generated by PULSEPORTRAITURE, which account for pulse shape evolution across wide frequency bands. These findings underscore the importance of template design in wideband timing. At the same time, the large EQUAD and whitened RMS values observed in the MTM and STM results suggest additional sources of systematic white noise. Residual polarization calibration errors, particularly in the full-polarization data used by MTM and STM, could be contributing to the observed discrepancies [van Straten, 2013]. Advanced calibration techniques, such as METM, could be used in future work to mitigate these errors and could yield even greater timing precision.

Pulsar timing precision lies at the heart of PTA science, underpinning both GW detection and broader astrophysical studies. Beyond GWs, these advancements enhance the scientific reach of pulsar timing (e.g., the discovery of new astrophysical parameters). For instance, the improved calibration techniques described in Chapters 3 and 4 allowed precise measurements of binary parameters, such as the secular variation of the projected semi-major axis and Shapiro delay, for PSR J1022+1001 [van Straten, 2013]. No new model parameters beyond those already established were derived in this work, as the focus is on noise characterization and improving timing precision for PTA applications. Precision timing of relativistic binaries, such as the double-pulsar system, PSR J0737−3039A/B [Burgay et al., 2003, Kramer et al., 2006], can also provide stringent tests of gravitational theories, validating or refining existing models [Taylor, 1992, Weisberg and Taylor, 2005, Weisberg et al., 2010, Antoniadis et al., 2013]. Extending these techniques to improve timing precision in other pulsars could uncover new phenomena (e.g., exoplanets [Wolszczan and Frail, 1992, Wolszczan, 1994]—where high-precision pulsar timing aids in detecting minute deviations in pulse arrival

times caused by orbiting planets) and address critical research questions in astrophysics (e.g., constraining the dense matter EOS [Demorest et al., 2010, Özel and Freire, 2016, Fonseca et al., 2021, Riley et al., 2021]—precise measurements of pulsar masses and radii inform the EOS for NSs).

5.4 Noise Mitigation

Red noise, arising from intrinsic pulsar spin irregularities, DM variations, and long-term instrumental instabilities, remain an ongoing challenge for PTA experiments [Verbiest et al., 2009, Alam et al., 2021b, Goncharov et al., 2021b]. In Chapter 3, METM reduced red noise in PSR J0437−4715 by addressing unmodeled steps in instrumental response. This reduction is particularly significant for PTAs aiming to detect the stochastic GWB and directly impacts the third research question (see 2.6.3), demonstrating the extent to which improved calibration can enhance timing precision by mitigating noise sources.

Similarly, white noise, caused by radiometer noise and unmodeled instrumental effects, reduces the accuracy of pulse arrival time estimates [Cordes and Shannon, 2010, Liu et al., 2012, Shannon et al., 2014, Lam et al., 2019]. Advanced instrumental calibration and ToA estimation techniques help reduce both sources of noise [Rogers et al., 2024]. Both Chapters 3 and 4 show MTM can successfully reduce white noise over the conventional STM method—by a median of 33% and 20% across the majority of pulsars in each of the PPTA and MPTA datasets, respectively. Accurate noise characterization also reduces systematic biases in pulsar timing residuals, leading to more robust astrophysical interpretations.

By reducing red and white noise, PTAs have greater potential to detect GW signals, including those from individual SMBHBs [Jenet et al., 2004, Arzoumanian et al., 2015a, Mingarelli et al., 2017] or cosmological sources like first-order phase transitions in the early universe [Caprini et al., 2010, Xue et al., 2021].

5.5 Future Directions

For the PPTA analysis in chapter 3, we focused solely on 20-cm band observations recorded with the CASPSR backend. Future work should extend the application of METM (§2.3.3) and MTM (§2.2.2) to other observing bands (10-cm and 40/50-cm) and backend instruments (e.g., CPSR2, PDFBs, WBCORR). Extending the analysis to these systems may require addressing non-linearities in the instrumental polarization response using impure Mueller matrices [Lu and Chipman, 1996], as described in the MTM formalism in §2.2.2. These matrices account for complex instrumental effects that cannot be modeled with idealized linear transformations, helping to mitigate residual calibration errors. Such corrections were not applied to the CASPSR or MeerKAT data, as CASPSR has well-characterized calibration procedures, and for MeerKAT we assumed that the polarization calibration was sufficiently accurate for our purposes. However, older or less stable systems may exhibit non-linear distortions that, if uncorrected, could degrade timing precision when using methods like METM or MTM.

Although there is limited availability of 10-cm data and significant RFI contamination in the 40/50-cm band at Parkes [Parthasarathy et al., 2019], the MTM theory developed by van Straten [2013] predicts substantial reductions in both arrival time uncertainty and systematic timing error at these wavelengths. As part of this work, we computed the quantities shown in Tables 5.1 and 5.2 using the polarization profiles from Yan et al. [2011]. These include the arrival time uncertainties relative to STM for the conditional MTM uncertainty (given $\mathbf{J}$), $\hat{\sigma}_{\varphi|\mathbf{J}}$; the MTM uncertainty when $\mathbf{J}$ is unknown, $\hat{\sigma}_{\varphi}$; and the invariant interval, $\hat{\sigma}_{\tilde{\varphi}}$.

Also presented are the multiple correlation between the estimated phase shift and $\mathbf{J}$, $R_{\varphi\mathbf{J}}$; the gradient of the phase shift with respect to instrumental boost, $\dot{\varphi}_{\beta}$; and the systematic error due to 1% mixing between total and polarized flux, τ_{β}. For PSRs

Table 5.1: Relative Arrival Time Uncertainties at 50 cm

Pulsar	$\hat{\sigma}_{\varphi\|\mathbf{J}}$	$R_{\varphi\mathbf{J}}$	$\hat{\sigma}_{\varphi}$	$\hat{\sigma}_{\bar{\varphi}}$	$\dot{\varphi}_{\beta}$	τ_{β} (ns)
J0437-4715	0.71	0.16	0.72	1.44	0.014	413
J0613-0200	0.72	0.26	0.74	1.76	0.0027	42
J0711-6830	0.85	0.05	0.86	1.53	0.004	111
J1017-7156	0.73	0.43	0.81	1.73	0.0055	65
J1022+1001	0.68	0.36	0.73	2.57	0.0036	293
J1024-0719	0.75	0.05	0.75	1.57	0.0023	60
J1045-4509	0.91	0.24	0.94	1.43	0.0088	330
J1446-4701	0.77	0.29	0.80	1.11	0.0083	91
J1545-4550	0.80	0.17	0.81	1.97	0.0089	158
J1600-3053	0.87	0.08	0.88	1.37	0.0078	141
J1603-7202	0.79	0.27	0.82	1.63	0.002	152
J1643-1224	0.89	0.11	0.90	1.39	0.017	402
J1713+0747	0.75	0.06	0.75	1.37	0.006	137
J1730-2304	0.80	0.10	0.81	1.51	0.0069	279
J1744-1134	0.72	0.90	1.68	4.00	0.0061	124
J1824-2452	0.74	0.13	0.75	2.57	0.0012	18
J1832-0836	0.52	0.06	0.52	0.98	4.4e-05	1
J1857+0943	0.85	0.07	0.85	1.42	0.0066	178
J1909-3744	0.81	0.55	0.97	1.57	0.0021	31
J1939+2134	0.86	0.06	0.86	1.58	0.005	39
J2124-3358	0.81	0.07	0.81	1.57	0.012	291
J2129-5721	0.66	0.71	0.93	2.21	0.018	327
J2145-0750	0.90	0.10	0.91	1.41	0.0036	289
J2241-5236	0.86	0.15	0.87	1.37	0.0022	24

Table 5.2: Relative Arrival Time Uncertainties at 10 cm

Pulsar	$\hat{\sigma}_{\varphi\|\mathbf{J}}$	$R_{\varphi\mathbf{J}}$	$\hat{\sigma}_{\varphi}$	$\hat{\sigma}_{\tilde{\varphi}}$	$\dot{\varphi}_{\beta}$	τ_{β} (ns)
J0437-4715	0.92	0.11	0.92	1.45	0.0015	43
J0613-0200	0.89	0.06	0.89	1.45	0.004	61
J0711-6830	0.88	0.10	0.89	1.52	0.0023	63
J1017-7156	0.80	0.64	1.04	1.71	0.0083	97
J1022+1001	0.80	0.28	0.84	1.26	0.0034	280
J1024-0719	0.72	0.06	0.72	1.46	0.0027	70
J1045-4509	0.81	0.32	0.86	1.42	0.012	440
J1446-4701	0.90	0.11	0.90	1.26	0.0032	35
J1545-4550	0.81	0.29	0.84	1.79	0.0023	41
J1600-3053	0.84	0.20	0.85	1.50	0.0028	51
J1603-7202	0.87	0.19	0.89	1.47	0.0029	215
J1643-1224	0.84	0.31	0.88	1.39	0.0072	166
J1713+0747	0.91	0.14	0.92	1.52	0.00085	20
J1730-2304	0.69	0.28	0.72	2.05	0.0055	224
J1744-1134	0.73	0.83	1.29	3.39	0.0036	73
J1824-2452	0.72	0.23	0.74	3.92	0.0019	29
J1832-0836	0.89	0.12	0.90	1.33	7.7e-05	1
J1857+0943	0.92	0.10	0.92	1.44	0.0022	60
J1909-3744	0.92	0.30	0.96	1.45	0.00079	12
J1939+2134	0.98	0.19	0.99	1.41	0.0056	43
J2124-3358	0.87	0.09	0.87	1.42	0.01	259
J2129-5721	0.74	0.12	0.75	1.34	0.0063	118
J2145-0750	0.97	0.12	0.98	1.42	0.0011	91
J2241-5236	0.94	0.11	0.95	1.36	0.0027	29

J1022+1001, J1730−2304, and J2124−3358, τ_β exceeds 200 ns in both frequency bands, while for PSR J1045−4509, τ_β reaches approximately 300 ns at 50 cm and 400 ns at 10 cm. These values show that even small calibration errors can lead to large timing offsets at these frequencies.

Advanced instrumental calibration techniques should be applied to minimize these systematic timing errors in each backend instrument, across all bands. Additionally, these efforts could provide new insights into the frequency-dependent propagation effects of pulsar emissions traversing the ISM, such as DM variations [Yao et al., 2017], RM variations [Han et al., 2018] and interstellar scattering [Rickett, 1990], and address timing errors caused by pulse shape variations (e.g., jitter [Cordes and Downs, 1985, Cordes et al., 1990, Liu et al., 2012, Parthasarathy et al., 2021]), further increasing arrival timing precision.

From the MPTA analysis in chapter 4, future work should extend the application of robust frequency-dependent modeling of PULSEPORTRAITURE [Pennucci, 2019] from total intensity "portraits" to full-polarization pulse profiles. These portraits, applied in conjunction with the timing capabilities of MTM, could further enhance the timing precision of the MPTA, and future pulsar timing analyses. Furthermore, a detailed follow-up analysis of individual pulsars would be useful to investigate outliers/oddities in our MPTA analysis results.

To address residual calibration errors and further improve timing precision, a hybrid approach incorporating METM, MTM, and PULSEPORTRAITURE could be highly effective. Such a methodology would account for both polarization-related errors and pulse shape evolution while leveraging the improved timing precision expected of MTM, offering a more robust framework for wideband timing.

RFI is also an important and ongoing challenge for PTA experiments [Lazarus et al., 2016, Rafiei-Ravandi and Smith, 2023, Lourenço et al., 2024]. The development of more sophisticated techniques for robust automatic, real-time detection of outliers

and flagging of RFI-contaminated data will be increasingly essential as pulsar timing datasets expand in both size and complexity.

Advanced instrumental calibration and ToA estimation techniques have shown the ability to mitigate systematic errors and improve timing precision, which has far-reaching implications for GW astronomy. Increased arrival time precision has the potential to enhance our ability to detect errors in SSEs [Vallisneri et al., 2020] and terrestrial time models [Hobbs et al., 2020], facilitate new or more accurate measurements of pulsar properties [e.g. van Straten, 2013], and increase PTA sensitivity towards the robust detection of the stochastic GWB and individual GW sources.

As PTAs transition into the era of the Square Kilometer Array [SKA; Dewdney et al., 2009], these methods will become indispensable. The SKA promises to revolutionize PTA science with its unprecedented sensitivity and frequency coverage, enabling:

- Timing of hundreds of MSPs, at sub-μs precision, significantly enhancing PTA sensitivity to GWs [Jenet et al., 2005, Liu et al., 2020].
- Detailed studies of SMBHBs, providing new insights into galaxy evolution through precise timing of extensive pulsar populations [Keith et al., 2013, Jones et al., 2017].
- Exploration of exotic GW phenomena, including cosmic strings and primordial backgrounds, offering a unique window into early universe physics that remains beyond the reach of current PTAs [Grishchuk, 2005, Damour and Vilenkin, 2005, Sanidas et al., 2012].

Advanced calibration and ToA estimations methods will be critical for realizing the full potential of the SKA, ensuring that calibration errors do not limit the sensitivity of the SKA to GW signals.

The implications of enhanced pulsar timing extend across multiple domains. Beyond

GW detection, the methods explored in this thesis can contribute to the SKA's broader capabilities, enabling new discoveries in pulsar astrophysics:

- Improved timing precision could lead to better constraints of subtle variations in DM, offering fresh insights into the structure and dynamics of the ISM and enhancing our understanding of galactic dynamics [You et al., 2007, Han et al., 2015, Lam et al., 2016, Krishnakumar et al., 2021].
- High-precision timing of relativistic binaries could enable stringent tests of alternative theories of gravity [Kramer et al., 2021a, Miao et al., 2021, Freire and Wex, 2024].
- The SKA's sensitivity is also likely to uncover previously undetected pulsars (e.g., Ahmad et al. [2024], Wang et al. [2024b]), expanding the known population.

The enhanced precision achieved in this thesis should be considered by all future PTA analyses. Extending these methods for use with newer datasets, including MeerKAT's ongoing observations and contributions from other PTA collaborations, will further validate the scalability and robustness of both methods. Additionally, the incorporation of γ-ray timing data from facilities like Fermi Gamma-ray Space Telescope (FGST) could complement PTA results (e.g., Liu et al. [2024, 2025]).

5.6 Conclusion

This thesis set out to demonstrate the impact of advanced instrumental calibration and ToA estimation techniques in high-precision, high-fidelity pulsar timing experiments.

A thorough analysis (see chapter 3) of ~10 years of Parkes 20-cm band data recorded with the CASPSR backend instrument, demonstrated that METM [van Straten, 2013] and MTM [van Straten, 2006] could achieve better timing precision over conventional

methods such as IFA [Lorimer and Kramer, 2012] and STM [Taylor, 1992]. We observed a significant reduction in white noise in pulse arrival times across all 25 high-priority PPTA pulsars in our sample, with significantly smaller uncertainty-weighted standard deviations of whitened post-fit timing residuals (up to 6.6 times smaller). For PSR J0437−4715, these advanced techniques also reduced the best-fit amplitude of the red noise in the timing residuals. Compared to STM, we found that regardless of the instrumental calibration technique used, MTM also showed an improved template matching goodness-of-fit and significantly decreased the median values of the error scale factor (EFAC) and error added in quadrature (EQUAD), while METM yielded marginal improvements over IFA for these parameters. Therefore, MTM is able to model most residual calibration errors and mitigate their impact on arrival time estimates. In future work, we would like to expand this analysis by applying MTM to the 10-cm and 40/50-cm bands and other backend instruments of the PPTA project. Depending on the instrument, achieving sufficiently well-calibrated observations may necessitate use of either MEM [van Straten, 2006] or METM.

Application of the MTM ToA estimation method to 4.5 years of wideband data (see chapter 4) for 75 high-priority pulsars observed regularly as part of the MPTA project, yielded similar improvements to the white noise and white noise parameters across the majority of pulsars. However, when we compared our results with the MPTA 4.5 year analysis [Miles et al., 2025], we found that their combined use of the FDM ToA estimation method and frequency-dependent templates from PULSEPORTAITURE [Pennucci, 2019] had overall superior performance. As STM and FDM both estimate arrival times using only the Fourier transform of the total intensity profile, our use of high S/N templates for the STM and MTM analysis is most likely the key difference; that is, templates created using PULSEPORTRAITURE have less noise and more accurately model pulse shape evolution across wide frequency bands. Furthermore, the higher EFAC and EQUAD values observed in the MTM and STM results suggest that FDM,

which uses MCMC to estimate arrival time uncertainty, yields more accurate error bars than STM and MTM; and additional sources of white, systematic noise, such as residual calibration errors that depolarize the signal and cannot be modeled using MTM, could play a significant role. For future work, we would like to search for possible residual polarization calibration errors in the full-polarization data and further investigate those pulsars where STM unexpectedly outperformed both MTM and MPTA. Furthermore, a new approach that integrates the strengths of both MTM and PULSEPORTRAITURE could address the limitations identified in this study.

By addressing instrumental errors and improving timing precision, the methods developed in this thesis have the potential to significantly enhance PTA sensitivity to GWs and possibly aid in new astrophysical discoveries. The insights gained from the Parkes and MeerKAT timing analysis results should provide a solid foundation for future work, helping to unlock the full scientific potential of the IPTA collaboration, particularly in the SKA era, which will undoubtedly redefine the limits of what PTAs can achieve.

References

J. Aasi, J. Abadie, B. P. Abbott, et al. Characterization of the LIGO detectors during their sixth science run. *Classical and Quantum Gravity*, 32(11):115012, 2015. doi: 10.1088/0264-9381/32/11/115012.

B. P. Abbott, R. Abbott, T. D. Abbott, et al. Observation of Gravitational Waves from a Binary Black Hole Merger. *Physical Review Letters*, 116(6):061102, 2016a. doi: 10.1103/PhysRevLett.116.061102.

B. P. Abbott, R. Abbott, T. D. Abbott, et al. Binary Black Hole Mergers in the First Advanced LIGO Observing Run. *Physical Review X*, 6(4):041015, 2016b. doi: 10.1103/PhysRevX.6.041015.

B. P. Abbott, R. Abbott, T. D. Abbott, et al. GW170817: Observation of Gravitational Waves from a Binary Neutron Star Inspiral. *Physical Review Letters*, 119(16):161101, 2017a. doi: 10.1103/PhysRevLett.119.161101.

B. P. Abbott, R. Abbott, T. D. Abbott, et al. Multi-messenger Observations of a Binary Neutron Star Merger. *Astrophysical Journal, Letters*, 848(2):L12, 2017b. doi: 10.3847/2041-8213/aa91c9.

B. P. Abbott, R. Abbott, T. D. Abbott, et al. GWTC-1: A Gravitational-Wave Transient Catalog of Compact Binary Mergers Observed by LIGO and Virgo during the First and Second Observing Runs. *Physical Review X*, 9(3):031040, 2019. doi: 10.1103/PhysRevX.9.031040.

R. Abbott, T. D. Abbott, S. Abraham, et al. GWTC-2: Compact Binary Coalescences Observed by LIGO and Virgo during the First Half of the Third Observing Run. *Physical Review X*, 11(2):021053, 2021. doi: 10.1103/PhysRevX.11.021053.

R. Abbott, T. D. Abbott, F. Acernese, et al. GWTC-3: Compact Binary Coalescences Observed by LIGO and Virgo during the Second Part of the Third Observing Run. *Physical Review X*, 13(4):041039, 2023. doi: 10.1103/PhysRevX.13.041039.

F. Acernese, M. Agathos, K. Agatsuma, et al. Advanced Virgo: a second-generation interferometric gravitational wave detector. *Classical and Quantum Gravity*, 32(2): 024001, 2015. doi: 10.1088/0264-9381/32/2/024001.

G. Agazie, M. F. Alam, A. Anumarlapudi, et al. The NANOGrav 15 yr Data Set: Observations and Timing of 68 Millisecond Pulsars. *Astrophysical Journal, Letters*, 951(1):L9, 2023a. doi: 10.3847/2041-8213/acda9a.

G. Agazie, A. Anumarlapudi, A. M. Archibald, et al. The NANOGrav 15 yr Data Set: Evidence for a Gravitational-wave Background. *Astrophysical Journal, Letters*, 951 (1):L8, 2023b. doi: 10.3847/2041-8213/acdac6.

G. Agazie, J. Antoniadis, A. Anumarlapudi, et al. Comparing Recent Pulsar Timing Array Results on the Nanohertz Stochastic Gravitational-wave Background. *Astrophysical Journal*, 966(1):105, 2024. doi: 10.3847/1538-4357/ad36be.

K. Aggarwal, Z. Arzoumanian, P. T. Baker, et al. The NANOGrav 11 yr Data Set: Limits on Gravitational Waves from Individual Supermassive Black Hole Binaries. *Astrophysical Journal*, 880(2):116, 2019. doi: 10.3847/1538-4357/ab2236.

A. Ahmad, S. Dai, S. Lazarević, et al. PSR J1631-4722: The Discovery of a Young and Energetic Pulsar in the Supernova Remnant G336.7+0.5. *arXiv e-prints*, page arXiv:2412.11345, 2024. doi: 10.48550/arXiv.2412.11345.

M. Ajello, W. B. Atwood, L. Baldini, et al. A gamma-ray pulsar timing array constrains the nanohertz gravitational wave background. *Science*, 376(6592):521–523, 2022. doi: 10.1126/science.abm3231.

K. Akiyama, A. Alberdi, W. Alef, et al. First M87 Event Horizon Telescope Results. I. The Shadow of the Supermassive Black Hole. *Astrophysical Journal, Letters*, 875(1): L1, 2019. doi: 10.3847/2041-8213/ab0ec7.

M. F. Alam, Z. Arzoumanian, P. T. Baker, et al. The NANOGrav 12.5 yr Data Set: Observations and Narrowband Timing of 47 Millisecond Pulsars. *Astrophysical Journal, Supplement*, 252(1):4, 2021a. doi: 10.3847/1538-4365/abc6a0.

M. F. Alam, Z. Arzoumanian, P. T. Baker, et al. The NANOGrav 12.5 yr Data Set: Wideband Timing of 47 Millisecond Pulsars. *Astrophysical Journal, Supplement*, 252(1):5, 2021b. doi: 10.3847/1538-4365/abc6a1.

M. A. Alpar, A. F. Cheng, M. A. Ruderman, and J. Shaham. A new class of radio pulsars. *Nature*, 300(5894):728–730, 1982. doi: 10.1038/300728a0.

L. G. Althaus, A. H. Córsico, J. Isern, and E. García-Berro. Evolutionary and pulsational properties of white dwarf stars. *Astronomy and Astrophysics Reviews*, 18(4):471–566, 2010. doi: 10.1007/s00159-010-0033-1.

P. Amaro-Seoane, H. Audley, S. Babak, et al. Laser Interferometer Space Antenna. *arXiv e-prints*, page arXiv:1702.00786, 2017. doi: 10.48550/arXiv.1702.00786.

P. W. Anderson and N. Itoh. Pulsar glitches and restlessness as a hard superfluidity phenomenon. *Nature*, 256(5512):25–27, 1975. doi: 10.1038/256025a0.

J. Antoniadis, P. C. C. Freire, N. Wex, et al. A Massive Pulsar in a Compact Relativistic Binary. *Science*, 340(6131):448, 2013. doi: 10.1126/science.1233232.

J. Antoniadis, Z. Arzoumanian, S. Babak, et al. The International Pulsar Timing Array second data release: Search for an isotropic gravitational wave background. *Monthly Notices of the RAS*, 510(4):4873–4887, 2022. doi: 10.1093/mnras/stab3418.

J. Antoniadis, P. Arumugam, S. Arumugam, et al. The second data release from the European Pulsar Timing Array. III. Search for gravitational wave signals. *Astronomy and Astrophysics*, 678:A50, 2023a. doi: 10.1051/0004-6361/202346844.

J. Antoniadis, P. Arumugam, S. Arumugam, et al. The second data release from the European Pulsar Timing Array: V. Implications for massive black holes, dark matter and the early Universe. *arXiv e-prints*, page arXiv:2306.16227, 2023b. doi: 10.48550/arXiv.2306.16227.

J. Antoniadis, S. Babak, A. S. Bak Nielsen, et al. The second data release from the European Pulsar Timing Array. I. The dataset and timing analysis. *Astronomy and Astrophysics*, 678:A48, 2023c. doi: 10.1051/0004-6361/202346841.

D. Antonopoulou, C. M. Espinoza, L. Kuiper, and N. Andersson. Pulsar spin-down: the glitch-dominated rotation of PSR J0537-6910. *Monthly Notices of the RAS*, 473 (2):1644–1655, 2018. doi: 10.1093/mnras/stx2429.

A. M. Archibald, N. V. Gusinskaia, J. W. T. Hessels, et al. Universality of free fall from the orbital motion of a pulsar in a stellar triple system. *Nature*, 559(7712):73–76, 2018. doi: 10.1038/s41586-018-0265-1.

Z. Arzoumanian, A. Brazier, S. Burke-Spolaor, et al. Gravitational Waves from Individual Supermassive Black Hole Binaries in Circular Orbits: Limits from the North American Nanohertz Observatory for Gravitational Waves. *Astrophysical Journal*, 794(2):141, 2014. doi: 10.1088/0004-637X/794/2/141.

Z. Arzoumanian, A. Brazier, S. Burke-Spolaor, et al. NANOGrav Constraints on Gravitational Wave Bursts with Memory. *Astrophysical Journal*, 810(2):150, 2015a. doi: 10.1088/0004-637X/810/2/150.

Z. Arzoumanian, A. Brazier, S. Burke-Spolaor, et al. The NANOGrav Nine-year Data Set: Observations, Arrival Time Measurements, and Analysis of 37 Millisecond Pulsars. *Astrophysical Journal*, 813(1):65, 2015b. doi: 10.1088/0004-637X/813/1/65.

Z. Arzoumanian, A. Brazier, S. Burke-Spolaor, et al. The NANOGrav Nine-year Data Set: Limits on the Isotropic Stochastic Gravitational Wave Background. *Astrophysical Journal*, 821(1):13, 2016. doi: 10.3847/0004-637X/821/1/13.

Z. Arzoumanian, A. Brazier, S. Burke-Spolaor, et al. The NANOGrav 11-year Data Set: High-precision Timing of 45 Millisecond Pulsars. *Astrophysical Journal, Supplement*, 235(2):37, 2018. doi: 10.3847/1538-4365/aab5b0.

Z. Arzoumanian, P. T. Baker, H. Blumer, et al. The NANOGrav 12.5 yr Data Set: Search for an Isotropic Stochastic Gravitational-wave Background. *Astrophysical Journal, Letters*, 905(2):L34, 2020. doi: 10.3847/2041-8213/abd401.

S. Babak, A. Petiteau, A. Sesana, et al. European Pulsar Timing Array limits on continuous gravitational waves from individual supermassive black hole binaries. *Monthly Notices of the RAS*, 455(2):1665–1679, 2016. doi: 10.1093/mnras/stv2092.

R. Bachiller. Bipolar Molecular Outflows from Young Stars and Protostars. *Annual Review of Astron and Astrophysis*, 34:111–154, 1996. doi: 10.1146/annurev.astro.34.1.111.

D. C. Backer. Pulsar Nulling Phenomena. *Nature*, 228(5266):42–43, 1970. doi: 10.1038/228042a0.

D. C. Backer and J. M. Rankin. Statistical summaries of polarized pulsar radiation. *Astrophysical Journal, Supplement*, 42:143–173, 1980. doi: 10.1086/190647.

D. C. Backer, J. M. Rankin, and D. B. Campbell. Orthogonal mode emission in geometric models of pulsar polarisation. *Nature*, 263:202–207, 1976. doi: 10.1038/263202a0.

D. C. Backer, S. R. Kulkarni, C. Heiles, M. M. Davis, and W. M. Goss. A millisecond pulsar. *Nature*, 300(5893):615–618, 1982. doi: 10.1038/300615a0.

D. C. Backer, S. Hama, S. van Hook, and R. S. Foster. Temporal Variations of Pulsar Dispersion Measures. *Astrophysical Journal*, 404:636, 1993. doi: 10.1086/172317.

M. Bailes, E. Barr, N. D. R. Bhat, et al. MeerTime - the MeerKAT Key Science Program on Pulsar Timing. In *MeerKAT Science: On the Pathway to the SKA*, page 11, 2016. doi: 10.22323/1.277.0011.

M. Bailes, A. Jameson, F. Abbate, et al. The MeerKAT telescope as a pulsar facility: System verification and early science results from MeerTime. *Publications of the Astron. Soc. of Australia*, 37:e028, 2020. doi: 10.1017/pasa.2020.19.

J. Ballesteros-Paredes, R. S. Klessen, M. M. Mac Low, and E. Vazquez-Semadeni. Molecular Cloud Turbulence and Star Formation. In B. Reipurth, D. Jewitt, and K. Keil, editors, *Protostars and Planets V*, page 63, 2007. doi: 10.48550/arXiv.astro-ph/0603357.

L. Barack, V. Cardoso, S. Nissanke, et al. Black holes, gravitational waves and fundamental physics: a roadmap. *Classical and Quantum Gravity*, 36(14):143001, 2019. doi: 10.1088/1361-6382/ab0587.

M. Bartnik and E. Fonseca. Verifying the Existence of a Third Planet in the PSR B1257+12 System. In *American Astronomical Society Meeting Abstracts*, volume 241 of *American Astronomical Society Meeting Abstracts*, page 209.01, 2023.

H. A. Bethe. Supernova mechanisms. *Reviews of Modern Physics*, 62(4):801–866, 1990. doi: 10.1103/RevModPhys.62.801.

D. Bhattacharya and E. P. J. van den Heuvel. Formation and evolution of binary and millisecond radio pulsars. *Physics Reports*, 203(1-2):1–124, 1991. doi: 10.1016/0370-1573(91)90064-S.

J. J. Blanco-Pillado, K. D. Olum, and X. Siemens. New limits on cosmic strings from gravitational wave observation. *Physics Letters B*, 778:392–396, 2018. doi: 10.1016/j.physletb.2018.01.050.

M. Blaskiewicz, J. M. Cordes, and I. Wasserman. A Relativistic Model of Pulsar Polarization. *Astrophysical Journa*, 370:643, 1991. doi: 10.1086/169850.

L. A. Boyle and P. J. Steinhardt. Probing the early universe with inflationary gravitational waves. *Physical Review D*, 77(6):063504, 2008. doi: 10.1103/PhysRevD.77.063504.

R. P. Brent. *Algorithms for Minimization without Derivatives*. Prentice-Hall, Englewood Cliffs, New Jersey, 1st edition, 1973.

M. C. Britton. Radio Astronomical Polarimetry and the Lorentz Group. *Astrophysical Journal*, 532(2):1240–1244, 2000. doi: 10.1086/308595.

M. Burgay, N. D'Amico, A. Possenti, et al. An increased estimate of the merger rate of double neutron stars from observations of a highly relativistic system. *Nature*, 426 (6966):531–533, 2003. doi: 10.1038/nature02124.

S. Burke-Spolaor, S. R. Taylor, M. Charisi, et al. The astrophysics of nanohertz gravitational waves. *Astronomy and Astrophysics Reviews*, 27(1):5, 2019. doi: 10.1007/s00159-019-0115-7.

R. N. Caballero, Y. J. Guo, K. J. Lee, et al. Studying the Solar system with the International Pulsar Timing Array. *Monthly Notices of the RAS*, 481(4):5501–5516, 2018. doi: 10.1093/mnras/sty2632.

M. Caleb, W. van Straten, E. F. Keane, et al. Polarization studies of rotating radio transients. *Monthly Notices of the RAS*, 487(1):1191–1199, 2019. doi: 10.1093/mnras/stz1352.

C. Caprini, R. Durrer, and X. Siemens. Detection of gravitational waves from the QCD phase transition with pulsar timing arrays. *Physical Review D*, 82(6):063511, 2010. doi: 10.1103/PhysRevD.82.063511.

A. Chalumeau, S. Babak, A. Petiteau, et al. Noise analysis in the European Pulsar Timing Array data release 2 and its implications on the gravitational-wave background search. *Monthly Notices of the RAS*, 509(4):5538–5558, 2022.

D. J. Champion, G. B. Hobbs, R. N. Manchester, et al. Measuring the Mass of Solar System Planets Using Pulsar Timing. *Astrophysical Journal, Letters*, 720(2):L201–L205, 2010. doi: 10.1088/2041-8205/720/2/L201.

S. Chandrasekhar. The highly collapsed configurations of a stellar mass. *Monthly Notices of the RAS*, 91:456–466, 1931. doi: 10.1093/mnras/91.5.456.

S. Chandrasekhar. *Radiative transfer.* n/a, 1950.

S. Chen, R. N. Caballero, Y. J. Guo, et al. Common-red-signal analysis with 24-yr high-precision timing of the European Pulsar Timing Array: inferences in the stochastic gravitational-wave background search. *Monthly Notices of the RAS*, 508 (4):4970–4993, 2021. doi: 10.1093/mnras/stab2833.

W. Coles, G. Hobbs, D. J. Champion, R. N. Manchester, and J. P. W. Verbiest. Pulsar timing analysis in the presence of correlated noise. *Monthly Notices of the RAS*, 418 (1):561–570, 2011. doi: 10.1111/j.1365-2966.2011.19505.x.

W. A. Coles, M. Kerr, R. M. Shannon, et al. Pulsar Observations of Extreme Scattering Events. *Astrophysical Journal*, 808(2):113, 2015. doi: 10.1088/0004-637X/808/2/113.

J. M. Comella, H. D. Craft, R. V. E. Lovelace, and J. M. Sutton. Crab Nebula Pulsar NP 0532. *Nature*, 221(5179):453–454, 1969. doi: 10.1038/221453a0.

J. J. Condon and S. M. Ransom. *Essential Radio Astronomy*. Princeton, NJ: Princeton University Press, 2016., 2016.

V. Corbin and N. J. Cornish. Pulsar Timing Array Observations of Massive Black Hole Binaries. *arXiv e-prints*, page arXiv:1008.1782, 2010. doi: 10.48550/arXiv.1008.1782.

J. Cordes and M. A. McLaughlin. Gravitational Waves, Extreme Astrophysics, and Fundamental Physics with Precision Pulsar Timing. *Bulletin of the AAS*, 51(3):447, 2019. doi: 10.48550/arXiv.1903.08653.

J. M. Cordes and G. S. Downs. JPL pulsar timing observations. III. Pulsar rotation fluctuations. *Astrophysical Journal, Supplement*, 59:343–382, 1985. doi: 10.1086/191076.

J. M. Cordes and T. J. W. Lazio. NE2001.I. A New Model for the Galactic Distribution of Free Electrons and its Fluctuations. *arXiv e-prints*, pages astro–ph/0207156, 2002. doi: 10.48550/arXiv.astro-ph/0207156.

J. M. Cordes and B. J. Rickett. Diffractive Interstellar Scintillation Timescales and Velocities. *Astrophysical Journal*, 507(2):846–860, 1998. doi: 10.1086/306358.

J. M. Cordes and R. M. Shannon. A Measurement Model for Precision Pulsar Timing. *arXiv e-prints*, page arXiv:1010.3785, 2010. doi: 10.48550/arXiv.1010.3785.

J. M. Cordes, A. Wolszczan, R. J. Dewey, M. Blaskiewicz, and D. R. Stinebring. Timing and Scintillations of the Millisecond Pulsar 1937+214. *Astrophysical Journal*, 349: 245, 1990. doi: 10.1086/168310.

J. M. Cordes, N. D. R. Bhat, T. H. Hankins, M. A. McLaughlin, and J. Kern. The Brightest Pulses in the Universe: Multifrequency Observations of the Crab Pulsar's Giant Pulses. *Astrophysical Journal*, 612(1):375–388, 2004. doi: 10.1086/422495.

J. M. Cordes, R. M. Shannon, and D. R. Stinebring. Frequency-dependent Dispersion Measures and Implications for Pulsar Timing. *Astrophysical Journal*, 817(1):16, 2016. doi: 10.3847/0004-637X/817/1/16.

H. T. Cromartie, E. Fonseca, S. M. Ransom, et al. Relativistic Shapiro delay measurements of an extremely massive millisecond pulsar. *Nature Astronomy*, 4:72–76, 2020. doi: 10.1038/s41550-019-0880-2.

R. M. Crutcher. Magnetic Fields in Molecular Clouds. *Annual Review of Astron and Astrophysis*, 50:29–63, 2012. doi: 10.1146/annurev-astro-081811-125514.

J. D. Cummings, J. S. Kalirai, P. E. Tremblay, E. Ramirez-Ruiz, and J. Choi. The White Dwarf Initial-Final Mass Relation for Progenitor Stars from 0.85 to 7.5 $M_{\odot}$. *Astrophysical Journal*, 866(1):21, 2018. doi: 10.3847/1538-4357/aadfd6.

S. Dai, G. Hobbs, R. N. Manchester, et al. A study of multifrequency polarization pulse profiles of millisecond pulsars. *Monthly Notices of the RAS*, 449(3):3223–3262, 2015. doi: 10.1093/mnras/stv508.

T. Damour and A. Vilenkin. Gravitational Wave Bursts from Cosmic Strings. *Physical Review Letters*, 85(18):3761–3764, 2000. doi: 10.1103/PhysRevLett.85.3761.

T. Damour and A. Vilenkin. Gravitational radiation from cosmic (super)strings: Bursts, stochastic background, and observational windows. *Physical Review D*, 71(6):063510, 2005. doi: 10.1103/PhysRevD.71.063510.

P. B. Demorest. *Measuring the gravitational wave background using precision pulsar timing*. PhD thesis, University of California, Berkeley, 2007.

P. B. Demorest, T. Pennucci, S. M. Ransom, M. S. E. Roberts, and J. W. T. Hessels. A two-solar-mass neutron star measured using Shapiro delay. *Nature*, 467(7319): 1081–1083, 2010. doi: 10.1038/nature09466.

P. B. Demorest, R. D. Ferdman, M. E. Gonzalez, et al. Limits on the Stochastic Gravitational Wave Background from the North American Nanohertz Observatory for Gravitational Waves. *Astrophysical Journal*, 762(2):94, 2013. doi: 10.1088/0004-637X/762/2/94.

G. Desvignes, R. N. Caballero, L. Lentati, et al. High-precision timing of 42 millisecond pulsars with the European Pulsar Timing Array. *Monthly Notices of the RAS*, 458(3): 3341–3380, 2016. doi: 10.1093/mnras/stw483.

S. Detweiler. Pulsar timing measurements and the search for gravitational waves. *Astrophysical Journal*, 234:1100–1104, 1979. doi: 10.1086/157593.

P. E. Dewdney, P. J. Hall, R. T. Schilizzi, and T. J. L. W. Lazio. The Square Kilometre Array. *IEEE Proceedings*, 97(8):1482–1496, 2009. doi: 10.1109/JPROC.2009.2021005.

T. Dolch, D. R. Stinebring, G. Jones, et al. Deconvolving Pulsar Signals with Cyclic Spectroscopy: A Systematic Evaluation. *Astrophysical Journal*, 913(2):98, 2021. doi: 10.3847/1538-4357/abf48b.

F. D. Drake and H. D. Craft. Second Periodic Pulsation in Pulsars. *Nature*, 220(5164): 231–235, 1968. doi: 10.1038/220231a0.

R. C. Duncan and C. Thompson. Formation of Very Strongly Magnetized Neutron Stars: Implications for Gamma-Ray Bursts. *Astrophysical Journal, Letters*, 392:L9, 1992. doi: 10.1086/186413.

J. Dyks and B. Rudak. The origin of the frequency-dependent behaviour of pulsar radio profiles. *Monthly Notices of the RAS*, 446(3):2505–2522, 2015. doi: 10.1093/mnras/stu2262.

R. T. Edwards. The polarization of drifting subpulses. *Astronomy and Astrophysics*, 426:677–686, 2004. doi: 10.1051/0004-6361:20041029.

R. T. Edwards, G. B. Hobbs, and R. N. Manchester. TEMPO2, a new pulsar timing package - II. The timing model and precision estimates. *Monthly Notices of the RAS*, 372(4):1549–1574, 2006. doi: 10.1111/j.1365-2966.2006.10870.x.

P. H. C. Eilers and B. D. Marx. Flexible smoothing with B-splines and penalties. *Statistical Science*, 11(2):89 – 121, 1996. doi: 10.1214/ss/1038425655.

A. Einstein. Die Grundlage der allgemeinen Relativitätstheorie. *Annalen der Physik*, 354(7):769–822, 1916. doi: 10.1002/andp.19163540702.

J. A. Ellis. A Bayesian analysis pipeline for continuous GW sources in the PTA band. *Classical and Quantum Gravity*, 30(22):224004, 2013. doi: 10.1088/0264-9381/30/22/224004.

J. A. Ellis, M. Vallisneri, S. R. Taylor, and P. T. Baker. ENTERPRISE: Enhanced Numerical Toolbox Enabling a Robust PulsaR Inference SuitE. Astrophysics Source Code Library, record ascl:1912.015, 2019.

B. G. Elmegreen and J. Scalo. Interstellar Turbulence I: Observations and Processes. *Annual Review of Astron and Astrophysis*, 42(1):211–273, 2004. doi: 10.1146/annurev.astro.41.011802.094859.

C. M. Espinoza, A. G. Lyne, B. W. Stappers, and M. Kramer. A study of 315 glitches in the rotation of 102 pulsars. *Monthly Notices of the RAS*, 414(2):1679–1704, 2011. doi: 10.1111/j.1365-2966.2011.18503.x.

Event Horizon Telescope Collaboration et al. First M87 Event Horizon Telescope Results. VII. Polarization of the Ring. *Astrophysical Journal, Letters*, 910(1):L12, 2021. doi: 10.3847/2041-8213/abe71d.

J. E. Everett and J. M. Weisberg. Emission Beam Geometry of Selected Pulsars Derived from Average Pulse Polarization Data. *Astrophysical Journal*, 553(1):341–357, 2001. doi: 10.1086/320652.

C. Federrath and R. S. Klessen. The Star Formation Rate of Turbulent Magnetized Clouds: Comparing Theory, Simulations, and Observations. *Astrophysical Journal*, 761(2):156, 2012. doi: 10.1088/0004-637X/761/2/156.

R. D. Ferdman, R. F. Archibald, and V. M. Kaspi. Long-term Timing and Emission Behavior of the Young Crab-like Pulsar PSR B0540-69. *Astrophysical Journal*, 812 (2):95, 2015. doi: 10.1088/0004-637X/812/2/95.

F. Feroz and M. P. Hobson. Multimodal nested sampling: an efficient and robust alternative to Markov Chain Monte Carlo methods for astronomical data analyses. *Monthly Notices of the RAS*, 384(2):449–463, 2008. doi: 10.1111/j.1365-2966.2007.12353.x.

F. Feroz, M. P. Hobson, and M. Bridges. MULTINEST: an efficient and robust Bayesian inference tool for cosmology and particle physics. *Monthly Notices of the RAS*, 398 (4):1601–1614, 2009. doi: 10.1111/j.1365-2966.2009.14548.x.

E. Fonseca, H. T. Cromartie, T. T. Pennucci, et al. Refined Mass and Geometric Measurements of the High-mass PSR J0740+6620. *Astrophysical Journal, Letters*, 915(1):L12, 2021. doi: 10.3847/2041-8213/ac03b8.

G. Foster, A. Karastergiou, R. Paulin, et al. Intrinsic instrumental polarization and high-precision pulsar timing. *Monthly Notices of the RAS*, 453(2):1489–1502, 2015. doi: 10.1093/mnras/stv1722.

R. S. Foster and D. C. Backer. Constructing a Pulsar Timing Array. *Astrophysical Journal*, 361:300, 1990. doi: 10.1086/169195.

P. C. C. Freire and N. Wex. Gravity experiments with radio pulsars. *Living Reviews in Relativity*, 27(1):5, 2024. doi: 10.1007/s41114-024-00051-y.

P. C. C. Freire, N. Wex, G. Esposito-Farèse, et al. The relativistic pulsar-white dwarf binary PSR J1738+0333 - II. The most stringent test of scalar-tensor gravity. *Monthly Notices of the RAS*, 423(4):3328–3343, 2012. doi: 10.1111/j.1365-2966.2012.21253.x.

C. L. Fryer. Mass Limits For Black Hole Formation. *Astrophysical Journal*, 522(1): 413–418, 1999. doi: 10.1086/307647.

C. R. García, D. F. Torres, and A. Patruno. Visualizing the pulsar population using graph theory. *Monthly Notices of the RAS*, 515(3):3883–3897, 2022. doi: 10.1093/mnras/stac1997.

T. Gold. Rotating Neutron Stars as the Origin of the Pulsating Radio Sources. *Nature*, 218(5143):731–732, 1968. doi: 10.1038/218731a0.

P. Goldreich and W. H. Julian. Pulsar Electrodynamics. *Astrophysical Journal*, 157: 869, 1969. doi: 10.1086/150119.

B. Goncharov, D. J. Reardon, R. M. Shannon, et al. Identifying and mitigating noise sources in precision pulsar timing data sets. *Monthly Notices of the RAS*, 502(1): 478–493, 2021a. doi: 10.1093/mnras/staa3411.

B. Goncharov, R. M. Shannon, D. J. Reardon, et al. On the Evidence for a Common-spectrum Process in the Search for the Nanohertz Gravitational-wave Background with the Parkes Pulsar Timing Array. *Astrophysical Journal, Letters*, 917(2):L19, 2021b. doi: 10.3847/2041-8213/ac17f4.

E. Graikou, J. P. W. Verbiest, S. Osłowski, et al. Limits on the mass, velocity and orbit of PSR J1933-6211. *Monthly Notices of the RAS*, 471(4):4579–4586, 2017. doi: 10.1093/mnras/stx1795.

B. Grimstad et al. SPLINTER: a library for multivariate function approximation with splines. http://github.com/bgrimstad/splinter, 2015. Accessed: 2015-05-16.

L. P. Grishchuk. Amplification of gravitational waves in an isotropic universe. *Soviet Journal of Experimental and Theoretical Physics*, 40:409, 1975.

L. P. Grishchuk. REVIEWS OF TOPICAL PROBLEMS: Relic gravitational waves and cosmology. *Physics Uspekhi*, 48(12):1235–1247, 2005. doi: 10.1070/PU2005v048n12ABEH005795.

L. Guillemot, I. Cognard, W. van Straten, G. Theureau, and E. Gérard. Improving pulsar polarization and timing measurements with the Nançay Radio Telescope. *Astronomy and Astrophysics*, 678:A79, 2023. doi: 10.1051/0004-6361/202347018.

Y. J. Guo, G. Y. Li, K. J. Lee, and R. N. Caballero. Studying the Solar system dynamics using pulsar timing arrays and the LINIMOSS dynamical model. *Monthly Notices of the RAS*, 489(4):5573–5581, 2019. doi: 10.1093/mnras/stz2515.

J. P. Hamaker, J. D. Bregman, and R. J. Sault. Understanding radio polarimetry. I. Mathematical foundations. *Astronomy and Astrophysics, Supplement*, 117:137–147, 1996.

J. L. Han, R. N. Manchester, A. G. Lyne, G. J. Qiao, and W. van Straten. Pulsar Rotation Measures and the Large-Scale Structure of the Galactic Magnetic Field. *Astrophysical Journal*, 642(2):868–881, 2006. doi: 10.1086/501444.

J. L. Han, W. van Straten, T. J. W. Lazio, et al. Three-dimensional Tomography of the Galactic and Extragalactic Magnetoionic Medium with the SKA. In *Advancing Astrophysics with the Square Kilometre Array (AASKA14)*, page 41, 2015. doi: 10.22323/1.215.0041.

J. L. Han, R. N. Manchester, W. van Straten, and P. Demorest. Pulsar Rotation Measures and Large-scale Magnetic Field Reversals in the Galactic Disk. *Astrophysical Journal, Supplement*, 234(1):11, 2018. doi: 10.3847/1538-4365/aa9c45.

Harvard-Smithsonian Center for Astrophysics. Pulsating Variable Stars and the Hertzsprung-Russell (H-R) Diagram, 2015. URL https://chandra.harvard.edu/edu/formal/variable_stars/bg_info.html.

T. E. Hassall, B. W. Stappers, P. Weltevrede, et al. Differential frequency-dependent delay from the pulsar magnetosphere. *Astronomy and Astrophysics*, 552:A61, 2013. doi: 10.1051/0004-6361/201220764.

M. Haverkorn, B. M. Gaensler, J. C. Brown, et al. Enhanced Small-Scale Faraday Rotation in the Galactic Spiral Arms. *Astrophysical Journal, Letters*, 637(1):L33–L35, 2006. doi: 10.1086/500543.

J. S. Hazboun, J. Simon, X. Siemens, and J. D. Romano. Model Dependence of Bayesian Gravitational-wave Background Statistics for Pulsar Timing Arrays. *Astrophysical Journal, Letters*, 905(1):L6, 2020. doi: 10.3847/2041-8213/abca92.

A. Heger and S. E. Woosley. The Nucleosynthetic Signature of Population III. *Astrophysical Journal*, 567(1):532–543, 2002. doi: 10.1086/338487.

A. Heger, C. L. Fryer, S. E. Woosley, N. Langer, and D. H. Hartmann. How Massive Single Stars End Their Life. *Astrophysical Journal*, 591(1):288–300, 2003. doi: 10.1086/375341.

C. Heiles, P. Perillat, M. Nolan, et al. Mueller Matrix Parameters for Radio Telescopes and Their Observational Determination. *Publications of the ASP*, 113(788):1274–1288, 2001. doi: 10.1086/323289.

D. J. Helfand, R. N. Manchester, and J. H. Taylor. Observations of pulsar radio emission. III. Stability of integrated profiles. *Astrophysical Journal*, 198:661–670, 1975. doi: 10.1086/153644.

R. W. Hellings and G. S. Downs. Upper limits on the isotropic gravitational radiation background from pulsar timing analysis. *Astrophysical Journal, Letters*, 265:L39–L42, 1983. doi: 10.1086/183954.

D. A. Hemberger and D. R. Stinebring. Time Variability of Interstellar Scattering and Improvements to Pulsar Timing. *Astrophysical Journal, Letters*, 674(1):L37, 2008. doi: 10.1086/528985.

P. Hennebelle and S. Inutsuka. The role of magnetic field in molecular cloud formation and evolution. *Frontiers in Astronomy and Space Sciences*, 6:5, 2019. doi: 10.3389/fspas.2019.00005.

J. W. T. Hessels, S. M. Ransom, I. H. Stairs, et al. A Radio Pulsar Spinning at 716 Hz. *Science*, 311(5769):1901–1904, 2006. doi: 10.1126/science.1123430.

A. Hewish, S. J. Bell, J. D. H. Pilkington, P. F. Scott, and R. A. Collins. Observation of a Rapidly Pulsating Radio Source. *Nature*, 217(5130):709–713, 1968. doi: 10.1038/217709a0.

W. Hillebrandt and J. C. Niemeyer. Type IA Supernova Explosion Models. *Annual Review of Astronomy and Astrophysics*, 38:191–230, 2000. doi: 10.1146/annurev.astro.38.1.191.

G. Hobbs, A. Archibald, Z. Arzoumanian, et al. The International Pulsar Timing Array project: using pulsars as a gravitational wave detector. *Classical and Quantum Gravity*, 27(8):084013, 2010. doi: 10.1088/0264-9381/27/8/084013.

G. Hobbs, W. Coles, R. N. Manchester, et al. Development of a pulsar-based time-scale. *Monthly Notices of the RAS*, 427(4):2780–2787, 2012. doi: 10.1111/j.1365-2966.2012.21946.x.

G. Hobbs, S. Dai, R. N. Manchester, et al. The role of FAST in pulsar timing arrays. *Research in Astronomy and Astrophysics*, 19(2):020, 2019. doi: 10.1088/1674-4527/19/2/20.

G. Hobbs, L. Guo, R. N. Caballero, et al. A pulsar-based time-scale from the International Pulsar Timing Array. *Monthly Notices of the RAS*, 491(4):5951–5965, 2020. doi: 10.1093/mnras/stz3071.

G. B. Hobbs, R. T. Edwards, and R. N. Manchester. TEMPO2, a new pulsar-timing package - I. An overview. *Monthly Notices of the RAS*, 369(2):655–672, 2006. doi: 10.1111/j.1365-2966.2006.10302.x.

A. W. Hotan, M. Bailes, and S. M. Ord. PSR J1022+1001: profile stability and precision timing. *Monthly Notices of the RAS*, 355(3):941–949, 2004. doi: 10.1111/j.1365-2966.2004.08376.x.

A. W. Hotan, M. Bailes, and S. M. Ord. PSR J0737-3039A: baseband timing and polarimetry. *Monthly Notices of the RAS*, 362(4):1267–1272, 2005. doi: 10.1111/j.1365-2966.2005.09389.x.

E. A. Huerta, S. T. McWilliams, J. R. Gair, and S. R. Taylor. Detection of eccentric supermassive black hole binaries with pulsar timing arrays: Signal-to-noise ratio calculations. *Physical Review D*, 92(6):063010, 2015. doi: 10.1103/PhysRevD.92.063010.

I. Iben. Stellar Evolution Within and off the Main Sequence. *Annual Review of Astron and Astrophysis*, 5:571, 1967. doi: 10.1146/annurev.aa.05.090167.003035.

I. Iben and A. V. Tutukov. Supernovae of type I as end products of the evolution of binaries with components of moderate initial mass. *Astrophysical Journal, Supplement*, 54:335–372, 1984. doi: 10.1086/190932.

C. D. Ilie, S. Johnston, and P. Weltevrede. Evidence for magnetospheric effects on the radiation of radio pulsars. *Monthly Notices of the RAS*, 483(2):2778–2794, 2019. doi: 10.1093/mnras/sty3315.

A. H. Jaffe and D. C. Backer. Gravitational Waves Probe the Coalescence Rate of Massive Black Hole Binaries. *Astrophysical Journal*, 583(2):616–631, 2003. doi: 10.1086/345443.

H. Janka. Explosion Mechanisms of Core-Collapse Supernovae. *Annual Review of Nuclear and Particle Science*, 62(1):407–451, 2012. doi: 10.1146/annurev-nucl-102711-094901.

J. H. Jeans. The Stability of a Spherical Nebula. *Philosophical Transactions of the Royal Society of London Series A*, 199:1–53, 1902. doi: 10.1098/rsta.1902.0012.

F. A. Jenet and S. B. Anderson. The Effects of Digitization on Nonstationary Stochastic Signals with Applications to Pulsar Signal Baseband Recording. *Publications of the ASP*, 110(754):1467–1478, 1998. doi: 10.1086/316273.

F. A. Jenet, A. Lommen, S. L. Larson, and L. Wen. Constraining the Properties of Supermassive Black Hole Systems Using Pulsar Timing: Application to 3C 66B. *Astrophysical Journal*, 606(2):799–803, 2004. doi: 10.1086/383020.

F. A. Jenet, G. B. Hobbs, K. J. Lee, and R. N. Manchester. Detecting the Stochastic Gravitational Wave Background Using Pulsar Timing. *Astrophysical Journal, Letters*, 625(2):L123–L126, 2005. doi: 10.1086/431220.

A. D. Johnson, S. J. Vigeland, X. Siemens, and S. R. Taylor. Gravitational-wave Statistics for Pulsar Timing Arrays: Examining Bias from Using a Finite Number of Pulsars. *Astrophysical Journal*, 932(2):105, 2022. doi: 10.3847/1538-4357/ac6f5e.

S. Johnston, D. R. Lorimer, P. A. Harrison, et al. Discovery of a very bright, nearby binary millisecond pulsar. *Nature*, 361(6413):613–615, 1993. doi: 10.1038/361613a0.

S. Johnston, A. Karastergiou, M. J. Keith, et al. The Thousand-Pulsar-Array programme on MeerKAT - I. Science objectives and first results. *Monthly Notices of the RAS*, 493(3):3608–3615, 2020. doi: 10.1093/mnras/staa516.

M. L. Jones, M. A. McLaughlin, M. T. Lam, et al. The NANOGrav Nine-year Data Set: Measurement and Analysis of Variations in Dispersion Measures. *Astrophysical Journal*, 841(2):125, 2017. doi: 10.3847/1538-4357/aa73df.

B. C. Joshi, P. Arumugasamy, M. Bagchi, et al. Precision pulsar timing with the ORT and the GMRT and its applications in pulsar astrophysics. *Journal of Astrophysics and Astronomy*, 39(4):51, 2018. doi: 10.1007/s12036-018-9549-y.

V. M. Kaspi and A. M. Beloborodov. Magnetars. *Annual Review of Astron and Astrophysis*, 55(1):261–301, 2017. doi: 10.1146/annurev-astro-081915-023329.

V. M. Kaspi, J. H. Taylor, and M. F. Ryba. High-Precision Timing of Millisecond Pulsars. III. Long-Term Monitoring of PSRs B1855+09 and B1937+21. *Astrophysical Journal*, 428:713, 1994. doi: 10.1086/174280.

M. J. Keith, W. Coles, R. M. Shannon, et al. Measurement and correction of variations in interstellar dispersion in high-precision pulsar timing. *Monthly Notices of the RAS*, 429(3):2161–2174, 2013. doi: 10.1093/mnras/sts486.

M. Kerr, D. J. Reardon, G. Hobbs, et al. The Parkes Pulsar Timing Array project: second data release. *Publications of the Astron. Soc. of Australia*, 37:e020, 2020. doi: 10.1017/pasa.2020.11.

R. P. Kerr. Gravitational Field of a Spinning Mass as an Example of Algebraically Special Metrics. *Physical Review Letters*, 11(5):237–238, 1963. doi: 10.1103/PhysRevLett.11.237.

T. W. B. Kibble. Topology of cosmic domains and strings. *Journal of Physics A Mathematical General*, 9(8):1387–1398, 1976. doi: 10.1088/0305-4470/9/8/029.

A. Kobakhidze, C. Lagger, A. Manning, and J. Yue. Gravitational waves from a supercooled electroweak phase transition and their detection with pulsar timing arrays. *European Physical Journal C*, 77(8):570, 2017. doi: 10.1140/epjc/s10052-017-5132-y.

B. Kocsis and A. Sesana. Gas-driven massive black hole binaries: signatures in the nHz gravitational wave background. *Monthly Notices of the RAS*, 411(3):1467–1479, 2011. doi: 10.1111/j.1365-2966.2010.17782.x.

J. Kocz, F. H. Briggs, and J. Reynolds. Radio Frequency Interference Removal through the Application of Spatial Filtering Techniques on the Parkes Multibeam Receiver. *Astronomical Journal*, 140(6):2086–2094, 2010. doi: 10.1088/0004-6256/140/6/2086.

J. Kormendy and L. C. Ho. Coevolution (Or Not) of Supermassive Black Holes and Host Galaxies. *Annual Review of Astron and Astrophysis*, 51(1):511–653, 2013. doi: 10.1146/annurev-astro-082708-101811.

J. Kormendy and D. Richstone. Inward Bound—The Search For Supermassive Black Holes In Galactic Nuclei. *Annual Review of Astron and Astrophysis*, 33:581, 1995. doi: 10.1146/annurev.aa.33.090195.003053.

C. Kouveliotou, S. Dieters, T. Strohmayer, et al. An X-ray pulsar with a superstrong magnetic field in the soft γ-ray repeater SGR1806 - 20. *Nature*, 393(6682):235–237, 1998. doi: 10.1038/30410.

M. Kramer and D. J. Champion. The European Pulsar Timing Array and the Large European Array for Pulsars. *Classical and Quantum Gravity*, 30(22):224009, 2013. doi: 10.1088/0264-9381/30/22/224009.

M. Kramer, R. Wielebinski, A. Jessner, J. A. Gil, and J. H. Seiradakis. Geometrical analysis of average pulsar profiles using multi-component Gaussian FITS at several frequencies. I. Method and analysis. *Astronomy and Astrophysics, Supplement*, 107: 515–526, 1994.

M. Kramer, K. M. Xilouris, F. Camilo, et al. Profile Instabilities of the Millisecond Pulsar PSR J1022+1001. *Astrophysical Journal*, 520(1):324–334, 1999. doi: 10.1086/307449.

M. Kramer, I. H. Stairs, R. N. Manchester, et al. Tests of General Relativity from Timing the Double Pulsar. *Science*, 314(5796):97–102, 2006. doi: 10.1126/science.1132305.

M. Kramer, I. H. Stairs, R. N. Manchester, et al. Strong-Field Gravity Tests with the Double Pulsar. *Physical Review X*, 11(4):041050, 2021a. doi: 10.1103/PhysRevX.11.041050.

M. Kramer, I. H. Stairs, V. Venkatraman Krishnan, et al. The relativistic binary programme on MeerKAT: science objectives and first results. *Monthly Notices of the RAS*, 504(2):2094–2114, 2021b. doi: 10.1093/mnras/stab375.

M. A. Krishnakumar, P. K. Manoharan, B. C. Joshi, R. Girgaonkar, S. Desai, M. Bagchi, K. Nobleson, L. Dey, A. Susobhanan, S. C. Susarla, M. P. Surnis, Y. Maan,

A. Gopakumar, A. Basu, N. D. Batra, A. Choudhary, K. De, Y. Gupta, A. K. Naidu, D. Pathak, J. Singha, and T. Prabu. High precision measurements of interstellar dispersion measure with the upgraded GMRT. *Astronomy and Astrophysics*, 651:A5, 2021. doi: 10.1051/0004-6361/202140340.

S. Krishnamohan and G. S. Downs. Intensity dependence of the pulse profile and polarization of the VELA pulsar. *Astrophysical Journal*, 265:372–388, 1983. doi: 10.1086/160682.

M. R. Krumholz and C. F. McKee. A General Theory of Turbulence-regulated Star Formation, from Spirals to Ultraluminous Infrared Galaxies. *Astrophysical Journal*, 630(1):250–268, 2005. doi: 10.1086/431734.

M. T. Lam, J. M. Cordes, S. Chatterjee, et al. Systematic and Stochastic Variations in Pulsar Dispersion Measures. *Astrophysical Journal*, 821(1):66, 2016. doi: 10.3847/0004-637X/821/1/66.

M. T. Lam, J. M. Cordes, S. Chatterjee, et al. The NANOGrav Nine-year Data Set: Excess Noise in Millisecond Pulsar Arrival Times. *Astrophysical Journal*, 834(1):35, 2017. doi: 10.3847/1538-4357/834/1/35.

M. T. Lam, J. A. Ellis, G. Grillo, et al. A Second Chromatic Timing Event of Interstellar Origin toward PSR J1713+0747. *Astrophysical Journal*, 861(2):132, 2018. doi: 10.3847/1538-4357/aac770.

M. T. Lam, M. A. McLaughlin, Z. Arzoumanian, et al. The NANOGrav 12.5 yr Data Set: The Frequency Dependence of Pulse Jitter in Precision Millisecond Pulsars. *Astrophysical Journal*, 872(2):193, 2019. doi: 10.3847/1538-4357/ab01cd.

R. B. Larson. Turbulence and star formation in molecular clouds. *Monthly Notices of the RAS*, 194:809–826, 1981. doi: 10.1093/mnras/194.4.809.

P. D. Lasky, C. M. F. Mingarelli, T. L. Smith, et al. Gravitational-Wave Cosmology across 29 Decades in Frequency. *Physical Review X*, 6(1):011035, 2016. doi: 10.1103/PhysRevX.6.011035.

J. M. Lattimer and M. Prakash. The Physics of Neutron Stars. *Science*, 304(5670): 536–542, 2004. doi: 10.1126/science.1090720.

P. Lazarus, R. Karuppusamy, E. Graikou, et al. Prospects for high-precision pulsar timing with the new Effelsberg PSRIX backend. *Monthly Notices of the RAS*, 458(1): 868–880, 2016. doi: 10.1093/mnras/stw189.

P. Lazarus, R. Karuppusamy, E. Graikou, et al. CoastGuard: Automated timing data reduction pipeline. Astrophysics Source Code Library, record ascl:2003.008, 2020.

K. J. Lee. Prospects of Gravitational Wave Detection Using Pulsar Timing Array for Chinese Future Telescopes. In L. Qain and D. Li, editors, *Frontiers in Radio Astronomy and FAST Early Sciences Symposium 2015*, volume 502 of *Astronomical Society of the Pacific Conference Series*, page 19, 2016.

K. J. Lee, C. G. Bassa, G. H. Janssen, et al. Model-based asymptotically optimal dispersion measure correction for pulsar timing. *Monthly Notices of the RAS*, 441(4): 2831–2844, 2014. doi: 10.1093/mnras/stu664.

L. Lentati, P. Alexander, M. P. Hobson, et al. TEMPONEST: a Bayesian approach to pulsar timing analysis. *Monthly Notices of the RAS*, 437(3):3004–3023, 2014. doi: 10.1093/mnras/stt2122.

L. Lentati, S. R. Taylor, C. M. F. Mingarelli, et al. European Pulsar Timing Array limits on an isotropic stochastic gravitational-wave background. *Monthly Notices of the RAS*, 453(3):2576–2598, 2015. doi: 10.1093/mnras/stv1538.

L. Lentati, R. M. Shannon, W. A. Coles, et al. From spin noise to systematics: stochastic processes in the first International Pulsar Timing Array data release. *Monthly Notices of the RAS*, 458(2):2161–2187, 2016. doi: 10.1093/mnras/stw395.

L. Lentati, M. Kerr, S. Dai, et al. Wide-band profile domain pulsar timing analysis. *Monthly Notices of the RAS*, 466(3):3706–3727, 2017. doi: 10.1093/mnras/stw3359.

B. Link, R. I. Epstein, and J. M. Lattimer. Pulsar Constraints on Neutron Star Structure and Equation of State. *Physical Review Letters*, 83(17):3362–3365, 1999. doi: 10.1103/PhysRevLett.83.3362.

K. Liu, J. P. W. Verbiest, M. Kramer, et al. Prospects for high-precision pulsar timing. *Monthly Notices of the RAS*, 417(4):2916–2926, 2011. doi: 10.1111/j.1365-2966.2011.19452.x.

K. Liu, E. F. Keane, K. J. Lee, et al. Profile-shape stability and phase-jitter analyses of millisecond pulsars. *Monthly Notices of the RAS*, 420(1):361–368, 2012. doi: 10.1111/j.1365-2966.2011.20041.x.

K. Liu, G. Desvignes, I. Cognard, et al. Measuring pulse times of arrival from broad-band pulsar observations. *Monthly Notices of the RAS*, 443(4):3752–3760, 2014. doi: 10.1093/mnras/stu1420.

K. Liu, L. Guillemot, A. G. Istrate, et al. A revisit of PSR J1909-3744 with 15-yr high-precision timing. *Monthly Notices of the RAS*, 499(2):2276–2291, 2020. doi: 10.1093/mnras/staa2993.

P. Liu, J. P. Yuan, M. Y. Ge, et al. Pulse profile variability associated with the glitch of PSR J1048-5832. *Monthly Notices of the RAS*, 533(4):4274–4286, 2024. doi: 10.1093/mnras/stae1973.

P. Liu, J. P. Yuan, M. Y. Ge, and others. A multi-band study of pulsar glitches with Fermi-LAT and Parkes. *Monthly Notices of the RAS*, 2025. doi: 10.1093/mnras/staf101.

D. R. Lorimer. Binary and Millisecond Pulsars. *Living Reviews in Relativity*, 11(1):8, 2008. doi: 10.12942/lrr-2008-8.

D. R. Lorimer and M. Kramer. *Handbook of Pulsar Astronomy*. Cambridge, UK: Cambridge University Press, 2012.

L. Lourenço, A. P. Chippendale, B. Indermuehle, et al. Survey and monitoring of ASKAP's RFI environment and trends I: Flagging statistics. *Publications of the Astron. Soc. of Australia*, 41:e012, 2024. doi: 10.1017/pasa.2024.4.

M. E. Lower, M. Bailes, R. M. Shannon, et al. The UTMOST pulsar timing programme - II. Timing noise across the pulsar population. *Monthly Notices of the RAS*, 494(1): 228–245, 2020. doi: 10.1093/mnras/staa615.

S. Lu and R. A. Chipman. Interpretation of Mueller matrices based on polar decomposition. *Journal of the Optical Society of America A*, 13(5):1106–1113, 1996. doi: 10.1364/JOSAA.13.001106.

J. Luo, S. Ransom, P. Demorest, et al. PINT: A Modern Software Package for Pulsar Timing. *Astrophysical Journal*, 911(1):45, 2021. doi: 10.3847/1538-4357/abe62f.

A. Lyne, G. Hobbs, M. Kramer, I. Stairs, and B. Stappers. Switched Magnetospheric Regulation of Pulsar Spin-Down. *Science*, 329(5990):408, 2010. doi: 10.1126/science.1186683.

M. Mac Low and R.S. Klessen. Control of star formation by supersonic turbulence. *Reviews of Modern Physics*, 76(1):125–194, 2004. doi: 10.1103/RevModPhys.76.125.

J. Magorrian, S. Tremaine, D. Richstone, et al. The Demography of Massive Dark Objects in Galaxy Centers. *Astronomical Journal*, 115(6):2285–2305, 1998. doi: 10.1086/300353.

R. N. Manchester. The Parkes Pulsar Timing Array Project. In C. Bassa, Z. Wang, A. Cumming, and V. M. Kaspi, editors, *40 Years of Pulsars: Millisecond Pulsars, Magnetars and More*, volume 983 of *American Institute of Physics Conference Series*, pages 584–592. AIP, 2008. doi: 10.1063/1.2900303.

R. N. Manchester and J. H. Taylor. *Pulsars*. San Francisco : W. H. Freeman, c1977., 1977.

R. N. Manchester, J. H. Taylor, and G. R. Huguenin. Frequency Dependence of Pulsar Polarization. *Astrophysical Journal, Letters*, 179:L7, 1973. doi: 10.1086/181105.

R. N. Manchester, J. H. Taylor, and G. R. Huguenin. Observations of pulsar radio emission. II. Polarization of individual pulses. *Astrophysical Journal*, 196:83–102, 1975. doi: 10.1086/153395.

R. N. Manchester, G. B. Hobbs, A. Teoh, and M. Hobbs. VizieR Online Data Catalog: ATNF Pulsar Catalog (Manchester+, 2005). VizieR On-line Data Catalog: VII/245. Originally published in: 2005AJ....129.1993M, 2005.

R. N. Manchester, G. Hobbs, M. Bailes, et al. The Parkes Pulsar Timing Array Project. *Publications of the Astron. Soc. of Australia*, 30:e017, 2013. doi: 10.1017/pasa.2012.017.

D. N. Matsakis, J. H. Taylor, and T. Marshall Eubanks. A statistic for describing pulsar and clock stabilities. *Astronomy and Astrophysics*, 326:924–928, 1997.

C. F. McKee and E. C. Ostriker. Theory of Star Formation. *Annual Review of Astron and Astrophysis*, 45(1):565–687, 2007. doi: 10.1146/annurev.astro.45.051806.110602.

M. A. McLaughlin. The North American Nanohertz Observatory for Gravitational Waves. *Classical and Quantum Gravity*, 30(22):224008, 2013. doi: 10.1088/0264-9381/30/22/224008.

A. Melatos and B. Link. Pulsar timing noise from superfluid turbulence. *Monthly Notices of the RAS*, 437(1):21–31, 2014. doi: 10.1093/mnras/stt1828.

S. Mereghetti, J. A. Pons, and A. Melatos. Magnetars: Properties, Origin and Evolution. *Space Science Reviews*, 191(1-4):315–338, 2015. doi: 10.1007/s11214-015-0146-y.

X. Miao, H. Xu, L. Shao, C. Liu, and B. Ma. Stringent Tests of Gravity with Highly Relativistic Binary Pulsars in the Era of LISA and SKA. *Astrophysical Journal*, 921 (2):114, 2021. doi: 10.3847/1538-4357/ac1d48.

M. T. Miles, R. M. Shannon, M. Bailes, et al. Mode changing in J1909 - 3744: the most precisely timed pulsar. *Monthly Notices of the RAS*, 510(4):5908–5915, 2022. doi: 10.1093/mnras/stab3549.

M. T. Miles, R. M. Shannon, M. Bailes, et al. The MeerKAT Pulsar Timing Array: first data release. *Monthly Notices of the RAS*, 519(3):3976–3991, 2023. doi: 10.1093/mnras/stac3644.

M. T. Miles, R. M. Shannon, D. J. Reardon, et al. The MeerKAT Pulsar Timing Array: the 4.5-yr data release and the noise and stochastic signals of the millisecond pulsar population. *Monthly Notices of the RAS*, 536(2):1467–1488, 2025. doi: 10.1093/mnras/stae2572.

M. C. Miller and E. J. M. Colbert. Intermediate-Mass Black Holes. *International Journal of Modern Physics D*, 13(1):1–64, 2004. doi: 10.1142/S0218271804004426.

M. C. Miller and J. M. Miller. The masses and spins of neutron stars and stellar-mass black holes. *Physics Reports*, 548:1–34, 2015. doi: 10.1016/j.physrep.2014.09.003.

M. C. Miller, F. K. Lamb, A. J. Dittmann, et al. The Radius of PSR J0740+6620 from NICER and XMM-Newton Data. *Astrophysical Journal, Letters*, 918(2):L28, 2021. doi: 10.3847/2041-8213/ac089b.

C. M. F. Mingarelli, T. J. W. Lazio, A. Sesana, et al. The local nanohertz gravitational-wave landscape from supermassive black hole binaries. *Nature Astronomy*, 1:886–892, 2017. doi: 10.1038/s41550-017-0299-6.

D. Mitra, R. Basu, and G. I. Melikidze. On the flux density spectral property of high linearly polarized signal from Pulsar J0332+5434. *arXiv e-prints*, page arXiv:2408.10020, 2024. doi: 10.48550/arXiv.2408.10020.

V. Morello, E. D. Barr, S. Cooper, et al. The High Time Resolution Universe survey - XIV. Discovery of 23 pulsars through GPU-accelerated reprocessing. *Monthly Notices of the RAS*, 483(3):3673–3685, 2019. doi: 10.1093/mnras/sty3328.

J. Navarro, R. N. Manchester, J. S. Sandhu, S. R. Kulkarni, and M. Bailes. Mean Pulse Shape and Polarization of PSR J0437-4715. *Astrophysical Journal*, 486(2): 1019–1025, 1997. doi: 10.1086/304563.

C. Ng. Pulsar science with the CHIME telescope. In P. Weltevrede, B. B. P. Perera, L. L. Preston, and S. Sanidas, editors, *Pulsar Astrophysics the Next Fifty Years*, volume 337 of *IAU Symposium*, pages 179–182, 2018. doi: 10.1017/S1743921317010638.

T. Nguyen, G. Brown, V. Smedile, et al. Determining Properties of the Interstellar Medium through Scintillation of 166 Pulsars. In *American Astronomical Society Meeting #240*, volume 240 of *American Astronomical Society Meeting Abstracts*, page 226.06, 2022.

G. M. Nita and D. E. Gary. The generalized spectral kurtosis estimator. *Monthly Notices of the RAS*, 406(1):L60–L64, 2010. doi: 10.1111/j.1745-3933.2010.00882.x.

K. Nomoto, F. K. Thielemann, and K. Yokoi. Accreting white dwarf models for type I supernovae. III. Carbon deflagration supernovae. *Astrophysical Journal*, 286: 644–658, 1984. doi: 10.1086/162639.

A. Noutsos, S. Johnston, M. Kramer, and A. Karastergiou. New pulsar rotation measures and the Galactic magnetic field. *Monthly Notices of the RAS*, 386(4):1881–1896, 2008. doi: 10.1111/j.1365-2966.2008.13188.x.

S. Ölmez, V. Mandic, and X. Siemens. Gravitational-wave stochastic background from kinks and cusps on cosmic strings. *Physical Review D*, 81(10):104028, 2010. doi: 10.1103/PhysRevD.81.104028.

J. R. Oppenheimer and G. M. Volkoff. On Massive Neutron Cores. *Physical Review*, 55(4):374–381, 1939. doi: 10.1103/PhysRev.55.374.

S. M. Ord, W. van Straten, A. W. Hotan, and M. Bailes. Polarimetric profiles of 27 millisecond pulsars. *Monthly Notices of the RAS*, 352(3):804–814, 2004. doi: 10.1111/j.1365-2966.2004.07963.x.

S. Osłowski, W. van Straten, G. B. Hobbs, M. Bailes, and P. Demorest. High signal-to-noise ratio observations and the ultimate limits of precision pulsar timing. *Monthly Notices of the RAS*, 418(2):1258–1271, 2011. doi: 10.1111/j.1365-2966.2011.19578.x.

S. Osłowski, W. van Straten, P. Demorest, and M. Bailes. Improving the precision of pulsar timing through polarization statistics. *Monthly Notices of the RAS*, 430(1):416–424, 2013. doi: 10.1093/mnras/sts662.

F. Özel and P. Freire. Masses, Radii, and the Equation of State of Neutron Stars. *Annual Review of Astron and Astrophysis*, 54:401–440, 2016. doi: 10.1146/annurev-astro-081915-023322.

F. Pacini. Rotating Neutron Stars, Pulsars and Supernova Remnants. *Nature*, 219(5150):145–146, 1968. doi: 10.1038/219145a0.

A. Parthasarathy, R. M. Shannon, S. Johnston, et al. Timing of young radio pulsars - I. Timing noise, periodic modulation, and proper motion. *Monthly Notices of the RAS*, 489(3):3810–3826, 2019. doi: 10.1093/mnras/stz2383.

A. Parthasarathy, M. Bailes, R. M. Shannon, et al. Measurements of pulse jitter and single-pulse variability in millisecond pulsars using MeerKAT. *Monthly Notices of the RAS*, 502(1):407–422, 2021. doi: 10.1093/mnras/stab037.

T. T. Pennucci. Frequency-dependent Template Profiles for High-precision Pulsar Timing. *Astrophysical Journal*, 871(1):34, 2019. doi: 10.3847/1538-4357/aaf6ef.

T. T. Pennucci, P. B. Demorest, and S. M. Ransom. Elementary Wideband Timing of Radio Pulsars. *Astrophysical Journal*, 790(2):93, 2014. doi: 10.1088/0004-637X/790/2/93.

R. Penrose. Gravitational Collapse and Space-Time Singularities. *Physical Review Letters*, 14(3):57–59, 1965. doi: 10.1103/PhysRevLett.14.57.

B. B. P. Perera, B. W. Stappers, S. Babak, et al. Improving timing sensitivity in the microhertz frequency regime: limits from PSR J1713+0747 on gravitational waves produced by supermassive black hole binaries. *Monthly Notices of the RAS*, 478(1):218–227, 2018. doi: 10.1093/mnras/sty1116.

B. B. P. Perera, M. E. DeCesar, P. B. Demorest, et al. The International Pulsar Timing Array: second data release. *Monthly Notices of the RAS*, 490(4):4666–4687, 2019. doi: 10.1093/mnras/stz2857.

G. Petit and P. Tavella. Pulsars and time scales. *Astronomy and Astrophysics*, 308: 290–298, 1996.

A. Philippov and M. Kramer. Pulsar Magnetospheres and Their Radiation. *Annual Review of Astron and Astrophysis*, 60:495–558, 2022. doi: 10.1146/annurev-astro-052920-112338.

E. S. Phinney. A Practical Theorem on Gravitational Wave Backgrounds. *arXiv e-prints*, pages astro–ph/0108028, 2001. doi: 10.48550/arXiv.astro-ph/0108028.

J. D. H. Pilkington, A. Hewish, S. J. Bell, and T. W. Cole. Observations of some further Pulsed Radio Sources. *Nature*, 218(5137):126–129, 1968. doi: 10.1038/218126a0.

N. S. Pol, S. R. Taylor, L. Z. Kelley, et al. Astrophysics Milestones for Pulsar Timing Array Gravitational-wave Detection. *Astrophysical Journal, Letters*, 911(2):L34, 2021. doi: 10.3847/2041-8213/abf2c9.

W. H. Press, S. A. Teukolsky, W. T. Vetterling, and B. P. Flannery. *Numerical recipes in C. The art of scientific computing*. Cambridge: University Press, |c1992, 2nd ed., 1992.

V. Radhakrishnan and D. J. Cooke. Magnetic Poles and the Polarization Structure of Pulsar Radiation. *Astrophysics Letters*, 3:225, 1969.

V. Radhakrishnan and G. Srinivasan. On the origin of the recently discovered ultra-rapid pulsar. *Current Science*, 51:1096–1099, 1982.

Masoud Rafiei-Ravandi and Kendrick M. Smith. Mitigating Radio Frequency Interference in CHIME/FRB Real-time Intensity Data. *Astrophysical Journal, Supplement*, 265(2):62, 2023. doi: 10.3847/1538-4365/acc252.

M. Rajagopal and R. W. Romani. Ultra–Low-Frequency Gravitational Radiation from Massive Black Hole Binaries. *Astrophysical Journal*, 446:543, 1995. doi: 10.1086/175813.

R. Ramachandran and M. Kramer. Unusual profile variations in pulsar PSR J1022+1001 - Evidence for magnetospheric “return currents”? *Astronomy and Astrophysics*, 407: 1085–1095, 2003. doi: 10.1051/0004-6361:20031036.

R. J. Rand and S. R. Kulkarni. The Local Galactic Magnetic Field. *Astrophysical Journal*, 343:760, 1989. doi: 10.1086/167747.

R. J. Rand and A. G. Lyne. New Rotation Measures of Distant Pulsars in the Inner Galaxy and Magnetic Field Reversals. *Monthly Notices of the RAS*, 268:497, 1994. doi: 10.1093/mnras/268.2.497.

J. M. Rankin. Toward an empirical theory of pulsar emission. I. Morphological taxonomy. *Astrophysical Journal*, 274:333–358, 1983. doi: 10.1086/161450.

S. Ransom, A. Brazier, S. Chatterjee, et al. The NANOGrav Program for Gravitational Waves and Fundamental Physics. In *Bulletin of the American Astronomical Society*, volume 51, page 195, 2019. doi: 10.48550/arXiv.1908.05356.

N. Rathnasree and J. M. Rankin. On the Approach to Stability of Pulsar Average Profiles. *Astrophysical Journal*, 452:814, 1995. doi: 10.1086/176349.

V. Ravi, J. S. B. Wyithe, R. M. Shannon, and G. Hobbs. Prospects for gravitational-wave detection and supermassive black hole astrophysics with pulsar timing arrays. *Monthly Notices of the RAS*, 447(3):2772–2783, 2015. doi: 10.1093/mnras/stu2659.

D. J. Reardon. Meerguard, 2021. URL https://github.com/danielreardon/MeerGuard.

D. J. Reardon, G. Hobbs, W. Coles, et al. Timing analysis for 20 millisecond pulsars in the Parkes Pulsar Timing Array. *Monthly Notices of the RAS*, 455(2):1751–1769, 2016. doi: 10.1093/mnras/stv2395.

D. J. Reardon, A. Zic, R. M. Shannon, et al. Search for an Isotropic Gravitational-wave Background with the Parkes Pulsar Timing Array. *Astrophysical Journal, Letters*, 951(1):L6, 2023. doi: 10.3847/2041-8213/acdd02.

R. A. Remillard and J. E. McClintock. X-Ray Properties of Black-Hole Binaries. *Annual Review of Astron and Astrophysis*, 44(1):49–92, 2006. doi: 10.1146/annurev.astro.44.051905.092532.

B. J. Rickett. Amplitude-modulated noise: an empirical model for the radio radiation received from pulsars. *Astrophysical Journal*, 197:185–191, 1975. doi: 10.1086/153501.

B. J. Rickett. Radio propagation through the turbulent interstellar plasma. *Annual Review of Astron and Astrophysis*, 28:561–605, 1990. doi: 10.1146/annurev.aa.28.090190.003021.

T. E. Riley, A. L. Watts, P. S. Ray, et al. A NICER View of the Massive Pulsar PSR J0740+6620 Informed by Radio Timing and XMM-Newton Spectroscopy. *Astrophysical Journal, Letters*, 918(2):L27, 2021. doi: 10.3847/2041-8213/ac0a81.

A. E. Rodin. Optimal filters for the construction of the ensemble pulsar time. *Monthly Notices of the RAS*, 387(4):1583–1588, 2008. doi: 10.1111/j.1365-2966.2008.13270.x.

C. Roedig, A. Sesana, M. Dotti, et al. Evolution of binary black holes in self gravitating discs. Dissecting the torques. *Astronomy and Astrophysics*, 545:A127, 2012. doi: 10.1051/0004-6361/201219986.

A. F. Rogers. Demonstrating the Impact of High-Fidelity Polarization Calibration on High-Precision Pulsar Timing. Master's thesis, Auckland University of Technology, 2020. URL https://openrepository.aut.ac.nz/items/705f03b3-5690-45bb-926b-9ca588cfae25.

A. F. Rogers, W. van Straten, S. Gulyaev, et al. Reducing Instrumental Errors in Parkes Pulsar Timing Array Data. *Astrophysical Journal*, 973(2):94, 2024. doi: 10.3847/1538-4357/ad656e.

A. F. Rogers, W. van Straten, S. Gulyaev, et al. Reducing Instrumental Errors in MeerKAT Pulsar Timing Array Data. In preparation, 2025.

M. A. Ruderman and P. G. Sutherland. Theory of pulsars: polar gaps, sparks, and coherent microwave radiation. *Astrophysical Journal*, 196:51–72, 1975. doi: 10.1086/153393.

J. S. Sandhu, M. Bailes, R. N. Manchester, et al. The Proper Motion and Parallax of PSR J0437-4715. *Astrophysical Journal, Letters*, 478(2):L95–L98, 1997. doi: 10.1086/310562.

S. A. Sanidas, R. A. Battye, and B. W. Stappers. Constraints on cosmic string tension imposed by the limit on the stochastic gravitational wave background from the European Pulsar Timing Array. *Physical Review D*, 85(12):122003, 2012. doi: 10.1103/PhysRevD.85.122003.

M. V. Sazhin. Opportunities for detecting ultralong gravitational waves. *Soviet Astronomy*, 22:36–38, 1978.

R. Schödel, T. Ott, R. Genzel, et al. A star in a 15.2-year orbit around the supermassive black hole at the centre of the Milky Way. *Nature*, 419(6908):694–696, 2002. doi: 10.1038/nature01121.

K. Schwarzschild. On the Gravitational Field of a Mass Point According to Einstein's Theory. *Abh. Konigl. Preuss. Akad. Wissenschaften Jahre 1906,92, Berlin,1907*, 1916, 1916.

M. Serylak, S. Johnston, M. Kramer, et al. The thousand-pulsar-array programme on MeerKAT IV: Polarization properties of young, energetic pulsars. *Monthly Notices of the RAS*, 505(3):4483–4495, 2021. doi: 10.1093/mnras/staa2811.

A. Sesana. Systematic investigation of the expected gravitational wave signal from supermassive black hole binaries in the pulsar timing band. *Monthly Notices of the RAS*, 433:L1–L5, 2013. doi: 10.1093/mnrasl/slt034.

A. Sesana. Prospects for Multiband Gravitational-Wave Astronomy after GW150914. *Physical Review Letters*, 116(23):231102, 2016. doi: 10.1103/PhysRevLett.116.231102.

A. Sesana, F. Haardt, P. Madau, and M. Volonteri. Low-Frequency Gravitational Radiation from Coalescing Massive Black Hole Binaries in Hierarchical Cosmologies. *Astrophysical Journal*, 611(2):623–632, 2004. doi: 10.1086/422185.

A. Sesana, A. Vecchio, and C. N. Colacino. The stochastic gravitational-wave background from massive black hole binary systems: implications for observations with Pulsar Timing Arrays. *Monthly Notices of the RAS*, 390(1):192–209, 2008. doi: 10.1111/j.1365-2966.2008.13682.x.

R. M. Shannon and J. M. Cordes. Assessing the Role of Spin Noise in the Precision Timing of Millisecond Pulsars. *Astrophysical Journal*, 725(2):1607–1619, 2010. doi: 10.1088/0004-637X/725/2/1607.

R. M. Shannon, J. M. Cordes, T. S. Metcalfe, et al. An Asteroid Belt Interpretation for the Timing Variations of the Millisecond Pulsar B1937+21. *Astrophysical Journal*, 766(1):5, 2013a. doi: 10.1088/0004-637X/766/1/5.

R. M. Shannon, V. Ravi, W. A. Coles, et al. Gravitational-wave limits from pulsar timing constrain supermassive black hole evolution. *Science*, 342:334–337, 2013b. doi: 10.1126/science.1238012.

R. M. Shannon, S. Osłowski, S. Dai, et al. Limitations in timing precision due to single-pulse shape variability in millisecond pulsars. *Monthly Notices of the RAS*, 443(2):1463–1481, 2014. doi: 10.1093/mnras/stu1213.

R. M. Shannon, V. Ravi, L. T. Lentati, et al. Gravitational waves from binary supermassive black holes missing in pulsar observations. *Science*, 349(6255):1522–1525, 2015. doi: 10.1126/science.aab1910.

S. L. Shapiro and S. A. Teukolsky. *Black holes, white dwarfs and neutron stars. The physics of compact objects*. A Wiley-Interscience Publication, New York: Wiley, 1983, 1983. doi: 10.1002/9783527617661.

F. Shu, J. Najita, E. Ostriker, et al. Magnetocentrifugally Driven Flows from Young Stars and Disks. I. A Generalized Model. *Astrophysical Journal*, 429:781, 1994. doi: 10.1086/174363.

F. H. Shu, F. C. Adams, and S. Lizano. Star formation in molecular clouds: observation and theory. *Annual Review of Astron and Astrophysis*, 25:23–81, 1987. doi: 10.1146/annurev.aa.25.090187.000323.

X. Siemens, V. Mandic, and J. Creighton. Gravitational-Wave Stochastic Background from Cosmic Strings. *Physical Review Letters*, 98(11):111101, 2007. doi: 10.1103/PhysRevLett.98.111101.

X. Siemens, J. Ellis, F. Jenet, and J. D. Romano. The stochastic background: scaling laws and time to detection for pulsar timing arrays. *Classical and Quantum Gravity*, 30(22):224015, 2013. doi: 10.1088/0264-9381/30/22/224015.

J. Simon and S. Burke-Spolaor. Constraints on Black Hole/Host Galaxy Co-evolution and Binary Stalling Using Pulsar Timing Arrays. *Astrophysical Journal*, 826(1):11, 2016. doi: 10.3847/0004-637X/826/1/11.

J. Skilling. Nested Sampling. In Rainer Fischer, Roland Preuss, and Udo Von Toussaint, editors, *Bayesian Inference and Maximum Entropy Methods in Science and Engineering: 24th International Workshop on Bayesian Inference and Maximum Entropy Methods in Science and Engineering*, volume 735 of *American Institute of Physics Conference Series*, pages 395–405. AIP, 2004. doi: 10.1063/1.1835238.

C. Sobey, A. V. Bilous, J. M. Grießmeier, et al. Low-frequency Faraday rotation measures towards pulsars using LOFAR: probing the 3D Galactic halo magnetic field. *Monthly Notices of the RAS*, 484(3):3646–3664, 2019. doi: 10.1093/mnras/stz214.

R. Spiewak, M. Bailes, M. T. Miles, et al. The MeerTime Pulsar Timing Array: A census of emission properties and timing potential. *Publications of the Astron. Soc. of Australia*, 39:e027, 2022. doi: 10.1017/pasa.2022.19.

D. H. Staelin and E. C. Reifenstein. Pulsating Radio Sources near the Crab Nebula. *Science*, 162(3861):1481–1483, 1968. doi: 10.1126/science.162.3861.1481.

I. H. Stairs. Testing General Relativity with Pulsar Timing. *Living Reviews in Relativity*, 6(1):5, 2003. doi: 10.12942/lrr-2003-5.

I. H. Stairs, S. E. Thorsett, and F. Camilo. Coherently Dedispersed Polarimetry of Millisecond Pulsars. *Astrophysical Journal, Supplement*, 123(2):627–638, 1999. doi: 10.1086/313245.

I. H. Stairs, S. E. Thorsett, R. J. Dewey, M. Kramer, and C. A. McPhee. The formation of the double pulsar PSR J0737-3039A/B. *Monthly Notices of the RAS*, 373(1): L50–L54, 2006. doi: 10.1111/j.1745-3933.2006.00241.x.

D. R. Stinebring, J. M. Cordes, J. M. Rankin, J. M. Weisberg, and V. Boriakoff. Pulsar polarization fluctuations. I. 1404 MHz statistical summaries. *Astrophysical Journal, Supplement*, 55:247–277, 1984. doi: 10.1086/190954.

D. R. Stinebring, M. F. Ryba, J. H. Taylor, and R. W. Romani. Cosmic gravitational-wave background: Limits from millisecond pulsar timing. *Physical Review Letters*, 65(3):285–288, 1990. doi: 10.1103/PhysRevLett.65.285.

A. Susobhanan, A. Gopakumar, G. Hobbs, and S. R. Taylor. Pulsar timing array signals induced by black hole binaries in relativistic eccentric orbits. *Physical Review D*, 101 (4):043022, 2020. doi: 10.1103/PhysRevD.101.043022.

C. M. Tan, C. G. Bassa, S. Cooper, et al. LOFAR Discovery of a 23.5 s Radio Pulsar. *Astrophysical Journal*, 866(1):54, 2018. doi: 10.3847/1538-4357/aade88.

P. Tarafdar, K. Nobleson, P. Rana, et al. The Indian Pulsar Timing Array: First data release. *Publications of the Astron. Soc. of Australia*, 39:e053, 2022. doi: 10.1017/pasa.2022.46.

J. H. Taylor. Pulsar Timing and Relativistic Gravity. *Philosophical Transactions of the Royal Society of London Series A*, 341(1660):117–134, 1992. doi: 10.1098/rsta.1992.0088.

J. H. Taylor and R. N. Manchester. Galactic distribution and evolution of pulsars. *Astrophysical Journal*, 215:885–896, 1977. doi: 10.1086/155426.

J. H. Taylor and J. M. Weisberg. A new test of general relativity - Gravitational radiation and the binary pulsar PSR 1913+16. *Astrophysical Journal*, 253:908–920, 1982. doi: 10.1086/159690.

J. H. Taylor, R. N. Manchester, and G. R. Huguenin. Observations of pulsar radio emission. I. Total intensity measurements of individual pulses. *Astrophysical Journal*, 195:513–528, 1975. doi: 10.1086/153351.

S. R. Taylor and J. R. Gair. Searching for anisotropic gravitational-wave backgrounds using pulsar timing arrays. *Physical Review D*, 88(8):084001, 2013. doi: 10.1103/PhysRevD.88.084001.

S. R. Taylor, M. Vallisneri, J. A. Ellis, et al. Are We There Yet? Time to Detection of Nanohertz Gravitational Waves Based on Pulsar-timing Array Limits. *Astrophysical Journal, Letters*, 819(1):L6, 2016. doi: 10.3847/2041-8205/819/1/L6.

S. R. Taylor, J. Simon, and L. Sampson. Constraints on the Dynamical Environments of Supermassive Black-Hole Binaries Using Pulsar-Timing Arrays. *Physical Review Letters*, 118(18):181102, 2017. doi: 10.1103/PhysRevLett.118.181102.

C. Thompson and R. C. Duncan. The soft gamma repeaters as very strongly magnetized neutron stars - I. Radiative mechanism for outbursts. *Monthly Notices of the RAS*, 275(2):255–300, 1995. doi: 10.1093/mnras/275.2.255.

C. Thompson and R. C. Duncan. The Soft Gamma Repeaters as Very Strongly Magnetized Neutron Stars. II. Quiescent Neutrino, X-Ray, and Alfven Wave Emission. *Astrophysical Journal*, 473:322, 1996. doi: 10.1086/178147.

K. S. Thorne and J. R. Ipser. White-Dwarf and Neutron-Star Interpretations of Pulsating Radio Sources. *Astrophysical Journal, Letters*, 152:L71, 1968. doi: 10.1086/180180.

C. Tiburzi, G. Hobbs, M. Kerr, et al. A study of spatial correlations in pulsar timing array data. *Monthly Notices of the RAS*, 455(4):4339–4350, 2016. doi: 10.1093/mnras/stv2143.

R. C. Tolman. Static Solutions of Einstein's Field Equations for Spheres of Fluid. *Physical Review*, 55(4):364–373, 1939. doi: 10.1103/PhysRev.55.364.

J. W. Tukey. *Exploratory data analysis*. Addison-Wesley Series in Behavioral Science: Quantitative Methods, Reading, Mass.: Addison-Wesley, 1977, 1977.

M. Vallisneri and R. van Haasteren. Taming outliers in pulsar-timing data sets with hierarchical likelihoods and Hamiltonian sampling. *Monthly Notices of the RAS*, 466 (4):4954–4959, 2017. doi: 10.1093/mnras/stx069.

M. Vallisneri, S. R. Taylor, J. Simon, et al. Modeling the Uncertainties of Solar System Ephemerides for Robust Gravitational-wave Searches with Pulsar-timing Arrays. *Astrophysical Journal*, 893(2):112, 2020. doi: 10.3847/1538-4357/ab7b67.

R. van Haasteren and Y. Levin. Understanding and analysing time-correlated stochastic signals in pulsar timing. *Monthly Notices of the RAS*, 428(2):1147–1159, 2013. doi: 10.1093/mnras/sts097.

R. van Haasteren, Y. Levin, P. McDonald, and T. Lu. On measuring the gravitational-wave background using Pulsar Timing Arrays. *Monthly Notices of the RAS*, 395(2): 1005–1014, 2009. doi: 10.1111/j.1365-2966.2009.14590.x.

R. van Haasteren, Y. Levin, G. H. Janssen, et al. Placing limits on the stochastic gravitational-wave background using European Pulsar Timing Array data. *Monthly Notices of the RAS*, 414(4):3117–3128, 2011. doi: 10.1111/j.1365-2966.2011.18613.x.

W. van Straten. Radio Astronomical Polarimetry and Point-Source Calibration. *Astrophysical Journal, Supplement*, 152(1):129–135, 2004. doi: 10.1086/383187.

W. van Straten. Radio Astronomical Polarimetry and High-Precision Pulsar Timing. *Astrophysical Journal*, 642(2):1004–1011, 2006. doi: 10.1086/501001.

W. van Straten. The Statistics of Radio Astronomical Polarimetry: Bright Sources and High Time Resolution. *Astrophysical Journal*, 694(2):1413–1422, 2009. doi: 10.1088/0004-637X/694/2/1413.

W. van Straten. High-fidelity Radio Astronomical Polarimetry Using a Millisecond Pulsar as a Polarized Reference Source. *Astrophysical Journal, Supplement*, 204(1): 13, 2013. doi: 10.1088/0067-0049/204/1/13.

W. van Straten, M. Bailes, M. Britton, et al. A test of general relativity from the three-dimensional orbital geometry of a binary pulsar. *Nature*, 412(6843):158–160, 2001. doi: 10.1038/35084015.

W. van Straten, R. N. Manchester, S. Johnston, and J. E. Reynolds. PSRCHIVE and PSRFITS: Definition of the Stokes Parameters and Instrumental Basis Conventions. *Publications of the Astron. Soc. of Australia*, 27(1):104–119, 2010. doi: 10.1071/AS09084.

W. van Straten, P. Demorest, and S. Oslowski. Pulsar Data Analysis with PSRCHIVE. *Astronomical Research and Technology*, 9(3):237–256, 2012. doi: 10.48550/arXiv.1205.6276.

J. P. W. Verbiest, M. Bailes, W. A. Coles, et al. Timing stability of millisecond pulsars and prospects for gravitational-wave detection. *Monthly Notices of the RAS*, 400(2):951–968, 2009. doi: 10.1111/j.1365-2966.2009.15508.x.

J. P. W. Verbiest, L. Lentati, G. Hobbs, et al. The International Pulsar Timing Array: First data release. *Monthly Notices of the RAS*, 458(2):1267–1288, 2016. doi: 10.1093/mnras/stw347.

A. Vilenkin. Gravitational radiation from cosmic strings. *Physics Letters B*, 107(1-2):47–50, 1981. doi: 10.1016/0370-2693(81)91144-8.

M. Vivekanand, J. G. Ables, and D. McConnell. Radio Emission of PSR J0437-4715 at 327 MHz. *Astrophysical Journal*, 501(2):823–829, 1998. doi: 10.1086/305847.

G. Voisin, I. Cognard, P. C. C. Freire, et al. An improved test of the strong equivalence principle with the pulsar in a triple star system. *Astronomy and Astrophysics*, 638:A24, 2020. doi: 10.1051/0004-6361/202038104.

J. Wang, N. Wang, H. Tong, and J. Yuan. Recent glitches detected in the Crab pulsar. *Astrophysics and Space Science*, 340(2):307–315, 2012. doi: 10.1007/s10509-012-1058-x.

J. Wang, G. M. Shaifullah, J. P. W. Verbiest, et al. A comparative analysis of pulse time-of-arrival creation methods. *Astronomy and Astrophysics*, 658:A181, 2022. doi: 10.1051/0004-6361/202141121.

S. Q. Wang, N. Wang, J. B. Wang, et al. Pulse Jitter and Single-pulse Variability in Millisecond Pulsars. *Astrophysical Journal*, 964(1):6, 2024a. doi: 10.3847/1538-4357/ad217b.

Z. Wang, N. Rea, T. Bao, et al. Detection of X-ray Emission from a Bright Long-Period Radio Transient. *arXiv e-prints*, page arXiv:2411.16606, 2024b. doi: 10.48550/arXiv.2411.16606.

J. M. Weisberg and Y. Huang. Relativistic Measurements from Timing the Binary Pulsar PSR B1913+16. *Astrophysical Journal*, 829(1):55, 2016. doi: 10.3847/0004-637X/829/1/55.

J. M. Weisberg and J. H. Taylor. The Relativistic Binary Pulsar B1913+16: Thirty Years of Observations and Analysis. In Fred A. Rasio and Ingrid H. Stairs, editors, *Binary Radio Pulsars*, volume 328 of *Astronomical Society of the Pacific Conference Series*, page 25, 2005. doi: 10.48550/arXiv.astro-ph/0407149.

J. M. Weisberg, D. J. Nice, and J. H. Taylor. Timing Measurements of the Relativistic Binary Pulsar PSR B1913+16. *Astrophysical Journal*, 722(2):1030–1034, 2010. doi: 10.1088/0004-637X/722/2/1030.

C. M. Will. The Confrontation between General Relativity and Experiment. *Living Reviews in Relativity*, 17(1):4, 2014. doi: 10.12942/lrr-2014-4.

A. Wolszczan. Confirmation of Earth-Mass Planets Orbiting the Millisecond Pulsar PSR B1257+12. *Science*, 264(5158):538–542, 1994. doi: 10.1126/science.264.5158.538.

A. Wolszczan and D. A. Frail. A planetary system around the millisecond pulsar PSR1257 + 12. *Nature*, 355(6356):145–147, 1992. doi: 10.1038/355145a0.

S. E. Woosley, A. Heger, and T. A. Weaver. The evolution and explosion of massive stars. *Reviews of Modern Physics*, 74(4):1015–1071, 2002. doi: 10.1103/RevModPhys.74.1015.

J. S. B. Wyithe and A. Loeb. Self-regulated Growth of Supermassive Black Holes in Galaxies as the Origin of the Optical and X-Ray Luminosity Functions of Quasars. *Astrophysical Journal*, 595(2):614–623, 2003. doi: 10.1086/377475.

K. M. Xilouris, M. Kramer, A. Jessner, et al. The Characteristics of Millisecond Pulsar Emission. II. Polarimetry. *Astrophysical Journal*, 501(1):286–306, 1998. doi: 10.1086/305791.

H. Xu, S. Chen, Y. Guo, et al. Searching for the Nano-Hertz Stochastic Gravitational Wave Background with the Chinese Pulsar Timing Array Data Release I. *Research in Astronomy and Astrophysics*, 23(7):075024, 2023. doi: 10.1088/1674-4527/acdfa5.

X. Xue, L. Bian, J. Shu, et al. Constraining Cosmological Phase Transitions with the Parkes Pulsar Timing Array. *Physical Review Letters*, 127(25):251303, 2021. doi: 10.1103/PhysRevLett.127.251303.

W. M. Yan, R. N. Manchester, G. Hobbs, et al. Rotation measure variations for 20 millisecond pulsars. *Astrophysics and Space Science*, 335(2):485–498, 2011. doi: 10.1007/s10509-011-0756-0.

J. M. Yao, R. N. Manchester, and N. Wang. A New Electron-density Model for Estimation of Pulsar and FRB Distances. *Astrophysical Journal*, 835(1):29, 2017. doi: 10.3847/1538-4357/835/1/29.

D. R. B. Yardley, G. B. Hobbs, F. A. Jenet, et al. The sensitivity of the Parkes Pulsar Timing Array to individual sources of gravitational waves. *Monthly Notices of the RAS*, 407(1):669–680, 2010. doi: 10.1111/j.1365-2966.2010.16949.x.

X. P. You, G. Hobbs, W. A. Coles, et al. Dispersion measure variations and their effect on precision pulsar timing. *Monthly Notices of the RAS*, 378(2):493–506, 2007. doi: 10.1111/j.1365-2966.2007.11617.x.

W. W. Zhu, I. H. Stairs, P. B. Demorest, et al. Testing Theories of Gravitation Using 21-Year Timing of Pulsar Binary J1713+0747. *Astrophysical Journal*, 809(1):41, 2015a. doi: 10.1088/0004-637X/809/1/41.

X. J. Zhu, G. Hobbs, L. Wen, et al. An all-sky search for continuous gravitational waves in the Parkes Pulsar Timing Array data set. *Monthly Notices of the RAS*, 444(4): 3709–3720, 2014. doi: 10.1093/mnras/stu1717.

X. J. Zhu, L. Wen, G. Hobbs, et al. Detection and localization of single-source gravitational waves with pulsar timing arrays. *Monthly Notices of the RAS*, 449(2): 1650–1663, 2015b. doi: 10.1093/mnras/stv381.

A. Zic, G. Hobbs, R. M. Shannon, et al. Evaluating the prevalence of spurious correlations in pulsar timing array data sets. *Monthly Notices of the RAS*, 516(1):410–420, 2022. doi: 10.1093/mnras/stac2100.

A. Zic, D. J. Reardon, A. Kapur, et al. The Parkes Pulsar Timing Array third data release. *Publications of the Astron. Soc. of Australia*, 40:e049, 2023. doi: 10.1017/pasa.2023.36.

Chapter 6

Glossary

AXP Anomalous X-ray Pulsar.

BH Black Hole.

DM Dispersion Measure.

ECORR Error of Correlated phase jitter per epoch.

EFAC Error Factor.

EPTA European Pulsar Timing Array.

EQUAD Error added in Quadrature.

CHIME Canadian Hydrogen Intensity Mapping Experiment.

CPTA Chinese Pulsar Timing Array.

CURN Common Uncorrelated Red Noise.

DR Data Release.

FDM Fourier Domain Monte-Carlo (method).

FGST Fermi Gamma-Ray Space Telescope.

GMC Giant Molecular Cloud.

GR General Relativity.

GW Gravitational Wave.

GWB Gravitational Wave Background.

HD Hellings-Downs (curve).

IFA Ideal Feed Assumption.

InPTA Indian Pulsar Timing Array.

IPTA International Pulsar Timing Array.

IQR Inter-Quartile Range.

ISM Inter-Stellar Medium.

ΛCDM Lambda Cold Dark Matter (model).

LIGO Laser Interferometer Gravitational-wave Observatory.

LISA Laser Interferometer Space Antenna.

MAD Median Absolute Deviation.

MCMC Markov Chain Monte-Carlo.

MEM Measurement Equation Modeling.

METM Measurement Equation Template Matching.

MJD Modified Julian Date.

MPTA MeerKAT Pulsar Timing Array.

MSP Millisecond Pulsar.

MTM Matrix Template Matching.

NANOGrav North American Nanohertz Observatory for Gravitational-waves.

NIS Nested Importance Sampling.

NS Neutron Star.

PA Position Angle.

PGS Phase Gradient Shift.

PCM Principal Component Analysis.

PPTA Parkes Pulsar Timing Array.

PSD Power Spectral Density.

PSR Pulsar.

PSRPL Polarimetric Calibration Pipeline.

PTA Pulsar Timing Array.

RFI Radio Frequency Interference.

RM Rotation Measure.

RMS Root-Mean-Square.

RVM Rotating Vector Model.

SARAO South African Radio Astronomy Observatory.

SECORR An ECORR variant.

SGR Soft Gamma-ray Repeater.

SKA Square Kilometer Array.

SMBH Super Massive Black Hole.

SMBHB Super Massive Black Hole Binary.

S/N Signal-to-Noise (ratio).

SSB Solar System Barycenter.

SSE Solar System Ephemeris.

STM Scalar Template Matching.

TAI International Atomic Time.

ToA Time-of-Arrival.

TOV Tolman-Oppenheimer-Volkoff (limit).

UTC Coordinated Universal Time.

WD White Dwarf.